

Proceedings of the 2001 Earthquake Engineering Symposium for Young Researchers



Sponsored by the National Science Foundation, Research Experiences for Undergraduates Program

August 2002



The Multidisciplinary Center for Earthquake Engineering Research

The Multidisciplinary Center for Earthquake Engineering Research (MCEER) is a national center of excellence in advanced technology applications that is dedicated to the reduction of earthquake losses nationwide. Headquartered at the University at Buffalo, State University of New York, the Center was originally established by the National Science Foundation (NSF) in 1986, as the National Center for Earthquake Engineering Research (NCEER).

Comprising a consortium of researchers from numerous disciplines and institutions throughout the United States, the Center's mission is to reduce earthquake losses through research and the application of advanced technologies that improve engineering, pre-earthquake planning and post-earthquake recovery strategies. Toward this end, the Center coordinates a nationwide program of multidisciplinary team research, education and outreach activities.

Funded principally by NSF, the State of New York and the Federal Highway Administration (FHWA), the Center derives additional support from the Federal Emergency Management Agency (FEMA), other state governments, academic institutions, foreign governments and private industry.

Proceedings of the 2001 Earthquake Engineering Symposium for Young Researchers

Compiled by
Andrea Dargush, Phillip Gould, and Gerard Pardoen

Salt Lake City, Utah
August 10-12, 2001

MCEER



Multidisciplinary Center for Earthquake Engineering Research
University at Buffalo, State University of New York
Red Jacket Quadrangle • Buffalo, NY 14261
phone: (716) 645-3391 • fax: (716) 645-3399
e-mail: mceer@mceermail.buffalo.edu
web site: <http://mceer.buffalo.edu>

MAE



Mid-America Earthquake Center
1241 Newmark Civil Engineering Lab
University of Illinois at Urbana-Champaign
205 N. Matthews Ave. • Urbana, IL 61801
phone: (217) 244-6302 • fax: (217) 333-3821
web site: <http://mae.ce.uiuc.edu>

PEER



Pacific Earthquake Engineering Research Center
University of California, Berkeley
1301 South 46th Street, RFS 451 • Richmond, California, 94804-4698
phone: (510) 231-9554 • fax: (510) 231-9471
e-mail: peer_ctr@eerc.berkeley.edu
web site: <http://peer.berkeley.edu>

MCEER-02-SP06

August 2002

*Sponsored by the National Science Foundation,
Research Experience for Undergraduates Program*

Preface

Undergraduates from across the nation converged upon Salt Lake City, Utah for the National Science Foundation (NSF) *Earthquake Engineering Symposium for Young Researchers* on August 10-12, 2001. Twenty-four student research interns attended the event.

The symposium, coordinated by the Multidisciplinary Center for Earthquake Engineering Research (MCEER), was the culmination of an eight-week program in which each student interned with a faculty advisor belonging to one of the three earthquake centers: the Mid-America Earthquake Center (MAE), the Pacific Earthquake Engineering Research Center (PEER), or MCEER. The program itself was sponsored as part of the National Science Foundation's Research Experiences for Undergraduates Program.

Primarily, the symposium served to provide a forum for the interns to present their work and get to know their peers. Over two days, participants gave a ten-minute talk regarding their project. The topics covered many different facets of earthquake engineering, thus providing a stimulating atmosphere for the interns to expand their knowledge of the field.

The presentations were complimented by numerous additional educational and social activities. First, Professor Ed Harris of Texas A & M University gave a talk on engineering ethics and the issues that face those in the field. To apply the methods for decision-making presented by Professor Harris, the session closed with the research interns breaking into groups to examine ethical case studies. An evening reception and banquet served to give the interns the opportunity to get to know one another, as well as the professors who were attending the symposium. Further, the banquet was followed by a talk by Mr. A. Parry Brown, Vice President of Reaveley Engineers & Associates, Inc. His presentation, "Designing for Earthquakes in Salt Lake City," discussed the efforts that the city is devoting to retrofitting certain buildings to mitigate the seismic hazard associated with the area. Finally, Professor T. Leslie Youd of Brigham Young University led a field trip to several seismically designed or retrofitted buildings in the Salt Lake City area. The tour included the historic Salt Lake City and County building, which had been retrofitted with base isolators, and the new Church of Latter Day Saints Conference Center, which seats about 21,000 people and is built to survive UBC Seismic Zone 4 forces.

Through the course of these internships and the symposium, the undergraduate interns learned a great deal about the discipline of earthquake engineering, while also getting a head start on meeting peers in their field from across the nation - an opportunity for which they otherwise may have had to wait for years. Given the quality of the presentations, and the fulfilling weekend of activities, the program was a great success for all those who participated..

*Submitted by Michal Orlikowski, REU Intern, Princeton University
Reprinted from the MCEER Bulletin, Volume 15, No. 3, Fall 2001*

Contents

Basic Bearing Study <i>Malita Anders, Central Florida University</i>	1
Pipeline Response to Ground Oscillation During Earthquakes <i>Laura Barton, Rensselaer Polytechnic Institute</i>	33
Nonstructural Loss Estimation: UC Berkeley Case Study <i>Rachel Dooley, University of Michigan</i>	55
A Model for the Long-Term Deformation of the New Madrid Seismic Zone and Surrounding Region <i>Matthew Dryden, University of Illinois at Urbana-Champaign</i>	67
Diagonal Tension in Unreinforced Masonry Assemblages <i>Malcolm Foss, Georgia Institute of Technology</i>	95
Estimating the Direct and Indirect Losses From a Midwest Earthquake <i>Peggy Ho, University of Illinois at Urbana-Champaign</i>	107
ED-13: Virtual Reality Retrofit Demonstrations <i>Cathleen Kennedy, Southern Illinois University, Edwardsville</i>	129
SG-12: Calibrating Intensity with Ground Motions <i>Ryan McDaniel, University of Tennessee at Martin</i>	147
3-D Cube <i>Michael Mio, University of California, Santa Barbara</i>	163
Peer Nonstructural Component Database <i>Carlos Nazario, University of Puerto Rico, Mayaguez</i>	173
Predictive Equations for Soil Shear-Wave Velocities: Tri-State Region of Connecticut, New Jersey, and New York <i>Gary Nottis, Bucknell University</i>	201
Simulating Highway Network Performance in an Earthquake's Aftermath <i>Michal Orlikowski, Princeton University</i>	225
Seismic Response of a Wood Frame Multi-Story Apartment: An Overview <i>Ryan Petersen, Texas A & M University</i>	245
Base Isolation in Steel Structures <i>Stephen Priddy, University of Tennessee at Martin</i>	261

Damage to Bridges During the 2001 Nisqually Earthquake <i>R. Tyler Ranf, Washington University in St. Louis</i>	273
Small Scale Rubber Bearing Isolators: A Brief Introduction Into Low Damping and Lead Core Bearings <i>Pamela Romano, The Catholic University of America</i>	295
Shear Strength of Rectangular Building Columns Under Seismic Loads <i>Mike Rookstool, University of Texas, Austin</i>	309
Seismic Performance of Existing Reinforced Concrete Beam-Column Joints <i>Susan Smilanich, California Polytechnic State University, San Luis Obispo</i>	329
Analytical Development of Bridge Structural Fragilities Under Near-Fault Loading <i>Carolyn Stegon, Virginia Polytechnic Institute and State University</i>	347
Finite Element Analysis of Northridge Connections <i>Josh Tolchinsky, University of Cincinnati</i>	365
Evaluation of Post-Earthquake Functionality of Highway Overpass Bridges <i>Ryan Vignes, University of Iowa</i>	375
1g Shake Table Tests on Lateral Spread and Liquefied Sand-Pile Seismic Interaction <i>Claire Vukajlovich, California Polytechnic State University, San Luis Obispo</i>	391
Seismic Instrumentation of the I-40 Mississippi River Bridge in Memphis, Tennessee <i>Vickie Watson, University of Memphis</i>	405
Agenda	417
Participants List	421

Basic Bearing Study

Malita D. Anders

Mechanical Engineering Student at the University of Central Florida

Hosted by University at Buffalo, State University of New York

Advised by Drs. Reinhorn and Whittaker

Abstract

This paper briefly discusses concepts of base isolation devices, and how they affect structures. In particular it shows the process and results from testing Low Damping Rubber Bearings and High Damping Rubber Bearings. It includes pictures and tables of tests run, a diagram of the machine used, a code written to calculate the effective stiffness and Damping ratio of the bearings.

Section One – Introduction

1.1 Conventional Framing

Conventional fixed base structures that comply with modern building code requirements will be damaged during severe earthquake shaking, and these structures are detailed to accommodate such damage. Structures are designed not to collapse during maximum earthquake shaking, however, the framing system is damaged in components that are responsible for resisting gravity loads: beams and columns. Repairing such damage after an earthquake tends to be very intensive, time-consuming, and expensive. Seismic isolation provides the structural engineer with an alternative to conventional construction that involves limited-to-no damage in the structure.

1.2 Seismic Isolation

To explain the fundamental principals of seismic isolation, consider Figure 1.1 below. Shown in the figure are typical acceleration and displacement responses to earthquake shaking. The period of the single-degree-of-freedom structure is given by:

$$(Eq.1) \quad T = 2\pi \sqrt{\frac{m}{k}},$$

where, m is the mass of the system and k is its stiffness. If k decreases, the value of the period will shift to the right, and reduce the acceleration felt by the structure. (See figure 1.1a) As the period increases and the acceleration decreases, the displacement increases as shown in Figure 1.1b. Seismic isolation facilitates the period shift from T_1 for conventional design to T_2 for a base isolated structure.

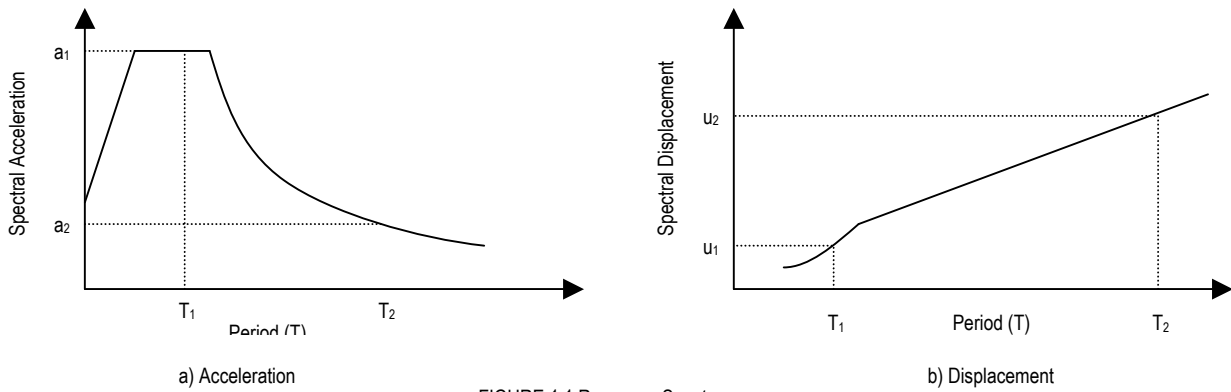


FIGURE 1.1 Response Spectra

Two styles of base isolation systems are used in the United States to achieve the period shift: sliding and elastomeric systems. The Friction Pendulum System (FPS) is a common sliding system. It has a concave sliding dish and a convex housing plate. An articulated slider moves on a stainless steel inlay that is placed on the concave dish. The isolator uses the weight of the building to bring the slider back to its original position and the friction between the slider and the top dish to absorb the input energy, in other words, to damp the system. Figure 1.2 is a picture of a FPS.

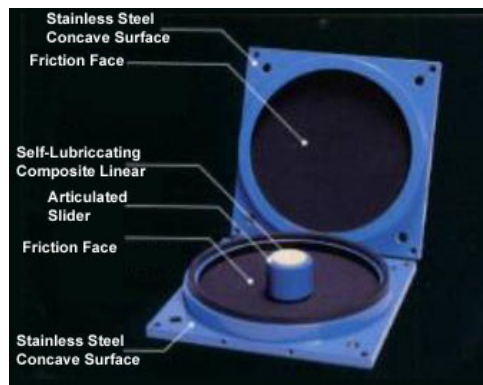


FIGURE 1.2

Elastomeric bearings include Low Damping Rubber (LDR) bearings, High Damping Rubber (HDR) bearings, and Lead Rubber (LR) bearings. Externally, these three types of bearings look the same. The type of rubber used distinguishes a bearing from LDR and HDR. A LR bearing is identical to a LDR bearing except for a cylindrical plug of lead that is inserted in the center of the bearing. LDR bearings are generally used with a supplemental damping device

to control displacements, and HDR bearings and LR bearings are typically used without supplemental damping devices. Figure 1.3 is a picture of a LR bearing.

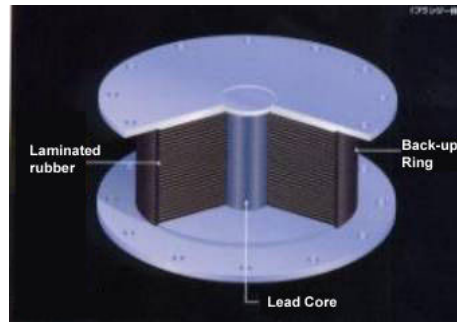


FIGURE 1.3 From <http://www.robot.com.tw/lrb.htm>

1.3 Scope of Study

This study addresses the behavior of low and high damping rubber bearings. The accurate characterization of such bearings is important as they are to be used to protect buildings and bridges. To this end, the performance of one LDR and one HDR bearing was studied with the objective of understanding their response to strain cycling, load history, and recovery.

Section Two - Initial Conditions

2.1 Dimensions of Low Damping and High Damping Rubber Bearings

	LDR	HDR
Diameter (in)	7.250	5.748
Rubber thickness (in)	0.125	0.250
Shim thickness (in)	0.075	0.118
Total thickness R (in)	2.250	3.000
Total height (in)	5.020	4.299
Loaded area (in ²)	41.282	25.967
Unloaded area (in ²)	114.338	77.676
Sleeve thickness (in)	0.125	0.118
Shape factor (in/in)	0.361	0.334

The table above summarizes the physical properties of the two types of bearings tested.

The shape factor of the LDR bearing is larger than the HDR bearing. This suggests that the LDR bearing is larger in diameter and shorter in total height. The shape factor is calculated by the following equation.

$$(Eq.2) \quad f_{shape} = \frac{A_{loaded}}{A_{unloaded}}$$

An AutoCAD drawing of the two bearing types is included in Appendix A.

Section Three - Testing Protocol

3.1 Low Damping Rubber Bearing

Six tests were conducted for each bearing. Each test consisted of five strain amplitudes, each amplitude had three cycles. Test 1 was conducted, with an increasing-amplitude sine function, on an unscragged bearing. The loading frequency for Test 2 was increased by a factor of 50 to study velocity effects on the LDR bearing. The strain-history of Test three was reversed from Test 1 to study strain-history effects. Vertical pressure on the bearing was reduced for Test 4 and Test 5 to study the effects of vertical pressure on bearing response. Test 6 was performed one or more days after Test 5 to evaluate recovery in LDR bearings. Refer to Table 3.1.

Table 3.1

Test #	Strain % 1	Strain % 2	Strain % 3	Strain % 4	Strain % 5	Frequency	Normal Force
1	5	25	50	100	200	0.01Hz	28 kips
2	5	25	50	100	200	0.5Hz	28 kips
3	200	100	50	25	5	0.01Hz	28 kips
4	5	25	50	100	200	0.01Hz	14 kips
5	5	25	50	100	200	0.01Hz	7 kips
6	5	25	50	100	200	0.01Hz	28 kips

For the Low Damping Rubber bearing two scanning rates were chosen for the data acquisition system: 200 samples per second for the testing frequency of 0.5 Hz, and 2 samples per second for the testing frequency of 0.01 Hz.

3.2 High Damping Rubber Bearing

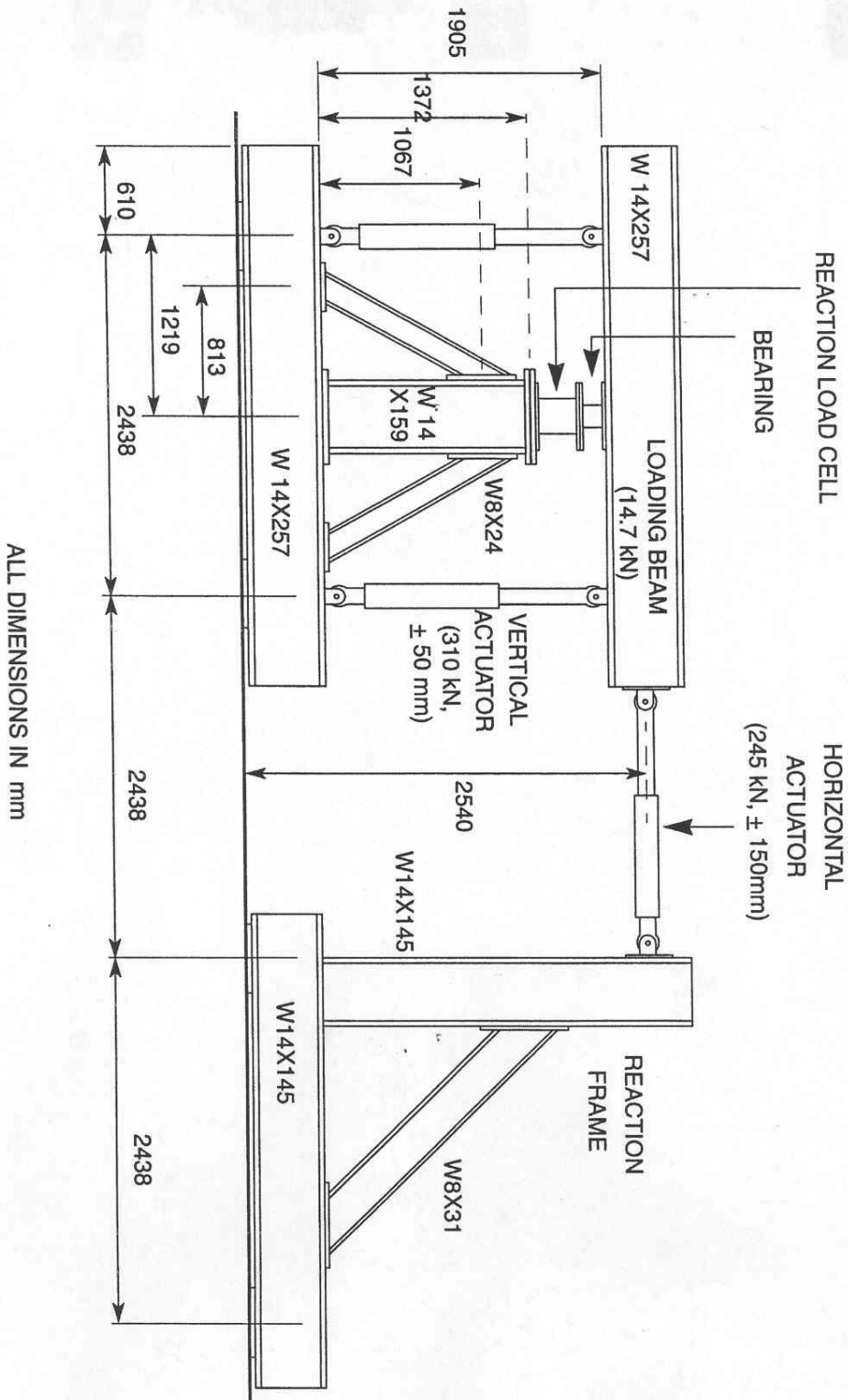
The testing protocol for the HDR bearings was most similar to that used for LDR bearings. Because the aspect ratio for the HDR bearings was greater than that of the LDR bearings, the maximum force was reduced to 6 kips. The maximum shear strain was limited to 150% to prevent buckling of the bearing at the axial load of 6 kips. See Table 3.2.

Table 3.2

Test #	Strain % 1	Strain % 2	Strain % 3	Strain % 4	Strain % 5	Frequency	Normal force
1	5	25	50	100	150	0.01Hz	6 kips
2	5	25	50	100	150	0.5Hz	6 kips
3	150	100	50	25	5	0.01Hz	6 kips

3.3 Bearing Testing Machine

The Isolator Testing Machine consists of six major parts; See Figure 3.1. Two vertical actuators maintain a constant axial load for the bearing. One horizontal actuator imposes the lateral displacement. Two load cells that are connected in-line-with the vertical actuators control the applied vertical load. A reaction load cell sits directly under the bearing to measure the axial, shear forces (Kasalanati and Constantinou, MCEER-99-0004). Each of the actuators and load cells are connected to a channel of a data acquisition system that simultaneously records information using 885 SH1 cards and TCS Optim Electronics software.



3.4 Data Processing and Calculations

The data was recorded in to ASCII format, and then exported to notepad text files. Appendix B contains the code that was used to import the ASCII text files into Mat LAB and calculate maximum and minimum displacement, maximum and minimum force, percent strain, stiffness, elastic modulus, and damping of the bearing.

The effective stiffness is calculated by

$$(Eq.3) K_{eff} = \frac{\Delta y}{\Delta x},$$

where Δy is the maximum force, and Δx is the maximum displacement within the hysteresis loop. Damping is calculated by

$$(Eq.4) \beta = \frac{A_{loop}}{2\pi K_{eff} D^2},$$

where β is the damping of the bearing, A_{loop} is the area of the hysteresis loop, K_{eff} is the maximum strain and D is the maximum displacement of the bearing. The maximum percent strain is show by

$$(Eq.5) \gamma = \frac{D}{T_{rubber}},$$

where T_{rubber} is the thickness of the rubber. The Shear Modulus is given by

$$(Eq.6) G_{eff} = \frac{K_{eff} T_{rubber}}{A_{rubber}},$$

where A_{rubber} is the loaded surface area of the bearing.

Section Four - Results

4.1 Low Damping Bearings

With each strain amplitude increase; the first cycle damping ratio was 1% greater than that of the second and third cycle initial test (Test #1) and the recovery test (Test #6). This suggests that for a bearing of this magnitude and load demand, scragging is not a major design concern. The effective stiffness did not change more .01 in/in with in each strain amplitude. When the frequency was increased, the maximum displacement, strain amplitude, and effective stiffness did not vary significantly with the values of the first test. When strain cycle was reversed the maximum displacement increased by a tenth of an inch. As the force increased the damping ratio decreased by a minimal amount. Summarized results are listed in the Appendix C.

4.2 High Damping Bearings

The maximum displacement increased by .5 inches over the course of testing, and the damping ratio increased by 10% over the course of the testing cycle. The effective stiffness increased by about 0.5 in the first test and by 1.0 in the increased frequency test (Test #2) and reversed strain amplitude test (Test #3). This could be because the recovery time is longer than testing availability of the program. Scragging has a greater effect on design concerns when using high damping bearings.

The thickness of the rubber is larger than the thickness of the shims. Even though the rubber in the HD bearing is harder than the rubber in the LD bearing the HD bearing exhibits more rubbery characteristics. The hysteretic loop is thin and wavy, rather than linear like the LD bearing loop or rectangular like the Lead Core bearing loop. Therefore the Modulus of Elasticity will be a value closer to that of rubber. When deciding what load to perform the test under, the

stability of the bearing was considered. The Modulus of elasticity and vertical height lowered the stability of the bearing under larger loads. Summarized results are listed in the Appendix D.

4.3 Importance of Base Isolation

Earthquake ground motions cause sudden movement in the horizontal direction, and depending upon the structural design, deformation will occur. Desired deformation depends on the expectable amount of damage, which changes with the function of the structure, how many people occupy it, and what items it holds? If a warehouse stores inexpensive equipment, the owner usually will cut his or her losses and rebuild after an earthquake. Infrastructure in an apartment building should at least remain intact and sustain its shape after an earthquake so that all occupants survive. Deciding if the apartment building should be able to be occupied right after an earthquake depends upon the investor. In the case critical structures, with acceleration sensitive equipment such as, emergency stations and utility providing buildings, it's critical that they remain operational during, and directly after an earthquake or some other disaster. For example, the Fire Command and Control Facility, of Los Angeles, California, the livelihood of the greater Los Angeles area depends on the facility to run at *all* times. Loosing vital functional operations such as power defeats the purpose of having a Fire and Control Facility. Base isolations systems are generally used in cases such as this, where all operational functions must be maintained. This classification is called "Immediate Occupancy" of IO for short.

Since the beginning of time man has tried to preserve Historical Sites. Society demands that they survive despite their brittle and weak nature. Most are made up of unrefined masonry and early forms of reinforced concrete. The relative displacement between each floor of such unprotected structures, due to ground motion, will destroy them.

Base isolation can sustain to both types of structures. In the case of buildings that are needed for the services they provide during and after a natural disaster, adding base isolation devices lowers the acceleration felt the electronic equipment. In the case of historical buildings, base isolation decreases the displacements relative to the floors caused by inertial forces. Base isolation works best for stiff buildings, so for weak or brittle structures, shear walls, frames, and braces are some times added. However, not as many reinforcement tools are needed when base isolation devices are added to a structure compared to the number needed in reinforced *fixed* structures. Base isolation appeals to retrofitters because the visual impact and ambiance intended by the architect is preserved.

The purpose of this paper is to provide general information on how bearings and base isolation work, and the reason for using such a system. Also, it looks at how Low Damping and High Damping Rubber Bearings respond to different loads and displacements, what physical characteristics the bearing posses, and what kind of damping they provide to the structure. When structures are base isolated with bearings, an engineer should know how the bearing would react under certain parameters, and be able to design for such reactions.

Section Five - References

Naeim, F., Kelly, J.. *Design of Seismic Isolated Structures, From Theory to Practice* . John Wiley & Sons, Inc., New York, 1999.

Chopra, A.. *Dynamics of Structures, Theory and Applications to Earthquake Engineering*. Prentice Hall, Upper Saddle River, 1995.

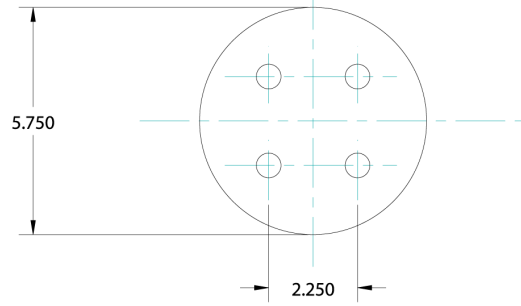
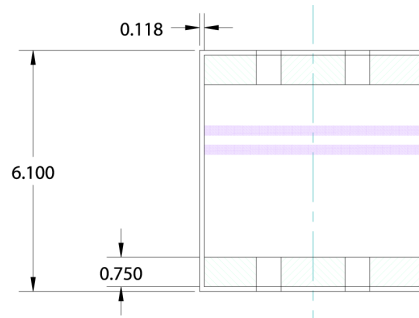
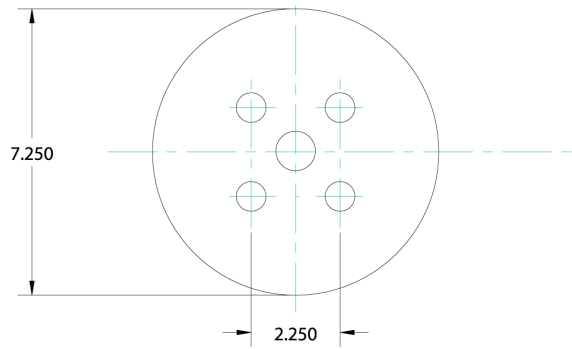
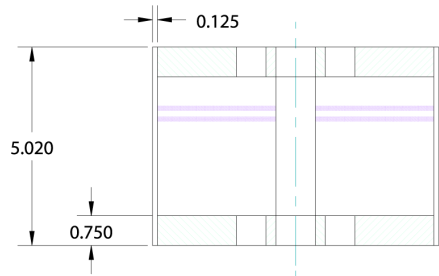
Kasalanati, A., Constantinou, M.. “Experimental Study of Bridge Elastomeric and Other Isolation and Energy Dissipation Systems with Emphasis on Uplift Prevention and High Velocity Near-Source Seismic Excitation” Technical Report MCEER-99-0004, February 26, 1999.

Special Thanks

I would like to thank the National Science Foundation (NSF) and the Multidisciplinary Center for Earthquake Engineering Research (MCEER) for making this opportunity possible. When I arrived in Buffalo, NY, I knew very little about earthquakes. Now I have a completely new perception of the importance of earthquake research. I have learned so much more than just the properties of bearings, uses for base isolation systems, how to program, use excel and write a technical paper. This opportunity has allowed me to think of what I want to do with my life, and given me memories that will last a lifetime. Thank you for providing me with this educational experience.

Thank you for your help and support this summer: Dr. Kunnath, Arvind, Gordy, Jeff, Lisa, Mike, Tony, Yasu, Siva, Diago, Dyah, Andrea Dargush, Dr. Whittaker, Dr. Reinhorn, Mom, and Daddy!

Appendix A



Appendix B

Unable to print this appendix

Appendix C

Start time	Cycle/%	Date	Time	Bearing #	Test #	Load (kips)	Max Disp. (in)	Strain	Temperature	Keff	Geff	Beta
3	1/5%	7/11/2001	10:24	LD1	1	28	0.1176	0.0522		2.274	0.1329	0.0553
103	2/5%	7/11/2001		LD1	1	28	0.1168	0.0519		2.2798	0.1333	0.0467
203	3/5%	7/11/2001		LD1	1	28	0.132	0.0587		2.2592	0.1321	0.038
303	1/25%	7/11/2001		LD1	1	28	0.5932	0.2637		1.8497	0.1081	0.0426
403	2/25%	7/11/2001		LD1	1	28	0.5889	0.2618		1.8434	0.1078	0.0406
503	3/25%	7/11/2001		LD1	1	28	0.5989	0.2662		1.8368	0.1074	0.0391
603	1/50%	7/11/2001		LD1	1	28	1.173	0.5213		1.6628	0.0972	0.038
703	2/50%	7/11/2001		LD1	1	28	1.1739	0.5218		1.6466	0.0963	0.0365
803	3/50%	7/11/2001		LD1	1	28	1.1745	0.522		1.6374	0.0957	0.0363
903	1/100%	7/11/2001		LD1	1	28	2.3083	1.0259		1.5142	0.0885	0.0345
1003	2/100%	7/11/2001		LD1	1	28	2.2933	1.0193		1.4853	0.0868	0.0335
1103	3/100%	7/11/2001		LD1	1	28	2.3014	1.0228		1.4774	0.0864	0.0332
1203	1/200%	7/11/2001		LD1	1	28	4.5566	2.0252		1.5189	0.0888	0.0445
1303	2/200%	7/11/2001		LD1	1	28	4.5478	2.0213		1.3938	0.0815	0.0382
1403	3/200%	7/11/2001		LD1	1	28	4.5473	2.021		1.3559	0.0793	0.0383

Start time	Cycle/%	Date	Time	Bearing #	Test #	Load (kips)	Max Disp. (in)	Strain	Temperature	Keff	Geff	Beta
1.65	1/5%	7/11/2001	10:55	LD1	2	0	0.1913	0.085		2.2863	0.1337	0.0211
3.65	2/5%	7/11/2001		LD1	2	0	0.1905	0.0847		2.2441	0.1312	0.024
5.65	3/5%	7/11/2001		LD1	2	0	0.1905	0.0847		2.2467	0.1314	0.0241
7.65	1/25%	7/11/2001		LD1	2	0.6904	0.6861	0.3068		1.8495	0.1081	0.0354
9.65	2/25%	7/11/2001		LD1	2	0.6887	0.6887	0.3049		1.8267	0.1068	0.0369
11.65	3/25%	7/11/2001		LD1	2	1.2454	1.2454	0.3061		1.8237	0.1066	0.036
13.65	1/50%	7/11/2001		LD1	2	1.2448	1.2448	0.5535		1.6464	0.0963	0.0401
15.65	2/50%	7/11/2001		LD1	2	1.2448	1.2448	0.5533		1.6283	0.0952	0.0403
17.65	3/50%	7/11/2001		LD1	2	1.2452	1.2452	0.5534		1.6251	0.095	0.0401
19.65	1/100%	7/11/2001		LD1	2	2.3628	2.3628	1.0499		1.4421	0.0843	0.0407
21.65	2/100%	7/11/2001		LD1	2	2.3627	2.3627	1.0501		1.4192	0.083	0.0407
23.65	3/100%	7/11/2001		LD1	2	2.3621	2.3621	1.0498		1.4128	0.0826	0.0407
25.65	1/200%	7/11/2001		LD1	2	4.5699	4.5699	2.0429		1.4252	0.0833	0.0392
27.65	2/200%	7/11/2001		LD1	2	4.5975	4.5975	2.0433		1.378	0.0806	0.0384
29.65	3/200%	7/11/2001		LD1	2	4.5969	4.5969	2.0431		1.3644	0.0798	0.0384

Start Time	Date	Time	Bearing #	Test #	Load (kips)	Max Disp. (in)	Strain	Temperature	Keff	Geff	Beta
3 1/200%	7/11/2001	11:02	LD1	3	28	4.6181	2.0525		1.3414	0.0784	0.0378
103 2/200%	7/11/2001		LD1	3	28	4.6181	2.0525		1.305	0.0763	0.0379
203 3/200%	7/11/2001		LD1	3	28	4.6176	2.0523		1.2926	0.0756	0.0381
303 1/100%	7/11/2001		LD1	3	28	2.3642	1.0507		1.2748	0.0745	0.0396
403 2/100%	7/11/2001		LD1	3	28	2.3646	1.0509		1.2841	0.0751	0.0383
503 3/100%	7/11/2001		LD1	3	28	2.3644	1.0508		1.2876	0.0753	0.0378
603 1/50%	7/11/2001		LD1	3	28	1.2409	0.5515		1.4274	0.0835	0.0415
703 2/50%	7/11/2001		LD1	3	28	1.2418	0.5519		1.4415	0.0845	0.0387
803 3/50%	7/11/2001		LD1	3	28	1.2409	0.5515		1.4466	0.0846	0.0381
903 1/25%	7/11/2001		LD1	3	28	0.6735	0.2993		1.583	0.0925	0.0394
1003 2/25%	7/11/2001		LD1	3	28	0.6726	0.2989		1.6065	0.0939	0.0363
1103 3/25%	7/11/2001		LD1	3	28	0.6793	0.3019		1.608	0.094	0.0351
1203 1/5%	7/11/2001		LD1	3	28	0.2319	0.1031		1.9227	0.1224	0.0197
1303 2/5%	7/11/2001		LD1	3	28	0.2318	0.103		1.946	0.1138	0.0145
1403 3/5%	7/11/2001		LD1	3	28	0.2338	0.1039		1.9556	0.1143	0.0138

Start time	Date	Time	Bearing #	Test #	Load (kips)	Max Disp. (in)	Strain	Temperature	Keff	Geff	Beta
4 1/5%	7/11/2001	11:32	LD1	4	14	0.2383	0.1059		2.1912	0.1281	0.0116
104 2/5%	7/11/2001		LD1	4	14	0.2379	0.1058		2.2204	0.1298	0.0127
202 3/5%	7/11/2001		LD1	4	14	0.2351	0.1045		2.2424	0.1311	0.0125
302 1/25%	7/11/2001		LD1	4	14	0.6991	0.3072		1.8407	0.1076	0.0288
402 2/25%	7/11/2001		LD1	4	14	0.6932	0.3081		1.8326	0.1071	0.0289
502 3/25%	7/11/2001		LD1	4	14	0.6949	0.3088		1.8316	0.1071	0.0289
602 1/50%	7/11/2001		LD1	4	14	1.2675	0.5633		1.6485	0.0964	0.0296
702 2/50%	7/11/2001		LD1	4	14	1.2705	0.5647		1.6407	0.0959	0.0295
802 3/50%	7/11/2001		LD1	4	14	1.2724	0.5655		1.6371	0.0957	0.0294
902 1/100%	7/11/2001		LD1	4	14	2.3994	1.0664		1.4367	0.084	0.0307
1002 2/100%	7/11/2001		LD1	4	14	2.4013	1.0673		1.4253	0.0833	0.0307
1102 3/100%	7/11/2001		LD1	4	14	2.4051	1.0689		1.4242	0.0833	0.0306
1202 1/200%	7/11/2001		LD1	4	14	4.6736	2.0772		1.4149	0.0827	0.0317
1302 2/200%	7/11/2001		LD1	4	14	4.6789	2.0795		1.3842	0.0809	0.0304
1402 3/200%	7/11/2001		LD1	4	14	4.6778	2.079		1.3736	0.0803	0.0307

Start Time	Date	Time	Bearing #	Test #	Load (kips)	Max Disp. (in)	Strain	Temperature	Keff	Geff	Beta
5 1/5%	7/11/2001	12:05	LD1	5	7	0.1594	0.0708		2.1995	0.1286	0.0253
105 2/5%	7/11/2001		LD1	5	7	0.1611	0.0716		2.2659	0.1325	0.0266
205 3/5%	7/11/2001		LD1	5	7	0.1639	0.0728		2.2509	0.1316	0.0265
305 1/25%	7/11/2001		LD1	5	7	0.6127	0.02723		1.8623	0.1089	0.0378
405 2/25%	7/11/2001		LD1	5	7	0.6156	0.2736		1.8584	0.1087	0.0368
505 3/25%	7/11/2001		LD1	5	7	0.6161	0.2738		1.8542	0.1084	0.0362
605 1/50%	7/11/2001		LD1	5	7	1.1863	0.5273		1.6657	0.0974	0.0342
705 2/50%	7/11/2001		LD1	5	7	1.1871	0.5276		1.6579	0.0969	0.0337
805 3/50%	7/11/2001		LD1	5	7	1.1869	0.5275		1.6559	0.0968	0.0338
905 1/100%	7/11/2001		LD1	5	7	2.3134	1.0282		1.4456	0.0845	0.0321
1005 2/100%	7/11/2001		LD1	5	7	2.3143	1.0286		1.4338	0.0838	0.0326
1105 3/100%	7/11/2001		LD1	5	7	2.3154	1.0291		1.4302	0.0836	0.0327
1205 1/200%	7/11/2001		LD1	5	7	4.5793	2.0352		1.4301	0.0836	0.0296
1305 2/200%	7/11/2001		LD1	5	7	4.5814	2.0362		1.4045	0.0821	0.0294
1405 3/200%	7/11/2001		LD1	5	7	4.5784	2.0348		1.3952	0.0816	0.0297

Start Time	Date	Time	Bearing #	Test #	Load (kips)	Max Disp. (in)	Strain	Temperature	Keff	Geff	Beta
1/5%			LD1	6	28						
2/5%			LD1	6	28						
3/5%			LD1	6	28						
1/25%			LD1	6	28						
2/25%			LD1	6	28						
3/25%			LD1	6	28						
1/50%			LD1	6	28						
2/50%			LD1	6	28						
3/50%			LD1	6	28						
1/100%			LD1	6	28						
2/100%			LD1	6	28						
3/100%			LD1	6	28						
1/200%			LD1	6	28						
2/200%			LD1	6	28						
3/200%			LD1	6	28						

Start time	Cycle/%	Date	Time	Bearing #	Test #	Load (kips)	Max Disp. (in)	Strain	Temperature	Keff	Geff	Beta
3	1/5%	7/10/2001	13:18	LD3	1	28	0.1202	0.0534		2.4002	0.1403	0.0497
103	2/5%	7/10/2001		LD3	1	28	0.1206	0.0536		2.3983	0.1402	0.05
203	3/5%	7/10/2001		LD3	1	28	0.1251	0.0556		2.3463	0.1372	0.0462
303	1/25%	7/10/2001		LD3	1	28	0.5764	0.2562		1.9051	0.1114	0.0498
403	2/25%	7/10/2001		LD3	1	28	0.5754	0.2557		1.8854	0.1102	0.0467
503	3/25%	7/10/2001		LD3	1	28	0.5797	0.2577		1.8861	0.1103	0.0456
603	1/50%	7/10/2001		LD3	1	28	1.1473	0.5099		1.689	0.0987	0.0426
703	2/50%	7/10/2001		LD3	1	28	1.1447	0.5088		1.681	0.0983	0.0406
803	3/50%	7/10/2001		LD3	1	28	1.1432	0.5081		1.673	0.0978	0.0407
903	1/100%	7/10/2001		LD3	1	28	2.2695	1.0087		1.5343	0.0897	0.0381
1003	2/100%	7/10/2001		LD3	1	28	2.2657	1.007		1.5019	0.0878	0.0365
1103	3/100%	7/10/2001		LD3	1	28	2.2729	1.0102		1.4904	0.0871	0.0361
1203	1/200%	7/10/2001		LD3	1	28	4.5349	2.0155		1.5143	0.0885	0.0448
1303	2/200%	7/10/2001		LD3	1	28	4.5261	2.0116		1.3821	0.0808	0.0381
1403	3/200%	7/10/2001		LD3	1	28	4.5234	2.0104		1.3422	0.0785	0.0385

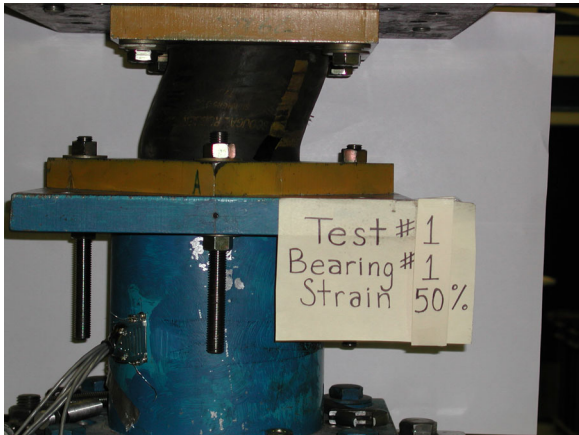
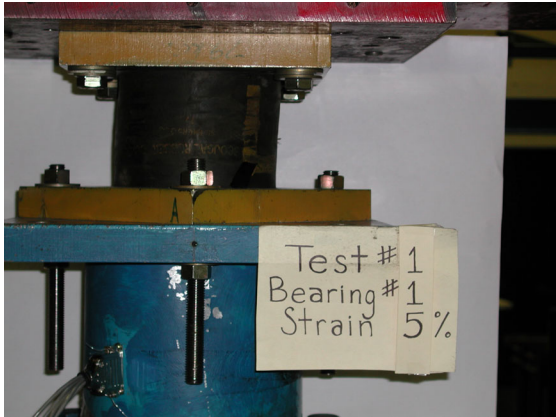
Start time	Cycle/%	Date	Time	Bearing #	Test #	Load (kips)	Max Disp. (in)	Strain	Temperature	Keff	Geff	Beta
1.3	1/5%	7/10/2001	14:17	LD3	2	28	0.1127	0.0501		2.4472	0.1431	0.063
3.3	2/5%	7/10/2001		LD3	2	28	0.1127	0.0501		2.4119	0.141	0.0644
5.3	3/5%	7/10/2001		LD3	2	28	0.1138	0.0506		2.3994	0.1403	0.0645
7.3	1/25%	7/10/2001		LD3	2	28	0.5612	0.2498		1.9313	0.1129	0.0599
9.3	2/25%	7/10/2001		LD3	2	28	0.561	0.2493		1.9149	0.112	0.058
11.3	3/25%	7/10/2001		LD3	2	28	0.5597	0.2488		1.9132	0.1119	0.058
13.3	1/50%	7/10/2001		LD3	2	28	1.125	0.5		1.7027	0.0995	0.0537
15.3	2/50%	7/10/2001		LD3	2	28	1.1218	0.4986		1.6924	0.0989	0.0523
17.3	3/50%	7/10/2001		LD3	2	28	1.1233	0.4992		1.6841	0.0985	0.0523
19.3	1/100%	7/10/2001		LD3	2	28	2.2433	0.997		1.479	0.0865	0.0488
21.3	2/100%	7/10/2001		LD3	2	28	2.2419	0.9964		1.455	0.0851	0.0474
23.3	3/100%	7/10/2001		LD3	2	28	2.2414	0.9962		1.4465	0.08446	0.0476
25.3	1/200%	7/10/2001		LD3	2	28	4.4771	1.9898		1.4369	0.084	0.0435
27.3	2/200%	7/10/2001		LD3	2	28	4.4771	1.9898		1.4369	0.084	0.0435
29.3	3/200%	7/10/2001		LD3	2	28	4.4767	1.9897		1.3593	0.0795	0.0414

Start time	Cycle/%	Date	Time	Bearing #	Test #	Load (kips)	Max Disp. (in)	Strain	Temperature	Keff	Geff	Beta
2	1/200%	7/10/2001	14:22	LD3	3	28	4.5126	2.0056		1.3284	0.0777	0.0403
102	2/200%	7/10/2001		LD3	3	28	4.5141	2.0062		1.291	0.0755	0.0397
202	3/200%	7/10/2001		LD3	3	28	4.5135	2.006		1.2758	0.0746	0.0401
302	1/100%	7/10/2001		LD3	3	28	2.2571	1.0032		1.2794	0.0748	0.0457
402	2/100%	7/10/2001		LD3	3	28	2.2584	1.0038		1.2876	0.0753	0.0442
502	3/100%	7/10/2001		LD3	3	28	2.2582	1.0037		1.2914	0.0755	0.0437
602	1/50%	7/10/2001		LD3	3	28	1.1344	0.5042		1.4423	0.0843	0.0526
702	2/50%	7/10/2001		LD3	3	28	1.1338	0.5039		1.4564	0.0851	0.0497
802	3/50%	7/10/2001		LD3	3	28	1.1351	0.5045		1.4582	0.0853	0.0487
902	1/25%	7/10/2001		LD3	3	28	0.5668	0.2519		1.6114	0.0942	0.0593
1002	2/25%	7/10/2001		LD3	3	28	0.5657	0.2514		1.6178	0.0946	0.0556
1102	3/25%	7/10/2001		LD3	3	28	0.5666	0.2518		1.6351	0.0956	0.0543
1202	1/5%	7/10/2001		LD3	3	28	N/A	N/A		N/A	N/A	N/A
1302	2/5%	7/10/2001		LD3	3	28	N/A	N/A		N/A	N/A	N/A
1402	3/5%	7/10/2001		LD3	3	28	N/A	N/A		N/A	N/A	N/A

Start time	Cycle/%	Date	Time	Bearing #	Test #	Load (kips)	Max Disp. (in)	Strain	Temperature	Keff	Geff	Beta
6	1/5%	7/10/2001	14:58	LD3	4	14	0.1157	0.0514		2.2533	0.1317	0.0568
106	2/5%	7/10/2001		LD3	4	14	0.1163	0.0517		2.2927	0.134	0.055
206	3/5%	7/10/2001		LD3	4	14	0.1204	0.0535		2.2617	0.1322	0.0554
306	1/25%	7/10/2001		LD3	4	14	0.5672	0.2521		1.8586	0.1087	0.047
406	2/25%	7/10/2001		LD3	4	14	0.5711	0.2538		1.8523	0.1083	0.0466
506	3/25%	7/10/2001		LD3	4	14	0.5677	0.2523		1.8501	0.1082	0.0467
606	1/50%	7/10/2001		LD3	4	14	1.1372	0.5054		1.6543	0.0967	0.0401
706	2/50%	7/10/2001		LD3	4	14	1.1387	0.5061		1.6456	0.0962	0.0398
806	3/50%	7/10/2001		LD3	4	14	1.14234	0.5082		1.6404	0.0959	0.0394
906	1/100%	7/10/2001		LD3	4	14	2.2693	1.0086		1.4319	0.0837	0.0368
1006	2/100%	7/10/2001		LD3	4	14	2.3186	1.0305		1.4199	0.083	0.0354
1106	3/100%	7/10/2001		LD3	4	14	2.3224	1.0322		1.1465	0.0828	0.0349
1206	1/200%	7/10/2001		LD3	4	14	4.5743	2.033		1.3975	0.0817	0.0342
1306	2/200%	7/10/2001		LD3	4	14	4.4791	2.0352		1.3642	0.0798	0.0317
1406	3/200%	7/10/2001		LD3	4	14	4.5789	2.0351		1.3535	0.0791	0.0319

Start time	Cycle/%	Date	Time	Bearing #	Test #	Load (kips)	Max Disp. (in)	Strain	Temperature	Keff	Geff	Beta
2	1/5%	7/10/2001	15:30	LD3	5	7	0.1476	0.0656		2.2592	0.1321	0.0382
102	2/5%	7/10/2001		LD3	5	7	0.1099	0.0488		2.3437	0.137	0.0497
202	3/5%	7/10/2001		LD3	5	7	0.1853	0.0823		2.3053	0.1348	0.0252
302	1/25%	7/10/2001		LD3	5	7	0.6443	0.2863		1.8777	0.1098	0.0373
402	2/25%	7/10/2001		LD3	5	7	0.6398	0.2843		1.8658	0.1091	0.0366
502	3/25%	7/10/2001		LD3	5	7	0.6461	0.2872		1.8707	0.1094	0.0358
602	1/50%	7/10/2001		LD3	5	7	1.2148	0.5399		1.6647	0.0973	0.0344
702	2/50%	7/10/2001		LD3	5	7	1.2283	0.5459		1.649	0.0964	0.0344
802	3/50%	7/10/2001		LD3	5	7	1.2161	0.5405		1.6501	0.0965	0.0347
902	1/100%	7/10/2001		LD3	5	7	2.3049	1.0244		1.437	0.084	0.034
1002	2/100%	7/10/2001		LD3	5	7	2.3027	1.0234		1.4229	0.0832	0.0349
1102	3/100%	7/10/2001		LD3	5	7	2.3036	1.0238		1.4188	0.083	0.0349
1202	1/200%	7/10/2001		LD3	5	7	4.5604	2.0268		1.4097	0.0824	0.0304
1302	2/200%	7/10/2001		LD3	5	7	4.5555	2.0247		1.3858	0.081	0.0297
1402	3/200%	7/10/2001		LD3	5	7	4.5589	2.0262		1.3756	0.0804	0.0299

Start time	Cycle/%	Date	Time	Bearing #	Test #	Load (kips)	Max Disp. (in)	Strain	Temperature	Keff	Geff	Beta
2	1/5%	7/11/2001	9:06	LD3	6	28	0.1046	0.0465		1.8525	0.1083	0.0753
102	2/5%	7/11/2001		LD3	6	28	0.1562	0.0694		1.8508	0.1082	0.0469
202	3/5%	7/11/2001		LD3	6	28	0.1249	0.0555		1.9135	0.1119	0.0526
302	1/25%	7/11/2001		LD3	6	28	0.5668	0.2519		1.5012	0.0878	0.0624
402	2/25%	7/11/2001		LD3	6	28	0.5869	0.2608		1.4878	0.087	0.06
502	3/25%	7/11/2001		LD3	6	28	0.5631	0.2502		1.4984	0.0876	0.0619
602	1/50%	7/11/2001		LD3	6	28	1.1663	0.50183		1.3509	0.079	0.0558
702	2/50%	7/11/2001		LD3	6	28	1.1467	0.5097		1.3393	0.0783	0.0546
802	3/50%	7/11/2001		LD3	6	28	1.1477	0.5101		1.332	0.0779	0.0544
902	1/100%	7/11/2001		LD3	6	28	2.2708	1.0093		1.2286	0.0718	0.0511
1002	2/100%	7/11/2001		LD3	6	28	2.2725	1.01		1.2057	0.0705	0.0508
1102	3/100%	7/11/2001		LD3	6	28	2.2733	1.0103		1.1993	0.0701	0.0509
1202	1/200%	7/11/2001		LD3	6	28	4.5276	2.0123		1.1914	0.0697	0.0579
1302	2/200%	7/11/2001		LD3	6	28	4.5274	2.0122		1.1272	0.0659	0.0577
1402	3/200%	7/11/2001		LD3	6	28	4.5274	2.0122		1.1054	0.0646	0.0586



Appendix D

Start time	Cycle/%	Date	Time	Bearing #	Test #	Load (kips)	Max Disp. (in)	Strain	Temperature	Keff	Geff	Beta
2	1/5%	8/3/2001	9:47	HD4	1	6	0.2576	0.0859		1.8027	0.2266	0.0607
102	2/5%			HD4	1	6	0.2557	0.0852		1.7968	0.2259	0.0563
202	3/5%			HD4	1	6	0.255	0.085		1.7896	0.225	0.0546
302	1/25%			HD4	1	6	0.8876	0.02959		1.1324	0.1424	0.107
402	2/25%			HD4	1	6	0.8876	0.2959		1.0785	0.1356	0.0975
502	3/25%			HD4	1	6	0.8842	0.2947		1.0556	0.1327	0.0974
602	1/50%			HD4	1	6	1.68	0.56		0.8972	0.1128	0.114
702	2/50%			HD4	1	6	1.68	0.56		0.8483	0.1067	0.1076
802	3/50%			HD4	1	6	1.6768	0.5589		0.80249	0.1037	0.1076
902	1/100%			HD4	1	6	3.2689	1.0896		0.7567	0.0951	0.1264
1002	2/100%			HD4	1	6	3.2704	1.0901		0.6732	0.0846	0.1223
1102	3/100%			HD4	1	6	3.247	1.0882		0.6467	0.0813	0.1232
1202	1/150%			HD4	1	6	4.8409	1.6136		0.773	0.0972	0.1228
1302	2/150%			HD4	1	6	4.9061	1.6354		0.6744	0.0848	0.1259
1402	3/150%			HD4	1	6	4.9041	1.6347		0.6555	0.0782	0.1279

Start time	Cycle/%	Date	Time	Bearing #	Test #	Load (kips)	Max Disp. (in)	Strain	Temperature	Keff	Geff	Beta
15	1/5%	8/3/2001	10:20	HD4	2	6	0.3293	0.1098		1.8902	0.2376	0.0427
17	2/5%			HD4	2	6	0.339	0.113		1.8395	0.2313	0.0379
19	3/5%			HD4	2	6	0.3276	0.1092		1.9045	0.2394	0.0385
21	1/25%			HD4	2	6	0.9549	0.3183		1.1637	0.1463	0.1153
23	2/25%			HD4	2	6	0.9549	0.3183		1.1637	0.1463	0.1153
25	3/25%			HD4	2	6	0.9549	0.3183		1.0947	0.1376	0.1124
27	1/50%			HD4	2	6	1.7426	0.5809		0.8856	0.1113	0.1422
29	2/50%			HD4	2	6	1.7417	0.5806		0.8375	0.1053	0.1434
31	3/50%			HD4	2	6	1.7408	0.5803		0.5803	0.8202	0.145
33	1/100%			HD4	2	6	3.3141	1.1047		0.6925	0.0871	0.1646
35	2/100%			HD4	2	6	3.315	1.105		0.6479	0.0815	0.1669
37	3/100%			HD4	2	6	3.3158	1.1053		0.6331	0.0796	0.1682
39	1/150%			HD4	2	6	4.8859	1.6286		0.7614	0.0957	0.1453
41	2/150%			HD4	2	6	4.8846	1.6282		0.714	0.0898	0.1492
43	3/150%			HD4	2	6	4.8847	1.6282		0.6928	0.0871	0.1503

Start time	Cycle/%	Date	Time	Bearing #	Test #	Load (kips)	Max Disp. (in)	Strain	Temperature	Keff	Geff	Beta
5	1/150%	8/3/2001	10:25	HD4	3	6	4.9052	1.6351		0.5749	0.0723	0.1344
105	2/150%			HD4	3	6	4.9061	1.6354		0.5516	0.0693	0.1339
205	3/150%			HD4	3	6	4.905	1.635		0.5352	0.0673	0.1347
305	1/100%			HD4	3	6	3.3283	1.1094		0.4177	0.0525	0.1672
405	2/100%			HD4	3	6	3.3283	1.1094		0.4198	0.0527	0.1654
505	3/100%			HD4	3	6	3.3281	1.1094		0.4231	0.0532	0.1659
605	1/50%			HD4	3	6	1.7488	0.5829		0.4904	0.0617	0.1602
705	2/50%			HD4	3	6	1.749	0.583		0.5029	0.0632	0.1521
805	3/50%			HD4	3	6	1.7494	0.5831		0.5076	0.0638	0.1474
905	1/25%			HD4	3	6	0.9587	0.3196		0.6162	0.0775	0.1277
1005	2/25%			HD4	3	6	0.9589	0.3196		0.6326	0.0795	0.1231
1105	3/25%			HD4	3	6	0.9465	0.3155		0.6532	0.0821	0.1207
1205	1/5%			HD4	3	6	0.3152	0.1051		0.9996	0.1257	0.0471
1305	2/5%			HD4	3	6	0.3144	0.1048		0.983	0.1236	0.0466
1405	3/5%			HD4	3	6	0.2955	0.0985		1.0346	0.1301	0.0481
												1.8745

Start time	Cycle/%	Date	Time	Bearing #	Test #	Load (kips)	Max Disp. (in)	Strain	Temperature	Keff	Geff	Beta
3	1/5%			HD6	1a	6	0.2272	0.0757		1.3615	0.1712	0.1042
103	2/5%			HD6	1a	6	0.1761	0.0587		1.4196	0.1785	0.1187
203	3/5%			HD6	1a	6	0.1779	0.0593		1.4454	0.1817	0.1141
303	1/25%			HD6	1a	6	0.8115	0.2705		1.0112	0.1271	0.1229
403	2/25%			HD6	1a	6	0.8066	0.2689		0.9861	0.124	0.1206
503	3/25%			HD6	1a	6	0.8066	0.2698		0.979	0.1231	0.1206
603	1/50%			HD6	1a	6	1.5966	0.5322		0.8457	0.1063	0.123
703	2/50%			HD6	1a	6	1.6138	0.5379		0.8052	0.1012	0.1185
803	3/50%			HD6	1a	6	1.6157	0.5386		0.7866	0.0989	0.1176
903	1/100%			HD6	1a	6	3.2001	1.0667		0.6598	0.0867	0.143
1003	2/100%			HD6	1a	6	n/a	n/a		n/a	n/a	n/a
1103	3/100%			HD6	1a	6	n/a	n/a		n/a	n/a	n/a
1203	1/150%			HD6	1a	6	n/a	n/a		n/a	n/a	n/a
1303	2/150%			HD6	1a	6	n/a	n/a		n/a	n/a	n/a
1403	3/150%			HD6	1a	6	n/a	n/a		n/a	n/a	n/a

X

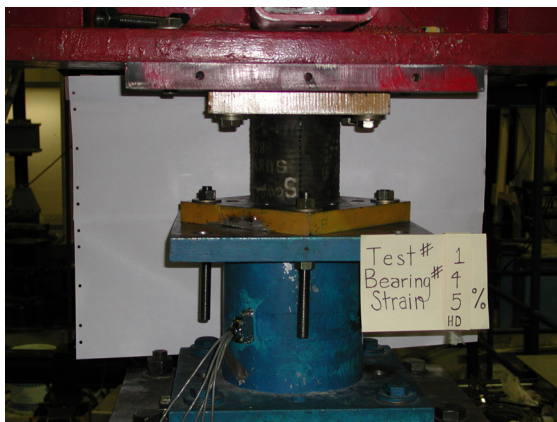
Start time	Cycle/%	Date	Time	Bearing #	Test #	Load (kips)	Max Disp. (in)	Strain	Temperature	Keff	Geff	Beta
118	1/5%			HD6	1b	6	0.2415	0.0805		1.3235	0.1664	0.0639
218	2/5%			HD6	1b	6	0.2413	0.0804		1.3171	0.1656	0.0332
318	3/5%			HD6	1b	6	0.2422	0.0808		1.3187	0.1658	0.0658
418	1/25%			HD6	1b	6	0.873	0.291		0.8567	0.1077	0.1153
518	2/25%			HD6	1b	6	0.8734	0.2911		0.846	0.1064	0.1164
618	3/25%			HD6	1b	6	0.8723	0.2908		0.8479	0.1066	0.1142
718	1/50%			HD6	1b	6	1.6607	0.5536		0.712	0.0895	0.1247
818	2/50%			HD6	1b	6	1.6633	0.5544		0.6904	0.0869	0.1234
918	3/50%			HD6	1b	6	1.6633	0.5544		0.6832	0.0859	0.1217
1018	1/100%			HD6	1b	6	3.2411	1.0804		0.6869	0.0864	0.1205
1118	2/100%			HD6	1b	6	3.2422	1.0807		0.6456	0.0812	0.1236
1218	3/100%			HD6	1b	6	3.2149	1.0806		0.6265	0.0788	0.1243
1318	1/150%			HD6	1b	6	4.818	1.606		0.7038	0.0885	0.1305
1418	2/150%			HD6	1b	6	4.818	1.606		0.6595	0.0829	0.1235
1518	3/150%			HD6	1b	6	4.8184	1.6061		0.608	0.0764	0.1307

X

Start time	Cycle/%	Date	Time	Bearing #	Test #	Load (kips)	Max Disp. (in)	Strain	Temperature	Keff	Geff	Beta
1.2	1/5%			HD6	2a	6	0.2422	0.0808		1.6785	0.211	0.0669
3.2	2/5%			HD6	2a	6	0.2415	0.0805		1.6588	0.2085	0.0686
5.2	3/5%			HD6	2a	6	0.2413	0.0804		1.6451	0.2063	0.0681
7.2	1/25%			HD6	2a	6	0.2413	0.0804		1.641	0.2063	0.0681
9.2	2/25%			HD6	2a	6	0.8715	0.2905		1.0345	0.1301	0.1367
11.2	3/25%			HD6	2a	6	0.8717	0.2906		1.0215	0.1284	0.1356
13.2	1/50%			HD6	2a	6	1.6583	0.5527		0.8316	0.1046	0.1529
15.2	2/50%			HD6	2a	6	1.6583	0.5527		0.7872	0.099	0.1589
17.2	3/50%			HD6	2a	6	1.6583	0.5527		0.7743	0.0973	0.159
19.2	1/100%			HD6	2a	6	3.2306	1.0769		0.6607	0.0831	0.1693
21.2	2/100%			HD6	2a	6	3.2303	1.0768		0.623	0.0783	0.1749
23.2	3/100%			HD6	2a	6	3.2304	1.0768		0.6109	0.0768	0.1754
25.2	1/150%			HD6	2a	6	4.7985	1.5995		0.727	0.0914	0.1606
27.2	2/150%			HD6	2a	6	4.7985	1.5995		0.727	0.0914	0.1606
29.2	3/150%			HD6	2a	6	4.8	1.6		0.6244	0.0785	0.1727

Start time	Cycle/%	Date	Time	Bearing #	Test #	Load (kips)	Max Disp. (in)	Strain	Temperature	Keff	Geff	Beta
2.7	1/5%			HD6	2b	6	0.2089	0.0696		1.9673	0.2473	0.0831
4.7	2/5%			HD6	2b	6	0.2091	0.0697		1.8963	0.2384	0.0865
6.7	3/5%			HD6	2b	6	0.2091	0.0697		1.8974	0.2386	0.0854
8.7	1/25%			HD6	2b	6	0.8378	0.2793		1.3105	0.1648	0.1263
10.7	2/25%			HD6	2b	6	0.8359	0.2786		1.2643	0.159	0.1279
12.7	3/25%			HD6	2b	6	0.8357	0.2786		1.2462	0.1567	0.1275
14.7	1/50%			HD6	2b	6	1.6217	0.5406		1.0403	0.1308	0.1407
16.7	2/50%			HD6	2b	6	1.6211	0.5404		0.9858	0.1239	0.1417
18.7	3/50%			HD6	2b	6	1.6219	0.5406		0.9656	0.1214	0.1419
20.7	1/100%			HD6	2b	6	3.0941	1.0649		0.843	0.106	0.1548
22.7	2/100%			HD6	2b	6	3.1954	1.0651		0.7701	0.0968	0.1566
24.7	3/100%			HD6	2b	6	3.195	1.065		0.7431	0.0934	0.1582
26.7	1/150%			HD6	2b	6	4.7638	1.5879		0.8454	0.1063	0.1473
28.7	2/150%			HD6	2b	6	4.7642	1.5881		0.7517	0.0945	0.1542
30.7	3/150%			HD6	2b	6	4.4561	1.5884		0.7134	0.0897	0.1581

Start time	Cycle/%	Date	Time	Bearing #	Test #	Load (kips)	Max Disp. (in)	Strain	Temperature	Keff	Geff	Beta
3	1/150%			HD6	3	6	4.7869	1.5956		0.5767	0.0725	0.1392
103	2/150%			HD6	3	6	4.7859	1.5953		0.5426	0.0682	0.1498
203	3/150%			HD6	3	6	4.7857	1.5952		0.5199	0.0654	0.1518
303	1/100%			HD6	3	6	3.2098	1.0698		0.4296	0.054	0.1802
403	2/100%			HD6	3	6	3.2098	1.0699		0.4264	0.0536	0.174
503	3/100%			HD6	3	6	3.2092	1.0698		0.4263	0.0536	0.1705
603	1/50%			HD6	3	6	1.6298	0.5433		0.5047	0.0634	0.1777
703	2/50%			HD6	3	6	1.6298	0.5433		0.5167	0.065	0.17
803	3/50%			HD6	3	6	1.6296	0.5432		0.523	0.0658	0.1644
903	1/25%			HD6	3	6	0.8398	0.2799		0.6291	0.0791	0.1658
1003	2/25%			HD6	3	6	0.8329	0.2776		0.6521	0.082	0.1539
1103	3/25%			HD6	3	6	0.8349	0.2783		0.6654	0.0837	0.1483
1203	1/5%			HD6	3	6	0.1839	0.0613		1.0171	0.1279	0.1283
1303	2/5%			HD6	3	6	0.1928	0.0643		1.014	0.1275	0.1183
1403	3/5%			HD6	3	6	0.1804	0.0601		1.0464	0.1316	0.1259



Pipeline Response to Ground Oscillation During Earthquakes

Laura K. Barton

Home Institution: Rensselaer Polytechnic Institute

REU Host Institution: Cornell University

REU Faculty Advisor: T. D. O'Rourke

PIPELINE RESPONSE TO GROUND OSCILLATION DURING EARTHQUAKES

Laura K. Barton

Home Institution: Rensselaer Polytechnic Institute

REU Host Institution: Cornell University

REU Faculty Advisor: T. D. O'Rourke

Abstract

During earthquakes, pipelines can be affected by both permanent ground deformation (PGD) and transient ground deformation (TGD). An important source of liquefaction-induced TGD is referred to as ground oscillation. When liquefiable soils are bounded by non-liquefiable soils, the resulting area may be described as a basin. Within the basin, during an earthquake, lateral surface displacements may be relatively constant, and consequentially stresses and strains on buried pipelines are small. At the interface with a non-liquefied soil, however, the displacements are often larger, creating damaging zones of compression and tension on pipelines.

The purpose of this research is to characterize pipeline response to ground oscillation. The research was accomplished using ABAQUS, a finite element software package. A closed form solution for an idealized model was also developed to compare the finite element analysis with idealized conditions.

The motivation for these studies is to ultimately provide a design tool for engineers to use to predict the demands that will be placed on pipeline systems. These preliminary studies will be used to determine mathematical relationships that will enable engineers to adjust the strain for an ideal condition to give a more realistic strain for a specific site.

Introduction

During earthquakes, pipelines may be damaged by both permanent ground deformation (PGD) and transient ground deformation (TGD). PGD, as the name implies, is permanent movement of the ground. Faulting, tectonic uplift, liquefaction, landslides, and densification are all examples of PGD. TGD is caused by occurrences such as traveling ground waves, vibration of soil-filled valleys, and ground oscillation (O'Rourke, 1998). The Committee on Earthquake Engineering (1985) identified ground oscillation as "a source of TGD associated with liquefaction in areas of virtually level ground where near-surface soils oscillate on top of an underlying liquefied layer."

Problems arise at the interface between liquefied and non-liquefied soils. When liquefiable soils are bounded by non-liquefiable soils, the resulting area may be described as a basin. Within the basin, during an earthquake, lateral surface displacements may be relatively small. Consequentially stresses and strains on buried pipelines are also small. At the boundaries between liquefied and non-liquefied soil, however, differential movements and strains may be large, creating damaging zones of compression and tension that can affect pipelines.

The liquefied soil oscillates below the water table, consequentially sending oscillating waves to the ground above it. The ground behaves as though it is floating in the liquefied soil, and it is being pushed into and pulled away from the relatively stationary ground that is not experiencing the effects of the ground oscillation. See Figure 1 for an illustration of this type of pipeline damage.

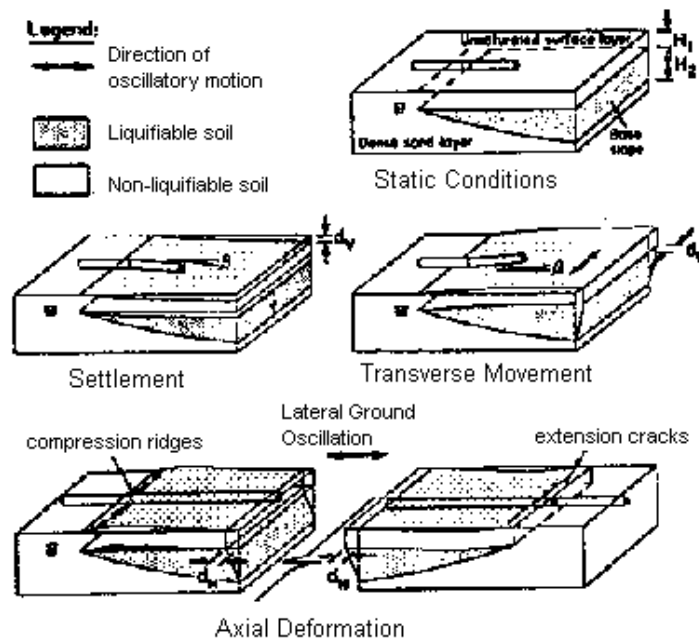
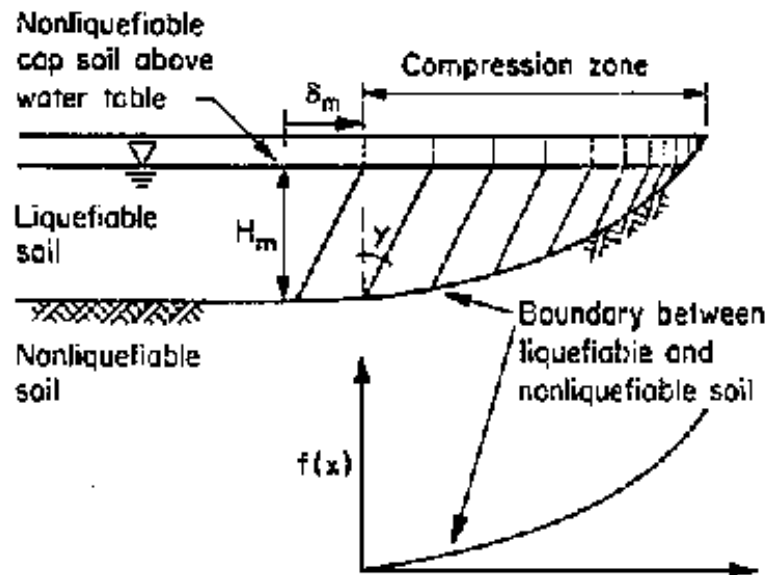


Figure 1: Pipeline Response to Ground Oscillations: a) Schematic of Buried Pipeline Response to Transient Displacements at Liquefaction Sites (Pease and O'Rourke, 1997)



b) Cross Section Showing Transient Shear Distortion and the Boundary Between Liquefiable and Underlying Competent Soils (O'Rourke, 1998)

This paper summarizes analytical studies to characterize pipeline response to ground oscillation. The idea behind these studies is to provide a design tool for engineers to predict the demands that can be based upon pipeline systems. In the future, these preliminary studies will help determine mathematical relationships that relate pipeline response to the complex soil-structure interaction in ground susceptible to liquefaction. This will enable engineers to predict actual values of strains on pipes by knowing the strain for an ideal condition and adjusting it to fit site-specific cases.

Ground Oscillation

The phenomenon of ground oscillation in basins has not been extensively studied. Work has been completed examining various examples of liquefaction, ground oscillation, and PGD in the vicinity of pipeline systems. Below is a summary of some of this research.

Zeghal and Elgamal (1994) performed an investigation of data collected from the Wildlife Site in southern California during the 1987 Superstition Hills earthquake. Motion at the surface and subsurface (7.5 m below ground surface) and corresponding pore water pressures were evaluated. The data showed that as the pore water pressure of the site increased, the site stiffness decreased. There were also large shear strains and small shear stresses recorded during the increase in pore water pressure. This evidence is indicative of a liquefied soil condition.

Pease and O'Rourke (1997) used a method similar to that of Zeghal and Elgamal by studying earthquake-induced displacements during the 1989 Loma Prieta earthquake, at the Treasure Island and Yerba Buena Island sites. At Treasure Island, the surface displacement was measured and at Yerba Buena, bedrock motion recordings were made. Pease and O'Rourke used the bedrock motions at Yerba Buena to compare with the ground surface motions recorded at Treasure Island. This solution is feasible since both sites were significantly far away (95km) from the epicenter, and there is no known seismic differences in the bedrock between the sites.

The displacement plots from the sites were compared to look for evidence of liquefaction. By visual comparison of the displacements from the surface measurements and the subgrade measurements, it was observed that at first there was a strong correlation between the surface and subsurface accelerations. However, after about 14 seconds into the record, there started to be a difference. This difference in was credited to the liquefaction and softening of the site.

There were many results of liquefaction after the 1977, 7.4 magnitude, San Juan Province earthquake in Argentina (Yourd and Keefer, 1994). One area in particular experienced severe

ground oscillation due to an underlying layer of liquefied sand. This area was composed of loosely compacted sand with a groundwater table only a few meters below the surface. These conditions were extremely favorable for liquefaction to occur.

Pipeline Response to Permanent Ground Deformation

O'Rourke and Liu (1999) investigated continuous and segmented pipeline response to parallel PGD. They accomplished this investigation using two models of the pipeline systems. One was a linear elastic model of a buried pipeline with slip joints, and the other was an arc welded butt joint modeled after Ramberg-Osgood type stress-strain behavior. Both models used springs to model the soil-pipe interaction.

The linear elastic model was analyzed under three different displacement patterns. These included a ramp, block, and symmetric ridge pattern. To model the soil-pipe interaction, O'Rourke and Liu concluded that for small displacements, a simplified rigid-plastic spring shear transfer would produce the same results as a complex elasto-plastic spring. Using the linear elastic model, it was found that the block pattern of displacement produced the largest strains on the pipe. It was also concluded that the block pattern was a reasonable estimate for all of the observed patterns.

Examples from the 1994 Northridge earthquake were used to compare the elastic model to real cases. Slip joints and arc welded joints, as were present in Northridge, have low strength, so the model was appropriate. The model predicted the failure correctly for the example cases.

The inelastic model was also analyzed using a block pattern displacement and it was found that this model, too, was successful in predicting the correct behavior when compared to actual events.

O'Rourke and Liu noted that compressive failure is more common in pipeline systems than tensile failure. This is because the peak force and strain in tension and compression are equal, but the critical failure strain in compression is less. Therefore, it is more likely that a pipe will fail in compression.

This study also investigated the effect of expansion joints being present in the pipelines. It was found that expansion joints may either help, hinder or have no effect on the pipeline, depending on the location of the joint. Expansion joints work best when one is placed close to one end of the PGD zone and another is placed at the other end of the PGD zone. However, there needs to be a good estimate of the boundaries of the PGD zone, and extreme care needs to be taken when making this estimation.

Analytical Modeling

Closed Form Solution

A closed form solution was derived to solve for the strain on a pipe running over an idealized basin with liquefied soils. For this derivation, elastic pipe material behavior and perfectly plastic shear transfer from soil to pipe were assumed.

The force in the pipe is a function of the shear force per unit length, f_{\max} , and a development length, ℓ , See Figure 3.

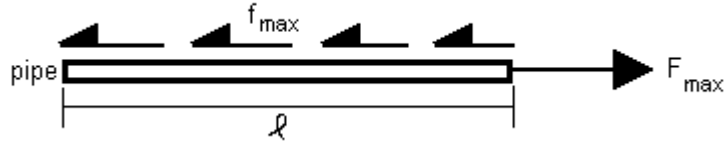


Figure 3: Force on pipe is a function of friction force and development length

$$dF = f_{\max} dx$$

$$\Delta = \int \frac{dFx}{EA} = \int_0^{\ell} \frac{f_{\max} x dx}{EA} = \frac{f_{\max} \ell^2}{2EA} \quad (1)$$

The Δ at peak force is $\Delta_{s,\max}/2$, As shown in Figure 4.

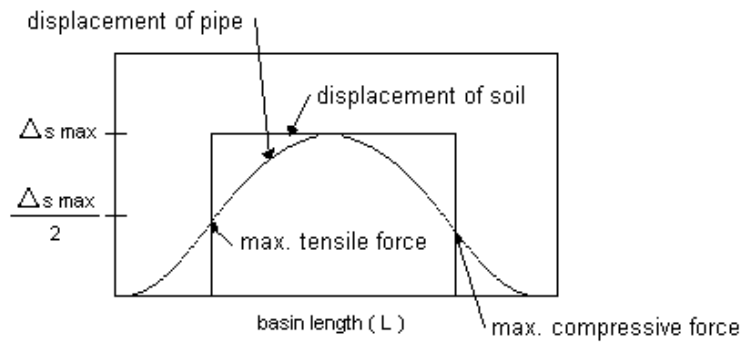


Figure 4: Displacement of the soil and pipe along the basin length

Substituting $\Delta_{s,\max}/2$ in Equation 1, results in:

$$\frac{\Delta_{s,\max}}{2} = \frac{f_{\max} \ell^2}{2EA}$$

$$\Delta_{s,\max} = \frac{f_{\max} \ell^2}{EA} \quad (2)$$

where ℓ is the length from zero to F_{\max} .

At the critical basin length, L_c , the distance between the maximum tensile forces and the maximum compressive forces is:

$$L_c = 2\ell$$

$$\ell = \frac{L_c}{2}$$

Therefore,

$$\Delta_{s,\max} = \frac{f_{\max}}{EA} \left(\frac{L_c}{2} \right)^2 \quad (3)$$

The area of the pipe may be approximated as the product of the circumference and the thickness. The shear force is the product of the interface shear stress, τ_{\max} , and the circumferential area. Making these substitutions, Equation 3 becomes:

$$\Delta_{s,\max} = \frac{\tau_{\max} \pi D \left(\frac{L_c}{2} \right)^2}{E \pi D t}$$

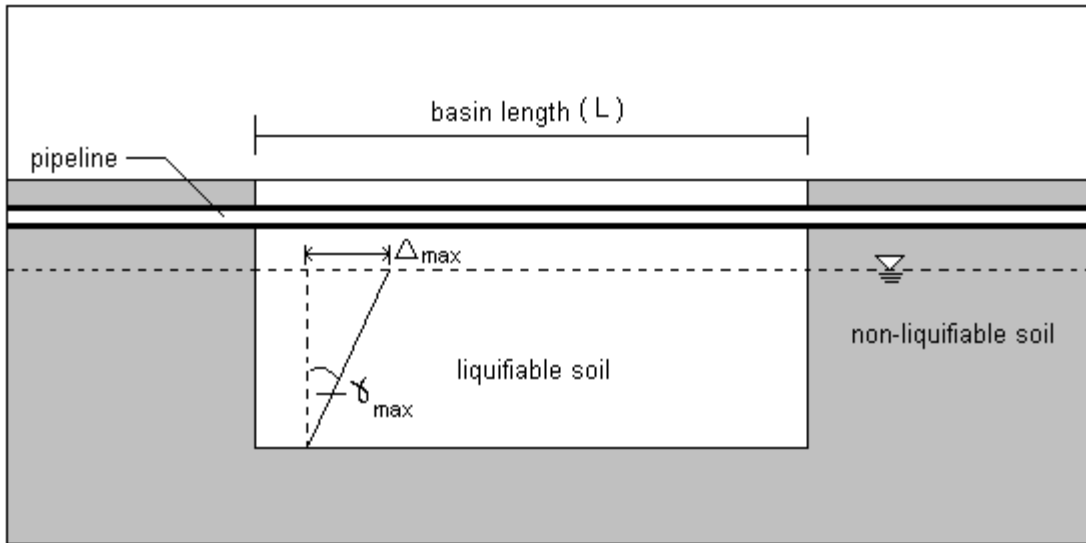
$$\Delta_{s,\max} = \frac{\tau_{\max} L_c^2}{4 E t} \quad (4)$$

For all basin lengths larger than the critical basin length, the strain will be equal to the maximum strain in the pipe. Therefore,

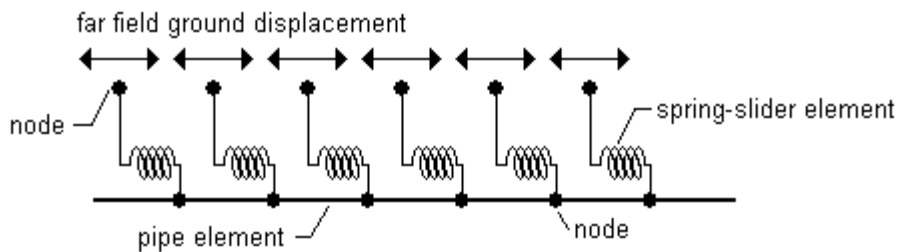
$$\begin{aligned}
F_{\max} &= f_{\max} \frac{L_c}{2} \\
\varepsilon_{\max} &= \frac{F_{\max}}{EA} \\
\varepsilon_{\max} &= \frac{f_{\max} L_c}{2EA} \\
\varepsilon_{\max} &= \frac{\tau_{\max} \pi D L_c}{2\pi D t E} \\
\varepsilon_{\max} &= \frac{\tau_{\max} L_c}{2tE} \\
\varepsilon_{\max} &= \sqrt{\frac{\Delta_{s,\max} \tau_{\max}}{Et}}
\end{aligned} \tag{5}$$

Numerical Model

The idealized basin with liquefiable soil was modeled with ABAQUS, a finite element software package (Hibbitt, Karlsson & Sorensen, Inc., 1997). Figure 5 shows a schematic of the basin. Pipe elements were used to model the pipe, and spring slider elements were used to model the soil-pipe interaction. When the soil around a pipe moves, the pipe resists the movement. Local soil deformations mobilize force around the pipe. The springs in the model were used to model these local soil deformations. The nodes on the spring slider elements were given a displacement parallel to the pipe to represent far field ground displacement that is independent of the pipe structure.



a) Idealized basin schematic showing maximum ground strain and associated maximum soil displacement parallel to the pipe.



b) Finite element model of pipe and spring slider elements

Figure 5: a) Basin Schematic, and b) Finite Element Model

The length of the pipe in the ABAQUS files was the chosen basin length, plus 500 m. The extra length allowed 250 m on each side of the basin to dissipate the forces on the pipe as a result of the displacement of the spring nodes.

The model was simulated under four conditions: 1) elastic pipe material and perfectly plastic shear transfer (to check the closed form solution); 2) elastic pipe material and bilinear shear transfer; 3) non-linear (plastic) pipe material and perfectly plastic shear transfer; and 4) non-linear (plastic) pipe material and bilinear shear transfer.

The maximum shear strain deduced from strong motion recordings during the Superstition Hills earthquake and Loma Prieta earthquakes was approximately $\gamma = 0.02$ (Zeghal and Elgamal, 1994; Pease and O'Rourke, 1997). The numerical model was developed for a basin with 6 meters of liquefiable soil underlying a non-liquefiable layer and a buried pipeline. Maximum shear strains of 0.02 and 0.03 were assumed for the analyses. The maximum ground displacement used in the analysis were 0.120 m and 0.180 m, corresponding to shear strains of 0.02 and 0.03, respectively.

The elastic pipeline properties used in the analysis are Young's modulus = 200×10^3 MN/m² and Poisson's ratio = 0.30. Various wall thicknesses were analyzed for the 760 mm pipeline, including 3.175 mm, 6.35 mm, 9.525 mm, 12.7 mm.

The non-linear material properties were taken from test results reported by Tutuncu (2001). The stress versus strain relationship is shown in Figure 6. These results were obtained from tensile coupons taken from two full scale specimens of pipe provided by the Los Angeles Department of Water and Power (LADWP), and are representative of the type of pipe steel used to fabricate water trunk and transmission lines.

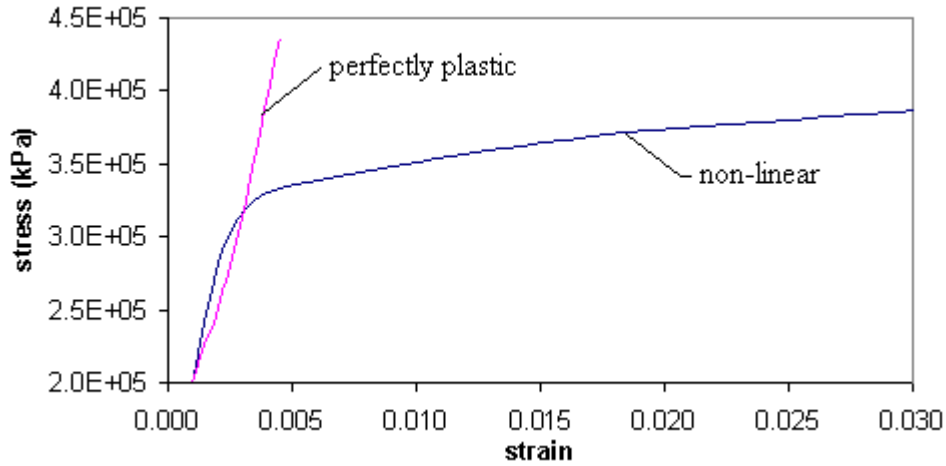


Figure 6: Stress-Strain Relationship from tensile coupons taken from LADWP pipe specimens.

The interface shear resistance between the pipe and ground was modeled for both cohesive and granular soil. The maximum shear resistance, τ_{\max} , for cohesive soil is given by

$$\tau_{\max} = \alpha S_u$$

In which S_u is the undrained shear strength of the clay adjacent to the pipe and α is a reduction factor that accounts for the degree of shear transfer as a function of undrained strength. To cover the range of strengths that would generally be encountered in the field, three combinations of S_u and α were evaluated: 1) $S_u = 25 \text{ kN/m}^2$ and $\alpha = 1.0$, 2) $S_u = 50 \text{ kN/m}^2$ and $\alpha = 1.0$, 3) $S_u = 100 \text{ kN/m}^2$ and $\alpha = 0.75$.

The maximum shear resistance, τ_{\max} , for granular soil is given by

$$\tau_{\max} = \frac{1}{2}(1 + K_o)\gamma z_p \tan \delta$$

where $K_o = 1$

$$\gamma = 125 \text{ pcf (19.65 kN/m}^3\text{)}$$

$$z_p = 51 \text{ in (1.2954 m)}$$

$$\delta/\phi = 1.0, \text{ where } \phi = 35^\circ$$

and, $\delta/\phi = 0.3$, to simulate a "frictionless wrap" reinforcement around the joints of the pipe.

Both rigid plastic and elastic-plastic shear transfer models were used. The elastic-plastic behavior was modeled as a bilinear relationship between interface shear, τ , and relative displacement between the pipe and soil, d , as illustrated in Figure 7.

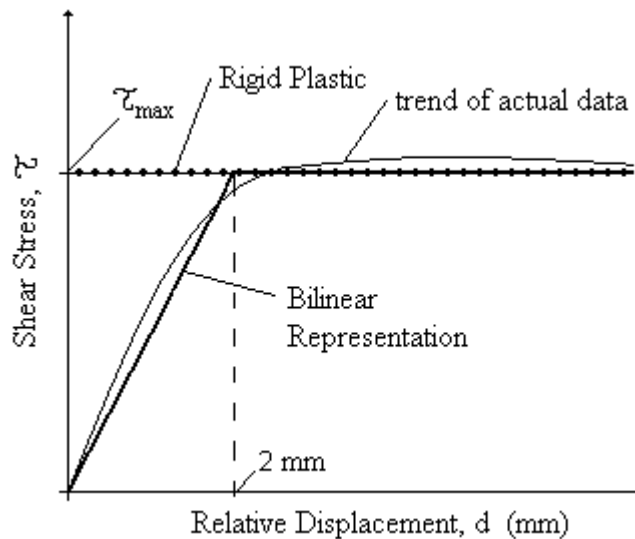


Figure 7: Rigid Plastic, Bilinear Representation compared to the trend of the data.

Analytical Results

By examining the results of all the simulations, there were three major points of interest in classifying the different types of basin behavior. These three points were the presence of

cohesive versus cohesionless soil, the phenomena of critical basin length, and the effects of elastic and plastic pipe material behavior.

Cohesive and Cohesionless Soils

Cohesive and granular (cohesionless) soils produced different stress and strain effects on the pipe. This can be seen in Figure 8, which shows the plot of axial force versus distance for elastic pipe behavior, bilinear shear transfer, $\gamma = 0.02$ and a pipe wall thickness of 0.250 in. A shear of 17.82 kPa corresponds to the shear in granular soil, and 50 kPa corresponds to the shear in cohesive soil. As the graph shows, with all other parameters the same, the axial force is higher for the cohesive soil plot.

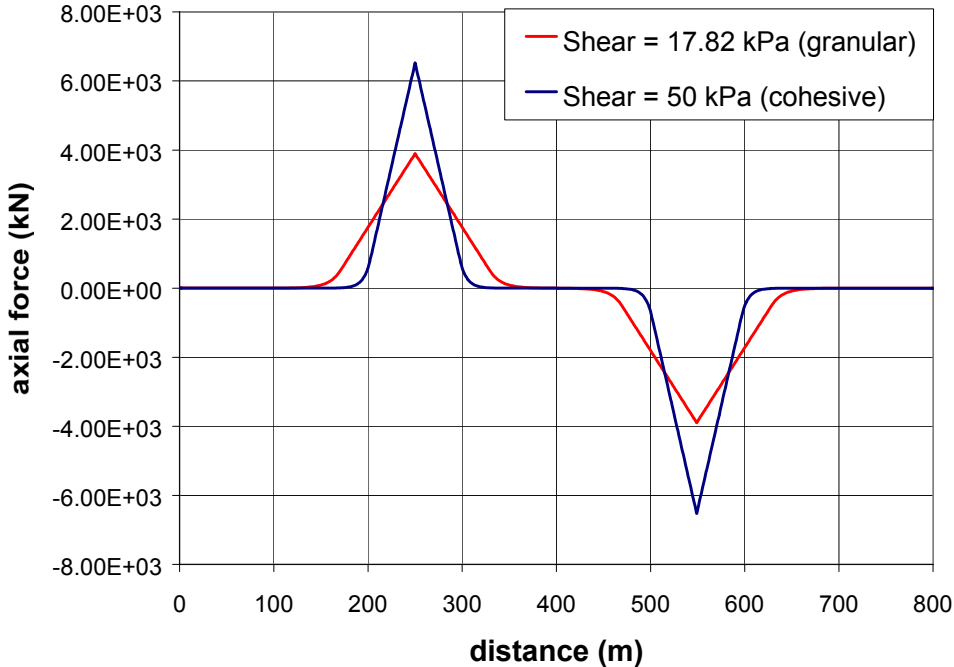


Figure 8: Axial Force for cohesive and granular soils for elastic pipe behavior, where $\gamma = 0.02$, and bilinear shear transfer

The perfectly plastic shear transfer, which plots practically identical to the bilinear shear transfer, is not shown on this plot.

Critical Basin Length

In both the plastic and the elastic runs of the model, the maximum strain in the pipe would increase as the basin length increased, but only up to a certain basin length. Any length beyond this length would result in the same maximum strain. This basin length is called the critical basin length. This phenomenon can be seen in the strain graph of Figure 9, which represents nonlinear (plastic) pipe and bilinear shear transfer for a pipe in cohesive soil where

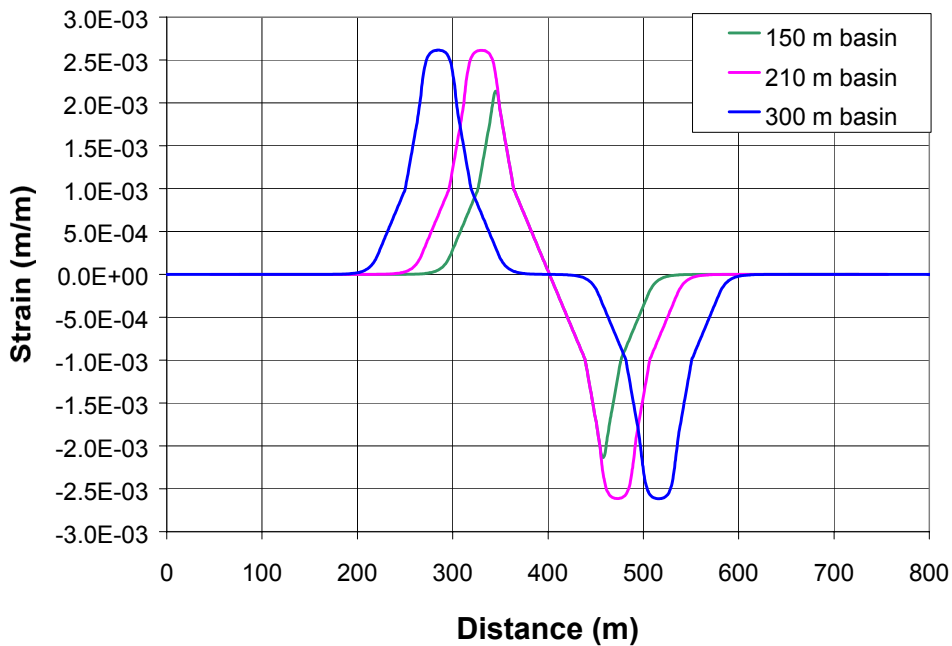


Figure 9: Strain for various basin lengths for nonlinear (plastic) pipe behavior and bilinear shear transfer for a pipe in cohesive soil where $\gamma = 0.03$.

$\gamma = 0.03$. As the graph shows, the maximum strain for both the 210 m basin and the 300 m basin is the same. 210 m is the approximate critical basin length for this particular model. The 150 m length is less than the critical, and therefore the strain on that plot is less than the maximum on the other plots.

This can also be seen by examining a graph of basin length versus peak axial stress.

Figure 10 shows that for any given pipe, there is a peak stress that may be obtained, regardless of the length of the basin in which the pipe is buried.

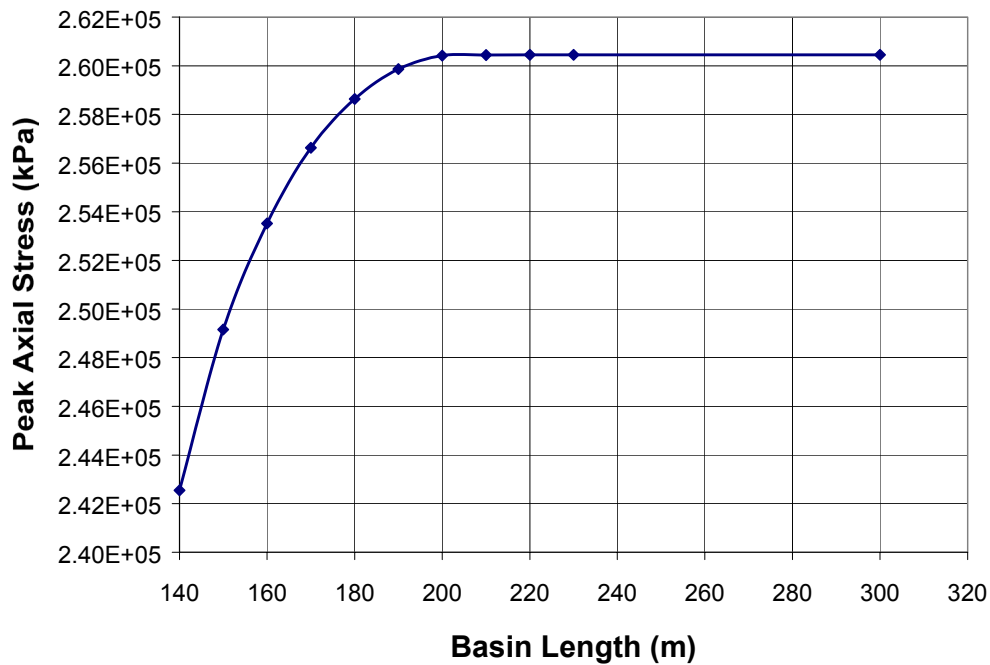


Figure 10: Basin Length versus Peak Axial Stress for cohesive soil, $\gamma = 0.02$, nonlinear (plastic) pipe material and bilinear shear transfer.

ABAQUS Results vs. Closed Form

The models with bilinear and perfectly plastic shear transfer arrived at the same values (within 1%) for the maximum stresses and strains. This shows that for this model, the bilinear approximation is a valid means of modeling perfectly plastic shear transfer.

The ABAQUS results were compared to the closed form solution as a check to see if ABAQUS was producing results as predicted. The difference between the ABAQUS results for elastic material and bilinear shear transfer and the closed form solutions was at the most less than 2%. See Figure 11.

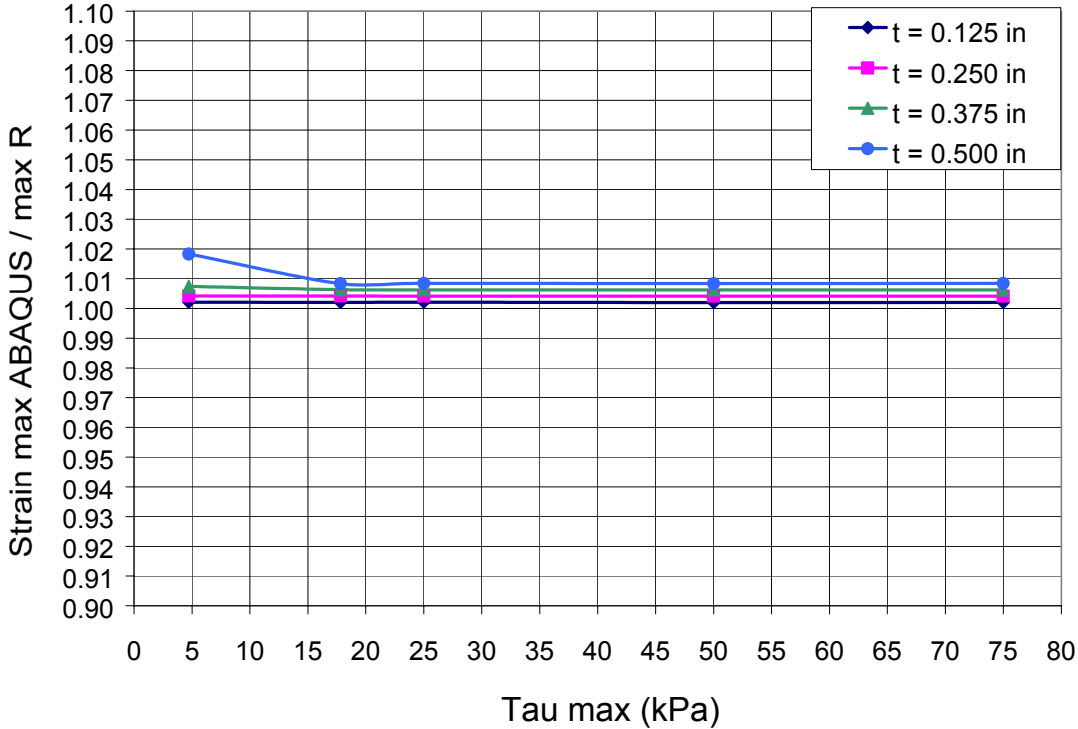


Figure 11: ABAQUS and closed form solution produce similar results for elastic case with $\gamma = 0.03$ and perfectly plastic shear transfer.

Differences in the closed form solution and the model arise when plastic pipe behavior is introduced in the model. The strain in the pipe can be increased almost ten times that of elastic material. Figure 12 shows a plot of the shear stress versus the Ratio of the ABAQUS result over the closed form result (labeled max R) for four different pipe wall thicknesses. Since the perfectly plastic shear transfer and the bilinear approximation are so similar, only the perfectly plastic shear transfer is shown below.

As the graph shows, as the pipe wall thickness decreases, the maximum strain calculated by ABAQUS increases at a faster rate than that of the closed form solution, consequentially, the ratio increases.

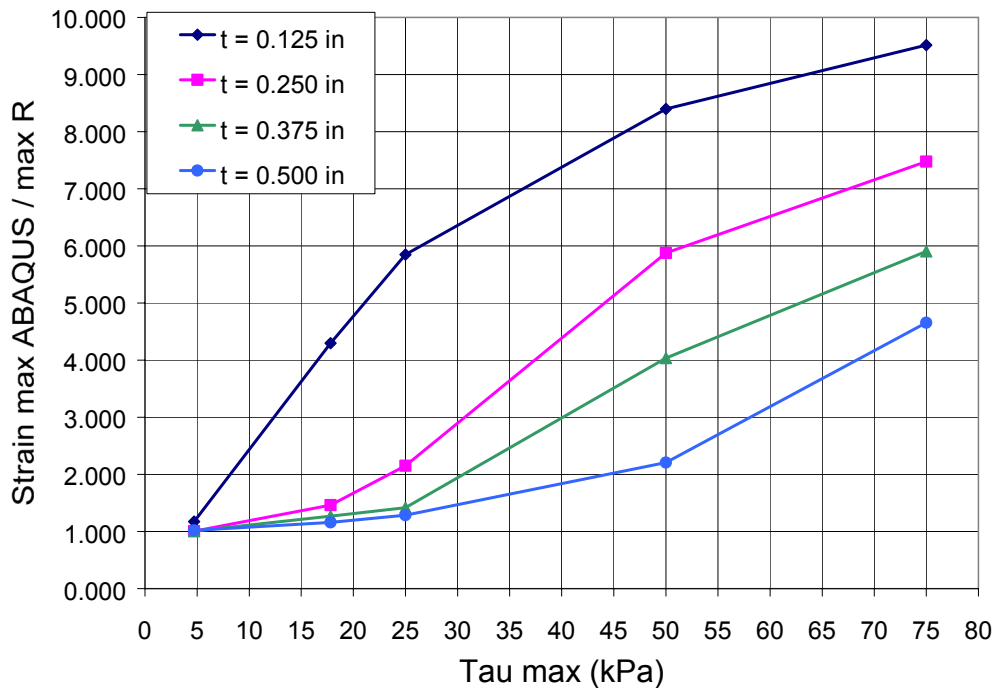


Figure 12: Plastic Material Behavior for $\gamma = 0.03$ and perfectly plastic shear transfer produced different results from the closed form solution.

Summary and Recommendations

The motivation for these studies is to ultimately provide a design tool for engineers to use to predict the demands that will be based upon pipeline systems. These preliminary studies may be used to determine mathematical relationships between all the parameters of this study. This will enable engineers to predict values of strains on pipes by knowing the strain for an ideal condition and adjusting it by various factors that will come out of these relationships.

For this study, a rectangular basin was used. It is suspected that the geometry of the basin may have some effect on the maximum stress and strain values obtained from the ABAQUS models. The geometry of the basin and its effects on the stress and strain produced is a problem that warrants further investigation.

Acknowledgements

This paper presents the results of research supported by the National Science Foundation Research Experiences for Undergraduates Program, EEC-9701471.

References

- Hibbitt, Karlsson & Sorensen, Inc. (1997). *ABAQUS / Standard User's Manual*, Version 5.7
- O'Rourke, M. J. and X. Liu (1999). Response of Buried Pipelines Subject to Earthquake Effects. Multidisciplinary Center for Earthquake Engineering Research, State University of New York at Buffalo, Buffalo, NY, 1999, Monograph Series 3.
- O'Rourke, T. D. (1998). "An Overview of Geotechnical and Lifeline Earthquake Engineering", *Proceedings*, Geotechnical Earthquake Engineering and Soil Dynamics III. (1), 1392-1426.
- Pease, J. W. and T. D. O'Rourke (1997). "Seismic response of liquefaction sites", *Journal of Geotechnical Engineering*, ASCE, 123(1), 37-45.
- Tutuncu, Ilker (2001). "Compressive Load and Buckling Response of Steel Pipelines During Earthquakes". Cornell University Ph.D. Thesis
- Youd, T. L. and Keefer, D. K. (1994). "Liquifaction during the 1977 San Juan Province, Argentina earthquake ($m_s = 7.4$).", *Engineering Geology*, 37(3), 211-233.
- Zeghal, M. and Elgamal, A. W. (1994). "Analysis of site liquifaction using earthquake records", *Journal of Geotechnical Engineering*, ASCE, 120(6), 996-1017.

Nonstructural Loss Estimation: UC-Berkeley

Case Study

Rachel Dooley
University of Michigan – Ann Arbor

UC Berkeley
Professor Mary Comerio

ABSTRACT

A common misconception regarding earthquakes' economic effects is that the major costs associated with this natural phenomenon are due to building structure damage. However, a large component of any earthquake's cost is the nonstructural damage within the building, especially at large research universities. Therefore, a case study of the UC Berkeley campus was conducted which collected nonstructural data in order to determine the cost of these nonstructural components in the event of an earthquake, and also to aid in approximating the cost the secure these components to prevent earthquake damage. This case study was limited to one large research building – the LSA building – because research was proven to be the most costly component for a university to lose. The data collected in this study was given to an engineering firm to be analyzed, and results of this analysis are currently pending. The university plans to incorporate this research into the planning of future seismic retrofitting.

Introduction

When the common person thinks about earthquake damage, he often thinks of the damage to the structure of a building, i.e., how many buildings were ruined. However, damage is commonly much more widespread than this person first assumes. In fact, the contents of the building can sometimes be worth more than the building structure itself in the event of an earthquake. Nonstructural damages, as it is called, can add up to millions or in some cases even billions of dollars in revenue that can be lost. Therefore, in order to assess the effects of any earthquake, the cost of the damages to the interior of buildings needs to be analyzed along with the exterior damage.

This phenomenon is possibly most obvious when considering a university with a large research pool. Research itself can be worth not only millions of dollars or more, but it can also be worth years of time. Often times this research is a compilation of testing throughout a long timeline and destroying the present data could also destroy years of modifications. Similarly, testing equipment can also be very rare and in the case of an earthquake, it may be possible for a university to lose another year of research while new equipment is located or made. Not only does the university lose money and time, but it may also lose valuable faculty because these persons do not want to wait around until their labs are fixed and their research is up and going again. They may opt to leave for a new research facility in order to start where they left off as quickly as possible. For these reasons and more, it is very important for major research universities to include an investigation into nonstructural damage in the event of an earthquake.

In order to narrow the scope of this research, it became necessary to choose a case study, from which all universities could detract data and apply it to their specific campus. This research was performed at University of California – Berkeley, so naturally this would make the easiest case study. Also, UC Berkeley is a large university with a substantial research sector, making this campus a prime candidate for the case study. The following report details the findings of this case study in nonstructural damages to the UC Berkeley campus.

Nonstructural Campus Conditions

The UC Berkeley campus has nonstructural elements in almost every building, but it became necessary to concentrate our efforts in the divisions that would loss the most money in the event of an earthquake. The typical nonstructural campus conditions we found involved laboratories, libraries, offices, classrooms, and mechanical systems dispersed throughout the buildings. In order to determine what areas we would include in our study, we did some book research to find out where the money was.

This research revealed that the entire UC Berkeley campus had nonstructural values upwards of three billion dollars. Of all of the space on the campus, nearly thirty percent of the space is used for various types of research. And finally, 75% of this research is located in only 17 buildings. However, we needed to choose just one building in order to perform a thorough and detailed study of all of the building’s nonstructural contents. We therefore identified the two buildings with the largest volume of research within them. We then chose the building with a “good” seismic rating so that the nonstructural and structural components of the building could be easily distinguished. The building we chose as our case study is called the Life Sciences Addition, or the LSA

building. This building also had the perk of housing large amounts of the biological research on campus. This meant that we would have the opportunity to discuss the lost revenues in the department of animal testing, where researches could lose ten years of research or more if their test subject were to be killed in an earthquake. This aspect added an additional twist to the cost of the research that would be lost because the research could be set back a decade or more.

LSA Building Case Study

The LSA building contained nonstructural components typical of a laboratory building. These labs usually contain heavy tanks or containers, unique research equipment, heavy machines, various shelving, and equipment that rest on the benchtop. All of these types of nonstructural elements were documented and analyzed in the LSA building. In some cases, a single element would cost thousands of dollars, and replacing this piece of equipment could increase the cost (because of lost research) even more. For example, an electron microscope (found in various LSA labs) costs about \$500,000 and could take up to a year to obtain. The destruction of this single item could cost the university upwards of 1 million dollars.

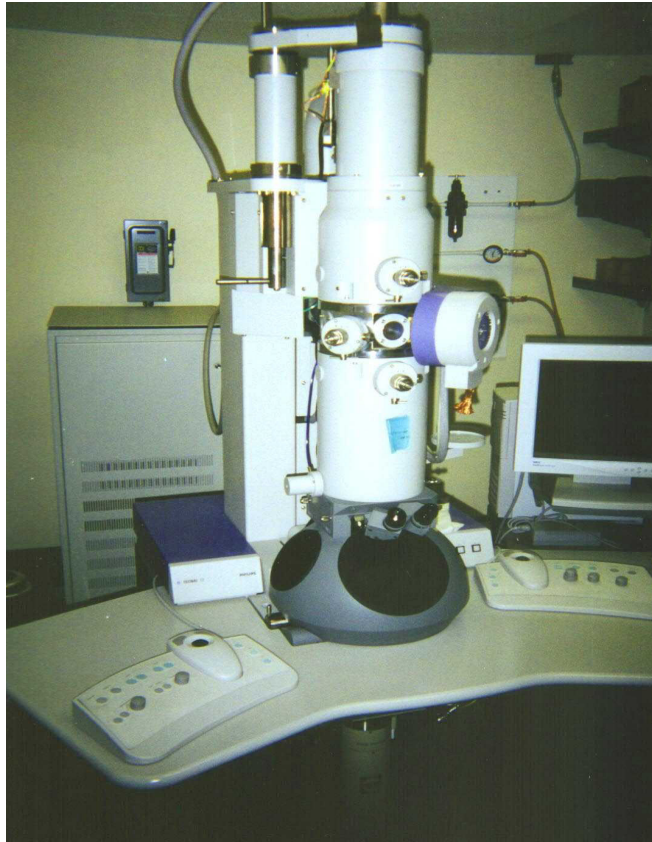


FIGURE 1. Typical Electron Microscope, Worth Nearly Half a Million Dollars.

Case Study Process

In order to collect thorough data, we had to devise a specific process in order to collect all the information regarding the nonstructural contents of the LSA building. We determined that the only way to obtain accurate and current listings of the contents of the LSA building was to go through each room on every floor of the building and draw and document every nonstructural component we found. We decided to also document the specifications of every piece of equipment so that we could accurately determine the worth of the lab equipment later on. After collecting this information, we would then input this specification data into a spreadsheet, and we would convert the drawings into computer sketches.

The overall purpose of this documentation was to collect information that a team of engineers could use to assess the cost of securing all of this nonstructural content in order to prevent damage of the lab components in the event of an earthquake. These engineers would go through the building with our spreadsheets and drawings to determine the cost of the unique hardware needed to secure the different elements in the lab. The engineers numbers could then be compared to the cost of the actual machinery to see if it would be cost effective to secure the item, or simply buy a new one in the event of an earthquake.

The first step in the process was to draw blueprints each room in the building. The building was seven floors, including the basement, which included about 150 rooms. These blueprints were made using AutoCAD® software, which enabled the floor to be looked at as a whole, or simply room by room, because of the range of zoom of the program. The blue prints were printed out room by room so that a detailed description of each room in the building could be recorded.

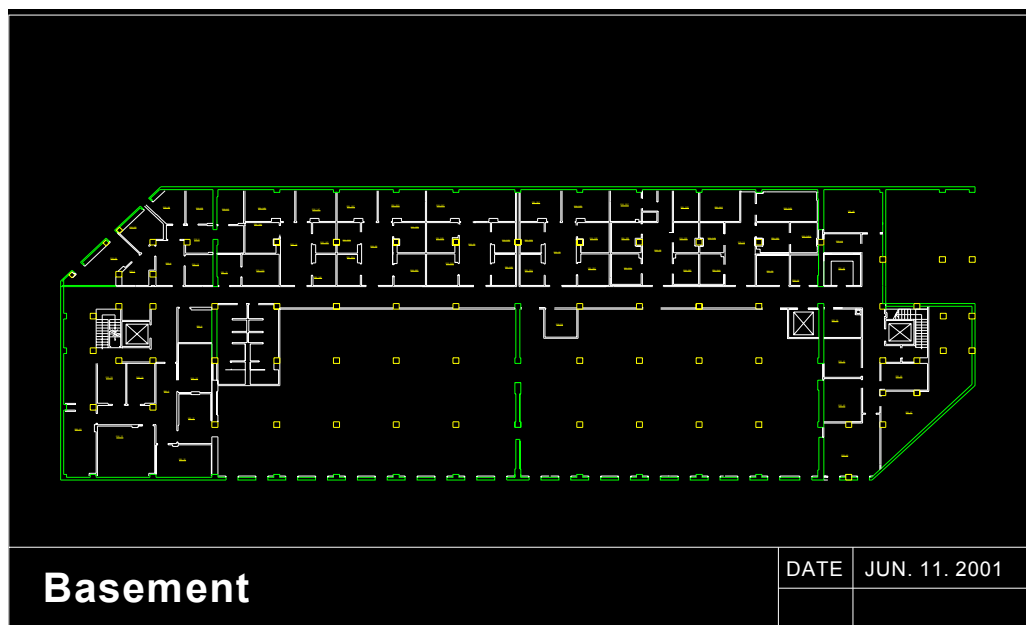


FIGURE 2. Example of LSA Building Blueprint, With Only Walls Drawn.

The next step was to take the blueprints to the building and sketch all of the components of the LSA building. We would typically do the building one floor at a time, in order to keep correlating information together with the sketches of the equipment. Some floors also required access to restricted areas, because of the presence of animal testing, and therefore we would do these floors all at once so that we would only need to obtain access a limited number of times. While we were sketching the placement of all of the nonstructural components in each lab, we would also take photographs of each of the labs in order to visually relate the blueprints to what the lab looked like in reality. This would aid the engineers in reading the blueprints we constructed.



FIGURE 3. Sketching the Equipment in a Restricted Clean Room.

Once the sketching was all finished, we would transfer all of the information from paper to computer. The data regarding the different types of machinery was transferred into an Excel® spreadsheet. The information gathered for this database included the equipment name, model number, dimensions, approximate weight, and location. The sketches were transferred onto the blueprints again using AutoCAD®. The different types of nonstructural components in the labs were divided up into three categories: furniture, equipment, and shelving. These categories were represented with three different colors of the blueprints to make the drawing easier to read and easier to identify specific components out of the database.

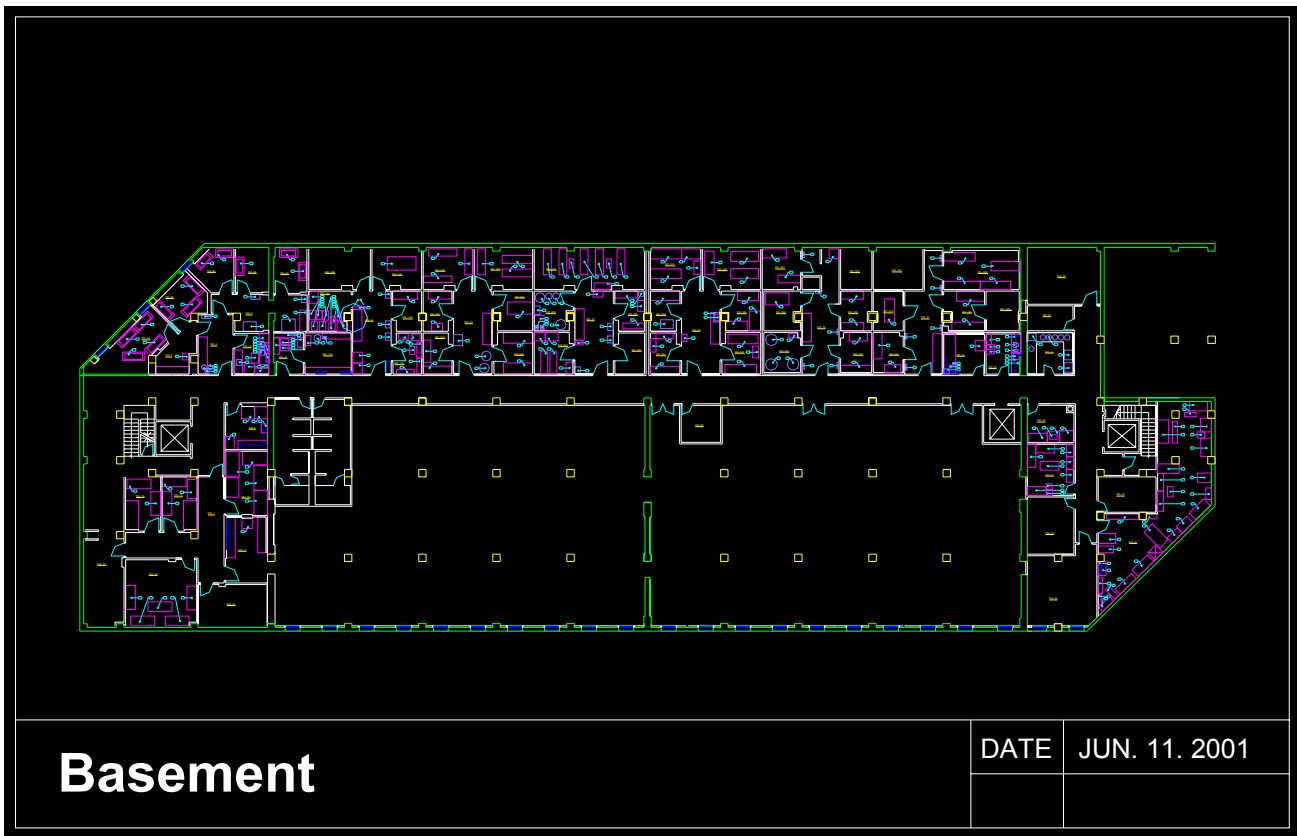


FIGURE 4. Blueprint of Basement Floor with Nonstructural Components.

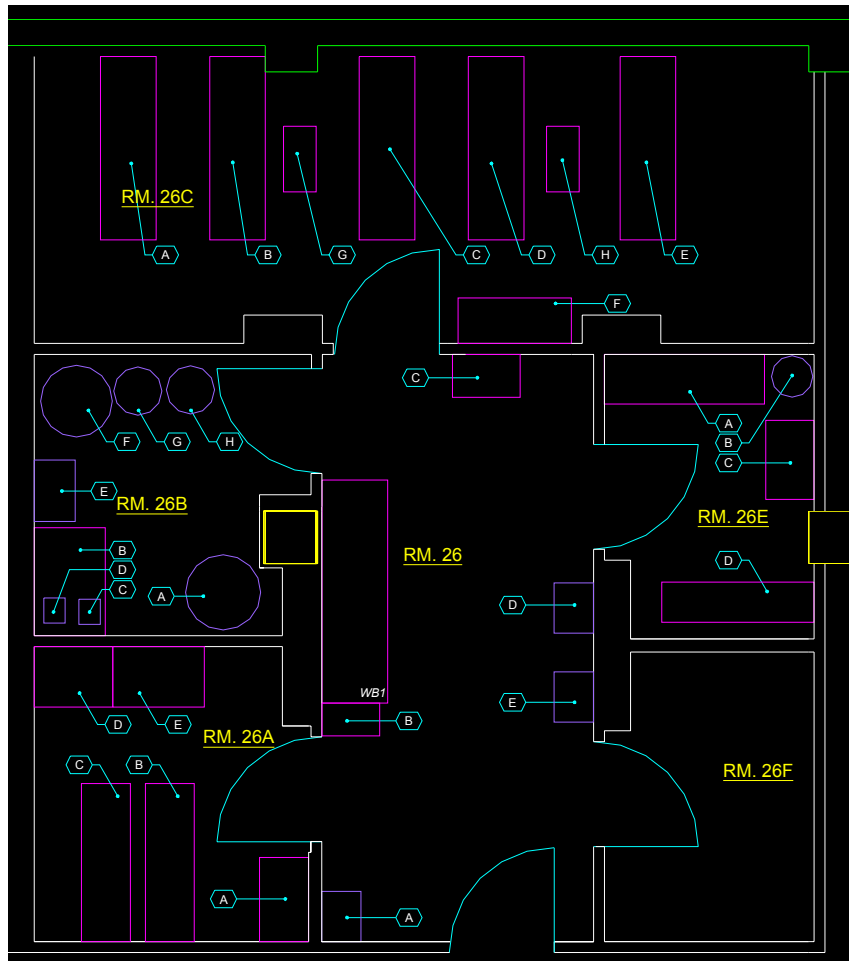


FIGURE 5. Close-up of One Room on Basement Floor

Future Plans

As previously discussed, the blueprints and database will be submitted to an engineering company that will determine the costs associated with securing the nonstructural elements in preparation for an earthquake. The engineering firm that has been hired to do this is Rutherford & Chekene, and they were expected to begin working at the start of the school year. Upon the completion of the engineers' work, the Academic Facilities Office of the UC Berkeley campus will be implementing the necessary precautions in the current labs. They will also be trained to identify these nonstructural risks in the future and design against them in all future lab constructions.

Long-term plans included dynamic earthquake testing, possibly even on a shake table. This would probably included building a scaled LSA lab with all of the

nonstructural components to determine how it will act in response to dynamic testing.

This research is expected to incorporate PEER methods in order to dynamically test the LSA building.

A Model for the Long-Term Deformation of the New Madrid Seismic Zone and Surrounding Region

Mid-America Earthquake Center

Project SG-6 of the Regional Damage Synthesis Program

Characterization of Seismic Sources in and around the
New Madrid Seismic Zone

Matthew Dryden

Faculty Advisors: Dr. Michael Ellis
Dr. Roy Van Arsdale

Research Experience for Undergraduates Program
Center for Earthquake Research and Information
University of Memphis
August 6, 2001

Abstract

Three great earthquakes ($M \sim 8.0$) produced significant damage and deformation in the central United States during 1811-1812. Modeling of this deformation is crucial to our understanding of what is the underlying mechanism that generates earthquakes in this area. With greater insight into what drives the deformation, we will be more prepared to establish recurrence intervals and predict future ground motions. We utilize a three-dimensional model based on the geometry of tectonic deformation in and around the New Madrid seismic zone. The model assumes that a deep shear zone from a right-lateral strike-slip fault generates slip on upper crustal faults. Results from the model are calibrated based on geomorphic features, river migration, geodetic tilting, and other anomalies produced by tectonic activity during Quaternary time. The model implies that the orientation of the deep fault greatly impacts the geometry of the deformation as well as the slip on the upper crustal faults. We produce a comparison of the slip on each upper crustal fault as a means of quantifying the relative activity of these faults. This model provides a powerful tool by accounting for many tectonic features seen not only in the New Madrid seismic zone, but also in the wide region surrounding it.

1.0 Introduction

The New Madrid seismic zone (NMSZ) is a highly studied area as a result of the devastating earthquakes that occurred there during the winter months of 1811-12. A model that is calibrated to the tectonic deformation in this region is vital to our understanding of what underlying mechanism drives this system of faults. We have numerically modeled active faults (Table 1, Fig. 1) in this region in an attempt to understand the mechanisms that govern long-term deformation in the NMSZ and its surrounding region. We seek to understand the consequences of driving the deformation with a shear zone produced by an underlying deep fault. Several methods have been

proposed for driving the deformation in this region, including a weak lower crustal zone within an elastic lithosphere (Kenner and Segall, 2000). This weak zone relaxes and then re-equilibrates, thereby transferring stress to the upper crust and generating earthquakes. Another model proposes a domed decollement or sub-horizontal detachment fault that is placed just above a “rift pillow”, which is a high-density layer (Stuart, et. al., 1997). This sub-horizontal fault beneath the rift slips due to regional compression and induces slip on the upper crustal faults. We drive the deformation with a strike-slip deep fault because there exists more precedence for driving upper crustal faults with a deep shear zone (Ellis, personal communication, 7/3/01). This model is also better applied to areas such as the Southern Appalachian seismic zone where a rift does not exist as in the NMSZ (Ellis, personal communication, 7/3/01). Our method of driving the deformation in the NMSZ remains as much a hypothesis as these other methods described, but our form of modeling allows us to calibrate the results with the topography of the region (Mihills and Van Arsdale, 1999; Cox, et. al., 2001a).

Using a boundary element program (Gomberg and Ellis, 1994), we have modeled the interaction of faults based on the known seismicity within the region. Faults are modeled as planes within an elastic half-space that is given appropriate constants (Poisson’s ratio, $\nu = 0.25$, Young’s Modulus, $E = 7 \times 10^{10}$ Pa). We drive the deformation by constraining an underlying deep fault (Fig. 1) to a specific relative displacement (100m). Upper crustal faults are given boundary conditions such that they slip until the resolved shear stress is zero. The strain field generated by the movement of the deep fault drives each of the other faults, and thereby generates deformation within the region. Calibration of these models is based on evidence of displaced Quaternary deposits and

tectonic geomorphic signatures in the region. Tilting seen in our models is compared to observations of geodetic tilting and migration of rivers within the region that have been attributed to tectonic activity (Adams, 1980; Cox, 1994; Cox, et. al., 2001a). Based on these models, we can understand how the inclusion or exclusion of various faults affects the vertical deformation and tilt within the region. We also provide a means of quantifying the relative slip that exists among the faults and predict which faults may be more active. Finally, we seek to establish slip rates for the modeled faults based on recurrence intervals that have been suggested for the NMSZ (Schweig and Ellis, 1994).

2.0 Model Design

2.1 Source Orientation

We model the deep fault as a vertical, right-lateral strike-slip fault based on the in-situ stresses of the region (Schweig and Ellis, 1994). As a result, an alternating pattern of uplift and subsidence is generated at each end of the deep fault (Fig. 2). In order to orient this deep fault correctly, we place its origin at the AR-LA border (93°W, 33°N), just west of the geologic structure known as the Monroe Uplift. Although resurveys in this area have indicated that relative subsidence has occurred from 1934-66, these data have been attributed to water level changes in the area and have been deemed to represent only temporary effects (Schumm, et. al., 1982). The evidence for tectonic deformation in this area has been asserted to be present due to "the parallel nature of the slope changes among the different [river] terraces" that lie within this region (Schumm, et. al., 1982). Further indicators of tectonic deformation in this area are the patterns of channel change on the Monroe Uplift (Burnett and Schumm, 1983). Based on this information, we have

oriented the deep fault in our model such that it will produce a region of uplift where the Monroe Uplift now exists. Additional support for starting the deep fault at this location is due to the W-SW preferred migration of the Ouachita, Saline, and Arkansas Rivers in southeastern Arkansas (Cox, 1994). Two different locations were chosen for the northern endpoint of the deep fault. We chose one orientation (N41°E) of the deep fault to terminate at 88.5°W, 37.5°N based on the evidence of Quaternary displacements in the Fluorspar Area Fault Complex (Nelson, 1997). Another orientation (N43.4°E) was chosen to terminate farther east at 88.15°W, 37.5°N, near the IL-KY border based on the presence of faulting that extends into Kentucky (Cox, personal communication, 6/01). In our subsequent discussion we shall refer to the two driving faults as the eastern (N43.4°E) fault and western (N41°E) fault.

2.2 Orientation of Shallow Faults

Upper crustal faults (Fig. 3) have been placed at their respective locations based on the known seismicity patterns in the area. Fault 1 is the southeastern Reelfoot rift fault that is part of the Big Creek fault zone (Cox, et. al., 2001b). Fault 2 is the southern arm of seismicity in the NMSZ. The bootheel lineament is included as fault 3 based on evidence that it was involved in the 1811-1812 earthquakes (Ellis, et. al., 2001). Fault 4 is a northeast striking fault just north of the NMSZ that is identified by seismicity in this area. The northern arm and east-west arm of the NMSZ are faults 5 and 6, respectively. Faults 7 and 8 comprise the Reelfoot thrust fault in the NMSZ. Fault 8 is extended back to the southeastern rift margin due to current seismicity and geologic patterns (Cox, et. al., 2001b). Fault 9 is the commerce fault which is currently seismically active (Harrison and Schultz, 1994). In each model, we have included the Reelfoot thrust fault (faults 7 &

8) and its northeast-striking arm (fault 5). The Reelfoot thrust has been modeled as two fault segments with dips of 30 and 34 degrees for faults 7 and 8, respectively. All other faults (1-6, 9) have been modeled as vertical strike-slip faults. Each of the upper crustal faults was terminated one-half km below the surface in order to minimize the anomalies that exist at the boundaries of the faults in our modeling process.

2.3 Model Constraints

Previous research provides us with several constraints that are useful in calibrating our results. On a regional scale, that is, within the NMSZ, we rely upon a structure contour map of deformation in Quaternary time (see Fig. 2 of Mihills and Van Arsdale, 1999). These regional constraints should include subsidence west of fault 2, uplift east of fault 2, subsidence northwest of the Lake County Uplift (LCU), uplift in the area including the LCU, Ridgely Ridge, and Tiptonville Dome, and subsidence at Reelfoot Lake. On a much larger scale extending from northern Louisiana to southern Illinois, we rely mainly upon evidence of geodetic tilting and river migration resulting from tectonic activity. These large-scale constraints include western cross-valley tilt of the Mississippi River between St. Louis, MO, and Cairo, IL, and eastern cross-valley tilt of the same between Cairo, IL and Memphis, TN (Adams, 1980). Another constraint includes northeast tilting at 89°W, 37°N, and southeast tilting at 89°W, 35°N, from drainage basin asymmetry analyses (Cox, et. al., 2001a). Southeast tilting of the Mississippi River should occur in the vicinity of the southern arm of the NMSZ (fault 2) (Cox, 1994). A final large-scale constraint is westward tilting of the lower Wabash River (Fraser, et. al., 1997). These constraints by no means encompass all of the requirements for this model to meet, but they do provide a means of calibration for our models.

3.0 Results and Interpretations

3.1 Relative Vertical Displacements

The inclusion of additional faults (i.e., faults 1, 4, 6, 9) in the models did not significantly impact the general pattern of vertical displacement seen on a large scale (see Fig. 4). The greatest impact on the models appears to derive from the orientation of the deep driving fault. For instance, in model E (Figs. 1b, 6), the western deep fault produces a region of subsidence along the east side of the southern fault (fault 2). In model A (Figs. 1a, 5), however, the eastern deep fault produces a region of subsidence along the west side of the southern fault. This feature makes model A (and thus the eastern deep fault) more consistent with structural contour maps that have been interpreted to represent structural deformation during Late Wisconsin through Holocene time (see Fig. 2 of Mihills and Van Arsdale, 1999). Model A also produced less pronounced areas of uplift and subsidence than were seen in model E. Based on this information alone, the eastern deep fault supports known evidence of tectonic deformation and allows a more gradual transition from areas of uplift to those of subsidence.

Another interesting comparison involved the changes in the deformation that occurred as a result of including either the bootheel fault (fault 3) or the southern fault (fault 2). In models B and F (Figs. 5, 6), the introduction of the bootheel fault produced a region of subsidence in the area of the Lake County Uplift (LCU). The southern fault (see models A and E in Figs. 5, 6) better represents the uplift seen in the LCU and provides a gradual transition from uplift to subsidence northwest of the LCU. These

factors support model A, and thus the use of the southern fault and the eastern deep fault, as the best representation of the deformation in the NMSZ.

Some concerns regarding the meaning of the model's relative displacements should be further investigated. In particular, the areas at each end of the deep fault (see Fig. 2) need to be examined as to whether these alternating patterns of subsidence and uplift do exist. At the south end of the deep fault, we do have evidence of uplift in the Monroe Uplift area, but the area west of this location should also have subsidence according to the model's predictions. Studies of the North Louisiana-South Arkansas Basin do indicate that tectonic subsidence has occurred in the area to the west of the Monroe Uplift, but this activity was long before Quaternary time (Lowrie, et. al., 1993). These investigations will help to determine if indeed the deep fault can be incorporated as an indicator of the deformation for a wide region. If not, we must confine the deep fault to be a descriptor of the much more limited region that includes only the NMSZ .

3.2 Tilt Plots

From the relative vertical displacements that the models dictate, we numerically determined the gradients for these displacements in order to examine the expected ground tilting. On a regional scale, the tilt plots remained very similar regardless of what faults were included or even how the deep fault was oriented. The tilts produced by the model (Fig. 8) supported the direction of cross-valley tilts measured from St. Louis, MO, to Cairo, IL (downward tilt to the west), and further south from Cairo, IL, to Memphis, TN (downward tilt to the east) (Adams, 1980). Southeast tilting of the Mississippi River is found in the vicinity of the southern arm of the NMSZ, which agrees with previous studies (Cox, 1994).

Some questions do arise concerning the accuracy of the tilt directions seen in this model. For instance, at 89°W, 37°N, basin-asymmetry vectors by Cox, et. al. (2001a) indicate northeast tilting while our model produces tilts to the southeast (see Fig. 8). Furthermore, basin-asymmetry vectors lying at 89°W, 35°N suggest southeast tilting, while our model produces northeastern tilts in this region (Cox, et. al., 2001a). Our models also have implications for the directions in which river migration should be occurring. The models predict an eastern migration of the lower Wabash River, but studies have indicated this area to be tilting westward (Fraser, et. al., 1997).

The tilt plots reveal that the large scale tilting associated with deep fault-driven deformation is largely unaffected by the configuration of the upper crustal faults in the models or the orientation of the deep driving fault. The far field tilts (i.e. western TN, southern IL, southern IN) are not completely consistent with evidence of tilting (or lack of it) in these areas, but these models do produce very accurate descriptions of the cross-valley tilts seen along the Mississippi River (Adams, 1980). Further investigation on a smaller scale reveals only small changes in tilt that occur for the different models in the vicinity of faults 5, 7, and 8.

3.3 Relative Slip among the Faults

Twenty models were run (see Table 3, ten models run for each deep fault) to compare the relative slip that occurred among the various faults in the model to give an indication of which faults were more active than others (Figs. 8, 9). The orientation of the deep fault did significantly impact which shallow fault was the most active and how much slip occurred on each fault. In general, the closer an upper crustal fault was to the location of the deep fault, the more slip it would experience. For the western orientation

of the deep fault, the bootheel fault (fault 3) experienced the most slip; whereas, for the eastern deep fault, the southern fault (fault 2) slipped the most. In each case little variation was seen to occur among the models concerning the amount of slip that each fault underwent. Faults lying far from the deep fault (i.e. the commerce fault) experienced very little slip regardless of the deep fault location. These models imply the activity of a shallow fault is dependent on its proximity to the deep fault that drives the deformation.

In order for us to understand the time scale of our models and the relative activity of the upper crustal faults, we have estimated slip rates for each of the faults. We establish slip rates for the faults in our models by making the following assumptions: 1) the moment magnitude of the deformation in our models is $M = 8.0$, and 2) the time scale necessary for the models to achieve this moment magnitude is either 500 or 1000 years. This time period is based upon recurrence intervals that have been estimated for the NMSZ (Schweig and Ellis, 1994). We then used the relationship:

$$M_w = 2\log|u| + 6.314 \quad (1)$$

where M_w is the moment magnitude, and u is the average slip (m) occurring. Therefore, for $M = 8.0$, we have $u = 6.97$ m of slip on the most active fault. In scaling the models, we chose the most active fault to be either the bootheel fault (fault 3) or the reelfoot thrust faults (faults 7 and 8). These faults were chosen based on modeling of the rupture scenarios for the New Madrid earthquakes during 1811-1812 (Ellis, et. al., 2001). We established a scaling factor for our model by dividing the slip on the most active fault (either fault 3 or faults 7, 8) by 6.97m for $M = 8.0$. We then estimated slip rates for each fault by applying a time period of either 500 or 1000 years. The results of these

calculations are listed in Figs. 10 and 11. These figures illustrate that, in general, the faults experience more slip with the eastern deep fault.

4.0 Conclusions

From the numerous models run, we found that the inclusion of additional faults (1, 4, 6, 9) did not significantly impact the large-scale displacement fields. The location of the deep fault largely determined the geometry of the relative displacements as well as the slip that the upper crustal faults underwent. In general, our models were able to produce both topographic and subsurface features that have been observed in the NMSZ. Tilts in our models agree with cross-valley tilts seen along the Mississippi River, but further investigation needs to be performed to produce a model that exhibits tilting features that have been observed far from the deep fault. Our models do produce a powerful means of predicting the migration of rivers (i.e., Ohio, Wabash, Tennessee, and Mississippi) and further observations should be performed to determine whether these migrations are indeed occurring as the model predicts. We have produced a means of driving the deformation in the NMSZ that can be calibrated by various geologic and geomorphic observations, and that provides wide-scale implications for the surrounding region as well.

5.0 Acknowledgements

This research project was conducted at the Center for Earthquake Research and Information at the University of Memphis. My involvement was made possible as part of the Research Experience for Undergraduates program through the Mid-America

Earthquake Center. Funding for this project was provided by the National Science Foundation. I would like to thank Dr. Michael Ellis of the University of Memphis for his guidance and advice during the course of this project. Many thanks are due to both Dr. Ellis and Dr. Van Arsdale of the University of Memphis for reviewing my results and making many helpful suggestions.

Table 1. Coordinates of modeled faults.

Fault	Starting Point (°)		Ending point (°)		Strike (°)	Dip (°)
	Latitude	Longitude	Latitude	Longitude		
1	35.32	-90.10	36.50	-88.95	39.80	90
2	35.50	-90.50	36.20	-89.58	49.00	90
	36.20	-89.58	36.25	-89.50	49.00	90
	36.25	-89.50	36.33	-89.42	49.00	90
3	35.50	-90.50	35.89	-90.07	44.20	90
	35.89	-90.07	36.05	-89.97	28.51	90
	36.05	-89.97	36.57	-89.71	23.59	90
4	36.83	-89.33	37.22	-89.00	36.20	90
5	36.62	-89.58	36.92	-89.42	25.60	90
6	36.58	-90.00	36.62	-89.58	86.00	90
7	36.62	-89.58	36.33	-89.42	156.07	30
8	36.33	-89.42	36.08	-89.33	166.30	34
9	35.33	-92.00	37.83	-88.50	50.85	90
deep (west)	33.00	-93.00	37.50	-88.52	41.00	90
deep (east)	33.00	-93.00	37.50	-88.15	43.40	90

Table 2. Fault configurations for each model.

model	Faults Included
A	2, 5, 7, 8, deep (eastward shift)
B	3, 5, 7, 8, deep (eastward shift)
C	1, 2, 4, 5, 6, 7, 8, 9, deep (eastward shift)
D	1, 3, 4, 5, 6, 7, 8, 9, deep (eastward shift)
E	2, 5, 7, 8, deep (no shift)
F	3, 5, 7, 8, deep (no shift)
G	1, 2, 4, 5, 6, 7, 8, 9, deep (no shift)
H	1, 3, 4, 5, 6, 7, 8, 9, deep (no shift)

Table 3. Models for slip comparison.

model	Faults Included
1	2, 5, 7, 8, deep
2	1, 2, 5, 7, 8, deep
3	2, 4, 5, 6, 7, 8, deep
4	3, 5, 7, 8, deep
5	1, 3, 5, 7, 8, deep
6	3, 4, 5, 6, 7, 8, deep
7	1, 2, 4, 5, 6, 7, 8, 9, deep
8	2, 5, 7, 8, 9, deep
9	3, 5, 7, 8, 9, deep
10	1, 3, 4, 5, 6, 7, 8, 9, deep

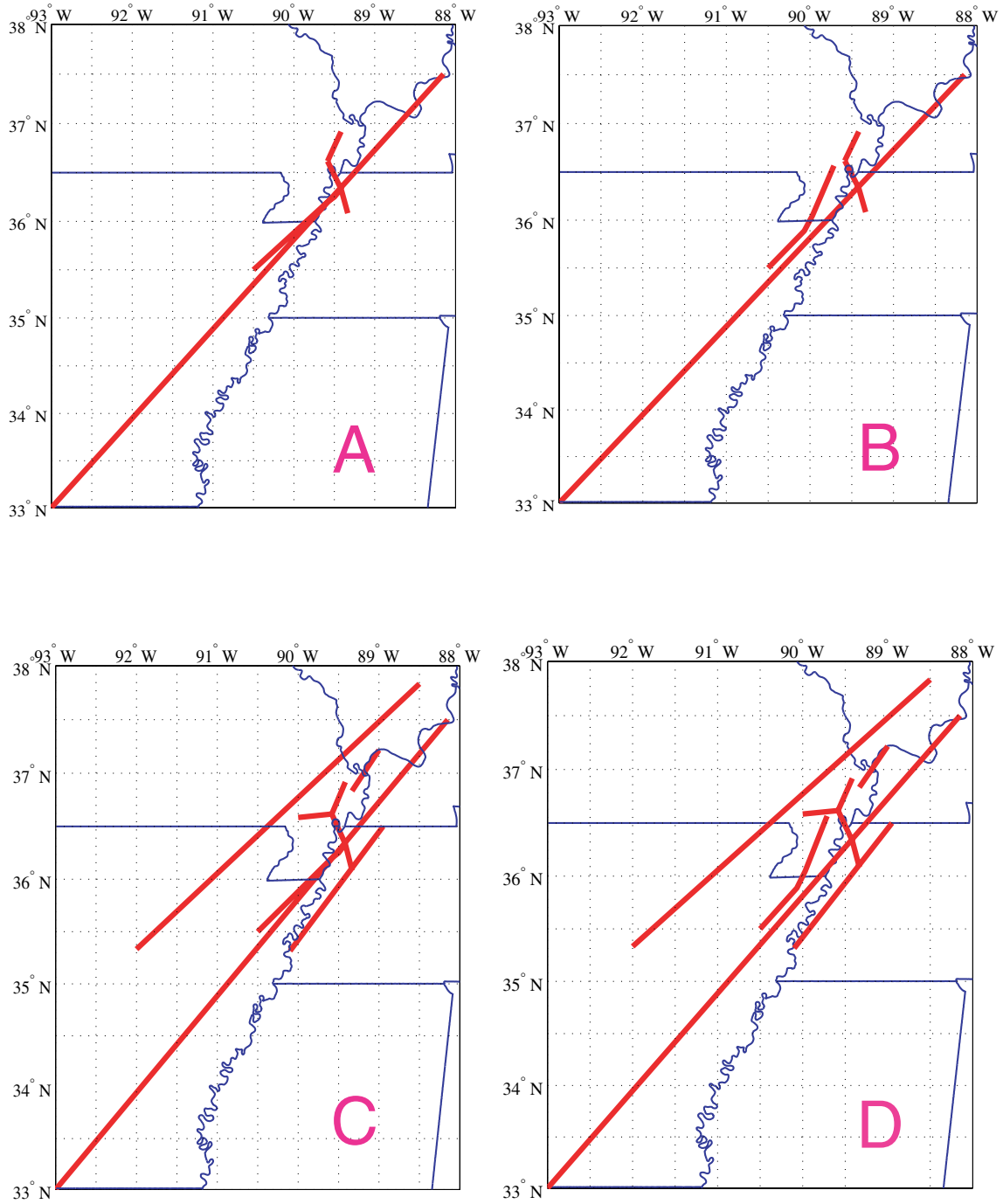


Fig. 1a

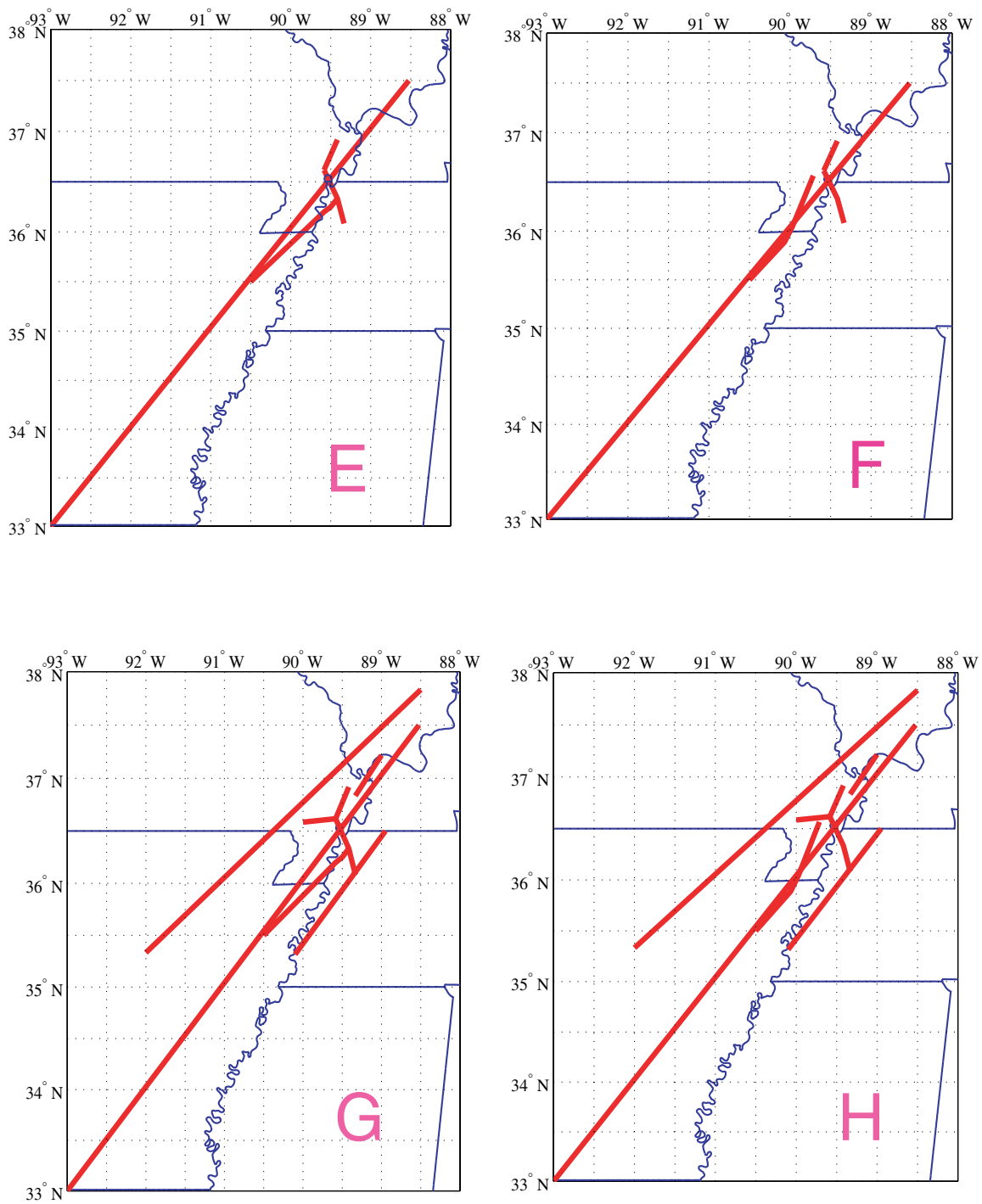


Fig. 1b

Figs. 1a-b Orientation of the faults for each respective model. The deep fault begins at 93°W, 33°N. (Models A-D include the eastern deep fault, while models E-H include the western deep fault.)

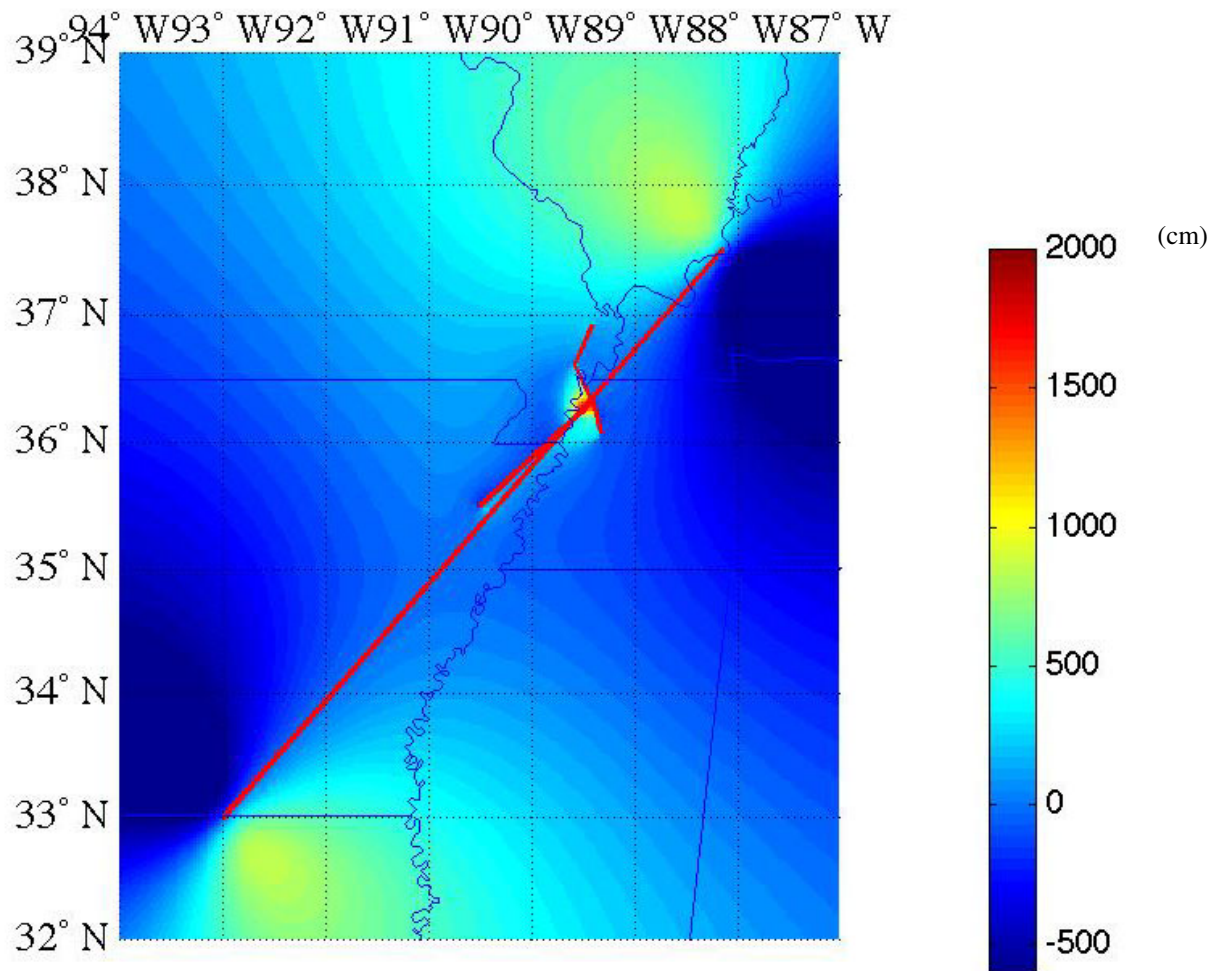


Fig. 2 Relative vertical displacements (cm) for model A. The deep fault begins at 93°W, 33°N. Notice the alternating pattern of uplift and subsidence at each end of the deep fault.

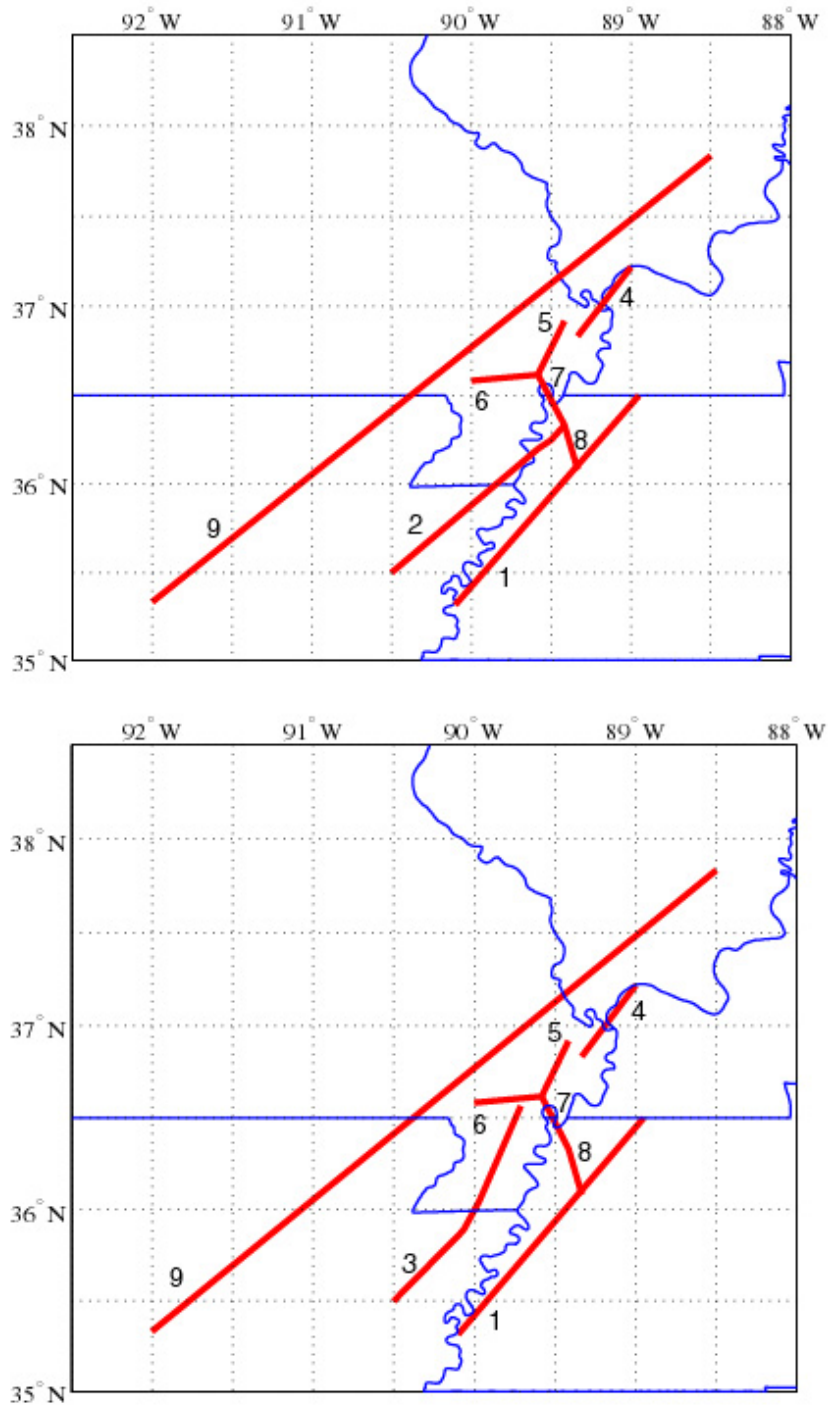
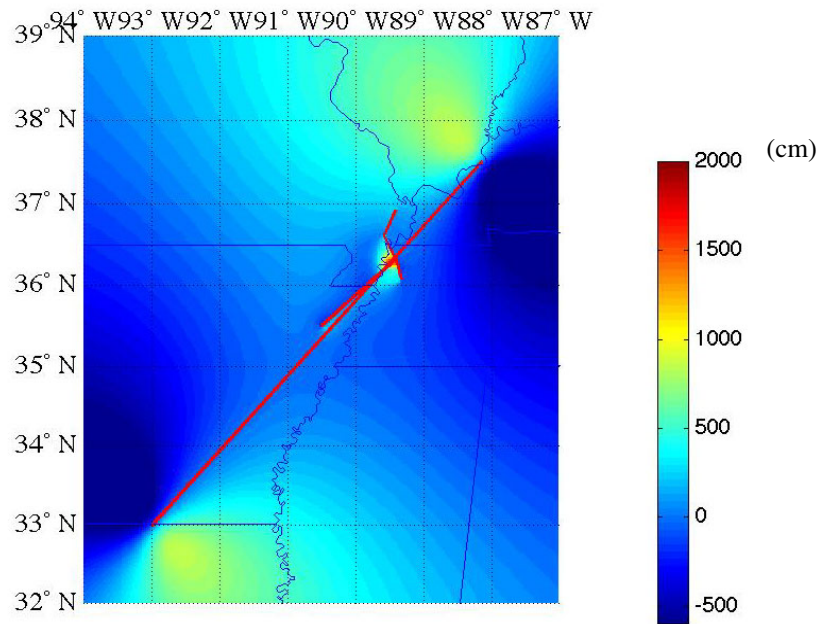
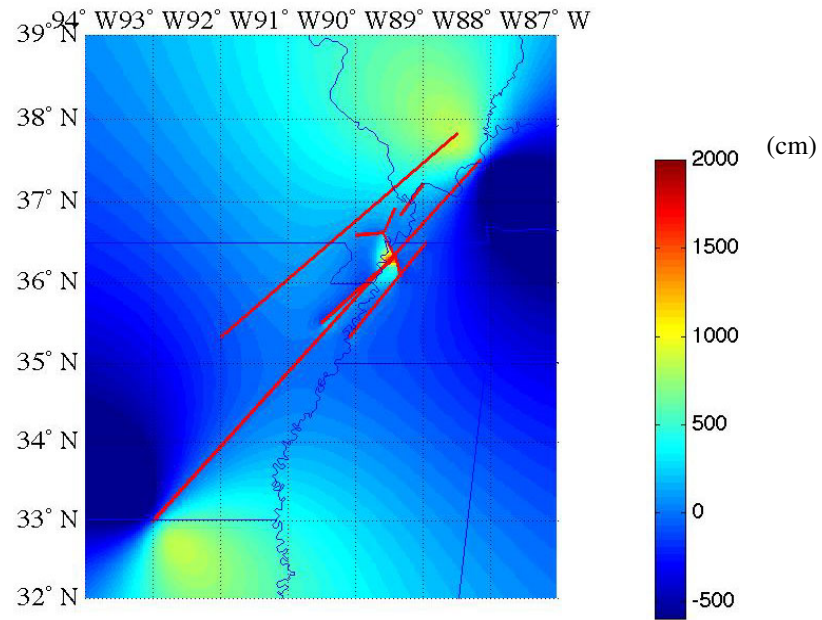


Fig. 3 Labeling and orientation of the upper crustal faults. Note the following terms may be applied in the description of these faults: Reelfoot thrust faults--7 & 8; Commerce Fault--9; Bootheel lineament--3; Southern Fault--2.

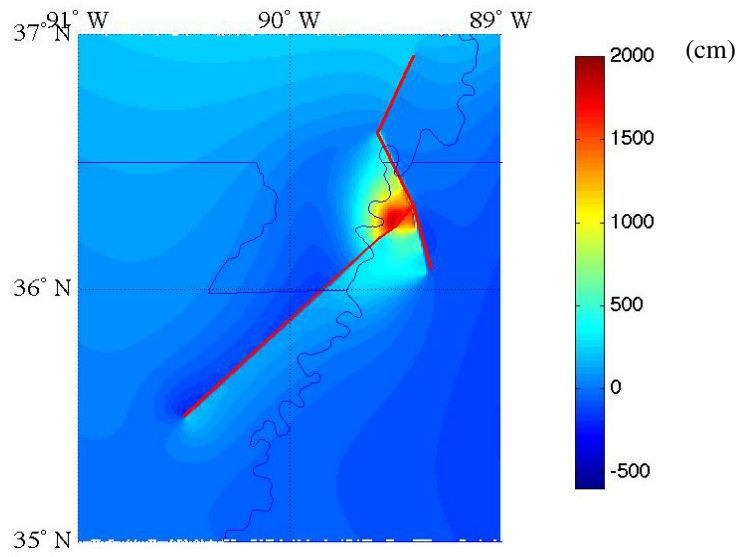


Model A

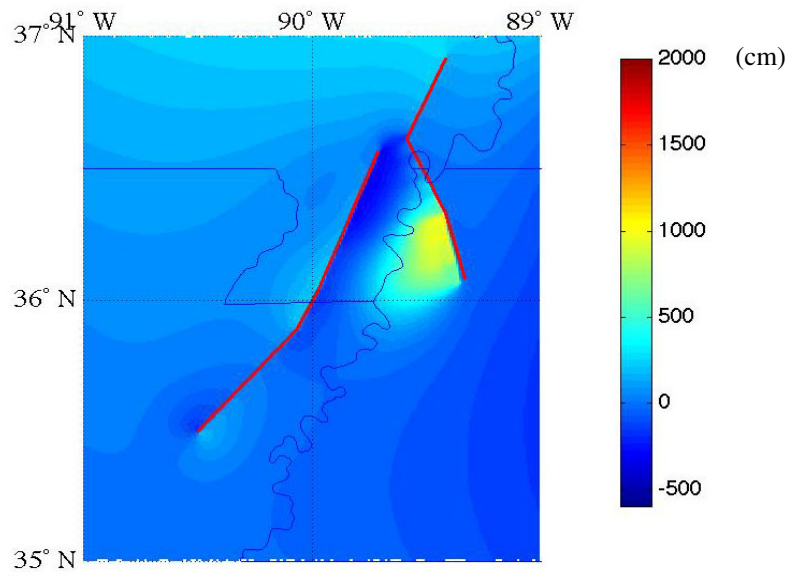


Model C

Fig. 4 Relative vertical displacements (in cm) for models A and C (eastern deep fault).



Model A



Model B

Fig. 5 Relative vertical displacements (in cm) for models A and B (eastern deep fault).

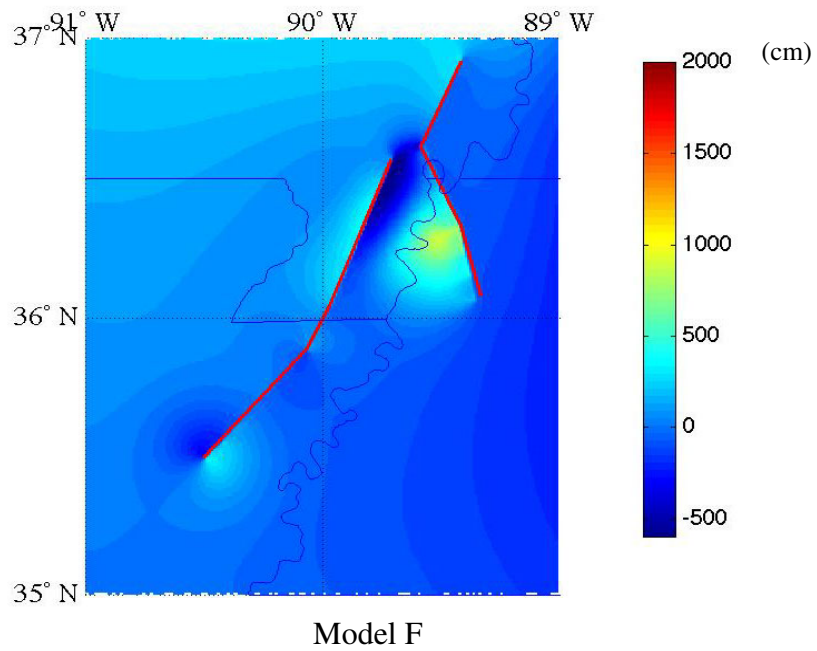
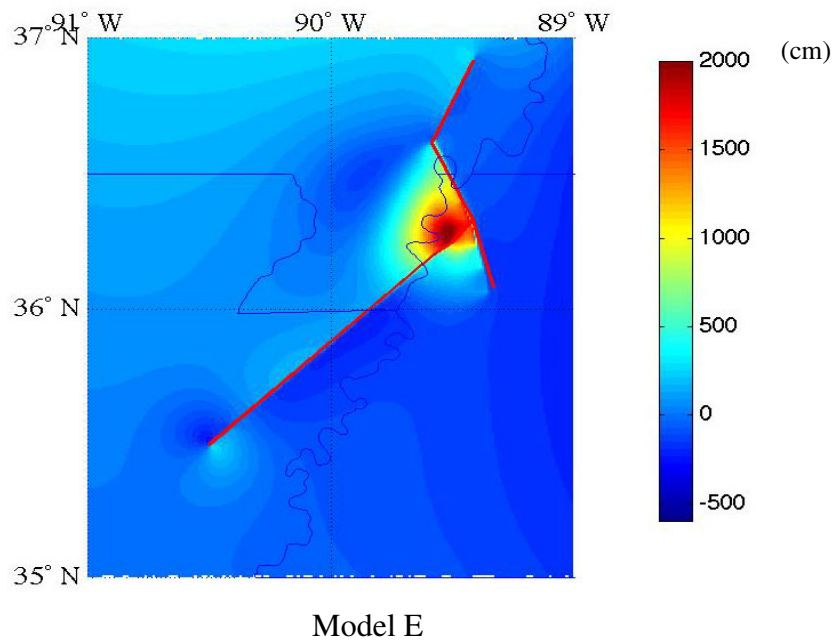


Fig. 6 Relative vertical displacements (in cm) for models E and F (western deep fault).

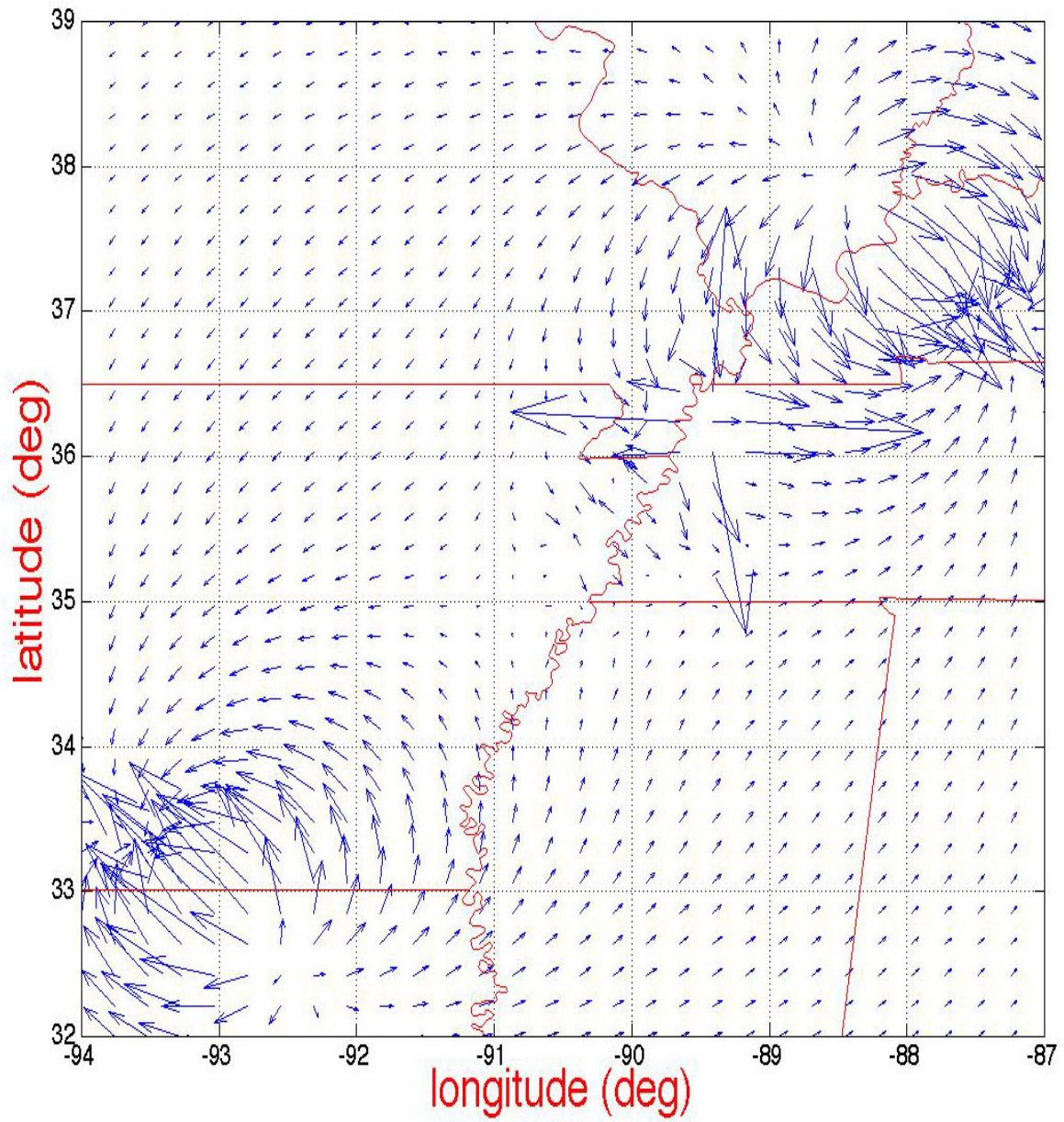


Fig. 7 Directional field for model A. Vectors are pointing in the direction of downward tilt.

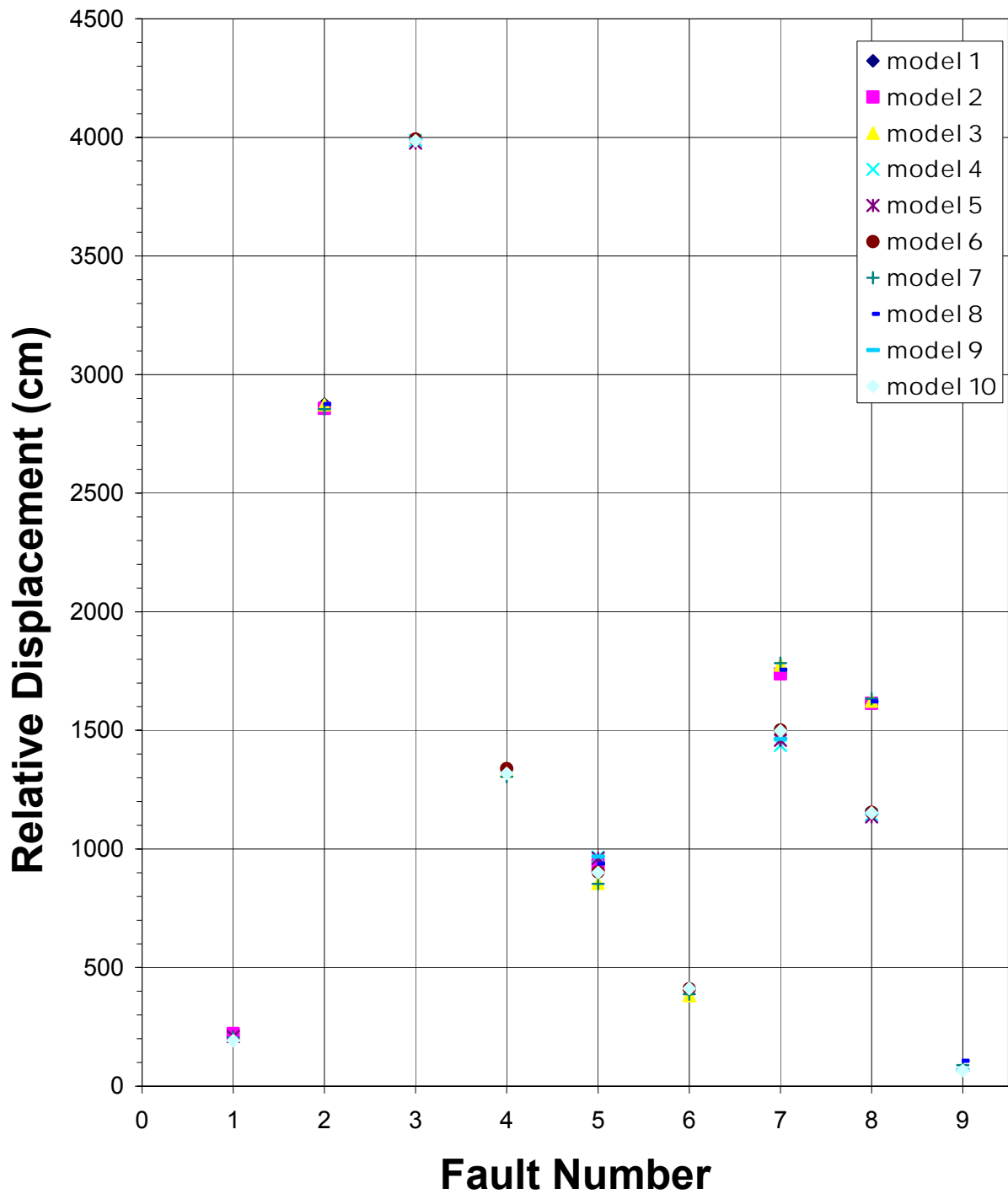


Fig. 8 Relative slip (per 100m slip of the deep fault) occurring for ten models with the western deep fault. See Fig. 2 for the locations of the respective fault numbers. Table 3 lists the faults included in each of the ten models.

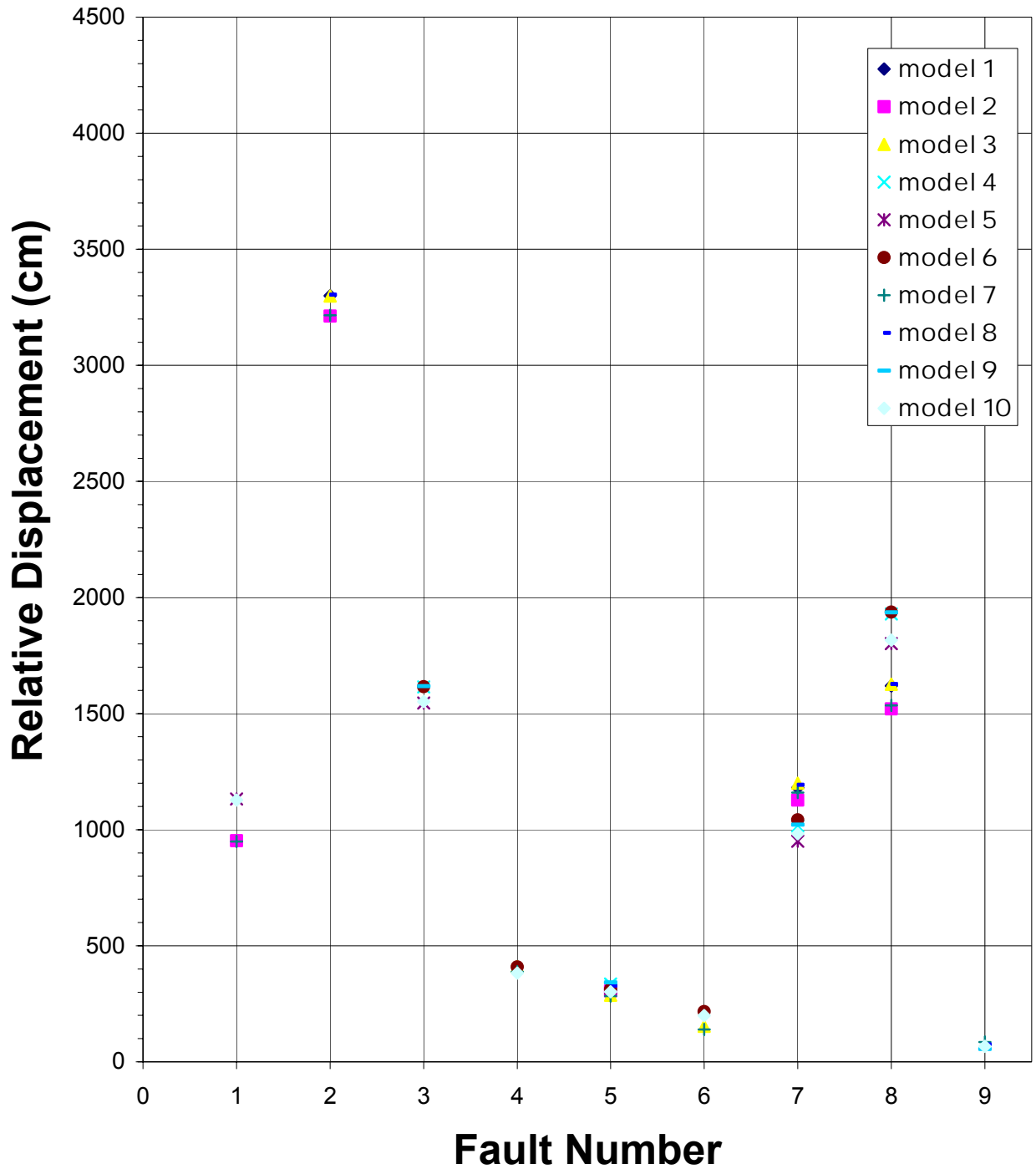


Fig. 9 Relative slip (per 100m slip of the deep fault) occurring for ten models with the eastern deep fault. See Fig. 2 for the respective fault numbers. Table 3 lists the faults included in each model.

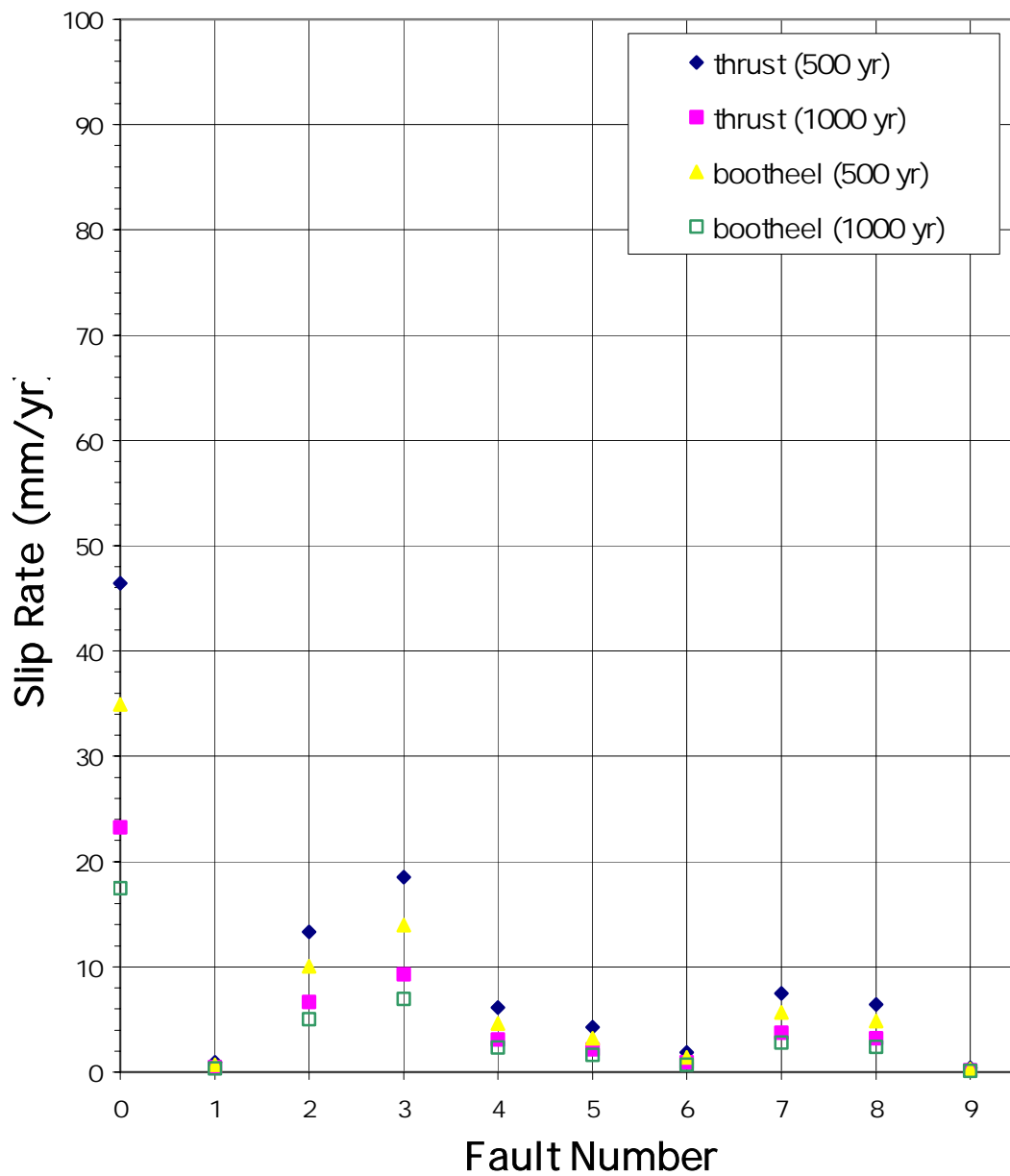


Fig. 10 Relative slip rates based on $M = 8.0$ on either the bootheel fault or the Reelfoot thrust fault for a time period of either 500 or 1000 years. (Fault 0 is the western deep fault.)

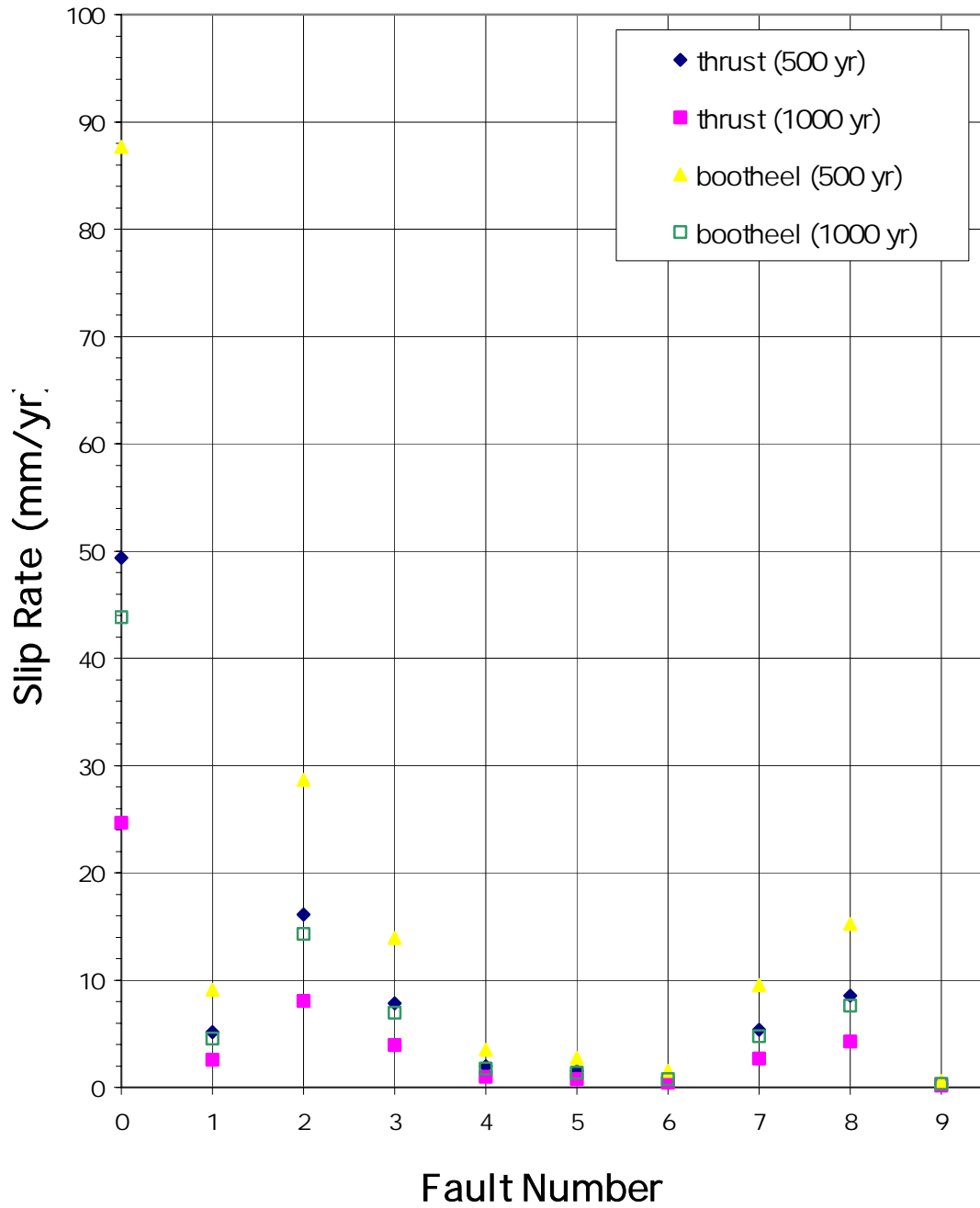


Fig. 11 Relative slip rates based on $M = 8.0$ on either the bootheel fault or the Reelfoot thrust fault for a time period of either 500 or 1000 years. (Fault 0 is the eastern deep fault.)

References

- Adams, J., 1980, Active tilting of the United States midcontinent: Geodetic and geomorphic evidence: *Geology*, v. 8, pp. 442-446.
- Burnett, A. W., and S. A. Schumm, 1983, Alluvial-River Response to Neotectonic Deformation in Louisiana and Mississippi: *Science*, v. 222, pp. 49-50.
- Cox, R. T., R. B. Van Arsdale, and J. B. Harris, 2001a, Identification of possible Quaternary deformation in the northeastern Mississippi Embayment using quantitative geomorphic analysis of drainage-basin asymmetry: *Geological Society of America Bulletin*, v. 113, pp. 615-624.
- Cox, R. T., R. B. Van Arsdale, J. B. Harris, and D. Larsen, 2001b, Neotectonics of the southeastern Reelfoot rift margin, central United States, and implications for regional strain accommodation: *Geology*, v. 29, pp. 419-422.
- Cox, R. T., R. B. Van Arsdale, J. B. Harris, S. L. Forman, W. Beard, and J. Galluzzi, 2000, Quaternary faulting in the southern Mississippi embayment and implications for tectonics and seismicity in an intraplate setting: *Geological Society of America Bulletin*, v. 112, pp. 1724-1735.
- Cox, R. T., 1994, Analysis of drainage-basin symmetry as a rapid technique to identify areas of possible Quaternary tilt-block tectonics: An example from the Mississippi Embayment: *Geological Society of America Bulletin*, v. 106, pp. 571-581.
- Ellis, M. A., S. G. Prejean, E. S. Schweig, and A. C. Johnston, 2001, A Rupture Scenario for the Great New Madrid Earthquakes of 1811-1812, in press.
- Fraser, G. S., T. A. Thompson, G. A. Olyphant, L. Furer, and S. W. Bennett, 1997, Geomorphic Response to Tectonically-Induced Ground Deformation in the Wabash Valley: *Seismological Research Letters*, v. 68, pp. 662-674.
- Gomberg, J., and M. Ellis, 1994, Topography and tectonics of the central New Madrid seismic zone: Results of numerical experiments using a three-dimensional boundary element program: *Journal of Geophysical Research*, v. 99, pp. 20,299-20,310.
- Harrison, R. W., and A. Schultz, 1994, Strike-slip faulting at Thebes Gap, Missouri and Illinois: Implications for New Madrid tectonism: *Tectonics*, v. 13, pp. 246-257.
- Kenner, S. J., and P. Segall, 2000, A Mechanical Model for Intraplate Earthquakes: Application to the New Madrid Seismic Zone: *Science*, v. 289, pp. 2329-2332.
- Lowrie, A., N. M. Sullivan, C. Krotzer, J. Carter, I. Lerche, and K. Peterson, 1993, Tectonic and Depositional Model of the North Louisiana-South Arkansas Basin: *Gulf Coast Association of Geological Societies Transactions*, v. 43, pp. 231-238.
- Mihills, R. K., and R. B. Van Arsdale, 1999, Late Wisconsin to Holocene Deformation in the New Madrid Seismic Zone: *Bulletin of the Seismological Society of America*, v. 89, pp. 1019-1024.

References

- Nelson, J. W., F. B. Denny, J. A. Devera, L. R. Follmer, and J. M. Masters, 1997, Tertiary and Quaternary tectonic faulting in southernmost Illinois: *Engineering Geology*, v. 46, pp. 235-258.
- Purser, J. L., and R. B. Van Arsdale, 1998, Structure of the Lake County Uplift: New Madrid Seismic Zone: *Bulletin of the Seismological Society of America*, v. 88, pp. 1204-1211.
- Schumm, S. A., C. C. Watson, and A. W. Burnett, US Army Corps of Engineers, Lower Mississippi Valley Division, 1982, Phase I Investigation of Neotectonic Activity within the Lower Mississippi Valley Division, Shreveport: Water Engineering and Technology, Inc.
- Schweig, E. S., and M. A. Ellis, 1994, Reconciling Short Recurrence Intervals with Minor Deformation in the New Madrid Seismic Zone: *Science*, v. 264, pp. 1308-1311.
- Stuart, W. D., T. G. Hildenbrand, and R. W. Simpson, 1997, Stressing of the New Madrid Seismic Zone by a lower crust detachment fault: *Journal of Geophysical Research*, v. 102, pp. 27,623-27,633.

Diagonal Tension in Unreinforced Masonry
Assemblages

MAEC ST-11: Large Scale Test of Low Rise Building
System

Malcolm Foss
Georgia Institute of Technology

Abstract

Diagonal tension, or what is commonly referred to as shear, is an important failure mode in unreinforced masonry structures, particularly because of the brittle nature of the failure. Though it is not generally the governing mode of failure in low-rise buildings like those under investigation by MAEC ST-11, it can come into play any time significantly large vertical forces are introduced, for example, when post-tensioning retrofits are installed. The primary focus of this paper will be the effects of the varying properties of different building materials on the ultimate diagonal tensile strength of unreinforced masonry (URM) assemblages. In particular, it will compare the strength characteristics of URM assemblages made from solid bricks with those of URM assemblages made from cored bricks. It is known that the diagonal tensile strength should decrease as the surface area of the bricks decreases. However, under investigation will be whether or not any significant resistance is provided by a mechanical keying action created by mortar within the holes of the cored bricks to counter the reduction in area. A statistical analysis of the test results will reveal that in fact, the diagonal tensile strength of URM assemblages is linearly dependent on masonry unit surface area, and is not effected by the mechanical connection between brick and mortar within the core holes.

Project Scope

MAEC ST-11 tests a large-scale building prototype subjected to cyclic load reversals. The primary objectives are to verify analytical models developed through component tests under other MAE Center projects and to assess the effectiveness of proposed retrofitting schemes. The project investigates a full-scale low rise building system subjected to slowly applied lateral force reversals. The lateral forces will be based on the dynamic tests of project ST-10 and will represent expected force levels per 1997 NEHRP seismic provisions. The building system is a large-scale companion to the reduced scale dynamic structure tested in ST-10. A multiple series of tests will run with the test structure in its original state as well as with several rehabilitation methods per previous studies (ST-6 through ST-8). Floor systems will be replaced to study lateral force distribution and torsional effects with flexible and rigid diaphragms. Measured response of the test structure will be compared with FEMA 273, based on nonlinear static analysis. Nondestructive tests will be run to provide data for correlation with ultimate lateral strength of the test structure.

Test Structure

The ST-11 test structure is a full-scale two story unreinforced masonry (URM) building. Some of the significant characteristics of the structure are that it is a box-type structure, it has two perforated, perimeter bearing walls in each direction, and it has flexible timber roof/floor diaphragms supported by shear/bearing walls. This particular type of structure was chosen for several reasons, including the need for research data in areas such as 2D vs. 3D analysis and in-plane/out-of-plane interaction. However,

perhaps the most significant reason for choosing this type of structure is the prevalence of such structures throughout Mid-America, coupled with their perceived vulnerability to seismic activity and high need for innovative retrofit strategies. Hence, in order to acquire useful data on the behavior of such structures, it was imperative that the material characteristics and construction practices used on the ST-11 structure accurately reproduced those of the said vintage/type.

Type of Masonry Units

The first issue at hand before construction could begin then, became what type of bricks to use in the test structure. The majority of vintage URM buildings in Mid-America were constructed from solid bricks. However, cored bricks can be obtained at less expense, and so, unless a significant difference in the performance of solid vs. cored bricks could be demonstrated, cored bricks would be used for economical reasons. Concerning the shear strength of unreinforced masonry assemblages; an interesting question arises when considering whether or not a difference in performance might exist between masonry assemblages comprised of solid bricks and those comprised of cored bricks. Intuitively, the reduction in surface area on which to develop bond strength between brick and mortar should result in lower shear strength in URM assemblages constructed from cored bricks. However, when a cored brick is set in a bed of mortar, the mortar protrudes up into the holes within the cored brick, and there is the possibility that the mechanical connection formed by this protrusion may serve to counteract the loss of shear strength resulting from the reduction in surface area. The remainder of this paper will present the results of tests performed to determine the nature of this relationship

between surface area of masonry units and shear strength of unreinforced masonry assemblages.

Test Procedure

Masonry shear strength was evaluated according to ASTM E519-00. This test method covers the determination of the diagonal tensile (shear) strength of 4 ft by 4 ft masonry assemblages by loading them in compression along one diagonal. The given loading causes a diagonal tension failure with the specimen splitting apart along an axis parallel to the direction of the compressive load. The shear stress is calculated as:

$$\tau = P/A$$

where:

τ = shear stress on gross area, (psi)

P = applied load, (lbf), and

A = gross cross sectional area of the specimen, (in²), calculated as follows:

$$A = 1.414ht$$

where:

h = height of the specimen, (in), and

t = thickness of the specimen, (in)

It should be noted that the tensile stress induced by the applied load develops along the diagonal of the specimen, hence the cross sectional area along the diagonal must be used in the calculation (the area is multiplied by 1.414).

The specimens used in the ST-11 shear test measured 2 ft by 2ft rather than 4 ft by 4 ft as specified by ASTM E519-00. The reduction in size was made in order to

facilitate ease of construction and handling of the specimens. This reduction is allowable under ASTM E519-00 which states, “as a research test method used only for the purpose of evaluating the effects of variables such as type of masonry unit, mortar, workmanship, etc., a smaller size specimen could be used”. Also, ST-11 shear test specimens were covered with vapor barrier and cured for 14 days rather than 28 days in laboratory air.

Results and Analysis

The ST-11 shear test consisted of twelve shear specimens, six of which were constructed of solid bricks and six of which were constructed of cored bricks. The specimens were constructed in such a manner as to yield six pairs of one solid and one cored specimen each. In other words, one solid sample and one cored sample were constructed from a particular batch of mortar by a particular student to ensure homogeneity resulting in a paired data set for analysis. The results of the shear test are summarized in Table 1 through Table 4 in Appendix A. One key element of interest in the results of the test is the fact that shear strength of the solid specimen exceeded that of the cored specimen for all six pairs. This would seem to suggest a positive correlation between surface area of masonry units and shear strength of masonry assemblages. Further more, the mean of the ratio of shear strength of solid specimens to shear strength of cored specimens is 1.24, while the ratio of the surface area of a solid brick (27 in²) to the surface area of a cored brick (21.6 in²) is 1.25. This suggests not only a positive correlation between surface area of masonry units and shear strength of masonry assemblages, but also a linear relationship between the two. Pearson’s sample correlation

coefficient was used as a quantitative measure of the extent to which surface area and shear strength are linearly related.

Pearson's sample correlation coefficient is defined as:

$$r = S_{xy}/(S_{xx})^{1/2}(S_{yy})^{1/2}$$

where:

$$S_{xx} = \sum x_i^2 - (\sum x_i)^2/n$$

$$S_{yy} = \sum y_i^2 - (\sum y_i)^2/n$$

$$S_{xy} = \sum x_i y_i - (\sum x_i)(\sum y_i)/n$$

It is important to note several properties of the correlation coefficient while interpreting the results. The value of r does not depend on the unit of measurement for either variable. The value of r does not depend on the choice of dependent or independent variable. The value of r is between -1 and 1 . A value near the upper limit is indicative of a substantial positive relationship, that is, a strong tendency for y to increase as x increases, whereas a value near the lower limit suggests a prominent negative relationship, or tendency for y to decrease as x increases. The value of r is 1 only when all the points in a scatter plot of the data lie exactly on a straight line with positive slope. Similarly, $r = -1$ only when all the points lie exactly on a line with negative slope.

In calculating the correlation coefficient for the ST-11 shear specimens, only the pairs with shear strength values in the middle 50% were used, in order to resist the effect of outliers. Though this technique reduces the sample size to only six specimens, three each of solid and cored, it is allowable under ASTM E519-00 which states that "tests shall be made on at least three like specimens constructed with the same size and type of masonry units, mortar, and workmanship". The resulting correlation coefficient (from

Table 4) for the ST-11 shear tests was 0.7. An r value in the range of 0-0.5 is considered a weak indicator of a linear relationship between x and y , while a value from 0.5-0.8 is considered a moderate indicator, and a value between 0.8 and 1 is considered a strong indicator. An r value of 0.7 lies on the high end of the moderate range and is therefore a good indication that there is indeed a positive correlation that is also likely a linear one between surface area and shear strength.

Summary

In review, the shear strength of the solid specimen exceeded that of the cored specimen in all pairs, and the mean of the ratios of the shear strength of solid specimens to the shear strength of cored specimens is nearly exactly equal to the ratio of the area of a solid brick to the area of a cored brick. These facts along with the correlation data leave little doubt concerning the nature of the relationship between area and shear strength. The diagonal tensile strength of URM assemblages is linearly dependent on masonry unit surface area, and is not effected by the mechanical connection between brick and mortar within core holes.

Acknowledgements

The research work described in this paper was funded primarily by the Earthquake Engineering Research Centers Program of the National Science Foundation. The author would like to thank Dr. Roberto Leon of the Georgia Institute of Technology for his guidance, as well as Ph.D. candidates Franklin Moon and Tianyi Yi for their assistance in conducting this research.

Appendix A

Table 1
Masonry Shear Test (ASTM E519-00)

Specimen	Date Cast	Date Tested	Failure Load (lb)	Shear Strength (psi)	Ratio
C-1	2/5/01	2/19/01	9260	80.82	1.62
S-1	2/5/01	2/19/01	14960	130.58	
C-2	2/7/01	2/21/01	9080	79.25	1.18
S-2	2/7/01	2/21/01	10740	93.74	
C-3	2/9/01	2/23/01	12900	112.59	1.27
S-3	2/9/01	2/23/01	16400	143.14	
C-4	2/13/01	2/27/01	9200	80.30	1.13
S-4	2/13/01	2/27/01	10360	90.43	
C-5	2/17/01	3/3/01	15600	136.16	1.19
S5	2/17/01	3/3/01	18600	162.35	
C-6	3/2/01	3/16/01	5600	48.88	1.05
S-6	3/2/01	3/16/01	5900	51.50	

Table 2
Shear Strength (psi)

	Mean	Standard Deviation
Cored	89.67	30.42
Solid	111.95	40.77

Table 3
Ratio

	Mean	Standard Deviation
ratio	1.24	0.20

Table 4 Correlation			
Specimen	Area (in²), x	Shear (psi), y	Correlation, r
C-1	21.60	80.82	0.69
C-2	21.60	79.25	
C-4	21.60	80.30	
S-1	27.00	130.58	
S-2	27.00	93.74	
S-4	27.00	90.43	

References

1. Moon, F., Yi, T., Leon, R., Kahn, L. (2000). "Retrofit of Unreinforced Masonry Structures with FRP Overlays and Post-Tensioning."
2. Kahn, L. (2001). "Masonry Structural Design."
3. Drysdale, R., Hamid, A., Baker, L. (1994). "Masonry Structures, Behavior and Design." Prentice Hall, Englewood Cliffs, NJ.
4. "NEHRP guidelines for seismic rehabilitation of buildings" (1997). Federal Emergency Management Agency, Pub. 273. Washington, D.C.

Estimating the Direct and Indirect Losses from a Midwest Earthquake

Project SE-10: Economic Loss Estimation

Peggy Ho
University of Illinois at Urbana-Champaign

Massachusetts Institute of Technology
Professor Joseph Sussman
Professor Daniele Veneziano

Mid-American Earthquake Center
August 2001

Table of Contents

- i. Abstract
- ii. Introduction

- 1. The Model
 - 1.1 Input Parameters
 - 1.2 Methodology
 - 1.3 Output
- 2. Recent Improvements In the Model
 - 2.1 Quantification of Direct Losses Due to Transportation Damage
 - 2.2 Quantification of Various Social Losses
 - 2.2.1 Casualties and Fatalities
 - 2.2.2 Homelessness
 - 2.2.3 Reduction in Final Consumptions
 - 2.2.4 Quantification of Contents Loss
 - 2.2.5 Reporting Losses in Various Ways
- 3. Sensitivity Runs
 - 3.1 Base Case
 - 3.2 Runs on the uncertainty of parameters
 - 3.2.1 Earthquake Location and Intensity
 - 3.2.2 Fragility Parameters
 - 3.2.3 Recovery Parameters
 - 3.2.4 Economic Model
 - 3.2.5 Pre-earthquake capacity of links
 - 3.3 Results
 - 3.3.1 Earthquake Location and Intensity
 - 3.3.2 Fragility Parameters
 - 3.3.3 Recovery Parameters
 - 3.3.4 Economic Model and Pre-earthquake capacity of links
 - 3.3.5 Analysis
 - 3.4 Effectiveness of Loss Mitigation Actions
 - 3.4.1 Strengthening Building and Bridges
 - 3.4.2 Speeding up Recovery Rates
 - 3.4.3 Results and Analysis
- 4. Conclusions
- 5. Suggestions of Further Research
- 6. Acknowledgements
- 7. Works Cited
- 8. Appendix
 - 8.1 A Matrix
 - 8.2 Sample Code

Abstract

A macroeconomic model has been developed to estimate the economic loss due to an earthquake. At this point, sensitivity runs will be made for two main reasons. The first objective is to determine the relationship between calculated losses and uncertain model parameters. The changes in the parameters considered for this part of the sensitivity analysis are chosen to reflect the current uncertainty on each parameter. In this way, sensitivity results can be used to identify the main sources of uncertainty on this model.

The second objective is to assess the effectiveness of various loss mitigation strategies. The types of actions considered include strengthening buildings and bridges as well as increasing the rate of recovery for certain occupancy classes. The results can be compared in order to assess the best strategy for loss mitigation.

Results indicate a strong sensitivity to bridge and link recovery parameters as well as epicenter location and intensity. Also, some sensitivity runs of the second kind indicate that strengthening bridges is the most effective mitigation strategy. This however seemed higher than expected and thus possible reasons for these results are discussed.

Introduction

One of the major issues concerning an earthquake is the amount of economic loss that it may produce. In order to reduce this loss, the nation must start to prepare for an earthquake before it even happens. But in preparation, certain critical decisions must be made with regard to the allocation of money. Should we spend money retrofitting buildings, bridges, or highways? Which components contribute the greatest loss in an earthquake? The model in this project helps to answer these questions by estimating the total economic loss to the nation after a devastating earthquake in the Midwest. By seeing which loss mitigating actions are the most efficient in reducing the economic loss, the model is able to aid decision makers in evaluating the numerous possibilities in allocating funds.

This model is unique in several ways. First, it provides estimates for the entire nation. Thus, even though an earthquake may happen at one location, decision makers on the other side of the country can tell how it will affect the industries and economic sectors where they live. Second, the model not only focuses upon the direct damage sustained, but also the indirect losses following an earthquake. This is extremely important in evaluating the long-term effects of an earthquake. By estimating the losses at 6 months after an earthquake, decision makers will be better able to make decisions that will affect them in the future. Finally, this model focuses mainly upon the transportation network. If a major earthquake occurs in the Midwest, shipping goods across the nation will be severely affected. It may essentially split the country into two halves. Thus, because of the intimate relationship between transportation of goods and the transportation system in the Midwest, loss estimates must be made to see the effect on the nation if the critical network is damaged.

This macroeconomic model is currently in a stage of refinement. Thus, recent improvements to refine the model have been made along with sensitivity analysis to test the uncertainty of the losses. These results are the main focus of this paper. The results of this portion of the project will help to indicate which parts of the model need greater refinement and attention.

1. The Model

1.1 Input Parameters

Nodes

The model is made up of 484 nodes, which represent different locations in the nation. These nodes are found by aggregating neighboring counties together using GIS data (Figure 1). The location of these nodes is found at the centroid of these aggregated counties.

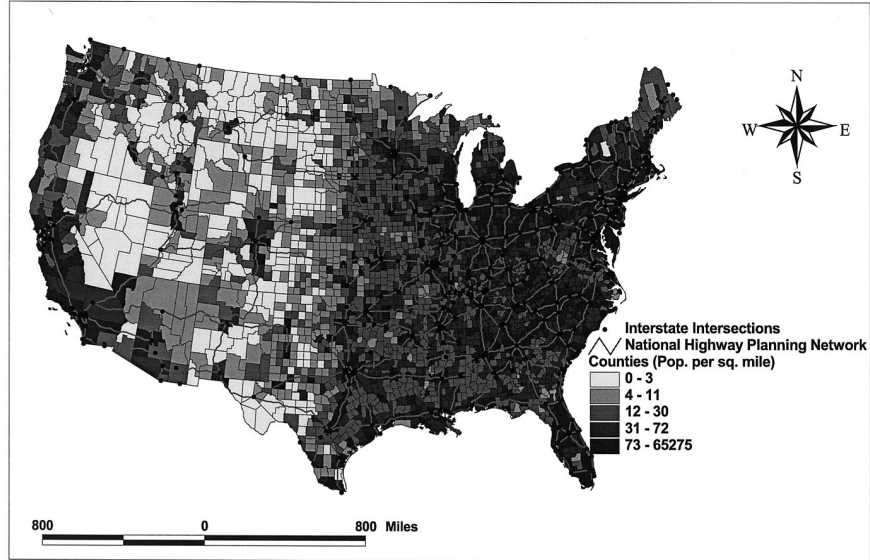


Figure 1: Population by county in the nation¹

Numerous data are available for each node. Along with population data and location, production data is present about each of the 13 commodities and 7 occupancy classes in that node. The 13 commodities are also mapped onto one of the 7 occupancy classes. Each occupancy class is further made up of a certain percentage of 8 different types of buildings. Each node has data for the number of buildings for each building type in each occupancy class. This mapping must be done in order to use existing data for both fragility modeling as well as economic loss modeling. The following table indicated the commodities, occupancy classes, and buildings.

Table 1: Various classifications in the model

Commodity (13)	Occupancy Class (7)	Building Types (6)
Agriculture	Residential	Unreinforced Masonry
Mining	Commercial	Reinforced Masonry
Construction	Heavy Industrial	Reinforced Concrete
Food	Light Industrial	Heavy Steel
Chemical	High Technology	Light Steel
Primary Metals	Food & Drug	Timber
Fabricated Metals	Chemical	
Industrial Machinery		
Electronic/Electric		
Transportation		
Non-Durable Manufacturing		
Durable Manufacturing		
Services		

¹ Veneziano, D., Sussman, J., Gupta, U., Kunnumkal, S. (2001). *Earthquake Loss Estimation Including Transportation Network Damage*.

Links

All of the nodes in the network are connected by links. The links are used to represent highways and other transportation routes. There are a total of 1440 links in the model. Data for each link includes the length, number of lanes and number of bridges. The following map indicates the locations of the nodes and links in this model.

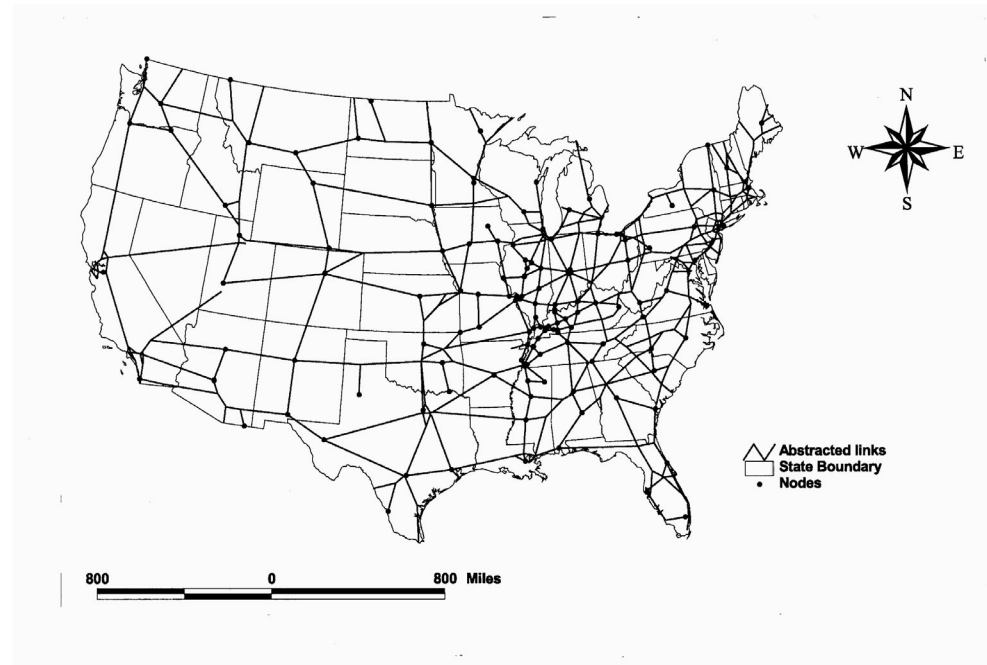


Figure 2: Abstracted node and link map²

Bridges

In the model, 28 bridge types are modeled, based upon HAZUS data. These bridges have 4 damage curves ranging from slight damage to complete damage. The bridge data also has information on the number of lanes and its location on a link.

Interaction Coefficients

There are various interaction coefficients that signal the relationship between various commodities and occupancy classes. The A-matrix indicates the relationship between each of the 13 commodities. A beta matrix indicates the relationship between the occupancy classes on with respect to the rate of recovery. The gamma matrix shows the relationship between each occupancy class with respect to functionality. These matrices are used to determine the amount of goods each commodity/occupancy class can produce based upon its relationship to each other. Appendix A will show the A-matrix.

² Veneziano, D., Sussman, J., Gupta, U., Kunnumkal, S. (2001). *Earthquake Loss Estimation Including Transportation Network Damage*.

1.2 Methodology

Scenario Earthquake

The first step to the process is to determine a scenario earthquake. The MMI intensity and location will be taken in as parameters. Although the location can be anywhere, this main focus of this project is upon earthquakes in and around the New Madrid Seismic Zone.

Attenuation Function

The model uses a bollinger attenuation function. The distance from each node to the epicenter is calculated. Then, the following formula is used to predict the intensity at that node.

$$I_d = I_{epi} + a - b * D - d * \log_{10} (D + 10) \quad (1)$$

The calculation of the intensity at any point I_d , comes from the epicentral intensity, I_{epi} , and the distance D away from the epicenter. The other variables are the bollinger coefficients ($a = 2.87$, $b = -.00052$, and $d = 1.25$).

Damage

Based upon the intensity calculated, the amount of damage to the occupancy classes can be calculated. The damage for the occupancy classes is found by using the building fragility curves since the occupancy classes are made up of a known percentage of each type of building. The building fragility curves and percentages are shown below.

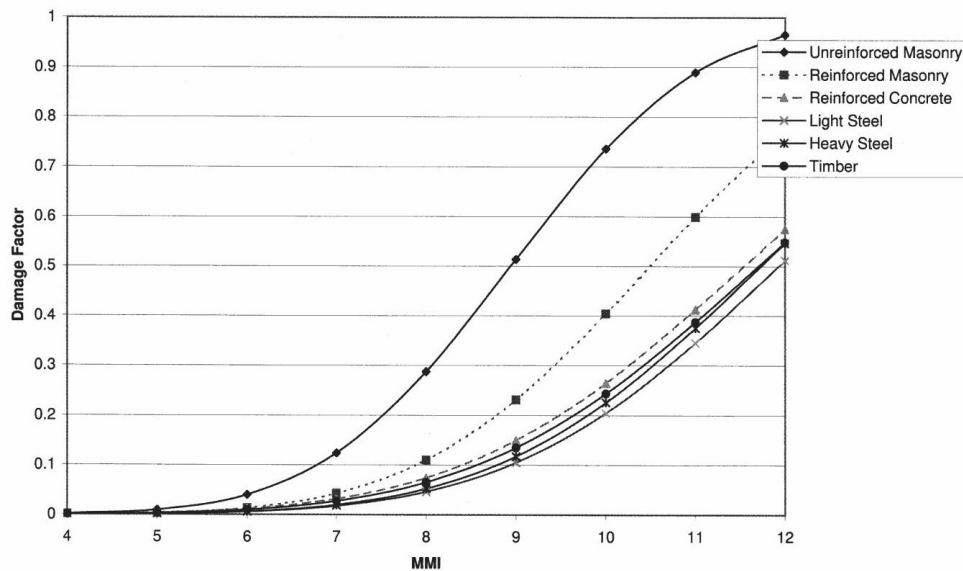


Figure 3: Building fragility curves³

³ Veneziano, D., Sussman, J., Gupta, U., Kunnumkal, S. (2001). *Earthquake Loss Estimation Including Transportation Network Damage*.

Table 2: Building percentages based upon occupancy class

Class	UM	RM	RC	HS	LS	Timber
Residential	28	8	7	0	0	58
Commercial	28	9	7	19	11	26
Chemical	27	17	16	19	11	10
High Ind	5	12	13	45	25	0
Light Ind	27	17	16	19	11	10
F&D	27	17	16	19	11	10
HiTech	28	16	16	19	11	10

The transportation related damage is also calculated for bridges and links. This is relayed in more detail later.

Functionality and Recovery

Based upon the amount of damage calculated, the initial functionality of each occupancy class and link are calculated. Then, based upon recovery curves (Figure 6), the amount of functionality can be calculated at certain times throughout the whole process until each element is at full functionality.

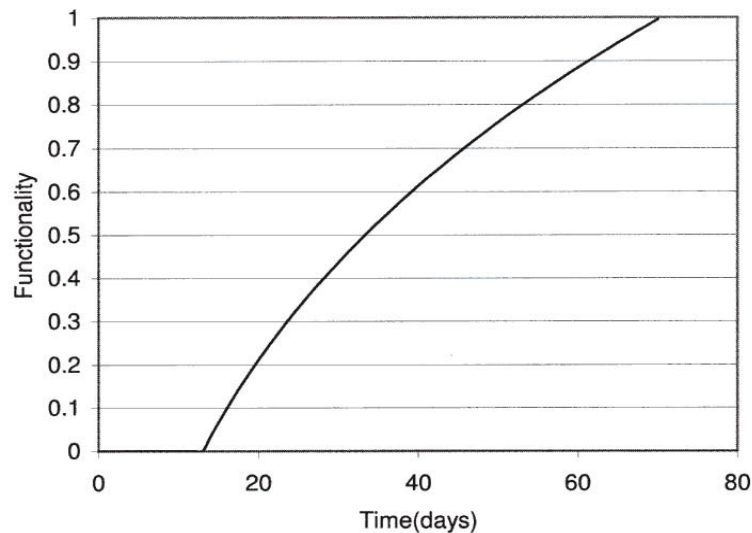


Figure 4: Sample functionality curve⁴

Network Analysis

At each time step, a local input-output model is used to balance the imports and exports of each node. The amount of goods produced at each node is based upon the functionality of each sector as well as the pre-earthquake production values. Thus, if a sector is at ten percent functionality, it only produces ten percent of its pre-earthquake production. Also, a network model is used to balance the flow of these imports and exports on the links. Interaction coefficients are used to relate the

⁴ Veneziano, D., Sussman, J., Gupta, U., Kunnumkal, S. (2001). *Earthquake Loss Estimation Including Transportation Network Damage*.

amount of goods that can be imported/exported. For example, if one commodity were completely destroyed in the earthquake, its absence would definitely cause a change in the exports and imports of other items that were dependent upon it. Thus, if a node could not import some commodities the local input-output model will try to balance what it currently has and works with the network model to balance the flow of goods in the entire nation.

Losses

The direct losses calculated for this model are based upon the amount of damage done by the earthquake and the amount of money to replace what was damaged. The indirect losses are calculated based upon the decrease in productions of the different industries. This decrease is due to the fact that the imports and exports at some nodes will decrease due to the earthquake. Thus, if a node isn't operating as well as it was before the earthquake, the loss in production is calculated as the indirect loss. Thus, at each time step, this loss is calculated. Finally, all the losses at each time step are aggregated to find the total indirect loss.

1.3 Output

Economic Loss

The model finds the direct loss at each node for each of the 7 occupancy classes. Also, it finds the direct loss due to damage in the bridges and links. The model also finds the indirect loss at each node for each of the 13 commodities as well as the loss due to a reduction in consumption.

Social Losses

The model also calculates the amount of casualties, fatalities and homelessness by node due to the earthquake. Further elaboration will be made later in the paper.

2. Recent Improvements In the Model

2.1 Quantification of Direct Losses Due to Transportation Damage

The transportation damage calculated in this model includes bridges and transportation links. The loss is calculated by multiplying the amount of damage done to the bridge by its replacement cost. There are 3 bridge replacement costs, based upon HAZUS 99 data, for the 28 types of bridges, as shown below:

Table 3: Bridge replacement costs

Bridge Type	Replacement Cost (\$1000s)
1,2	20,000
8,9,10,11,15,16,20,21,22,23,26,27	5,000
3,4,5,6,7,12,13,14,17,18,19,24,25,28	1,000

For the transportation links in the model, each link is divided up into equal intervals. The replacement cost for these links is taken as \$2,500,000 per kilometer/lane. At each point on the interval, the damage is calculated for that section. This damage is factored into the cost

to replace each section on the link. Finally, the damages from each interval are integrated together to find the total cost to replace that link.

2.2 Quantification of Various Social Losses

2.2.1 Casualties and Fatalities

The social losses calculated in this model are based upon 3 sets of data from ATC-13, HAZUS, and RMS studies. In each study, data was taken about severe casualties and fatalities. After combining all the data, the following equations and curves were obtained to represent the number of casualties based upon the damage state.

Table 4: Casualty Functions

Building Type	Function
UM, RM, RC	$Y = (6E-7) e^{(7.77x)}$ (From 0-.8) (2)
	$Y = (1E-5) e^{(14.396x)}$ (From .8-1) (3)
HS	$Y = (4E-7) e^{(8.6232x)}$ (4)
LS/ Timber	$Y = (2E-8) e^{(10.557x)}$ (5)

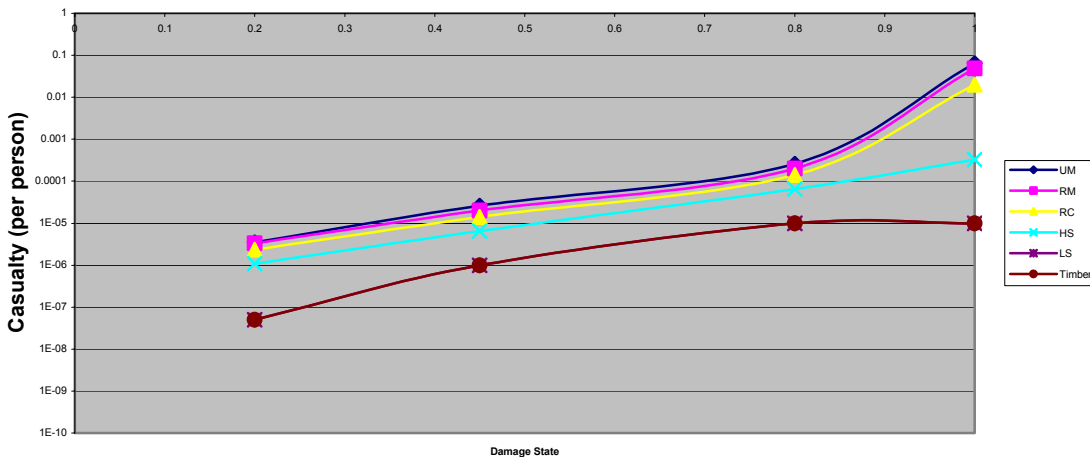


Figure 5: Graph of Casualty Functions

2.2.2 Homelessness

Another social loss that is calculated is the number of homeless people. The calculation is roughly based upon HAZUS data and is a simplified approach. The formula is:

$$\# \text{ of people homeless} = (\text{population at a node}) * (.75 * \text{damage factor}) \quad (6)$$

Using this equation, we will be able to use residential building damage data as well as population data to assess the number of people who will be homeless. This formula is directly based upon the damage factor since the more damaged a building is, the more likely it will be uninhabitable. The 0.75 value is currently used as an arbitrary value to regulate the affect the damage factor has upon the number of people homeless. In the future, this value must be calibrated to data from other studies.

2.2.3 Reduction in Final Consumptions

Another aspect of social losses includes the loss in consumption due to an earthquake. After an earthquake, many people will not be able to consume as many goods as they once did. Thus, due to the earthquake, there is a loss in consumption. The model calculates the loss in final consumption for each node. At each node, the loss in final consumption is further disaggregated into each of the 13 commodities. A sample of data from one simulation is shown.

Table 5: Loss in final consumptions

Commodity	Total Loss (millions of Dollars)
Agriculture	65.445
Mining	254.715
Construction	521.428
Food	418.232
Chemicals	461.329

2.2.4 Quantification of Contents Loss

Another aspect of economic loss is the losses due to the damage of contents inside a building. The value to the contents inside a building is calculated by multiplying the following values by the total replacement cost of the building. For example, if a residential building has a damage factor of 0.5 and a building replacement cost of R, the cost to replace the building would be 0.5R. Furthermore, the cost to replace the contents would be $0.5(0.5R) = 0.25R$.

Table 6: Coefficients for contents loss

Residential	.5
Commercial	1.25
Heavy Industrial	1.5
Light Industrial	1.5
Hi-Tech	1.5
Food & Drug	1.5
Chemical	1.5

2.2.5 Reporting Losses in Various Ways

This model can represent the losses in various ways since the output is disaggregated by node. For example, the direct losses can be calculated by node, by economic sector, and by building type. The indirect losses can be calculated by node, by commodity, and by geographic location (distance away from epicenter). The following tables show some of these reported losses.

Table 7: Direct loss by building type

Building Type	Loss (Dollars)
Unreinforced Masonry (UM)	29,511,236
Reinforced Masonry (RM)	9,062,655
Reinforced Concrete (RC)	7,786,730
High Steel (HS)	5,706,853
Light Steel (LS)	3,287,827
Timber (T)	457,725,693

Table 8: Indirect Loss by geographic location

Geographic Location (kms)	Total Loss (Millions of dollars)	Total Production	Percentage Lost (Loss/Production)
0-100	3894	8215	47
100-200	21786	163401	13
200-350	63770	241602	26
350-600	2137	280680	0.7
600-1000	64	891307	0.007
>1000	53817	8700146	0.6

3. Sensitivity Runs

3.1 Base Case

A base case will be used to compare all the results of the different sensitivity runs. This case is modeled for an intensity 11.5 earthquake near Memphis, Tennessee (Location: 320, -346). The parameters used are the parameters that have been found using data compiled from other sources. Variability of the bridge fragility is simulated. The results from this bridge simulation are the same in each sensitivity run. The data shown below contains the amount of direct loss by economic sector and transportation and the amount of indirect loss by commodity. These two key data sets will be used to compare the sensitivity runs.

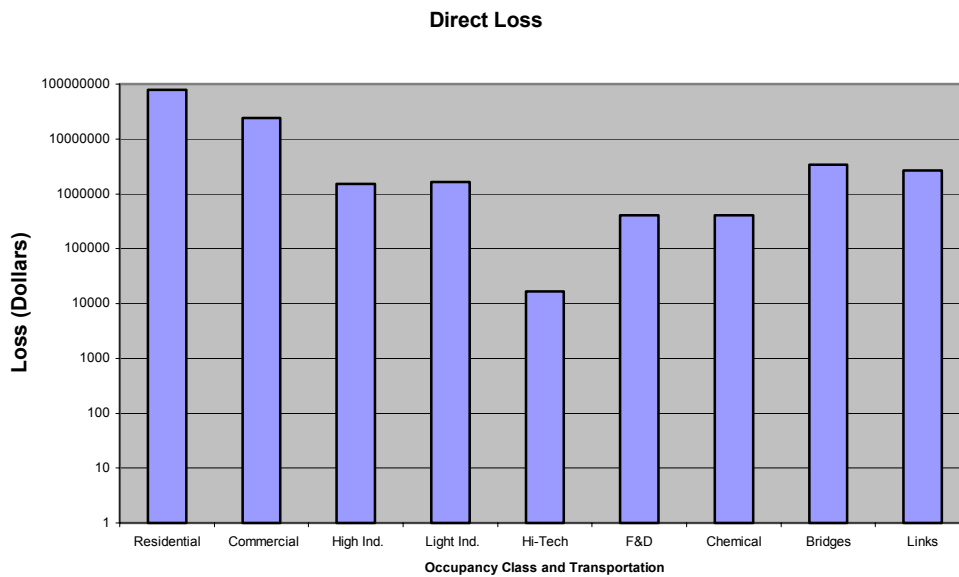


Figure 6: Direct loss from base case

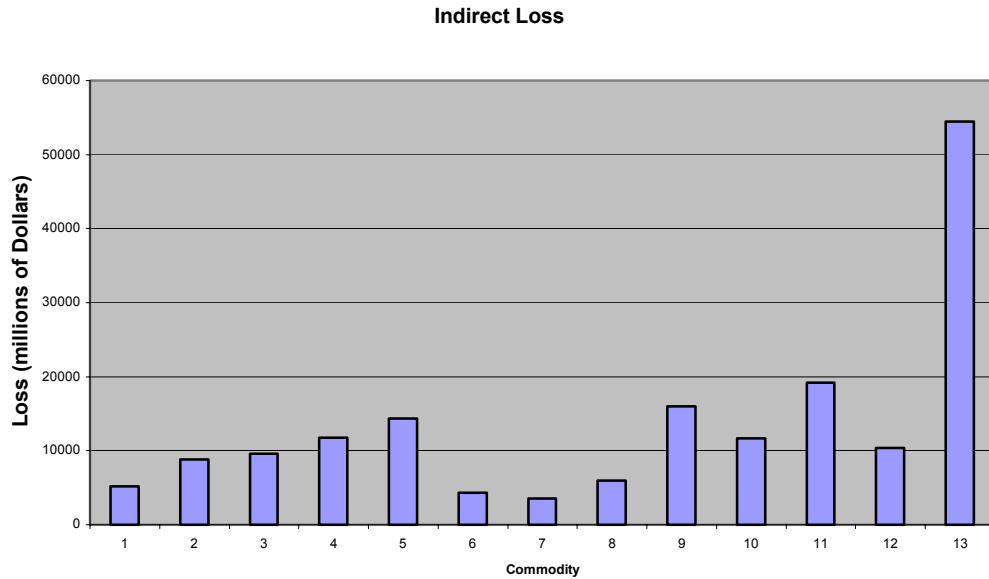


Figure 7: Indirect loss from base case

3.2 Runs on the Uncertainty of Parameters (First Objective)

3.2.1 Earthquake Location and Intensity

Sensitivity runs were made to test the uncertainty upon earthquake location and intensity. A MMI 10.5 and MMI 12 earthquake were modeled at the same point in Memphis. Also, other locations with different intensities were run. These values were chosen based upon data from other geological sources that indicated the likely places and intensities of another earthquake in the Midwest. Also, these some locations were put near major cities to cause the most damage. The following chart shows the test points and intensities run.

Table 9: Tested epicenter locations and intensities

Location	Intensity
340, -271 (New Madrid Seismic Zone)	11.5
292, -91 (Ozark Source Zone)	9.9
218, -337 (Arkansas Source Zone)	9.9
483, -257 (SE US Zone)	9.1

3.2.2 Fragility Parameters

Changes will be made to see the sensitivity to the building fragility functions in the model. A run will be made upon the mean values by changing them simultaneously by 0.75 both above and below the mean value. Also, the sensitivity on the standard deviation of the fragility function will be made by concurrently changing the base case values to 20 percent above and below the current standard deviation. All bridge and link fragilities will be tested in the same manner.

3.2.3 Recovery Parameters

The variability of the bridge recovery parameter will be changed to see its sensitivity to the model. This allows for variation among the time to full recovery of the different bridges.

The b value in the recovery function will also be changed. The function is currently in the form:

$$a * t^b + c(D), \quad (7)$$

where c(D) is another function based upon the damage incurred. This b value regulates the amount of time an element takes to recover fully. Thus, the b value for the bridges and links will be simultaneously changed to reflect 2 cases. One case will be to change this value so that the time to full recovery is halved. The other case will be to change it so the time to full recovery is doubled.

3.2.4 Economic Model

The percentage slack will be changed to find its sensitivity. The slack is given because of the assumption that, before the earthquake, all the facilities may not have been operating at its maximum. Therefore, after the earthquake, it is possible that some facilities are able to operate better than before. Currently, the slack in the model is approximately 10 percent. Thus, for these sensitivity runs, the slack will be changed to 5 percent and 20 percent.

3.2.5 Pre-earthquake capacity of links

Since the links are an abstraction of highways, some major roadways may not have been accounted for. Currently, the model estimates about 200 trucks per lane per day travel along a link. A 20 percent increase in the pre-earthquake capacity of the links will be tested. This increase is used to account for some roads that are not modeled.

3.3 Results

To compare the results of all the uncertainty runs, the total indirect loss from each run is divided by the base case run to find its uncertainty ratio. The following graph and charts sum up these results.

3.3.1 Earthquake Location and Intensity

Table 10: Uncertainty ratios on earthquake location and intensity

Sensitivity Run	Uncertainty Ratio (Run / Base case)
Intensity 10.5	0.5749
Intensity 12	1.2071
Location 340, -271 (MMI 11.5)	0.9528
Location 292, -91 (MMI 9.9)	0.4000
Location 218, -337 (MMI 9.9)	0.1355
Location 483, -257 (MMI 9,1)	0.2308

3.3.2 Fragility Parameters

Table 11: Uncertainty ratios on fragility parameters

Buildings	Sensitivity Run	Uncertainty Ratio (Run / Base case)
	Building Fragility +0.75	0.8610
	Building Fragility -0.75	1.3426
	Building Standard Deviation +20%	1.1435
	Building Standard Deviation -20%	0.9258
Bridges	Sensitivity Run	Uncertainty Ratio (Run / Base case)
	Bridge Fragility +0.75	0.9596
	Bridge Fragility -0.75	1.0495
	Bridge Standard Deviation +20%	1.001
	Bridge Standard Deviation -20%	0.9563
Links	Sensitivity Run	Uncertainty Ratio (Run / Base case)
	Link Fragility +0.75	0.9971
	Link Fragility -0.75	1.0023
	Link Standard Deviation +20%	1.006
	Link Standard Deviation -20%	0.9971

3.3.3 Recovery Parameters

Table 12: Uncertainty ratios on recovery parameters

Sensitivity Run	Uncertainty Ratio (Run / Base case)
Variability of Bridge Recovery	1.4034
Half b → bridge and link	0.7312
Double b → bridge and link	1.6041

3.3.4 Economic Model and Link Capacity

Table 13: Uncertainty ratios on recovery parameters

Sensitivity Run	Uncertainty Ratio (Run / Base case)
5% Slack	0.9963
20% Slack	1.000
20% Increase in Link Capacity	0.9963

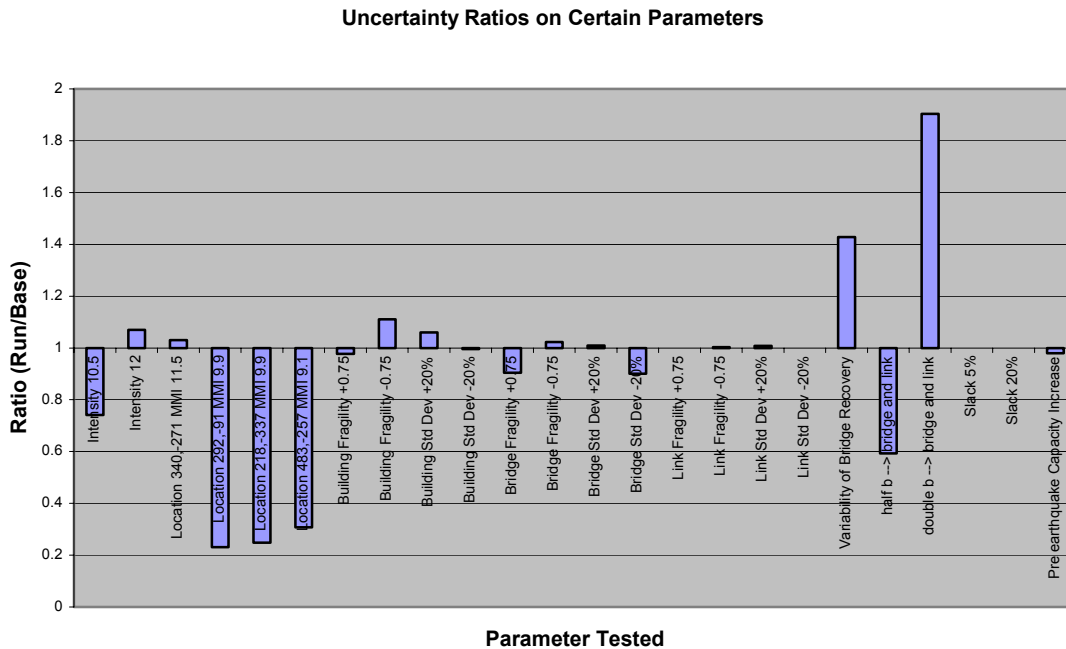


Figure 8: Graph of all uncertainty ratios

3.3.5 Analysis

From these results, three major points arise:

- The sensitivity to the b value in transportation recovery.* By doubling the time to full recovery of the bridges and links, the indirect losses increase by almost 50 percent. Of all the parameters tested, this was by far the most sensitive. This indicates that the model is highly sensitive to the recovery rates of transportation. By also testing the model when the b value cuts the time in half, the model indicates a reduction in losses of about 30 percent. This high sensitivity indicates that these values must be looked into more closely. Most likely, since the change in losses were much more significant than anticipated, both the bridge recovery times and the flow of trucks on the network is too large. These changes were made in order to accurately reflect the losses.
- The variability of bridge recovery.* The significant increase in the indirect losses when variability was included in the model indicates that variability on any element increases the uncertainty of the losses calculated. However, by including it, the model becomes more realistic because all bridges in the real world do not recover at the same rate. The recovery times for the bridges seemed too high, thus making the overall losses higher. Therefore, the recovery times were changed to reflect other studies with shorter bridge recovery times.
- The location of the epicenter and its intensity.* The changes in location and intensity of the earthquake also significantly decreased the amount of losses. Since the distance from the epicenter plays a major part in all the calculations of damage, the sensitivity on this parameter is high. The change in intensity also played a factor in

reducing these losses since all of the nodes rely upon the intensity to figure out the amount of damage sustained.

While almost all of the parameters have an effect upon the losses, the three previous ones have the greatest. This indicates that these 3 parameters make up the majority of the uncertainty in this model's loss estimation methodology.

3.4 Effectiveness of Loss Mitigation Actions (Second Objective)

3.4.1 Strengthening Buildings and Bridges (Pre-Earthquake Measures)

The fragility curve for unreinforced masonry building will be changed to match that of reinforced masonry buildings. This will simulate the effect to strengthening unreinforced buildings. Simulations on strengthening bridges will be carried out by changing its mean value by 1.5.

3.4.2 Speeding up Recovery Rates (Post-Earthquake Measures)

The rate of recovery for the different economic sectors as well as transportation and lifelines, will be changed to reflect the effect of speeding up the time to full recovery. By seeing which sector decreases the losses the most due to the quicker recovery, decisions can be made about which sector to focus attention to post earthquake.

3.4.3 Results and Analysis

The following charts indicate the results of these mitigation measures upon direct and indirect losses. The total direct loss is calculated by aggregating the direct loss from each occupancy class as well as the loss due to the transportation damage (bridges and links). Also, the total direct loss is not calculated to runs made by speeding up the recovery rate since they are the same as the base case. These results highlight 3 important ideas.

- *The importance of looking at both the indirect and direct losses.* If the model only looked at direct economic loss, conclusions may be drawn that retrofitting all unreinforced masonry to reinforced masonry may be the best choice. However, by also examining the effect of these measures upon the total indirect loss, strengthening bridges would turn out to be a much better strategy in terms of reducing economic loss, even though the decrease in direct loss was smaller when strengthening bridges. Note however that these values may be skewed because of the higher recovery time of the bridges.
- *The importance of the transportation network.* By looking at all these loss mitigation measures, strengthening the bridges seem to be the best in terms of reducing economic loss. Without the function of the bridges, especially in the Midwest, many goods cannot be transported across the country. If these goods cannot be moved, the amount of indirect loss is greatly increased. Although the significance of the bridges is important, in these runs, the amount of losses it produces seems too high. This is probably again due to the long recovery time in the bridges.

- *The importance of pre-earthquake planning.* According to this model, by retrofitting bridges before an earthquake, about 25 percent of the indirect losses can be reduced. If we had not retrofitted and only sped the recovery of the high technology sector, we would have only reduced the indirect loss by about 10 percent. Also, both the pre-earthquake mitigation strategies yielded lower indirect losses than the post mitigation strategies. So, planning ahead and preparing will reduce the costs of an earthquake more than just implementing post-earthquake measures.

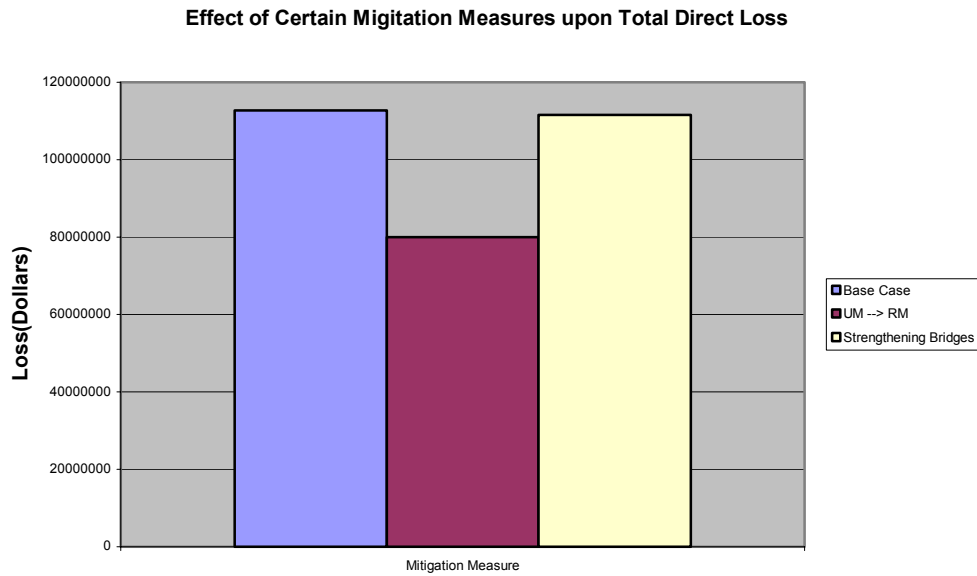


Figure 9: Total direct loss after mitigation measures

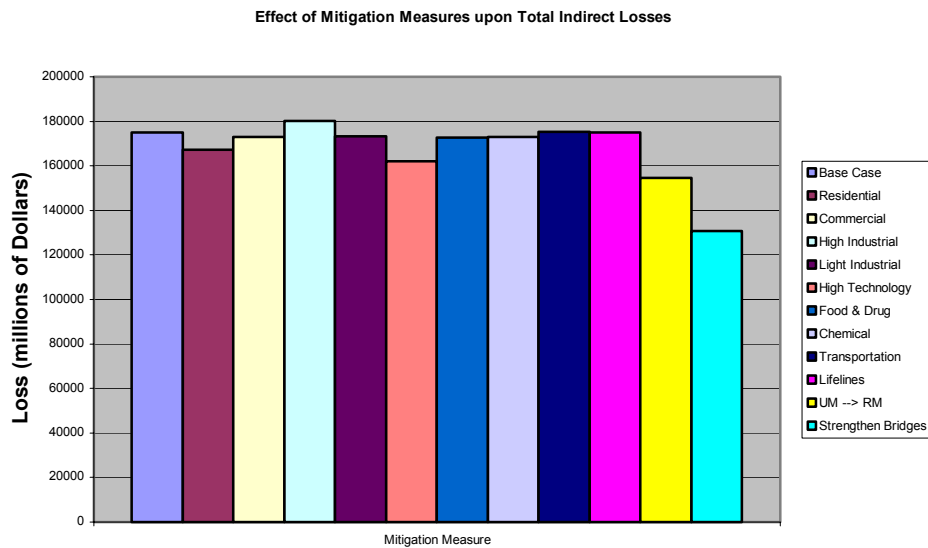


Figure 10: Total indirect loss after mitigation measures

4. Conclusions

Based upon the sensitivity analysis, more attention and focus should be placed upon the recovery model as well as the location of the epicenter and its intensity. These were the parameters that had the most sensitivity, and thus uncertainty, on the model. Refinement of the recovery model should be made to decrease the sensitivity by examining the current values used as well as the process to find the amount an element has recovered at each time step. Also, refinement of the epicenter and its intensity should be done. Possibly, using another attenuation function may help to reduce the sensitivity to intensity. Most importantly, the model supports the idea that the transportation network is an essential part of economic loss estimation. All nodes and commodities rely on the functionality of the transportation system. Thus, as the results show, by strengthening bridges, we are able to significantly reduce the indirect losses.

5. Suggestions for Further Research

In the future, more refinements must be made to the model to make it more accurate. First, geological site conditions should be incorporated into the model to allow for soil liquefaction and other geological hazards. Another item to include may be to model changes in the final demands after an earthquake. For example, more people will be requiring the use of construction and materials industry. Thus the interactions between the commodities will change. Also, a more specified way to estimate the number of homeless people should be developed. The current estimation may be too general and uncertain. Sensitivity runs should be made on these parameters too. Most importantly, the bridge recovery times and flows should be examined more closely in order to match data from other studies such as HAZUS. By changing these parameters, the losses should be closer to the known HAZUS data.

6. Acknowledgements

This project is funded by the National Science Foundation and made possible through the Mid-America Earthquake Center's Research Experience of Undergraduates. The author would like to thank the MAE Center, especially Sandra Menke, for its support throughout the research period and the Massachusetts Institute of Technology for their assistance in transitioning the author to Boston.

The author especially thanks Professor Daniele Veneziano, Professor Joseph Sussman, Umang Gupta and Sumit Kunnunkal for all their patience and guidance throughout these ten weeks.

7. Works Cited

Applied Technology Council (1985). *Earthquake Damage Evaluation Data for California*. ATC-13. Redwood City, CA: Applied Technology Council.

Coburn, A. W., Spence, R.J.S., Pomonis A. (1992). Factors Determining human casualty levels in earthquakes: Mortality prediction in building collapse. *Earthquake Engineering, Tenth World Conference*, Balkema, Rotterdam.

Kunnumkal, S. M. (2001, June-August). Recovery Model. Personal Communication.

Kunnumkal, S. M. (2001, September). Changes in Model Parameters, Data. Personal Communication.

National Institute of Building Sciences (2000a) *Hazus Technical Manuals*. National Institute of Building Sciences.

Veneziano, D., Sussman, J., Gupta, U., Kunnumkal S. (2001). *Earthquake Loss Estimation Including Transportation Network Damage*. Technical Report, Massachusetts Institute of Technology, Cambridge, Massachusetts.

8. Appendix

8.1 A Matrix

A _{ij}	1	2	3	4	5	6	7	8	9	10	11	12	13
1	0.232	0.000	0.006	0.264	0.003	0.000	0.000	0.000	0.001	0.000	0.010	0.019	0.002
2	0.002	0.166	0.009	0.001	0.028	0.044	0.000	0.000	0.001	0.001	0.102	0.009	0.009
3	0.012	0.017	0.001	0.004	0.008	0.007	0.006	0.006	0.008	0.005	0.007	0.005	0.020
4	0.067	0.000	0.000	0.146	0.006	0.001	0.001	0.001	0.001	0.001	0.003	0.001	0.011
5	0.048	0.013	0.014	0.010	0.224	0.020	0.020	0.005	0.015	0.014	0.068	0.019	0.004
6	0.000	0.011	0.016	0.000	0.002	0.264	0.246	0.087	0.051	0.050	0.002	0.022	0.000
7	0.002	0.006	0.066	0.028	0.009	0.021	0.073	0.042	0.036	0.068	0.003	0.024	0.002
8	0.006	0.022	0.023	0.002	0.005	0.030	0.020	0.132	0.024	0.046	0.005	0.013	0.004
9	0.004	0.002	0.030	0.001	0.001	0.007	0.004	0.081	0.163	0.041	0.001	0.038	0.004
10	0.001	0.001	0.002	0.001	0.000	0.006	0.001	0.003	0.001	0.204	0.001	0.006	0.004
11	0.032	0.017	0.039	0.069	0.072	0.022	0.030	0.031	0.048	0.061	0.212	0.059	0.027
12	0.004	0.004	0.109	0.011	0.006	0.017	0.007	0.009	0.022	0.036	0.015	0.122	0.005
13	0.189	0.237	0.225	0.155	0.209	0.244	0.164	0.157	0.154	0.173	0.183	0.170	0.226

8.2 Part of code (written by author)

```

void getrealdamage()
{
    float pcost, mydistance;
    float xinc, yinc;
    int myincrement = 10;

    totalcost = 0.0;

    xinc = (n[startnode].coord[0]-n[endnode].coord[0])/myincrement;
    yinc = (n[startnode].coord[1]-n[endnode].coord[1])/myincrement;

    for( int i = 0; i < myincrement; ++i)
    {
        xcoord = n[startnode].coord[0] + xinc*(2*i+1)/2;//mid point //
        of segment
        ycoord = n[startnode].coord[1] + yinc*(2*i+1)/2;//mid point //
        of segment
    }
}

```

```

mydistance=sqrt(pow(xcoord-epx,2)+pow(ycoord-epy,2))/0.62;
//intensity=epmmi+bollinger_a - (bollinger_b*distance) -
//bollinger_d*log(distance+10);

if(mydistance==0)
    intensity=epmmi;
else
{
    if(bollinger_a - (bollinger_b)*mydistance -
bollinger_d*log(mydistance)> 0)
        intensity=epmmi;
    else
        intensity=epmmi+bollinger_a -
        (bollinger_b*mydistance) - bollinger_d*log(mydistance);
}

// calculating the damage

pcost = (damage*lanes*(length/myincrement)/0.62)*replcost;
totalcost += pcost;
}
}

```


ED-13: Virtual Reality Retrofit Demonstrations

Cathleen Kennedy, GRA
Stephanie Arbogast, URA
Brad Cross, PI
Scott Smith, Co-PI
Southern Illinois University Edwardsville

Mid-America Earthquake Center
Headquartered at the University of Illinois Urbana-Champaign

August 2001

Abstract

The purpose of the ED-13 project, Virtual Reality Retrofit Demonstrations, is to provide an interactive, web-based application that simulates various levels of earthquakes for several building types. Users will have the option to interactively retrofit the buildings and compare the damage of an un-retrofitted building to that of a retrofitted one. The target audience of this application ranges from the general public to contractors, building owners, and public officials. For advanced users, links to detailed retrofitting techniques are provided.

Table of Contents

1. ED-13: Virtual Reality Retrofit Demonstrations

- 1.1 Introduction
- 1.2 Background
- 1.3 The Application Environment

2. Review of Past Earthquake Damage

- 2.1 Building Discussion
- 2.2 Northridge Earthquake
- 2.3 Types of Damage in Un-retrofitted URM Structures
 - 2.3.1 Cracking
 - 2.3.2 Partial Wall Collapse
 - 2.3.3 Parapet Damage
 - 2.3.4 Wall, Floor or Roof Separation
- 2.4 Retrofitted URM Building Damage
 - 2.4.1 Incomplete, Improper, or Partial Retrofit
 - 2.4.2 Weak Mortar
 - 2.4.3 Veneer Failures
- 2.5 Non-Structural Damage

3. Retrofit Techniques

- 3.1 Virtual Reality Retrofit Demonstrations
- 3.2 Wall Retrofits
- 3.3 Parapet Retrofits
- 3.4 Floor to Wall Connection
- 3.5 Non-Structural Retrofits

4. Conclusion

5. Acknowledgements

6. References

7. Figure References

Table of Figures

- 1-1. User Interface (Virtual Building)
- 2-1. Corner Cracking
- 2-2. Window Cracking
- 2-3. Cracks in Wall
- 2-4. Severe Cracking Seen from Inside Building (Virtual Building)
- 2-5. X-Shaped Cracking Along Exterior Wall (Virtual Building)
- 2-6. Partial Wall Collapse
- 2-7. Partial Wall Collapse (Virtual Building)
- 2-8. Collapsed Wall
- 2-9. Collapsed Wall (Virtual Building)
- 2-10. Damaged Parapet
- 2-11. Damaged Parapet (Virtual Building)
- 2-12. Fallen Book Case (Virtual Building)
- 3-1. Retrofit Choices (Virtual Building)
- 3-2. Braced Parapet (Virtual Building)
- 3-3. Detailed Parapet Brace (Virtual Building)
- 3-4. Cross Bracing
- 3-5. Cross Bracing (Virtual Building)
- 3-6. Concrete Wall Retrofit (Virtual Building)
- 3-7. Tension Tie for Wall to Floor Retrofit (Virtual Building)
- 3-8. Detailed Tension Tie Retrofit (Virtual Building)
- 3-9. Bookshelf Retrofit Technique (Virtual Building)
- 3-10. Detailed Bookshelf Retrofit Technique (Virtual Building)

1 ED-13: Virtual Reality Retrofit Demonstrations

1.1 Introduction

Earthquakes of different magnitudes cause various levels of destruction, and retrofitting buildings can help prevent potential damage due to earthquakes. A visual demonstration of the damaging effects of earthquakes and a comparison between retrofitted and non-retrofitted buildings would graphically demonstrate earthquake effects and retrofit benefits. The Mid-America Earthquake Center project, ED-13, offers a visual, web-based, interactive tool that demonstrates damage to un-retrofitted and retrofitted masonry, wood, steel and concrete buildings for various levels of MMI and relative Richter Scale values. This tool can be used as an educational tool for both students of all ages and community members, as well as by those with more advanced knowledge of earthquake damage and the effects of retrofitting.

1.2 Background

The ED-13 project is implemented using Virtual Reality Modeling Language (VRML) and Java as a web-based application, “VRML is a 3D analog to HTML. This means that VRML serves as a simple, multi-platform language for publishing 3D Web pages. VRML provides the technology that integrates three dimensions, two dimensions, text, and multimedia into a coherent model. When these media types are combined with scripting languages (such as Java) and Internet capabilities, an entirely new genre of interactive applications is possible,” (Web 3D Consortium, 2000). The 3D technology allows for users to move in and about the various buildings and view the damage and retrofits from all angles.

The only requirements for viewing and interacting with this project are having an Internet connection, having a web-browser and having a VRML plug-in installed on the browser. As of yet, no other interactive, 3D visual tool has been established for the purposes of demonstrating earthquake damage and retrofitting.

In addition, by using 3D technology, the School of Engineering at Southern Illinois University Edwardsville will be able to demonstrate this project on a WorkWall. This large-scale visualization environment will allow users to visually experience near life-sized earthquakes and interactively retrofit different portions of the building.

1.3 The Application Environment

Figure 1-1 seen below is the general layout of the application. The user will have the option of taking an audio-guided tour throughout the building or stepping through a self-guided tour. Users will choose the level of earthquake to occur and will have to option to retrofit various items before the next earthquake. Users will also be responsible for fixing all damage to the building after an earthquake occurs.

A text box explains the damage seen for the chosen level of earthquake as well as reminders to retrofit certain items that did not withstand the last earthquake.

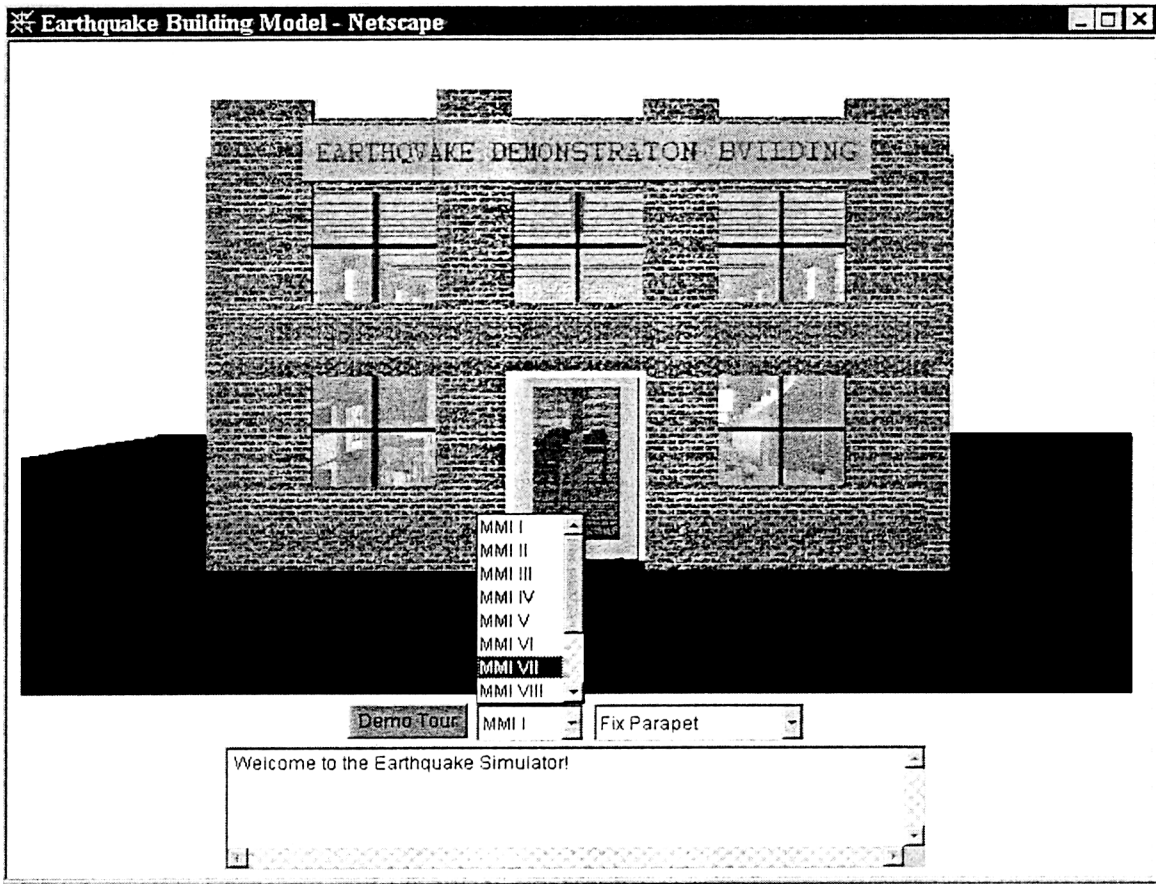


Figure 1-1. User Interface

2 Review of Past Earthquake Damage

2.1 Building Discussion

The building types that will be displayed as Virtual Reality Modeling Language (VRML) retrofit demonstration structures will consist of unreinforced masonry (URM), concrete, timber, and steel. As an example, the following discussion of damage and retrofit techniques will focus only on the unreinforced masonry building. Damage that will be included in this discussion consists of damage suffered by buildings that were fully, partially, or without applied retrofit techniques. Some retrofit methods will be discussed to provide the user of the VRML demonstration with adequate knowledge of what may happen in the event of an earthquake and what can be used to prevent what may be serious damage to structures or life. Images of actual earthquake damage will be shown along with a screen shot image of the VRML model to demonstrate how the damage is shown in virtual reality.

2.2 Northridge Earthquake

On January 17, 1994, a Richter magnitude 6.8 earthquake struck Northridge, California, just outside the Los Angeles area. Due to the Los Angeles Building Code Division 88 retrofit ordinance, put into effect in 1981, many buildings had been retrofitted prior to this earthquake with the intent to prevent injury or loss of life. It should be noted that no deaths were reported from falling or damaged URM buildings, but the time of the earthquake at 4:30 am may have contributed a large portion of why so few people were harmed (Bruneau 1995).

Since many buildings had been retrofitted, this earthquake study provides significant information on the effects of earthquakes on retrofitted structures, and is therefore useful to provide information as to future techniques. It also greatly aids in demonstrating the need for applying these techniques. It is even more important to the study of URM buildings because of their vulnerability to seismic loading. Within the Los Angeles area, an area with approximately 6000 retrofitted URM buildings with many more left unretrofitted, there were many examples of damage that occurred to all types of URM buildings. These include retrofitted URM buildings under the ordinance, and unretrofitted buildings outside the ordinance that were found to be very useful to the study for URM structures (Bruneau 1995).

2.3 Types of Damage in Un-retrofitted URM Structures

2.3.1 Cracking

A very common type of seismic damage that can be seen in most URM buildings is cracking. This cracking can result from weak mortar and mortar joints used to bond masonry units (Mehta & Saadeghvaziri, 1998). Cracking is commonly found in corners of buildings and openings such as windows seen in Figures 2-1 and 2-2. The walls located between two openings used for support, referred to as piers, often experience shear cracking possibly due to lack of stiffness causing the mortar strength to be less, allowing more movement, thus creating X-shaped cracks.

While piers most often experience this type of cracking, it is also common to see this in non-pier walls as well, along with general cracking, not necessarily the X-shaped cracking seen in Figure 2-3. The corner cracking is even more commonly found in buildings with irregular shaped floor plans, such as L-, U-, or H- shapes. These buildings tend to experience more damage than rectangular buildings. Since the floor is being pushed between the walls, the corners tend to be pushed outward, which is why these corner cracks are found, and found more commonly in irregular planned buildings (Moehle, 1996; Applied Technology Council 20 [ATC 20], 1989). Figures 2-4 and 2-5 display the cracking shown in the VRML model.

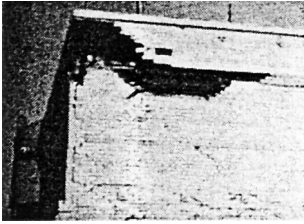


Figure 2-1. Corner Cracking (Moehle, 1996)

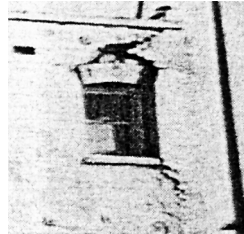


Figure 2-2. Window Cracking (Moehle, 1996)

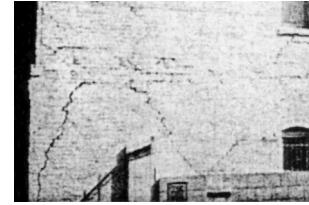


Figure 2-3. Cracks in Wall (Moehle, 1996)

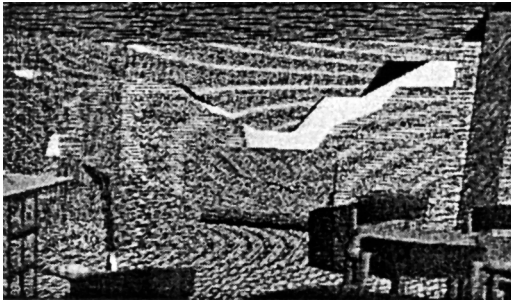


Figure 2-4. Severe Cracking Seen from Inside Building

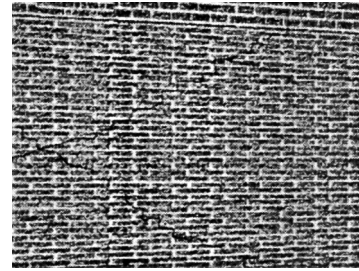


Figure 2-5. X-Shaped Cracking Along Exterior Wall

2.3.2 Partial Wall Collapse

Another type of common damage that may occur is partial wall collapse seen in reality in Figure 2-6. The VRML modeled wall failure can be seen in Figure 2-7. Partial wall collapse is an out-of-plane failure that results when a wall has a height to wall thickness ratio (h/t) that is too large, meaning that the wall is too tall for the given thickness. This may also occur when a wall lacks proper anchorage. Often times, this partial wall collapse consists of the outermost portion of the wall called the veneer, falling away from the rest of the wall due to lack of anchorage or bonding (Moehle, 1996). In some cases however, a wall not properly supported will fully collapse as seen in Figures 2-8 and 2-9.

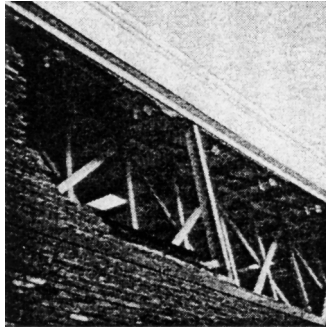


Figure 2-6. Partial Wall Collapse
(Moehle, 1996)

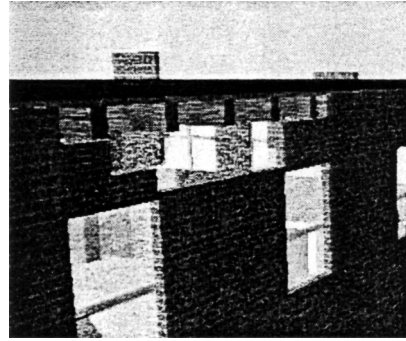


Figure 2-7. Partial Wall Collapse

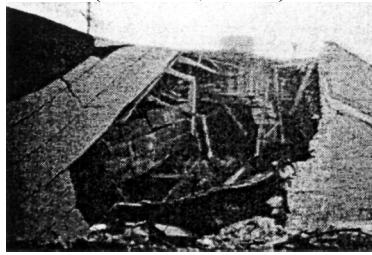


Figure 2-8. Collapsed Wall
(Moehle, 1996)

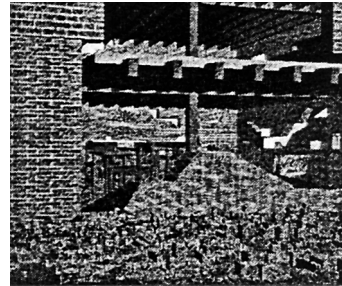


Figure 2-9. Collapsed Wall

2.3.3 Parapet Damage

Parapets are the portions of the wall extending just above the roof of a building. This type of damage, which is non-structural, results when parapets are improperly or not at all anchored causing them to fall. Since the parapet has nothing to affix to during the earthquake, it slides off the building, which is ultimately a safety hazard. An image of a damaged parapet can be seen in Figure 2-10 along with a VRML model of a damaged parapet in Figure 2-11.

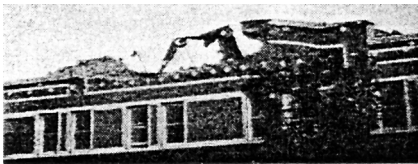


Figure 2-10. Damaged Parapet
(Moehle, 1996)

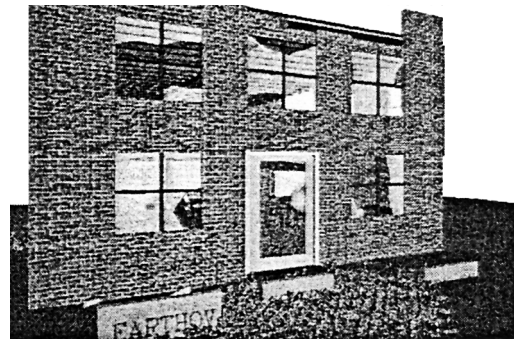


Figure 2-11. Damaged Parapet

2.3.4 Wall, Floor, or Roof Separation

Some structural damage that may occur is separation of the floor and wall, or separation of the roof from the wall or vertical support. Most old un-retrofitted URM buildings have floors that are not anchored to the wall. The floor joists set upon the masonry wall for support. In these cases, during an earthquake, the floor joists slide off the wall that supports them, ultimately causing the floor to separate from the wall entirely. The roof behaves in a similar manner (ATC 20, 1989). The floor and wall separation can be seen in Figure 2-9.

2.4 Retrofitted URM Building Damage

2.4.1 Incomplete, Improper, or Partial Retrofit

Incomplete retrofits contribute to much of the damage of retrofitted URM buildings. Anchorage that is not sufficient or bracing that is too far apart can cause parapet damage similar to that of an un-retrofitted parapet (Moehle, 1996). Improperly placed retrofit techniques that are intended to provide extra strength may fail to do so if they are not carefully detailed and placed, causing the building to act as if it has not been retrofitted at all. One reported partial retrofit case following the Northridge Earthquake was a store with excessive h/t ratios that was missing an additional bracing required for the retrofit. In this case, the wall that had not been braced collapsed while the others remained intact (Bruneau, 1995). Other examples of partial retrofits consisted of buildings with unanchored walls, unanchored veneer, and some buildings with anchored floors and walls while the roofs and walls remained unanchored. It was often found that construction of the retrofit techniques was not carefully executed causing the retrofit to act improperly (Moehle, 1996). An erroneous failure that was often found was the consideration of the veneer as part of the wall, which reduced the h/t ratio, ultimately reducing the amount of retrofit required (Bruneau, 1995; Moehle, 1996).

2.4.2 Weak Mortar

It is worth noting that many buildings after the Northridge Earthquake were found to have poor mortar strength prior to the earthquake. Like many buildings in the Northridge area, the United States has many old URM structures that may fall into the category of having poor, weak, or deteriorated mortar. This caused shear cracking and some out-of-plane failure. The out-of-plane failure likely occurred because wall anchors failed to have a good surface to lock onto (Moehle, 1996).

2.4.3 Veneer Failures

Many of the buildings inspected following the Northridge Earthquake had damaged veneer. The likely cause of this may be that the veneer course was unidentified in the retrofit process and was therefore not included. Other likely causes could have been from improperly unanchored veneer courses or poor mortar. It was often found that original veneer anchors were deteriorated (Moehle, 1996).

2.5 Non-Structural Damage

Other types of damage may occur in earthquakes that are not structural but are very important to consider because they may also cause serious harm. As mentioned earlier, parapets, which serve as ornamentation, are very important to secure. Other types of ornamentation consists of window and door fixtures, cornices crowning the uppermost portion of the wall, and decorative friezes adorning the wall just below the cornice that are often not securely attached to the wall. Other things to be careful to consider are canopies, awnings, signs, veneer, cladding, or roof shingles. These are all typical things found on buildings that are very important to secure as they may fall and cause serious injury or death. Some interior items to identify are bookshelves seen in figure 2-12, large and heavy objects, light fixtures, wall fixtures, ceiling tiles, partitions, glass, and any overhead objects that may swing or fall (ATC 20, 1989).

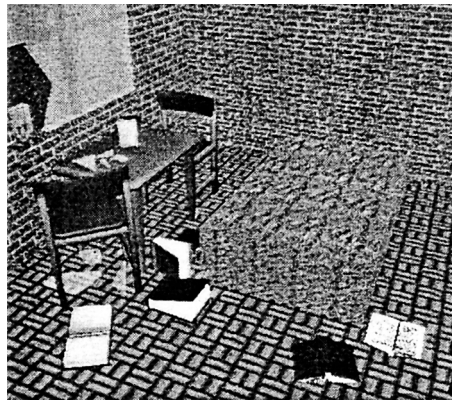


Figure 2-12. Fallen Book Case

3 Retrofit Techniques

3.1 Virtual Reality Retrofit Demonstrations

Techniques to retrofit buildings and nonstructural items are shown in the VRML model. In some cases, there may be more than one method to retrofit a particular item. In this case, the user will be allowed to choose either technique, shown below in Figure 3-1. The model has also been set up so that for particular retrofits, the user may click on the retrofit and a more detailed version will be brought up in another screen. The retrofit for a parapet, shown in Figure 3-2, is one of the retrofits in which a more detailed image can be viewed, seen in Figure 3.3.

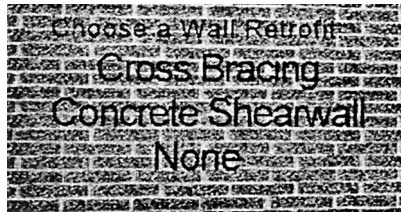


Figure 3-1 Retrofit Choices

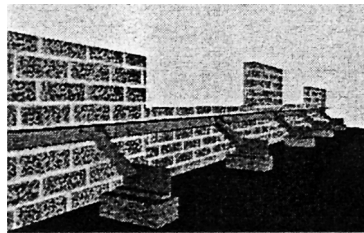


Figure 3-2 Braced Parapet



Figure 3-3 Detailed Parapet Brace

3.2 Wall Retrofits

One method that may be used to brace the URM walls is by using steel to diagonally brace the wall. This method was chosen because it is a common type of retrofit. Studies show that this diagonal bracing method improves the strength of the wall significantly (Mehta & Saadeghvaziri, 1998). Images of actual cross bracing and the VRML modeled cross bracing can be seen in Figures 3-4 and 3-5. The other option for wall bracing is another conventional method in which concrete is placed over the wall. This method requires that steel mesh be placed along the wall with a coating of shotcrete, a more liquefied form of concrete, placed over the mesh. This method has also shown an increase in wall strength (Ehsani et al., 1999). Images of modeled concrete placement can be seen in Figure 3-6.

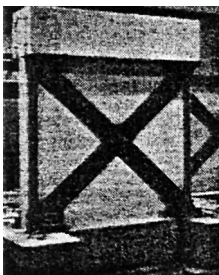


Figure 3-4 Cross Bracing (Taghdi, et al., 2000)



Figure 3-5 VRML Cross Bracing

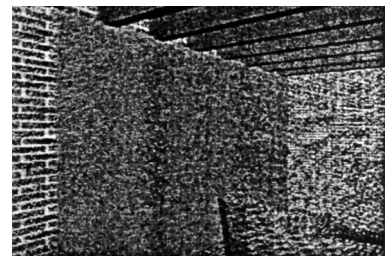


Figure 3-6 VRML Concrete Wall Retrofit

3.3 Parapet Retrofits

As seen in Figures 3-2 and 3-3, a general parapet bracing system has been chosen. This brace is a type of retrofit that requires some engineering (Eduardo et al., 1994). Appropriate distances and minimum heights from the top of the parapet and bracing system are necessary in order for the bracing to appropriately work.

3.4 Floor to Wall Connection

In order to anchor the floor and walls, metal strips are bolted to the joists and anchored to the wall seen in Figure 3-7. These metal strips, called tension ties, are what keep the floor from sliding off the portion of the wall on which they sit. The tension ties are placed on both the joists parallel and perpendicular to the walls (Mercer, 1997).

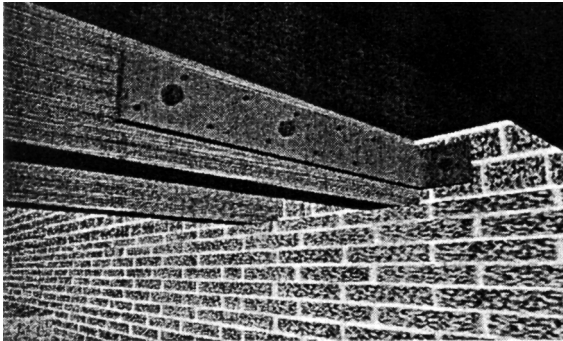


Figure 3-7 Tension Tie for Wall to Floor Retrofit

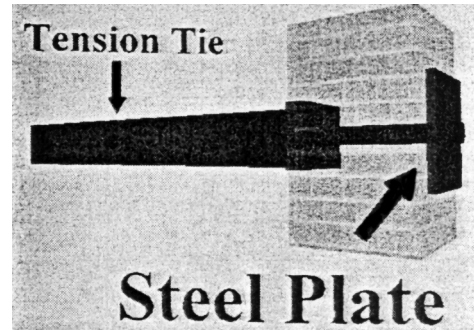


Figure 3-8 Detailed Tension Tie Retrofit

3.5 Non-Structural Retrofits

One specific non-structural retrofit that was included in the VRML model was the retrofit technique used for bookshelves. For this, small steel angles were screwed to the bookshelf and bolted to the wall seen in Figure 3-8, while the more detailed image of this retrofit can be seen in Figure 3-9. This prevents the bookshelf from tipping and falling.

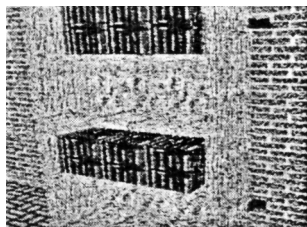


Figure 3-9 Bookshelf Retrofit Technique

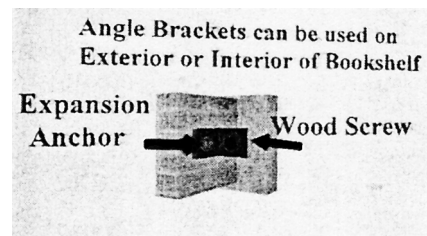


Figure 3-10 Detailed Bookshelf Retrofit Technique

4 Conclusions

The purpose of demonstrating the retrofitting techniques for unreinforced masonry, concrete, timber, and steel buildings is to heighten the awareness of possible injury and damage incurred by earthquakes. The ED-13 project has offered an interactive web based application to allow users to visually experience and compare damage of un-retrofitted and retrofitted structures. A user of the virtual building will have the ability to view the damage at different levels and see the retrofit techniques as they are applied. Advanced users can view these techniques on a more detailed level. This project, Virtual Reality Retrofit Demonstrations, will help people to better understand not only earthquakes but also the importance of retrofitting.

5 Acknowledgements

We would like to thank the National Science Foundation and the Mid-America Earthquake Center for their financial support on this project.

6 References

- Applied Technology Council. (1989). *Procedures for Postearthquake Safety Evaluation of Buildings* (20). San Francisco, CA: R.P. Gallagher Associates, Inc.
- Bruneau, M. (1995). Performance of masonry structures during the 1994 Northridge (Los Angeles) earthquake. *Canadian Journal of Civil Engineering*, 22, 378-402.
- Eduardo, A.F., et al., (1994). Reducing the Risks of Nonstructural Earthquake Damage, (FEMA 74/September 1994).
- Ehsani, M.R., et al., (1999). Behavior of retrofitted URM walls under simulated earthquake loading. *Journal of Composites for Construction*, 3, (3), 134-142.
- Klinger, R.E. (1995). Performance of masonry structures in the Northridge, California earthquake of January 17, 1994. Restructuring – America and Beyond: Proceedings of Structures Congress XIII (Vol. 2, pp. 1415-1418). New York: ASCE.
- Mercer, J.C. (1998). Simple low cost retrofit procedures for historic unreinforced masonry buildings. Proceedings of the 1998 ASCE Structures Congress. San Francisco, CA.
- Mehta, S., Saadeghvaziri, M.A. (1998). Analysis of unreinforced masonry (URM) walls and evaluation of retrofitting schemes for URM structures. Structural Engineering and Mechanics, 6, (7), 801-815.
- Moehle, J.P. (Ed.). (1996). Earthquake Spectra. (Suppl. C to Vol. 2, pp. 195-218). Oakland, CA: EERI.
- Taghdi, M., et al., (2000). Seismic retrofit of low-rise masonry and concrete walls using steel strips. *Journal of Structural Engineering*, 126, (9), 1017-1025,

7 Figure References

Figure 1-1: Screen Shot of VRML Model.

Figure 2-1, 2, 3: Moehle (1996). Earthquake Spectra, (Suppl. C to Vol. 11), p. 201 Fig. 8-6.

Figure 2-4, 5, 7, 9, 11, and 12: Screen Shots of VRML Model.

Figure 2-6: Moehle (1996). Earthquake Spectra, (Suppl. C to Vol. 11), p. 202 Fig. 8-7.

Figure 2-8: Moehle (1996). Earthquake Spectra, (Suppl. C to Vol. 11), p. 211 Fig. 8-18.

Figure 2-10: Moehle (1996). Earthquake Spectra, (Suppl. C to Vol. 11), p. 203 Fig. 8-9.

Figure 3-1, 2, 3, 5, 6, 7, 8, 9, and 10: Screen Shots of VRML Model.

Figure 3-4: Taghdi, M., et al., (2000). Journal of Structural Engineering, 126, (9), p. 1018, Fig. 2.

SG-12: Calibrating Intensity with Ground Motions

Ryan McDaniel

Conducted at
Center for Earthquake Research and Information
University of Memphis
Advisor: Dr. Steve Horton

ABSTRACT

This project, SG-12: Calibrating Intensity With Ground Motions, is attempting to take observations from the 1811-1812 New Madrid earthquakes and test those phenomena to obtain ground motion levels associated with their production. Values for minimum and in some cases maximum ground motion have been established for the production of phenomena associated with the items tested in this project. Phenomena tested so far are spilling and swaying of liquid in liquid filled open vessels (MMI I, II, and IV), stopping of a pendulum clock (MMI V), and ringing of a small bell (MMI VI). This paper shows how the minimum ground motion needed to induce the ringing of a bell and the stopping of a pendulum clock are very similar, even though they are ranked in different MMI levels. This shows the possible need for recalibrating the MMI scale, which this project will do as well as assign ground motion levels to each MMI level. Ground motions needed to stop a pendulum clock have an upper and lower limit for a certain range of frequencies and are very frequency dependent. From these results and future results of SG-12, it is certain that attenuation relationships for the eastern United States can be developed as well as the assigning of precise magnitudes to pre-seismograph earthquakes all over the world using SG-12 techniques. This information will be instrumental in determining seismic hazard maps which will improve earthquake knowledge and safety for the eastern United States.

I. INTRODUCTION

The 1811-1812 New Madrid Earthquakes caused large ground motions over a large area of the eastern United States. Effects of the three main shocks were observed from Louisiana to Canada and all the way to the eastern seaboard, as can be seen in Figure I-B. Scientists as well as regular citizens recorded many of the effects. There are many examples of these recorded observations including fallen or damaged chimneys, pendulum clocks stopping, various bells ringing, vibration of suspended objects, fallen objects, and many more. There are currently only estimates of the size of the New Madrid Quakes since they occurred before the seismograph was in existence and therefore the precise magnitudes of these earthquakes are not known. However, because these observations were recorded at various epicentral distances, the Modified Mercalli Intensity Scale can be applied.

Most seismologists do not use the Modified Mercalli Intensity Scale because it does not precisely provide important information such as ground velocities and accelerations. It truly only attempts to classify an earthquake according to the affect it has on the surrounding land, structures, and people. With the New Madrid Seismic zone still being very active, there is a very real threat of a large magnitude earthquake occurring in the near future.

Unfortunately because the last large earthquakes in the New Madrid Seismic zone did occur before the existence of the seismograph and the Modified Mercalli Intensity Scale cannot deliver precise values for ground motions, there is not enough knowledge about the 1811-1812 New Madrid quakes to help make accurate judgments on the future activity of the New Madrid Seismic zone. If another event like the 1811-1812 quakes were to occur now or in the near future, the results would be catastrophic. As can be seen from Figure I-A, at least seventeen states would be affected and more would definitely feel the impact since many of the United

States' major transportation networks such as Interstates and Railroads take a direct path through the New Madrid Seismic zone and in all likelihood would be damaged and possibly even rendered inoperable. The need to understand past, present and possible future earthquakes in the mid-eastern United States is of utmost importance to economic, social, and structural interests.

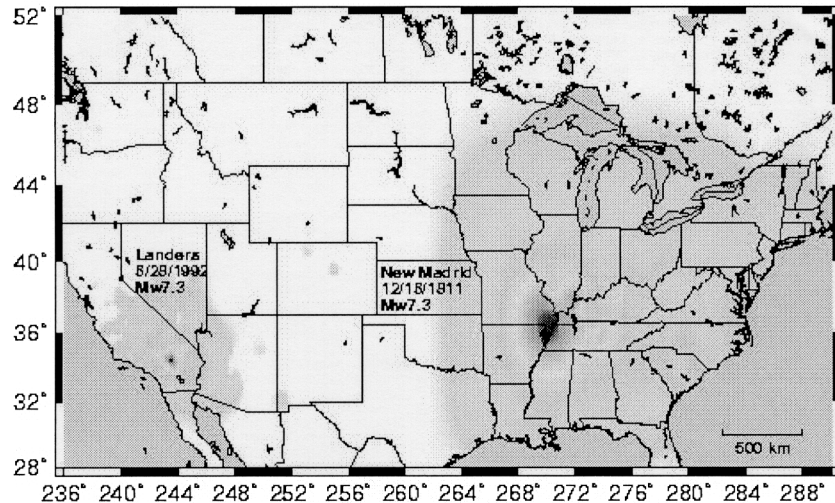


Figure I-A. This map compares the area affected by the December 16, 1811 quake and the Landers earthquake occurring in 1992. Both are known or currently estimated to be about a magnitude 7.3. This shows how a large magnitude earthquake in the eastern United States will impact the country when it occurs. The boundary of the shaded areas shows the limits of the areas of recorded observances. For the 1811 quake in the eastern U.S., there were very few settlers west of the Mississippi River, so it is unknown how far west the earthquake was felt. (Susan Hough web page, USGS Pasadena).

This project, SG-12: Calibrating Intensity with Ground Motion, is attempting to assign ground motion levels with certain observations that occurred during the 1811-1812 New Madrid earthquakes. Perhaps with a specific range of ground motion levels assigned to each occurrence recorded in various locations in the eastern United States, numerous conclusions can be made about earthquakes occurring in the New Madrid Seismic zone. The information gained from this project could possibly shed new light on what is already known or thought to be known about the 1811-1812 New Madrid earthquakes and the possibility of future large magnitude. Attenuation relationships for the central and eastern United States will be directly impacted by SG-12, which will in turn affect probabilistic seismic hazard assessment (PSHA), which is used by the MAEC and USGS for the region. The Modified Mercalli Intensity Scale (MMI) may also be recalibrated as a direct result of this project. Spectral acceleration values will be assigned to each level of the MMI scale further impacting magnitude estimates for earthquakes worldwide.

The following sections of this report provide information on what is projected for this project to have completed at its conclusion and what has been done thus far. This information includes the methods, results, discussions, and conclusions of current data collected from the project so far.

II. METHOD

The project aim has been to first identify testable phenomena from historical observed accounts, which are included in the MMI scale itself. The phenomena are included in levels I through VIII in the MMI scale and are testable on at least one of the shake tables available to the MAE center. These testable phenomena are as follows:

Felt (human response): rarely (I), few (II), several (III), many (IV), practically all (V), and all (VI)

Bells ringing: small bells (VI), large bells (VII)

Pendulum clocks stopping: (V)

Hanging objects swinging: slightly (II – III), numerous instances (IV), considerably (V)

Motion in liquid filled open vessels: swaying slightly (I – II), disturbed (IV), spilled in small amounts (V)

Glasses, glassware, etc.: rattle (IV), break (V)

Falling of knick knacks, books, etc.: (VI)

Furniture: moved moderately heavy (VI), overturned heavy (VII), moved or overturned very heavy (VIII)

The testing has been conducted at CERI (Center for Earthquake Research and Information) at the University of Memphis. CERI has a small shake table on site, which was used for testing and was the major factor in deciding what could initially be done on site in the ten-week period allotted for the REU (Research Experience for Undergraduates) program. Ultimately it was decided that the phenomena regarding liquid filled vessels, pendulum clocks, and small bells would be the main focus of the ten weeks.

1. LIQUIDS IN OPEN VESSELS

Behavior of liquid in open vessels was first on the agenda. The first consideration was what type of vessels should be included. For application purposes, it was decided that the main focus should be on containers representative of the type of containers that were inferred in the MMI scale and more importantly representative of the sizes and shapes of containers that were included in many of the recorded observations of the 1811 – 1812 New Madrid earthquakes. The containers are a bucket and coffee cup chosen for similarities in size and shape to those of the period and for comparison a Styrofoam cup, a rectangular plastic container, and a sherbet cup were also added to the list of things to shake.

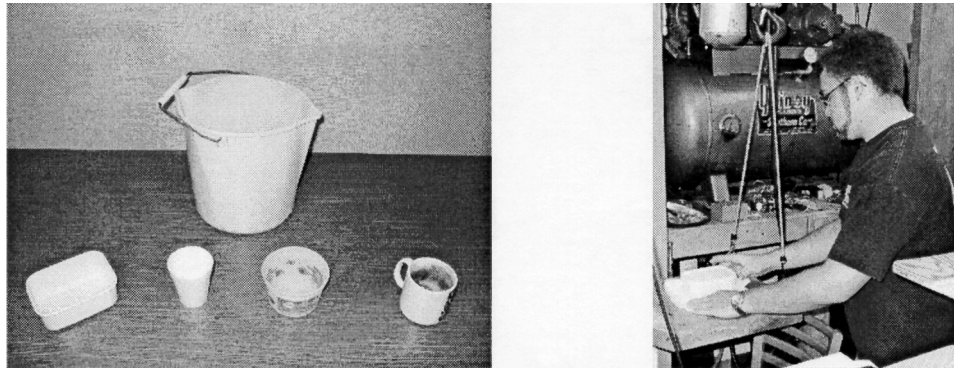


Figure II-A. (Left) Pictured are the containers filled with liquid and tested. The rectangular container was tested with the long axis and short axis parallel to the motion of the shake table. **Figure II-B** (Right) REU student Ryan McDaniel is placing the rectangular container on the CER shake table.

The level of the liquid was an important consideration before testing began. Since the MMI scale gives the description of “well-filled”, the choice was made to fill the containers to a level that would satisfy that constraint. Each container was filled until the water level was about eight to ten millimeters from the lip, except in the case of the bucket, in which case it was filled proportional equally to the smaller containers. The effect of water level on the results is contained in the Discussion portion of this paper. Each container was placed in the center of the shake table with an absorbent material underneath to help detect when water was “splashed out” in small amounts if needed.

Different input motions were considered and the decision was made to use a sinusoidal wave input for each container. Input was varied by frequency and amplitude and frequency ranges from 1Hz to 10 Hz in increasing increments of 1 Hz were chosen to produce a desirable range of data. While the shake table was set at each frequency level, amplitude was slowly increased until the desired outcome was produced or the maximum amplitude of +/- 1 inch was reached. This was carefully reproduced for each container. The amplitude needed to produce the desired effect of the liquid for each container at each frequency was carefully recorded and entered into a spreadsheet where the data could be converted to peak velocities and peak accelerations and compared.

2. CLOCKS STOPPING

A pendulum clock was the next item to be tested. There was consideration to find an antique clock in working order, but for practicality and cost, this idea was abandoned. It was discovered that the most cost-effective way of obtaining a working mechanical pendulum clock that could be attached to the shake table without damage would be to buy a mechanical movement and build a functional case for it. The spring wound movement was purchased and plans were made for the case. The movement was carefully assembled and a case was assembled from plywood, which was designed to represent a standard mantle pendulum clock case while providing rigidity and functionality. The case would be able to be fastened to the surface of the shake table to prevent damage to the movement.

The clock was studied to determine the various ways the actual timing mechanism could be halted. It was determined that the pendulum has a limit to how far it must swing to allow the escape mechanism to work. To stop motion of the pendulum, it was determined that some kind of counteracting motion must be introduced to the clock to reduce the swing of the pendulum within the limit for the escapement to stop working.

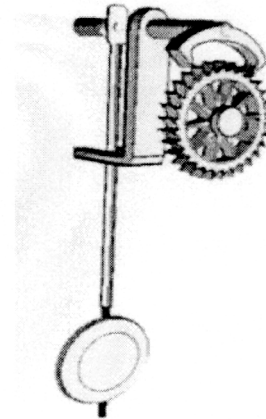
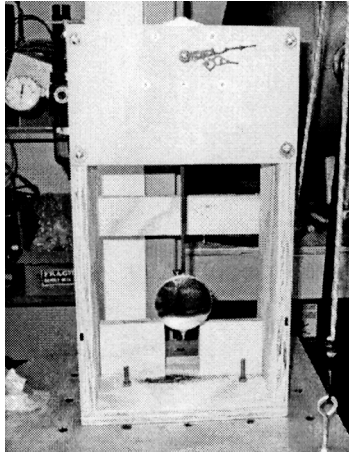


Figure II-C (Left) shows the pendulum clock on the CERI shake table. **Figure II-D** (Right) shows an example of a pendulum clock escapement. The gear is driven by a spring and the escapement is attached to the pendulum. When the pendulum stops swinging, the escapement will not allow the gear to turn, stopping the entire clock movement.

Once assembled, the clock was adjusted for timing and the period of the pendulum was determined. It was decided to find a way to test the clock with a shorter pendulum to include a different range of data to compare results with. The clock was fastened to the shake table and tested. Input motion was varied in both frequency and amplitude until a range was found that caused the pendulum to stop motion. Once the data was recorded, it was entered into a spreadsheet where, again, the peak velocity and peak acceleration values could be calculated for both pendulums.

3. BELLS RINGING

A small bell was the last item to be tested. Fortunately, Dr. Horton was able to bring a small bell from his residence for testing. The bell was fitted to a wood frame that could be fastened to the CERI shake table. Once again, the bell was shaken using arbitrary frequency and amplitude until a reasonable testing range was determined. The lowest frequency with a combined amplitude was determined as the starting point to test an increasing frequency range in increments of .1 Hz while at each frequency, the amplitude was increased until the bell rang, at which point the inputs were recorded. The data from the test was entered into a spreadsheet, and once more, the peak velocities and peak accelerations were calculated and compared graphically and numerically.

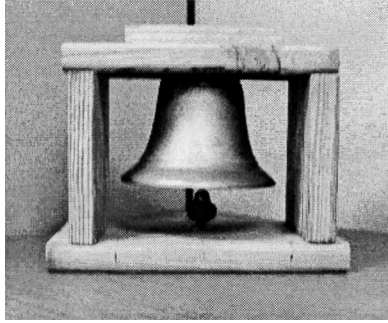


Figure III-E A photograph of the small bell mounted for testing. The mounting was designed to allow the clapper to have an unobstructed path for swinging.

Each of the tests for each of the items was repeated carefully to ensure that the data that had been collected was in fact accurate. Any discrepancies discovered were carefully examined and retested several times to ensure accuracy.

IV. RESULTS

The results from each of the tests are represented in graphical form. The results from the testing of the liquid filled vessels are graphed below. This information is shown in velocity and

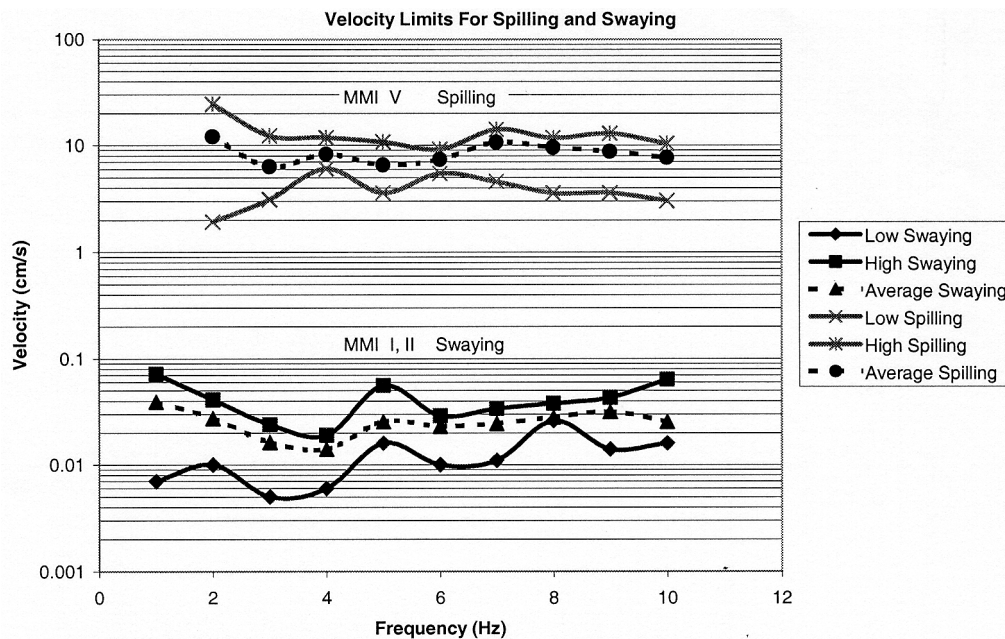


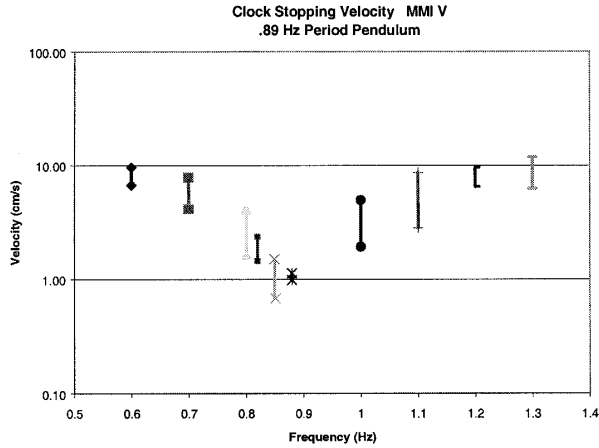
Figure IV-A This graph shows the average, lowest, and highest values of velocity recorded that produced the desired effect for each container at each frequency for both swaying liquid, (MMI I and II), and spilling liquid, (MMI V). There are no data points at 1 Hz for spilling liquid because the limit of the CERI shake table is +/- 1 inch and in every case the liquid would not spill unless a larger input motion was allowed at 1 Hz.

shows the averages of all recorded values of velocity needed to produce the desired effect as well as the lowest and highest values recorded of all of the containers to produce those effects, which are swaying and spilling. The average velocity it takes to splash water out of the open vessels tested is 8.58 cm/s. Figure IV-A also shows the upper limit average as well as the lower limit average of all of these containers. Anything over those values will cause splashing. The overall velocity it takes to sway water is an average of 0.0255 cm/s for the containers tested, while the low average is 0.0121 cm/s and the high average is 0.0420 cm/s. Values of minimum velocity for swaying represent the liquid swaying noticeably if the container is being watched. The upper limit of velocity for swaying is not as easy to determine because somewhere “swaying” turns into “disturbed” as described by the MMI, but the upper limit average values are representative of the largest velocity needed to produce the phenomena at any particular frequency for the containers tested.

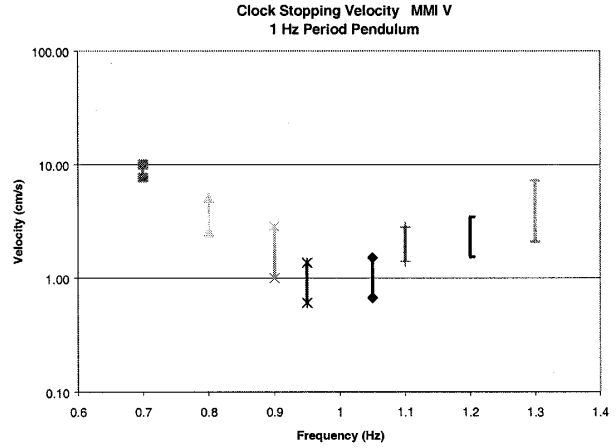
During testing it was observed that the surface shape of the liquid varied greatly from one input frequency to the next. It was observed after several tests that the surface shape of the water was a very good indication of when the liquid was about to spill out of the container. This pattern was consistent regardless of container size or shape.

When the information concerning stoppage of the pendulum clock was graphed, (Figure IV-B & C), it was seen that the range of motion required to stop the pendulum clock produced a much different curve than that of the data concerning the liquid filled containers. For sinusoidal wave input there was an observed limit to frequencies that would cause the pendulum to stop its motion. At each particular frequency there is a minimal limit as well as a maximum limit of velocity that will stop the pendulum’s motion. Any frequency lower than the lowest or higher than the highest frequency in the figure will not cause the pendulum to stop. Also, as can be seen from Figure IV B and IV C, the pendulum will not stop when an input motion with a frequency equal to that of the pendulum’s period is introduced. At that frequency the motion of the pendulum is only amplified. However, as the input frequency approaches the natural period of the pendulum, the values of velocity needed to stop motion become smaller. For example, when testing the pendulum with a natural frequency of .89 Hz, it was observed that at .86 Hz the lowest velocity that would stop motion was .41 cm/s while the largest velocity at that frequency was 1.24 cm/s. At an input frequency of .95 Hz for the pendulum with natural period of 1 Hz, the minimum velocity to stop motion is .61 cm/s while the maximum is 1.36 cm/s.

The length of time that the input motion has to cycle before the motion of the pendulum is halted, is dependent on both input frequency and amplitude, but for the most part the input frequencies that have the largest range of coinciding amplitudes (which in turn produce a larger range of velocities) are the most likely motions that cause stoppage of the clock.



Clock Stopping Velocity MMI V
.89 Hz Period Pendulum



Clock Stopping Velocity MMI V
1 Hz Period Pendulum

Figures IV-B-C These are the plots of the velocity ranges for each frequency that was required to stop motion of the pendulum. Figure IV-B shows the velocity plot for the .89 Hz pendulum and Fig. IV-C shows the velocity plot for the 1 Hz pendulum. Stopping of a pendulum clock is an MMI V.

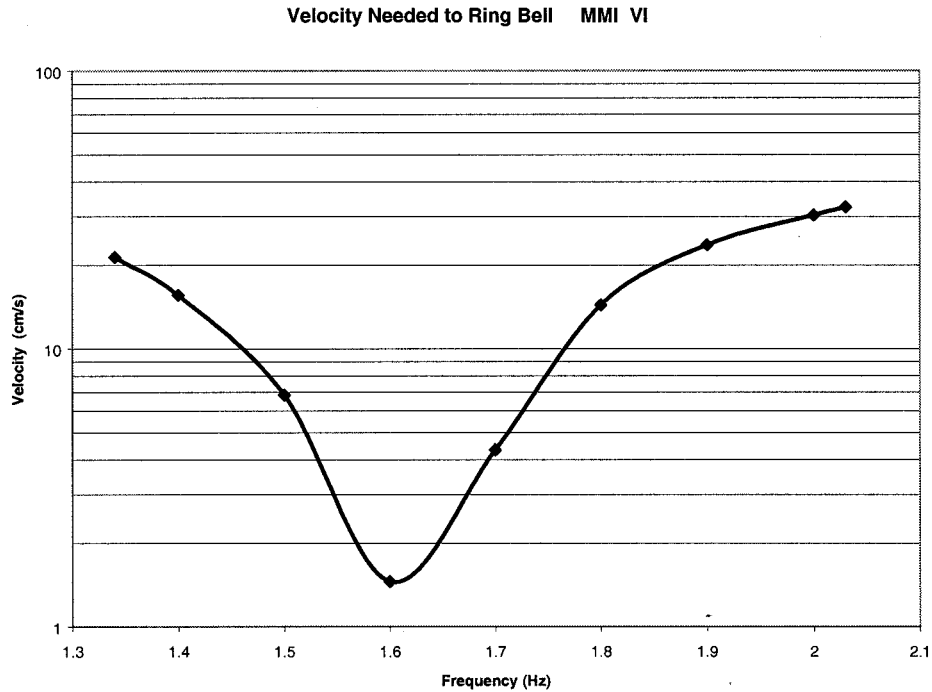


Figure IV-D This figure is a plot of the velocity needed at each frequency to produce a ringing of the small bell (MMI VI). At any other frequency lower than the lowest shown it may require an input amplitude greater than the +/- 1 inch limit of the CERI shake table to induce ringing of the bell.

The results from the test involving the ringing of the small bell are shown in Fig. IV-D. Each data point was recorded even at the smallest ring of the bell. The minimum velocity it takes to ring the bell with a sinusoidal input is 1.46 cm/s at 1.6 Hz. Values shown in Fig. IV-D represent the minimum values of velocity needed to produce ringing at each frequency. As can be seen by Figure IV-D, the minimum velocity occurs very near the natural period of the oscillator (clapper of the bell), which happens to be very near 1.6 Hz. Ringing of a small bell happens to be an MMI VI.

V. DISCUSSION

The tests are eventually going to include the “disturbed liquid in open vessels slightly” classification given in an MMI IV. For time constraint reasons, this could not be completed in the ten-week period of the REU program, but will most likely be added to the results at a later date. The primary reason it would take more time to complete is that for the data from the test to be accurate, there needs to be a consensus of the limits for “disturbed liquid” from more than just a few people. As a result of the wording of the Modified Mercalli Intensity scale, interpretation of what a disturbed liquid is different for different people as was proven from discussion with a few people. The need for input from several different people on their interpretation of “disturbed” is evident as is the possible need for rewording several items included in the Modified Mercalli Intensity Scale.

Other possibilities for what might stop a pendulum clock from working were also considered. These possibilities included the reality that the pendulum’s motion could be stopped by the weights and chains of a weight driven pendulum clock getting in the path of the pendulum, however this possibility could be caused by a very broad range of ground motions and it was decided to exclude this type of test. A test of a spring driven pendulum clock would give a much more useful range of data for determining ground motions needed to cause the phenomena. Different length pendulums were used to compare similarities in ground motion needed to stop their motion as well as to address the obvious fact that not every clock has the same gear ratio and swing rate. It was also observed that a longer pendulum has a broader range of ground motions needed to stop their motions. By including this information and testing the smaller range of data, the ground motion needed to stop pendulum clocks can be more accurately determined and in turn can be more accurately applied to the determination of ground motions needed to stop the clocks from historical observations. The more accurate information will also help in the calibration of attenuation relationships.

The small bell is one that satisfies the MMI scale level VI description. Since the bell that was tested was mounted in a manner that would keep the sound bow stationary, future tests may also include a test where the sound bow is allowed to swing freely. This may broaden or narrow the data range that will produce ringing of a small bell. It is virtually impossible to test all types of small bells, so every possible variable associated with the small bell tested was considered and addressed.

Every test was conducted with a sinusoidal input motion. The next tests will include other types of inputs, in particular impulse waves. Also data from recorded earthquakes may be

put into a wave generator to simulate one or more components of an earthquake. The results from these future tests will also be incorporated into the calculation of what ground motion causes each of the tested phenomena. The tests conducted on the CERI shake table incorporated one component of motion at a time. Future tests conducted on other shake tables with more degrees of freedom may incorporate more than one component of ground motion at a time, further broadening the range of available data.

To help give an idea of how accurate the information gathered from testing was, a comparison of data was made. In an entry in the BSSA, Gail M. Atkinson and David M. Boore presented a likely ground motion relation for Eastern North America. The entry is titled Ground-Motion Relations for Eastern North America and appeared in volume 85 of the Bulletin of the Seismological Society of America. The proposed relationship includes a range of input magnitude and distance with certain frequencies that would result in an accurate value for peak ground velocity or peak ground acceleration. The limit for input magnitude is 4.0 to 7.25 and for distance between 10 and 500 km. An observation from the December 16, 1811 New Madrid earthquake places a stopped pendulum clock about 600 km away and current estimates of that specific quake are magnitude 7.3. This puts the information just outside of the accurate limits. However, this is the closest observation of a stopped clock that could be used to compare the data from testing. Since peak ground velocity is the velocity obtained from testing, the magnitude and distance were plugged into the relationship even though they were both just over the limits and a PGV resulted. When compared to the range of PGV's from testing at the frequency used for the equation, it was found that the resultant PGV fell into the range of PGV's from testing. Assuming that the ground motion relationship equation is somewhat accurate, the data from testing seems to be in compliance. (G. M. Atkinson and D. M. Boore, 1995).

VI. CONCLUSIONS

Many conclusions can be made about each test and comparisons of the tests together thus far. Data was compiled and compared to relate the phenomena to each other and compare those relations with how they differed in the MMI scale.

The reaction of liquid in liquid filled open vessels is somewhat dependent on size, shape, and material of the vessel. For the containers tested, the average minimum velocity needed to cause spilling was 8.58 cm/s while the average minimum velocity needed to produce swaying was .0255 cm/s. More information will be gathered with further testing of various containers and with the addition of other waveform input motions. However, even with some difference in reaction to shaking, it seems that data received from testing of most sizes and shapes can be enveloped and maximum and minimum values for ground motion can still be assigned. If need be, certain sizes or shapes of well-filled open containers may be separated and regrouped into another MMI scale level. Only future testing will reveal what recommendations can be made concerning liquid filled vessels.

The data collected from testing of the clock shows that even for different length pendulum, the input motion needed to stop the clock has definite limits for sinusoidal input motion. The lowest velocity values needed to stop both pendulums tested, .41 cm/s and .61

cm/s, are very close. If input motion is at the same frequency of the pendulum, the motion of the pendulum will only be amplified, and there is a specific range of input frequencies that will affect the motion of the pendulum that is relative to the pendulum's period. Throughout the range of frequencies that will stop the pendulum's motion, there are upper and lower limits of input motion, which means that there is a definite envelope of input motion that is relative to the period of the pendulum. It seems that most pendulum clocks of similar size have similar length pendulums, which means that they would have relatively similar natural periods. From the data collected, it seems that ground motion needed to stop a clock is dependent on input frequency and pendulum natural frequency. This in turn means that a certain range of ground motion needed to stop clocks can be applied to historical observations.

Since most of the historical observances of clocks stopping do not specify what kind of clocks (grandfather, mantle, etc.) stopped and only say that "few" or "most" stopped, it is most likely that an average can be applied and will give a sufficient range of ground motion to make many conclusions. Future testing will produce more specific ranges of ground motion and will assist in the determination of magnitudes of historical earthquakes. It is also possible that future research into the historical observations and into the items of the time period will provide better information on what kind of clocks were stopped. Comparisons can also be made with other known recorded phenomena and their range of ground motions to cross-check and narrow the range of possible ground motions allowing for more accurate estimations in magnitude and attenuation.

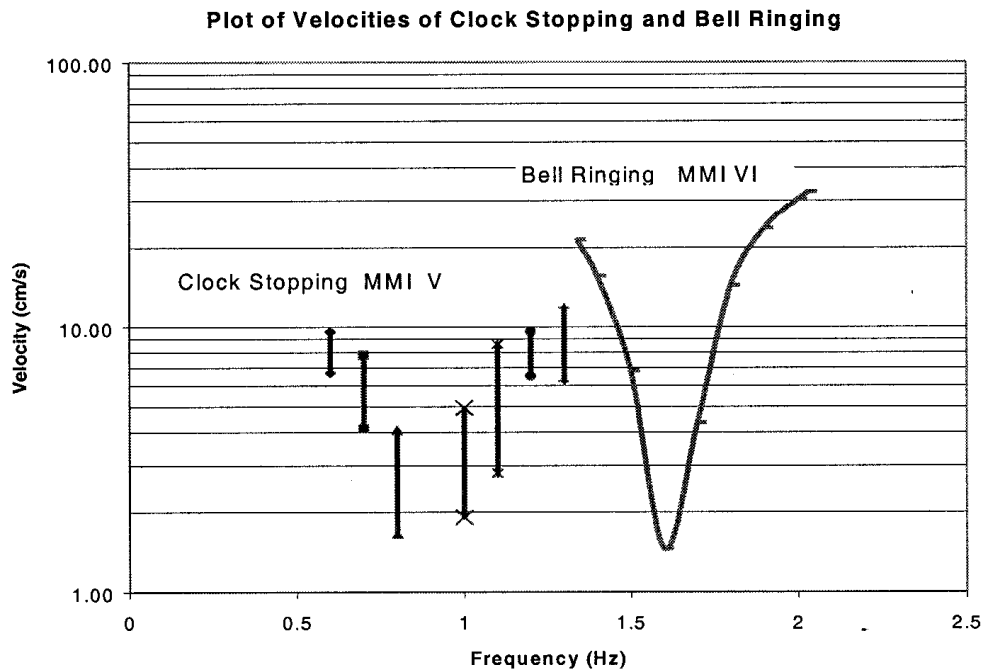


Figure VI-A This plot of the data collected from the test of the bell and the clock (.89 Hz period) shows the numeric similarity between the two phenomena. Though they are grouped into different categories in the MMI scale, it seems that they should be grouped together.

Comparison of the data collected from testing of the bell and the clock shows that even though belonging to different MMI levels, (VI and V respectively) the data of the two tests when plotted seem to be very similar as seen in Figure VI-A. For comparison of this data, the minimum recorded velocity for stopping the .89 Hz pendulum was .41 cm/s up to 1.24 cm/s at .86 Hz and the minimum velocity needed to ring the bell was 1.46 cm/s at 1.6 Hz. The differences in the velocity values for the two items are relatively negligible. This could be the start of what may result in the rewording or regrouping of items in the MMI scale. Future testing will help decide.

With more tests to come both for items that have been tested and those that haven't, there is a possibility of many other grouping inconsistencies arising. Current results show the certainty of the success of SG-12 in accomplishing all of its objects.

ACKNOWLEDGEMENTS

My participation in this project was through the Research Experience for Undergraduates program sponsored by the Mid-America Earthquake Center, which is funded by the National Science Foundation. I would like to extend my appreciation to the MAE Center for the opportunity to participate in this excellent program.

I would also like to thank Dr. Steve Horton for allowing me to work with him on this project and for all of his help. I would also like to thank Sandra Menke at the University of Illinois for all of her help. At the Center for Earthquake Research and Information at the University of Memphis, I would like to thank Gary Patterson for advice and for helping with photographs, Greg Steiner for assistance with the shake table, and Chris Watson for computer assistance. Thanks to The Clock Shop of Memphis, TN, for helping with the pendulum clock.

At the University of Tennessee at Martin, a special thanks to Dr. Richard Helgeson, Dr. J. Douglas Sterrett, Dr. William Zachry, and Linda Davis for encouragement and assistance in applying to the REU position.

REFERENCES CITED

Publications

G. M. Atkinson and D. M. Boore (1995). Ground-Motion Relations for Eastern North America, *Bull. Seism. Soc. Am.* **85**, 17-30.

Wood, H. O. and F. Neumann (1931). Modified Mercalli Intensity Scale of 1931, *Bull. Seism. Soc. Am.*, 277-283.

Websites

Center for Earthquake Research and Information, University of Memphis
<http://www.ceri.memphis.edu>

USGS Pasadena, Susan E. Hough information website
<http://pasadena.wr.usgs.gov/office/hough/>

3-D Cube

Michael Mio

Home Institution: University of California Santa Barbara

REU Institutions: ImageCat, Inc. and University of Southern California

REU Advisors: Charles K. Huyck and Ronald T. Eguchi

Abstract

When viewing a two-dimensional image of earthquake epicenters, including the main shock and any foreshocks or aftershocks, it is very difficult to tell exactly where these events are located and which fault plane they are associated with. With a three-dimensional representation of the hypocenters and fault planes, viewers will be able to see an image that will clearly display how the main shock, foreshocks, and aftershocks are distributed along the fault plane. Viewing an image like this will greatly simplify the task of identifying the source of an earthquake. Using emails from the Southern California Seismic Network's CalTech-USGS Broadcast of Earthquakes (CUBE) project, a real time system called 3-D CUBE has been created which plots the hypocenters of earthquakes in Southern California with a magnitude of a 3.0 or greater onto a three-dimensional map.

Problem

The problem with keeping track of earthquakes on a two-dimensional map is that it is very difficult to tell which fault plane the earthquake is associated with and how deep the origin of the earthquake is. With a two-dimensional map, only the epicenter of an earthquake is plotted. The epicenter is the surface projection of the hypocenter, the actual origin of the earthquake. With this two-dimensional view, there is no sense of depth and it is very hard to visualize where exactly the earthquake originated from. From a two-dimensional perspective, it is also very difficult to see which fault plane is responsible for causing an earthquake. In some areas, many fault planes overlap each other and are located very near one another. Figure. 1 shows a map from the USGS web site of California and Nevada. Here, one can clearly see how difficult it is to figure out how deep the source of the earthquake is and how difficult it is to identify which fault plane caused the earthquake.

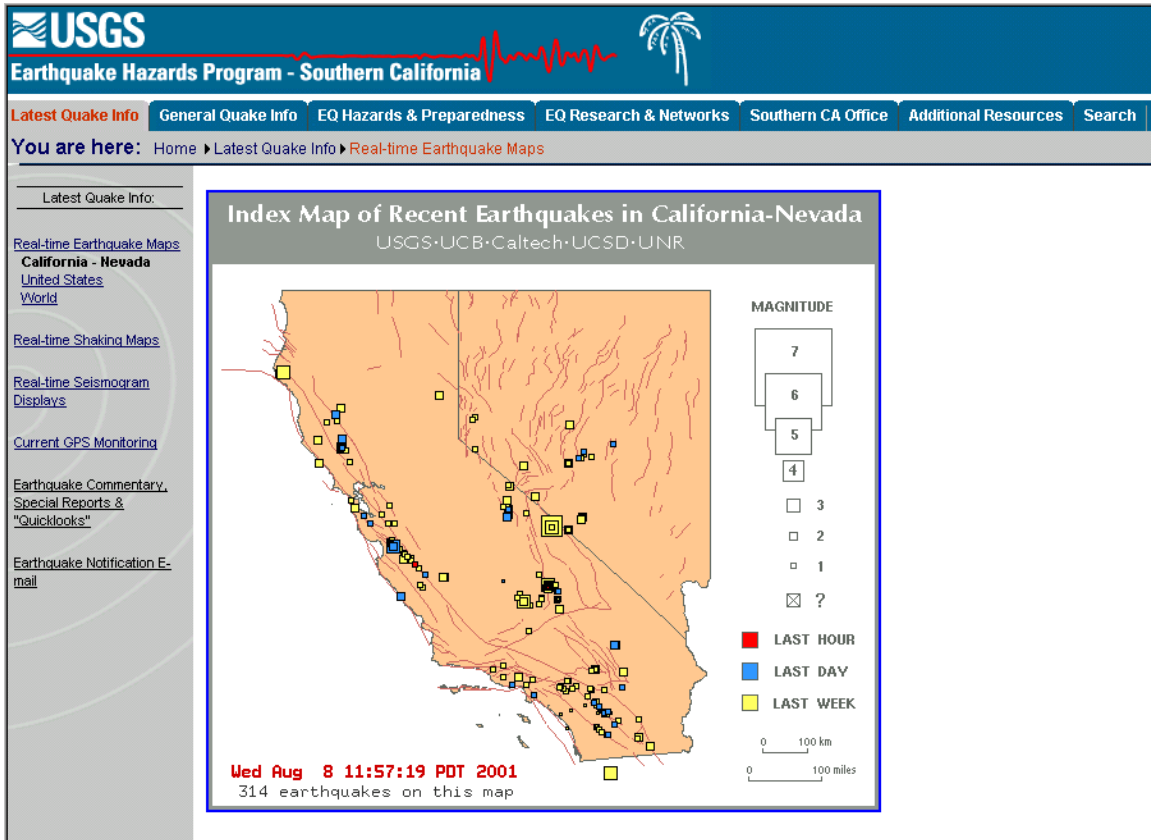


Figure 1. Map from the USGS website of California and Nevada with earthquake epicenters and fault lines displayed.

Solution

3-D CUBE was created to solve this problem. 3-D CUBE is a real-time system that keeps track of earthquakes (M3.0 and greater) that occur in Southern California in three dimensions, i.e., horizontal geographic coordinates and depth. A real-time system is one that provides updated information or data instantaneously, as events occur. This system (3-D CUBE) plots the hypocenters of earthquakes as they occur onto an interactive three-dimensional map of Southern California. Virtual Reality Modeling Language, or VRML is used to create this map. VRML is a programming language used to make three-dimensional images in which a user can navigate around. In order to view VRML images, a user must download a VRML plugin, such as Cosmo Player (<http://www.cai.com/cosmo/>). Plugins like Cosmo Player work within web browsers such as Microsoft Internet Explorer or Netscape Navigator.

Information about these earthquakes is also provided in 3-D CUBE. This information includes an earthquake's magnitude, the date and time that it occurred, the depth, the latitude and longitude of the event, its unique identification number, and the quality of the data, which tells the user how accurate the information is. Earthquake hypocenters are represented as spheres on the map, with the radius of the sphere representing the magnitude of the earthquake. There are six different colors that the hypocenters can be associated with. The colors of the hypocenters represent how old the earthquakes are.

The map contains all of the fault planes and highways that are known in Southern California; the locations of major cities are also labeled on the map.

This map can be navigated around so that users can look at it from many different angles and perspectives. This allows users to gain a good understanding about how deep the earthquake's origin is and which fault plane caused the earthquake to occur. Figure 2 shows the interactive three-dimensional map of Southern California with some hypocenters on it. The red lines represent the highways and the blue planes represent the fault planes. Figure 3 shows that by using 3-D CUBE, a viewer can easily see which fault plane caused the earthquake and how deep the origin of the earthquake is.

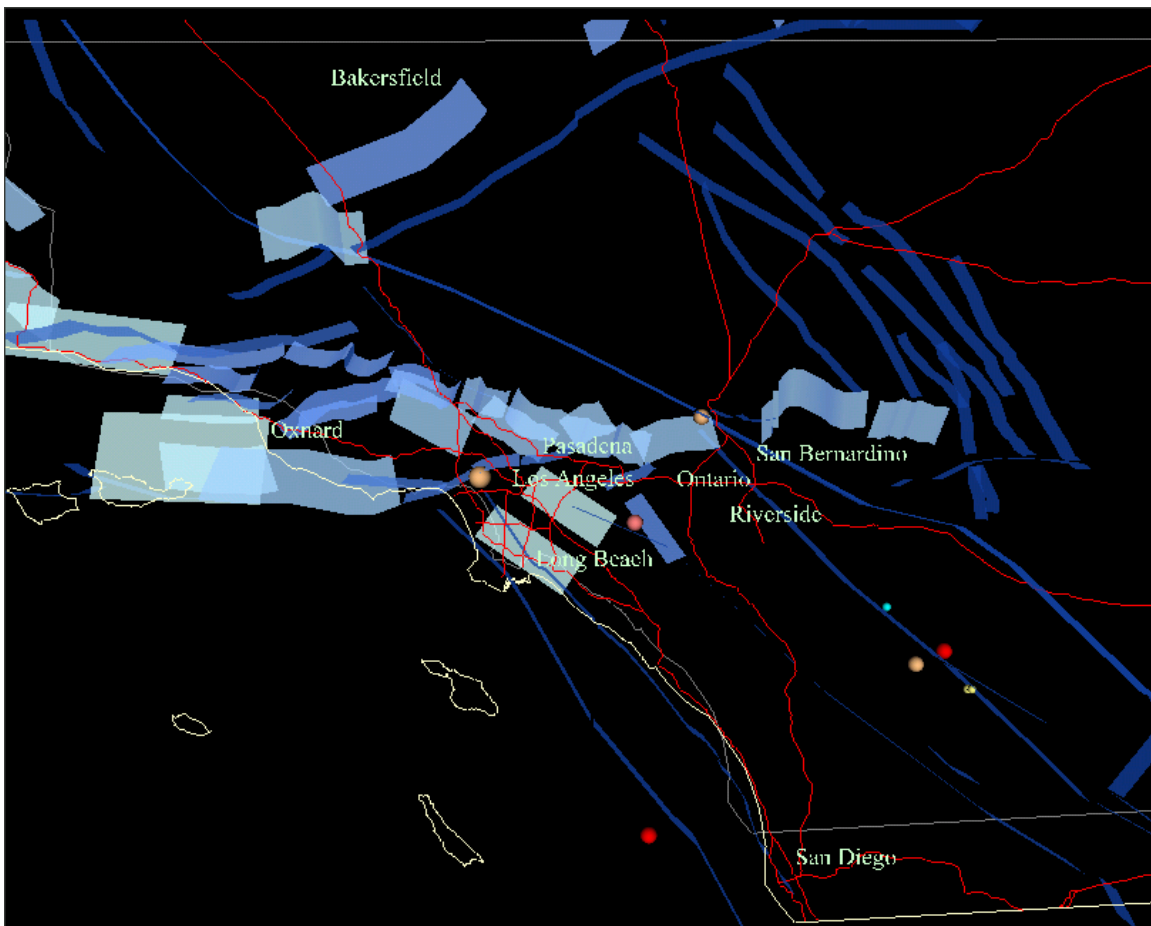


Figure 2. 3-D CUBE's map of Southern California with some hypocenters displayed.

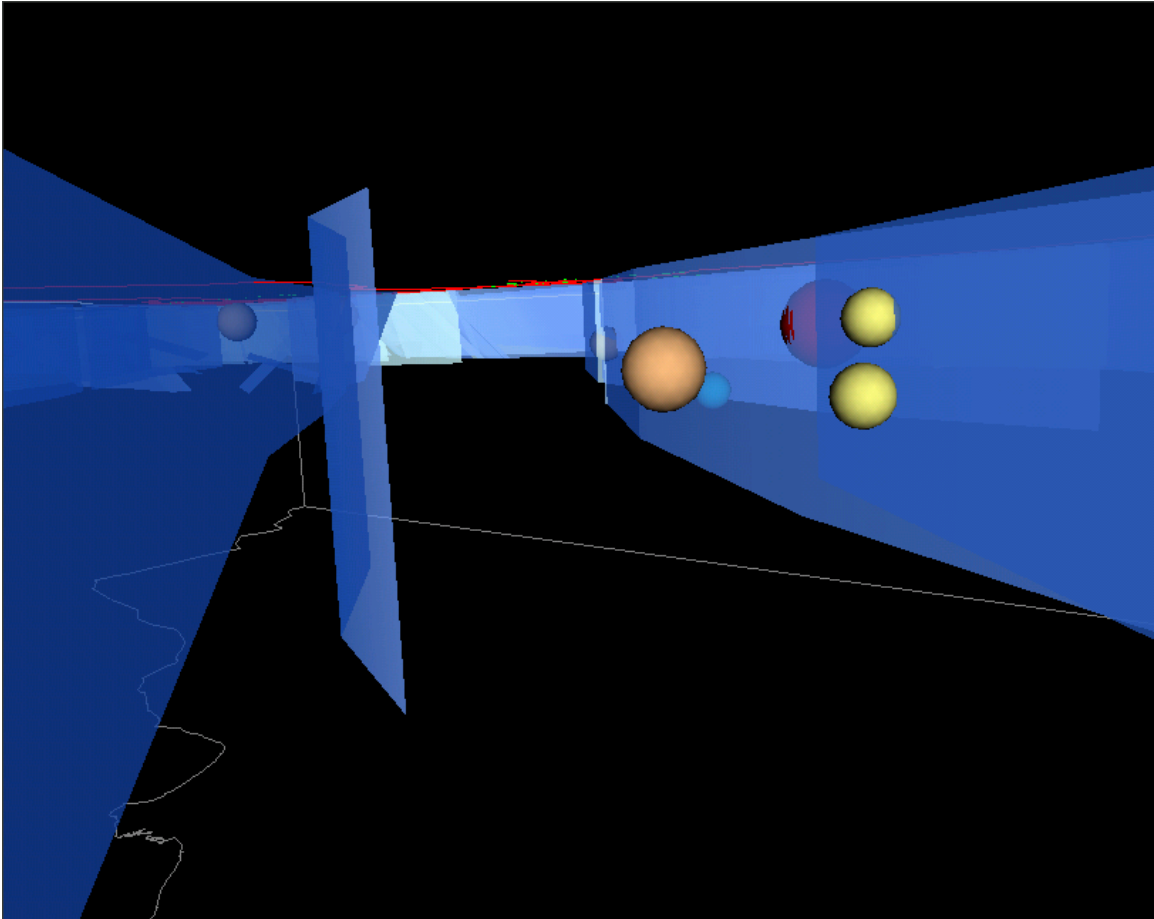


Figure 3. Side view to show the depth of the earthquakes' origin and to show how it is easy to see which fault plane caused the earthquakes.

Process

There were many steps involved to make 3-D CUBE work properly. First, whenever someone goes to the 3-D CUBE website, a PERL (Practical Extraction and Report Language) script runs to check and see if a new earthquake has occurred. PERL is a programming language that is useful for operations such as extracting text from files and combining files together. The PERL script checks if an email from the Southern California Seismic Network has been received. The Southern California Seismic Network has a real-time system that monitors earthquakes occurring in Southern California, which is known as CUBE (CalTech-USGS Broadcast of Earthquakes). The Southern California Seismic Network has a service in which it sends out an email whenever an earthquake occurs with a magnitude of a 3.0 or greater. An example of this email can be seen in Figure 4. If the PERL script finds an email when it checks, then the script extracts relevant information from it. The magnitude, date and time, longitude and latitude, depth, radius, event identification number, and quality of the earthquake are all extracted from this email. The script takes all this information and writes it to an HTML file. When a user clicks on a hypocenter, this file is called and information on the earthquake is displayed. The script takes the radius and uses it to create a sphere that is plotted on the three-dimensional map of Southern California. The coordinates in the email are longitude and latitude, so the script takes these coordinates and converts them into decimal degrees.

3-D CUBE has another PERL script that runs once a day to perform maintenance on the system. This script keeps track of how long the earthquakes have been in the system. Every five days the colors of the hypocenters change to visually show how old they are. There is a key that shows what the colors stand for and it also shows what the

highways and fault planes look like. After thirty days, the hypocenter is removed from the map and the earthquake's information is deleted from the system.

Southern California Seismic Network (TriNet) operated by Caltech and USGS

Version 1: This report supersedes any earlier reports about this event.
This is a computer generated solution and has not yet been reviewed by a human.

Magnitude : 3.0 Ml
Time : 20 Jun 2001 03:30:43 PM PDT
: 20 Jun 2001 22:30:43 UTC
Coordinates : 35 deg. 47.93 min. N, 118 deg. 2.41 min. W
Depth : 4.7 miles (7.5 km)
Quality : Excellent
Event ID : 9664317
Location : 18 mi. SSW of Coso Junction, CA
: 61 mi. ENE of Bakersfield, CA
: 19 mi. WSW of COSO (quarry)

More information is available on the Worldwide Web at:
<http://www.trinet.org/scsn/scsn.html>

--

You are receiving this message through the quake-all mailing list.
To subscribe, go to <http://pasadena.wr.usgs.gov/mailling-lists.html>
To unsubscribe, send mail to quake-all-unsubscribe@eqinfo.wr.usgs.gov

Figure 4. Sample email sent out by Southern California Seismic Network after an earthquake of a magnitude of a 3.0 or greater occurs.

Future Work

There are some things that can be added to 3-D CUBE as well. For one, this version of 3-D CUBE only tracks the earthquakes for Southern California. There are many other areas in the world where earthquakes occur, and a 3-D CUBE system could be created for those regions as well. Another addition could be to provide a screen shot of the 3-D CUBE image. This could be provided for users who choose not to download the VRML plugin. This could be useful to users that do not have a fast Internet connection.

Acknowledgements

Finally, I would like to thank the National Science Foundation for providing the Research Experience for Undergraduates Program, EEC-9701471. I would also like to thank my REU Advisors Mr. Charles K. Huyck and Mr. Ronald T. Eguchi, and my other fellow coworkers at ImageCat, Inc. for their guidance and support during the summer. Last and certainly not least, I would like to thank Ms. Andrea Dargush from MCEER for all of her hard work in organizing the symposium in Salt Lake City, Utah and for keeping me informed with what I needed to know in regards to the REU program.

PEER Nonstructural Component Database



Carlos R. Nazario
Home institution: University of Puerto Rico at Mayagüez

Host Institution: Stanford University
Faculty Advisor: Dr. Eduardo Miranda

October 2001

Foreword

“The great liability of the engineer...compared to men of other professions...

Is that his works are out in the open were all can see them.

His acts ...step by step...are hard substance.

He cannot bury his mistakes in the grave like doctors.

He cannot argue them into thin air ...or blame the judge ...like the lawyers.

He cannot like the architect, cover his failures with trees and vines.

He cannot, like the politicians, screen his shortcomings by blaming his opponents...

And hope that people will forget.

The engineer simply cannot deny he did it.

If his works do not work...he is damned.”

Herbert H. Hoover

ABSTRACT

PEER SUMMER INTERNSHIP REPORT

PEER Nonstructural Component Database: Essential Tool on Nonstructural Loss Estimation Methodology

Carlos R. Nazario

A very significant part of the economic losses caused by earthquakes on commercial and institutional buildings is directly related to the performance of nonstructural components. Research studies have demonstrated that approximately 70% to 85% of the cost of buildings comes from nonstructural components and contents. Also, nonstructural components are more vulnerable to earthquake damage than structural elements.

A computer database is being created with the purpose of collecting and organizing information about nonstructural components' costs and seismic performance. At the same time the database is an essential tool for the on-going research project titled *Seismic Performance and Loss Assessment of Nonstructural Building Components and Contents*

During the 2001 Summer I was involved in the search for information, including literary research and visits to construction sites and earthquake affected areas.

TABLE OF CONTENTS

INTRODUCTION

SCOPE

IMPORTANCE OF NONSTRUCTURAL COMPONENTS

PEER NONSTRUCTURAL COMPONENT DATABASE

 General Information

 Objectives of the PEER Nonstructural Component Database

 Information Available in the Database

CONCLUSION

ACKNOWLEDGEMENTS

REFERENCES

APPENDIX

LIST OF FIGURES

- Figure 1 Lateral shifting of library bookshelves.
- Figure 2 Damaged ceiling, sprinkler pipe, and lighting fixture; Northridge Earthquake, Jan. 1994.
- Figure 3 7 Story Hotel Cost Breakdown.
- Figure 4 Severe damage to roll - up door in a tilt-up warehouse; Northridge earthquake, Jan. 1994.
- Figure 5 Seismic damage to piping joint at the original Olive View Hospital, San Fernando Earthquake, Feb. 1971.
- Figure 6 Organization of Database.
- Figure 7 Ceiling damage to department store in Olympia, WA; Nisqually Earthquake Feb. 2001.
- Figure 8 Collapsed tank; Anchorage Earthquake, March 1964.
- Figure 9 Stucco damage on the façade of the South Library at Cal State University; Northridge, Jan 1994.
- Figure 10 Performance in previous earthquakes.

LIST OF TABLES

- Table 1 Frequency of occurrence of earthquakes based in observations since 1900, USGS, National Earthquake Information Center
- Table 2 Building types included in the database.
- Table 3 Classification of nonstructural components.
- Table 4 Components classification for cost purpose.
- Table 5 Earthquakes included in the database.

INTRODUCTION

Throughout history the engineering community has made great advances on providing effective earthquake structural designs. These designs minimize human life losses while aiming to obtain stabilized and repairable structures after ground motions. Parallel to the desire of human safety is the desire to prevent significant economic losses after ground motion events.

During the last decades a big improvement has been evidenced on the seismic performance of buildings' structural members such as foundations, beams, and columns. On the other hand, these same earthquakes have highlighted the poor performance of nonstructural components and contents, mainly on commercial and institutional buildings. A very interesting fact is that considerable economic losses caused by earthquakes are related to the nonstructural damage and the corresponding repair works.

Earthquake engineering research projects are being carried out to analyze the seismic performance and loss assessment of nonstructural components and contents. These will benefit future designs and will enhance the effectiveness of performance-based earthquake engineering.

SCOPE

The purpose of this report is to present a description of a database containing information about nonstructural building components. The PEER Nonstructural Database is an essential tool developed in the research project *Seismic Performance and Loss Assessment of Nonstructural Building Components and Contents*, being carried out in Stanford University. It contains detailed description of nonstructural components and respective original costs, performance on previous earthquakes, description of damage and respective repair costs. The information can be adapted to different types of buildings (i.e. apartment buildings, hotels, schools, etc.). It also contains ground motion information, references, and photos of damaged and undamaged nonstructural components. The operation of the database is very simple making the information accessible and manageable.



Figure 1 – Lateral shifting of library bookshelves.



Figure 2 – Damaged ceiling, sprinkler pipe, and lighting fixture; Northridge Earthquake, Jan. 1994.

IMPORTANCE OF NONSTRUCTURAL COMPONENTS AND CONTENTS

The following are the three main reasons for studying seismic performance of nonstructural components and contents.

1. Percentage of Building's Total Cost

Typical costs of nonstructural components used in commercial and institutional buildings have been identified and classified. Results of various investigations suggest that nonstructural components installed in these types of buildings represent approximately 70% of the total cost.

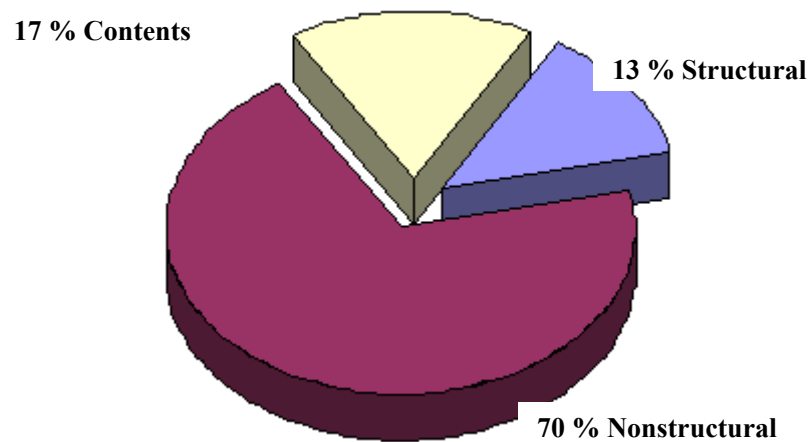


Figure 3 - 7 Story Hotel Cost Breakdown

2. Lower Levels of Deformation

It has been proven that in the majority of buildings damage caused to nonstructural components is triggered at levels of deformation much smaller than those required to trigger structural damage.



Figure 4 - Severe damage to roll - up door in a tilt-up warehouse; Northridge earthquake, Jan. 1994.



Figure 5 – Seismic damage to piping joint at the original Olive View Hospital, San Fernando Earthquake, Feb. 1971.

3. Smaller Earthquakes are More Frequent

The following data has been collected since 1900. The table presents the number of earthquakes and their respective magnitudes on the Richter Scale.

Description	Magnitude	Average Annually
Great	8 and higher	1
Major	7 - 7.9	18
Strong	6 - 6.9	120
Moderate	5 - 5.9	800
Light	4 - 4.9	6,200 (estimated)
Minor	3 - 3.9	49,000 (estimated)
Very Minor	< 3.0	Magnitude 2 - 3: about 1,000 per day
		Magnitude 1 - 2: about 8,000 per day

Table 1- Frequency of occurrence of earthquakes based in observations since 1900, USGS, National Earthquake Information Center

PEER NONSTRUCTURAL COMPONENT DATABASE

General Information

Early on 2001 a computer database was created using Microsoft Access Relational Database Management System for Windows operating systems. This database is an integral part of the earthquake engineering research project *Seismic Performance and Loss Assessment of Nonstructural Building Components and Contents*. The database is capable of storing large amounts of information about nonstructural components. The operation of the database is very

simple, making the information accessible and manageable. The following flowchart presents the main information accessible in the PEER Nonstructural Component Database.

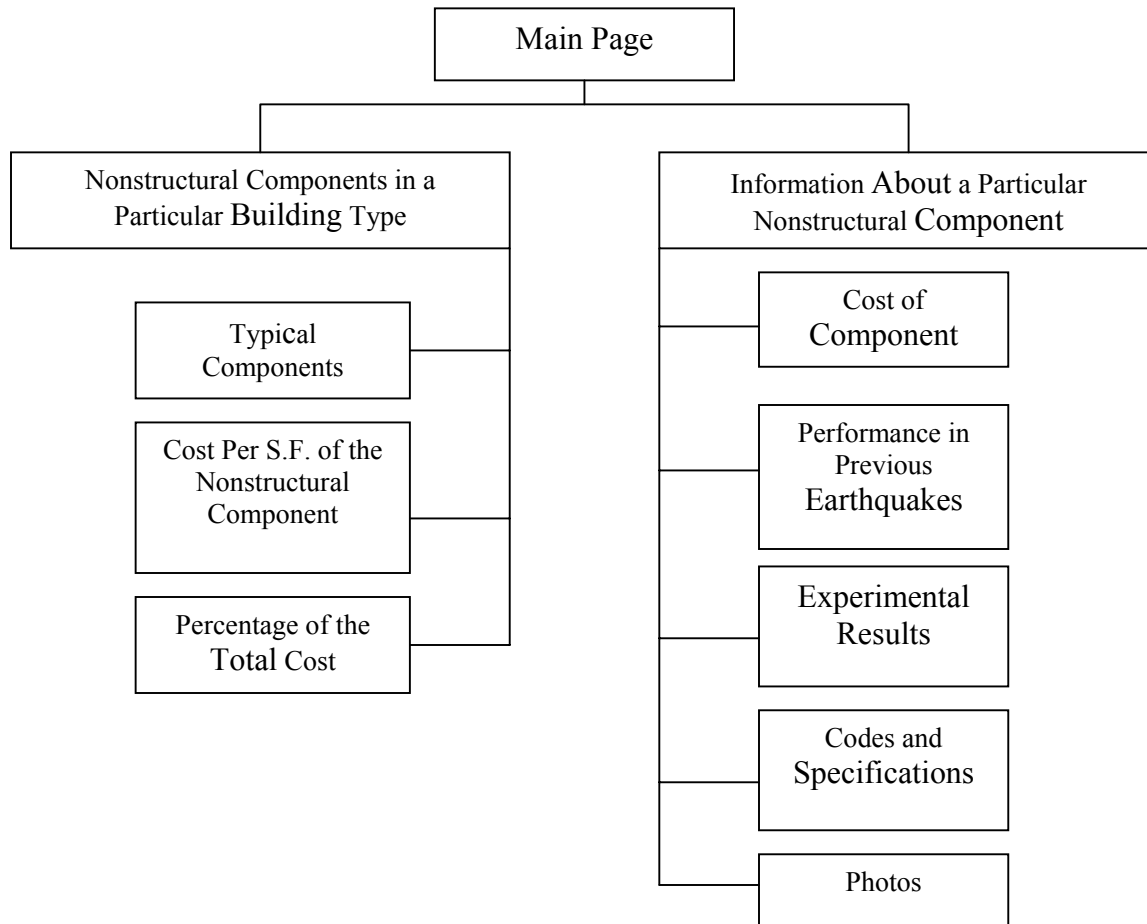


Figure 6 - Organization of Database



Figure 7 - Ceiling damage to department store in Olympia, WA; Nisqually Earthquake Feb. 2001.

Objectives of the PEER Nonstructural Component Database

The creation of the database will facilitate the manageability of large amount of detailed information within the research project. It will also be a very practical tool for future research projects resulting benefited the entire engineering and academia community.

The main objective of the PEER Nonstructural Component Database is to assist in the collection and organization of existing information about the cost of nonstructural components and to summarize the performance of building nonstructural components and contents in previous earthquake ground motions.

Information Available in the Database

The information contained in the PEER Nonstructural Database is classified in two main groups: (See Appendix A).

- (a) Information about nonstructural components in particular building types.
- (b) Information about a particular nonstructural component.

Within these main groups the information is structured as shown in Figure 3. A description of the content and the operation of the PEER Nonstructural Component Database are presented below.

1. Information About Nonstructural Components in Particular Building Types

Users searching for information about nonstructural components installed in particular buildings will have the option of accessing three data screens. These screens contain a list of typical components installed in commercial and institutional buildings of various heights. It also allows the user the opportunity to access information about different configurations of nonstructural components.

- (a) Typical nonstructural components. (See Appendix C)
- (b) Cost per square foot of the nonstructural component. (See Appendix D)
- (c) Percentage of the building’s total cost. (See Appendix E)

In order to access any of the three data screens the user must first specify what type of building he is interested in. The building types included in the database are: (See Appendix B).

Any	School
Apartment	Store
College	Supermarket
Garage	Industrial
Hospital	Essential Facility
Hotel	Other
Library	Academic
Motel	Various
Office	Unknown

Table 2 – Building types included in the database.

All three data screens classify nonstructural components as presented in Table 3, which at the same time are sub-classified as presented in Appendices C, D, E. Detailed cost information and short descriptions of each nonstructural component is presented in a very organized and convenient way; see Appendices C, D, E

Exterior Closure
Roofing
Interior
Conveying
Mechanical
Electrical
Special Construction

Table 3 - Classification of nonstructural components.

2. Information About a Particular Nonstructural Component

Users searching information about a particular nonstructural component will have the option of accessing five data screens (see Appendix F). These contain detailed information about components, and are not related to any specific building type.

Listed below are the five data screens:

- (a) Cost of component** – When accessing this screen the user must first specify what nonstructural component he is interested in. First, a component type must be selected and then a new window will appear showing the components available. See Table 4. Information will include: description of the component, cost of material, cost of installation, and total cost (all unit prices). A photo of

the corresponding component will also be available in this data screen. See Appendix G.

Component Type	Nonstructural Components Included
Any	All nonstructural components available.
Roofing	Any, insulation, opening and specialties, and roof coverings.
Interior Construction	Any, ceiling finishes, floor finishes, partitions and wall finishes.
Conveying	Elevators and others.
Mechanical	Any, cooling, fire protection, heating and plumbing.
Electrical	Any, Lighting and power, service and distribution, and special electrical.
Special Construction	Any and specialties.
Exterior Closure	Any, doors, exterior wall finishes, walls, and windows and glazed walls.
Content	Any.

Table 4 - Components classification for cost



Figure 8 - Collapsed tank; Anchorage Earthquake. March 1964.



Figure 9 – Stucco damage on the façade of the South Library at Cal State University; Northridge, Jan 1994.

(b) Performances in previous earthquakes – Nonstructural components have been classified into two response sensitivity categories: drift sensitive and acceleration sensitive. Information available in the database is the following: a short description of the nonstructural damage, damage level, location of damage, cost of repair, sensitivity measurement (if available), earthquake information (about 52 earthquakes included, see Table 5), building information, and references (see figure #3). See Appendix J.

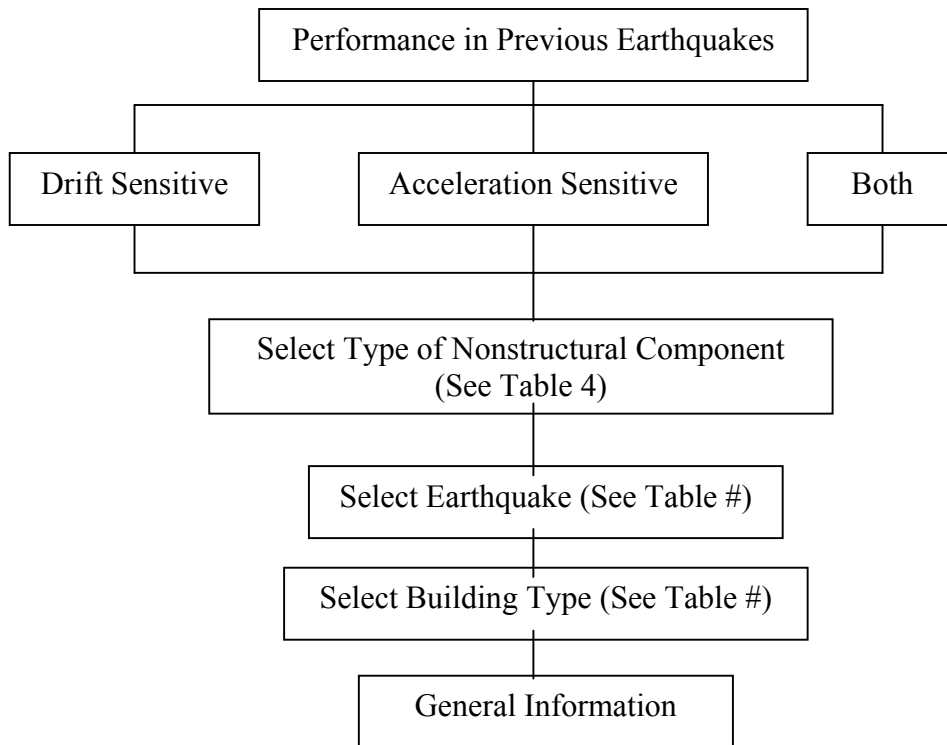


Figure 10 - Performance in previous earthquakes.

Earthquakes Included			
Northridge	Mexico	Iran	Killari
Loma Prieta	New Zealand	Costa Rica	Lima
Morgan Hill	Imperial Valley	Lijiang	Quindio
San Fernando	Livermore	Cape Mendocino	North Palm Springs
Alaska	Tokachi - Achi	San Salvador	Erzincan
Whittier Narrows	Guatemala	Adak Island	Superstition Hills
Kobe	N. Italy	Chile	Saguenay
Umbria - Marche	Mindanao	Negate	Armenia
Philippines	Miyagi-Ken-Oki	Sent Barbara	Managua
Landers	Seattle	Kushiro-oki	Northern Kentucky
Guam	Tonagawa	Sanriku-Haruka-oki	Alum Rock
Coalinga	Nihon-Kai Chubu	Newcastle	Gorman
Roermond	Izu Ohshima	Montenegro	Bay of Plenty

Table 5 - Earthquakes included in the database.

(c) Experimental results – Many experiments and tests have been performed on nonstructural components, especially on recent years. The main purpose on the majority of these experiments is to determine levels of damage suffered by specific components under ground motions of certain magnitudes.

Again, the experiments included in the database have been classified as drift sensitive and acceleration sensitive. The user must specify, the desired experiment and the desired component. Information included in the experiment data screen includes: name of investigator/s, references, description of the component used, description of the test performed including set-up and results, and photos of the actual test. See Appendix I.

(d) Codes and specifications – Numerous specifications found in building codes regarding the construction and installation of nonstructural components will be available in the database.

(e) Components' photos – Thousands of nonstructural components' photos will be available in the PEER Nonstructural Component Database.

CONCLUSION

Being exposed to a large-scale earthquake engineering research project I realized how important it is for society this type of studies.

This project emphasizes the importance of nonstructural components when trying to minimize economic losses caused by earthquakes. The selection and installation of the proper nonstructural components is vital when designing and building a safe structure. The engineering industry, building owners and contractors will benefit considerably from the information collected and organized in the PEER Nonstructural Components Database.

Large amount of detailed information is included in the database. Significant loss assessment studies will be based on this information also. The outcome of these studies will contribute to the improvement of performance based earthquake engineering.

ACKNOWLEDGEMENTS

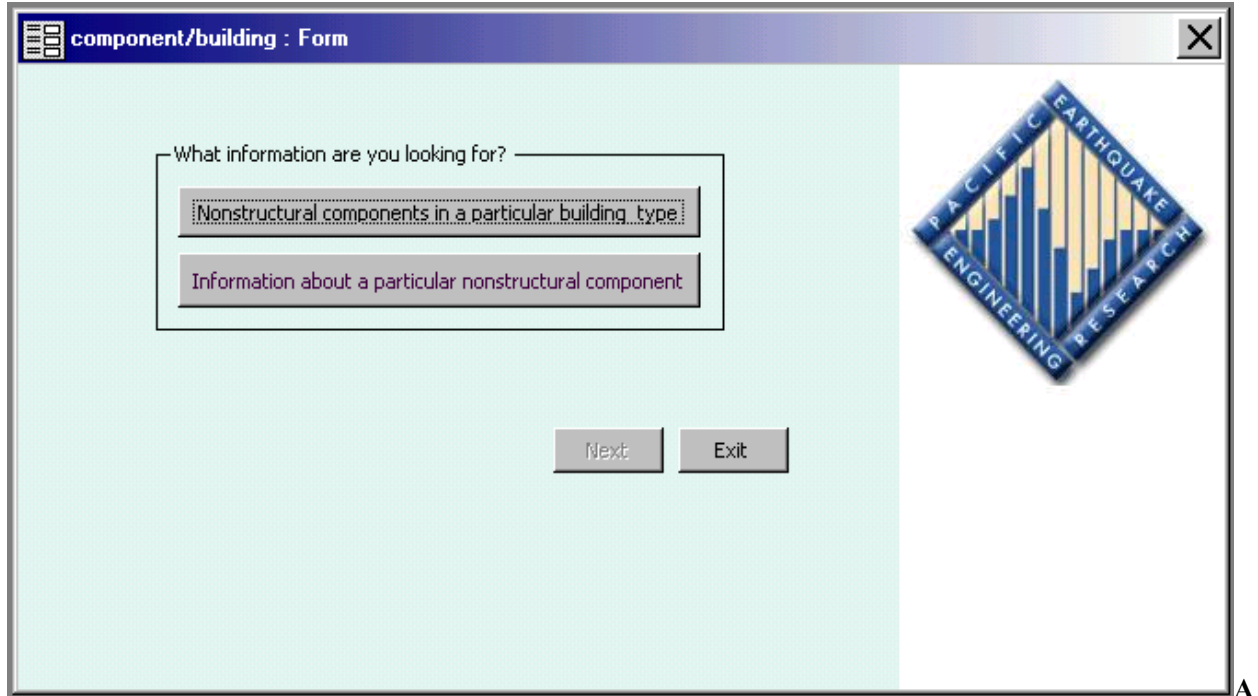
I would like to thank the National Science Foundation and the Pacific Earthquake Engineering Research Center for allowing me to work at Stanford University this past Summer of 2001, as part of the Research Experience for Undergraduates program.

I would like to thank Professor Eduardo Miranda for accepting my help; he never missed an opportunity to teach us about earthquakes and earthquake engineering. Also thanks to the PhD student Shahram Taghavi for his advice, his hard work was a real inspiration. To Mrs. Gina Ring and Professor Pardoen, thanks for such a wonderful program.

REFERENCES

1. Miranda, Eduardo and Taghavi, Shahram, Seismic Performance and Loss Assessment of Nonstructural Components, The John A. Blume Earthquake Engineering Center.
2. Miranda, Eduardo and Taghavi, Shahram, Response Assessment of Non-Structural Building Elements, PEER Project No. 5202000.
3. FEMA '99 Estimated Annualized Earthquake Losses for the United States.
4. USGS National Earthquake Information Center, Earthquakes, Magnitude 7 and Greater, 2001.

APPENDICES



ppendix A – Two main groups of information.

Building Cost Information : Form

Building Types

- Any
- Apartment
- College
- Garage
- Hospital
- Hotel
- Library
- Motel
- Office

What kind of information do you want for the selected building

- Typical components
- Cost per S.F. of the nonstructural component
- Percentage of total cost

Back Next Exit

PACIFIC EARTHQUAKE ENGINEERING RESEARCH

Appendix B – Information about nonstructural components in a particular building.

Exterior Closure		Apartment	1-3 Story
Walls	Face brick with concrete block backup, 88% o		
Exterior Walls	N/A		
Doors	Aluminium an glass		
Windows and Glazed Walls	Aluminium horizontal sliding 12% of wall		
Roofing			
Roof Coverings	Built-up tar and gravel with fashing		
Insulation	Perlite/EPS composite		
Opening and Specialties	N/A		
Interior			
Partitions	Gypsum board and sound deadening board or		
Interior Doors	15% solid core wood, 85% hollow core wood		
Wall Finishes	70% paint, 25% vinyl composition tile, 5% ce		
Floor Finishes	60% carpet, 30% vinyl, 10% ceramic tile		
Ceiling Finishes	Painted gypsum board on resilient channels		
Interior Surface	Painted gypsum board on furring, 80% of wal		
Conveying			
Elevators	One hydraulic passenger elevator		
Special Conveyors	N/A		
Mechanical			
Plumbing	Kitchen, bathroom and service fixtures, suppl		
Fire Protection	Wet pipe sprinkler system		
Heating	Oil fired hot water, baseboard radiation		
Cooling	Chilled water, air cooled condenser system		
Special Systems	N/A		
Electrical			
Lithing and Power	Incandescent fixtures, receptacles, switches,		
Special Electrical	Alarm systems and emergency lighting		
Specialties	Kitchen cabinet		
Special Construc.			
Service and Distribution	600 ampere service, panel board and feeders		

Do you want to look at the cost information of a specific component

Yes No

Select a component

Any

Record: ⏪ ⏩ 1 ⏴ ⏵ ⏶ ⏷ of 3 ⏴ ⏵

Appendix C - Typical nonstructural components.

Exterior Closure		10.23
Walls	Ribbed precast concrete panel	7.45049
Exterior Walls	N/A	0
Doors	Aluminium and glass	1.46369
Windows and Glazed Walls	Aluminium horizontal sliding, 13% of wall	1.32062
Roofing		0.286
Roof Coverings	Built-up tar and gravel with flashing	0.18709
Insulation	Perlite/EPS composite	0.09905
Opening and Specialties	N/A	0
Interior		27.23
Partitions	Gypsum board and sound deadening board or	9.05724
Interior Doors	15% solid core wood, 85% hollow core wood	6.55907
Wall Finishes	70% paint, 25% vinyl composition tile, 5% ce	2.45415
Floor Finishes	60% carpet, 30% vinyl, 10% ceramic tile	4.86428
Ceiling Finishes	Painted gypsum board on resilient channels	3.08144
Interior Surface	Painted gypsum board on furring, 80% of wal	1.21057
Conveying		6.999
Elevators	Four geared passenger elevators	6.99928
Special Conveyors	N/A	0
Mechanical		22.84
Plumbing	Kitchen, bathroom and service fixtures, suppl	10.1027
Fire Protection	Standpipe and wet pipe sprinkler system	2.3441
Heating	Oil fired hot water, baseboard radiation	4.30302
Cooling	Chilled water, air cooled condenser system	6.08585
Special Systems	N/A	0
Electrical		9.574
Lithing and Power	Incandescent fixtures, receptacles, switches,	5.42554
Special Electrical	Alarm systems and emergency lighting	1.80485
Specialties	Kitchen cabinet	2.3441
Special Construc.		1.453
Service and Distribution	4000 ampere service, panel board and feeder	1.45268

Apartment:

City: Year:

Cost Summary Cost per S.F.

Total Structural Cost	\$15.91
Total Nonstructural Cost	\$78.61
Total Cost	\$94.52

Do you want to look at the cost information of a specific component

Yes No

Select a component

Any

Record: 3 of 3

Appendix D - Cost per square foot of the nonstructural component.

Exterior Closure		11.9%
Walls	Face brick with concrete block backup, 88% o	9.9%
Exterior Walls	N/A	0.0%
Doors	Aluminium an glass	0.3%
Windows and Glazed Walls	Aluminium horizontal sliding 12% of wall	1.7%
Roofing		1.8%
Roof Coverings	Built-up tar and gravel with falshing	1.2%
Insulation	Perlite/EPS composite	0.6%
Opening and Specialties	N/A	0.0%
Interior		23.8%
Partitions	Gypsum board and sound deadening board or	3.7%
Interior Doors	15% solid core wood, 85% hollow core wood	6.5%
Wall Finishes	70% paint, 25% vinyl composition tile, 5% ce	2.4%
Floor Finishes	60% carpet, 30% vinyl, 10% ceramic tile	5.9%
Ceiling Finishes	Painted gypsum board on resilient channels	3.5%
Interior Surface	Painted gypsum board on furring, 80% of wal	1.7%
Conveying		3.8%
Elevators	One hydraulic passenger elevator	3.8%
Special Conveyors	N/A	0.0%
Mechanical		27.9%
Plumbing	Kitchen, bathroom and service fixtures, suppl	11.7%
Fire Protection	Wet pipe sprinkler system	2.3%
Heating	Oil fired hot water, baseboard radiation	6.0%
Cooling	Chilled water, air cooled condenser system	7.9%
Special Systems	N/A	0.0%
Electrical		9.2%
Lithing and Power	Incandescent fixtures, receptacles, switches,	6.1%
Special Electrical	Alarm systems and emergency lighting	0.9%
Specialties	Kitchen cabinet	2.3%
Special Construc.		2.1%
Service and Distribution	600 ampere service, panel board and feeders	2.1%

Apartment	1-3 Story
City	Year
Los Angeles	1999

Cost Summary	Cost percentage
Total Structural Cost	19.5%
Total Nonstructural Cost	80.5%
Total Cost	100%

Do you want to look at the cost information of a specific component

Yes No

Select a component

Any

Record: 1 of 3


Appendix E - Percentage of the building's total cost.

component data selection : Form

Please select one of the following

- Cost of Components
- Performance in Previous Earthquakes
- Experimental Results
- Codes and Specification
- Components' Photos

Back Next Exit



appendix F – Information about a particular nonstructural component.


cost/photo : Form

Description: Integrated ceilings, Luminaire, suspended, 5' x 5' modules, 50% lighted

Cost of Material: \$3.88 Unit: Each


Cost of Installation: \$8.65

Total Cost: \$12.53



Back Exit

Record: 23 of 237

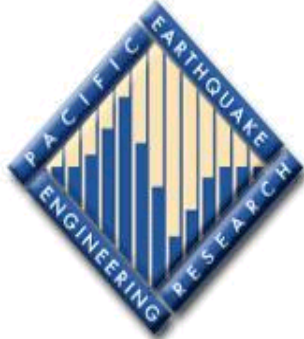


Appendix G – Cost information – photo.

performance/sensitivity : Form

What type of sensitivity are you looking for?

Drift Sensitive
 Acceleration Sensitive
 Both



Appendix H

experiment/result : Form

Investigator: C.P. Pantelides R.A. Behr

Reference: Earthquake Engineering and Structural Dynamics Vol. 23, pp. 211-228, 1994

Component: Windows and Glazed Walls

Description: Annealed monolithic with film, 1/4 in annealed monolithic glass with .10 mm polyethylene

Component Type: Exterior Closure

Drift sensitive
 Acceleration sensitive


Drift 1:	25 mm	Acceleration 1:		Damage % 1:	10 %
Drift 2:	64 mm	Acceleration 2:		Damage % 2:	40 %
Drift 3:	76 mm	Acceleration 3:		Damage % 3:	60 %

Description of damage at level 1: 10 percent fallout of tested specimens

Description of damage at level 2: 40 percent fallout of tested specimens

Description of damage at level 3: 60 percent fallout of tested specimens

Record: 1 of 1



Appendix I - Information about nonstructural components' tests.

<h3>Damage Information</h3> <p>Component</p> <p>Mechanical</p> <p>Fire Protection</p> <p>Description of Damage</p> <p>(sprinkler) no failure in 4" sprinkler lines crossing seismic separation (were installed per NFPA-13 detail).</p> <p>Damage Level at Floor</p> <p>No Damage 7</p> <p>Cost of Repair Unit</p> <p>0</p> <p>Drift</p> <p>0 <input checked="" type="checkbox"/> Drift Sensitive</p> <p>Acceleration</p> <p><input type="checkbox"/> Acceleration Sensitive</p>	<h3>Building Information</h3> <p>Building Name</p> <p>Northridge Hospital Medical Center, Farr Nursing To</p> <p>Building Information</p> <p>Building usage</p> <p>Hospital</p> <p>Location</p> <p>1.6 km from epicenter</p> <p>Station No. Height (Floor)</p> <p>6</p>
<h3>Earthquake Information</h3> <p>Name of Earthquake</p> <p>Northridge</p> <p>Earthquake Magnitude</p> <p>6.7</p> <p>PGA H. PGA V.</p> <p>0.5</p>	<h3>Reference Information</h3> <p>Author</p> <p>Ayres & Ezer Associates, Hillman Biddison and Loew</p> <p>Title</p> <p>NORTHRIDGE EARTHQUAKE HOSPITAL WATER DAMAGE STUDY</p> <p>Office of Statewide Health Planning & Development, California State Department of Health Services</p> <p>Published Year</p> <p>1996</p>

Appendix J – Performance in previous earthquakes.

**Predictive Equations for Soil
Shear-Wave Velocities:
Tri-State Region of Connecticut, New Jersey
and New York**

Gary Neil Nottis
Bucknell University

REU Institution: Lamont-Doherty Earth Observatory of Columbia
University
REU Advisor: Dr. Klaus Jacob

PREDICTIVE EQUATIONS FOR SOIL SHEAR-WAVE VELOCITIES: TRI-STATE REGION OF CONNECTICUT, NEW JERSEY, AND NEW YORK

Gary Neil Nottis
Bucknell University

REU Institution: Lamont-Doherty Earth Observatory of Columbia University
REU Advisor: Dr. Klaus Jacob

Abstract

A study was undertaken to develop equations to predict shear-wave velocities as a function of depth, for Late Wisconsin-substage glacial deposits and Holocene-age alluvium and alluvial fan deposits, in a 31-county study area roughly centered on New York City. Those equations are to be used to develop a more realistic seismic site classes map for input into a Level 2 HAZUS seismic hazard evaluation of the 31-county area. That evaluation is a Year-Three task of the Lamont-Doherty Earth Observatory (LDEO) under a project funded by the Federal Emergency Management Agency (FEMA), and coordinated by the Multidisciplinary Center for Earthquake Engineering. Equations were developed for seven deposits. Moderate correlations were found for depth vs. shear-wave velocities, as a function of deposit type. The equations were used to predict the average shear-wave velocities to be found in the upper 35 feet of the surficial deposits. Those values were compared to measured values for the same depth range in two New Jersey and two New York counties. The predictive equations did a very good job of estimating the average velocities observed. The equations should not be used for older glacial and non-glacial deposits in the study area, as they are likely to under-estimate shear-wave velocities as a function of depth.

Introduction and Objectives

An examination of seismicity in the northeastern United States and southeastern Canada by Ebel (1987), showed that a significant zone of moderate to large historical earthquakes, along with present-day magnitude > 2.0 earthquakes, occupies portions of eastern Connecticut, northern New Jersey, and southern New York. The zone can be defined by a 31-county area roughly centered on New York City. Wheeler and others (2001) note that New York City has experienced two magnitude 5.2 earthquakes. One event occurred on December 18, 1737, and the other took place on August 10, 1884. Both events caused slight to moderate damage. The United States Geological Survey currently estimates that there is a significant (10%) probability that buildings within this area may experience moderate earthquake damage during a 50-year building life (USGS, 2001a, 2001b).

The 12,656 square-mile, 31-county area, also called the Tri-State region, has a population of nearly 21.5 million people (Connecticut Department of Economic and Community Development, 2001a, 2001b; Empire State Development, 2001a, 2001b, 2001c; NJBRC, 2001; NJDOL, 2001; and NYSDED, 2001). Of special importance is New York City,

which is the largest city in the United States. New York City is a regional, national, and global center for culture, finance, industry, media, technology, and transportation. The surrounding counties also have significant centers of industry and technology. Regional and national transportation routes and oil transmission lines pass through the Tri-State region as well.

The Lamont-Doherty Earth Observatory (LDEO), as a member of the New York City Area Consortium for Earthquake Loss Mitigation (NYCEM), is undertaking a study to improve an earthquake loss estimation evaluation performed for the Tri-State region by Nordenson and others (1999). The location of the 31-county study area is shown in Fig. 1. The LDEO study is a Year-Three task of a multi-year study being funded by the Federal Emergency Management Agency (FEMA) and coordinated by the Multidisciplinary Center for Earthquake Engineering Research (MCEER).

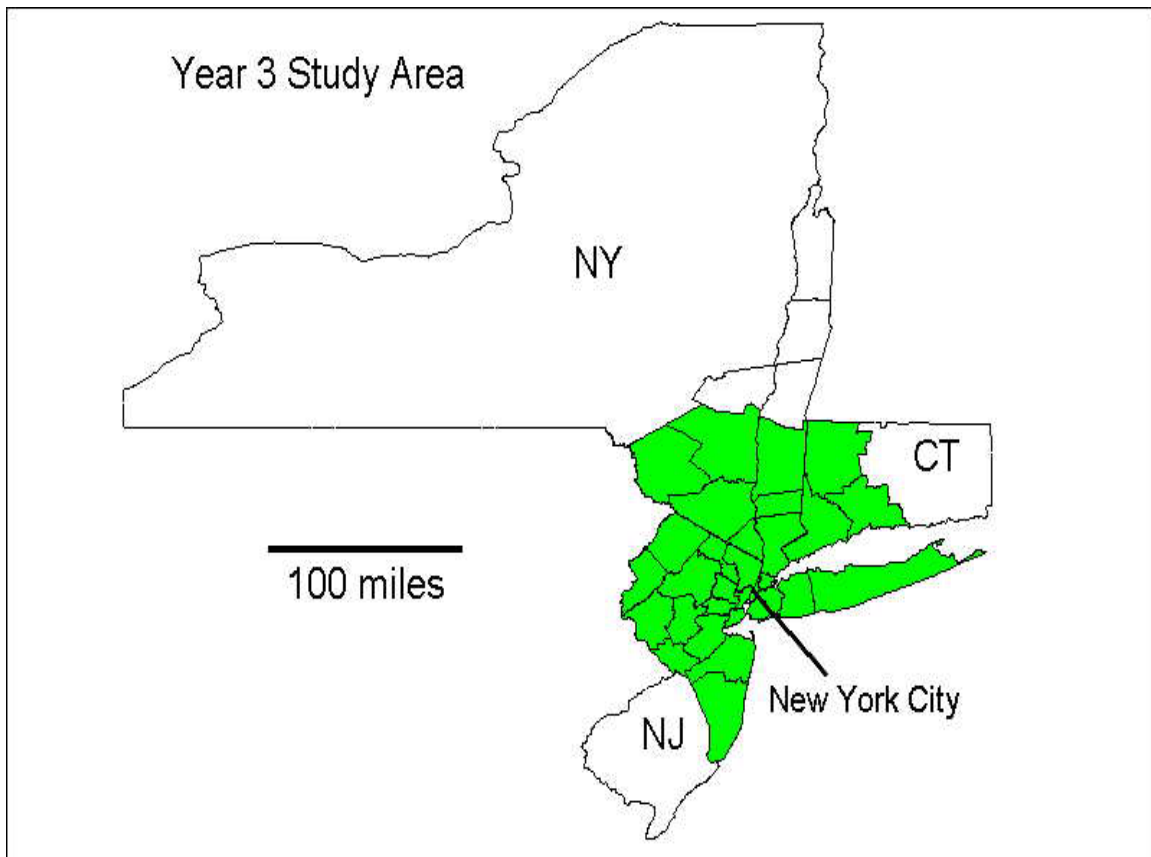


Figure 1. The 31-county Tri-State study area. The study area is highlighted in green (gray shading) and the county boundaries are delimited.

The original study by Nordenson and others (1999) was made using default values in the HAZUS computer program. This is referred to as a Level 1 analysis (Whitman and Lagorio, 2001). A Level 1 analysis assumes that the entire study region has a seismic site class of "D." This means that the average shear-wave velocity of the upper 100 feet of

surficial material, possibly including rock, had a value of 590 - 1,180 feet/second throughout the study area (FEMA, 1998a, 1998b). The LDEO study is to be performed using an improved seismic site classes map that will reflect the known variability in the study areas soil. This will be a Level 2 analysis (Whitman and Lagorio, 2001).

To create a seismic site class map, it is necessary to obtain surficial geology maps, bedrock geology maps, depth-to-bedrock information, down-hole shear-wave velocity profiles, shear-wave profiles from surface seismic studies, and an extensive collection of borehole logs, with geotechnical data, for the entire study area. If shear-wave profiles are not available, then equations that can estimate shear-wave velocity (V_s) as a function of depth and some other parameter (i.e. Standard Penetration Test [SPT] blowcounts), may be used to produce reasonable shear-wave profiles for borehole sites. These data can then be used to produce the required map for HAZUS input. An illustration of the procedure can be found in Jacob (1999).

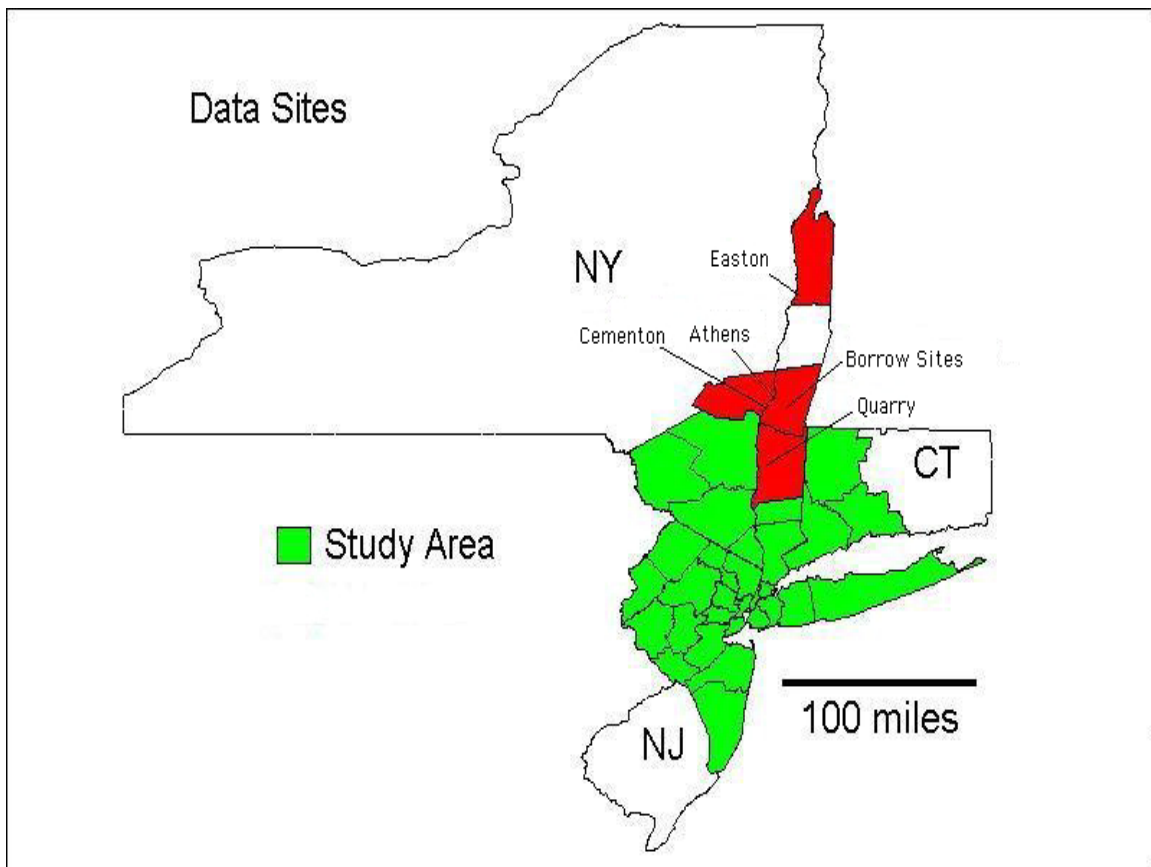


Figure 2. Locations of sites with borehole logs and geotechnical data. The counties containing the sites are highlighted in red (dark gray), and the study area is highlighted in green (gray). The lower-most county in red (dark gray) is Dutchess County, New York. Borehole logs from highway projects within the county were also used in this study.

Time and resource limitations prevented the gathering of extensive information for the Tri-State study area. Digital and paper versions of surficial geology, bedrock geology, and depth-to-bedrock maps were available for the study area, as well as water-well information. A limited collection of over 2,100 borehole logs, many with geotechnical data, for previously proposed nuclear and coal-fired electricity generation plant sites, and highway projects, were available for sites in the mid- to lower Hudson Valley. These sites are within, and north of the study area. The locations of the sites and the counties they lie in are shown in Fig. 2.

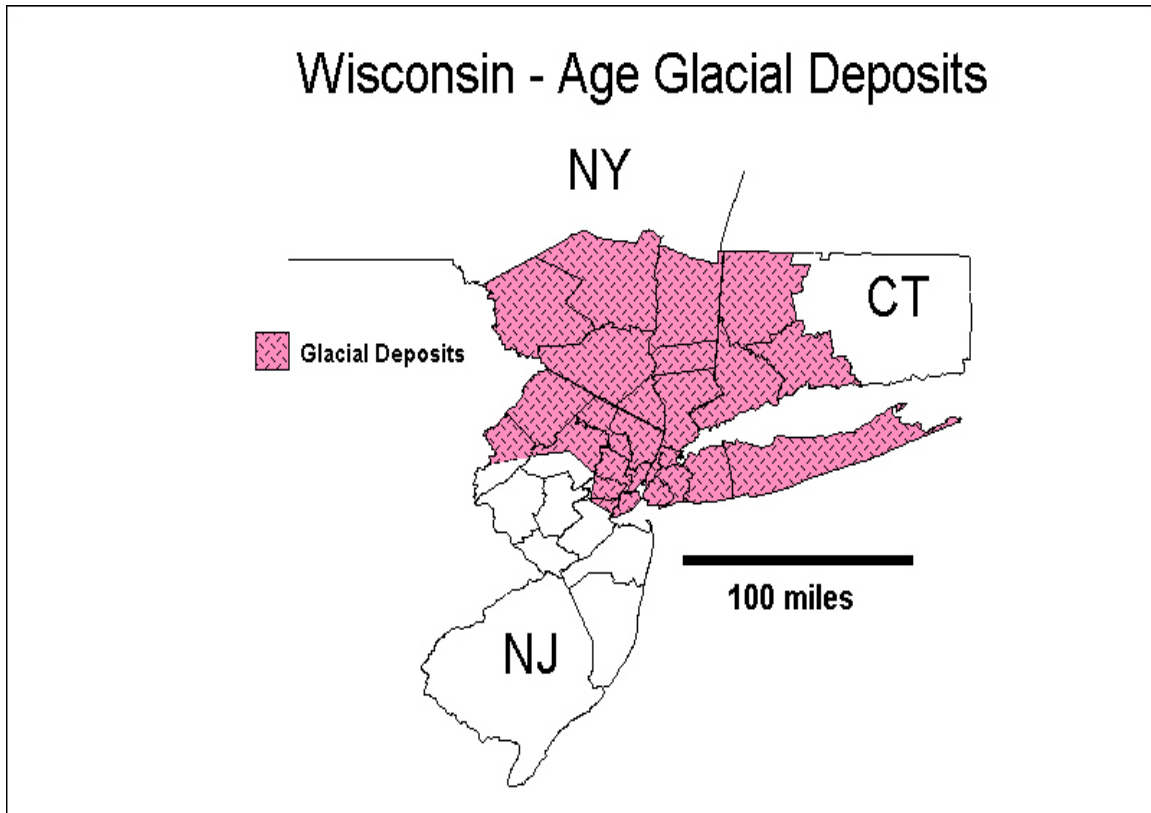


Figure 3. Extent of the Late Wisconsin-substage glacial deposits in the study area. Deposits of Holocene-age are also contained within the extent of the glacial deposits.

The available borehole logs all lie within a portion of the study area which has soils formed from Late Wisconsin-substage (10,000-21,000 year-old) glacial deposits, and some Holocene-age (<10,000 year-old) deposits. These soils cover about 77% of the study area. The extent of the glacial deposits is depicted in Fig. 3. The glacial deposits are laterally and vertically variable. Glacial kames, lake deltas, lake sands, lake silts and clays, outwash, and tills comprise the Wisconsin-age deposits. Contained within the extent of the glacial deposits are areas of Holocene-age alluvium, alluvial fans, and swamp deposits (Cadwell, 1999). Of these, borehole logs were available for seven of these different kinds of deposits. Logs were not available for swamp deposits. The other

soils of the study area are derived from Illinoian (>800,000 years old) glacial deposits, pre-Illinoian deposits of uncertain age, and Coastal Plain deposits (Witte, 1998).

No downhole shear-wave velocity profiles are known for the surficial materials formed from the Late Wisconsin-substage glacial deposits, or the deposits of Holocene-age north of New York City. Some velocity profiles for Holocene-age deposits are available for Manhattan Island (Jacob, 1999). Shear-wave profiles from seismic refraction studies were obtainable for Bergen and Hudson counties in New Jersey, and for Dutchess and Westchester counties in New York (Cadwell and Nottis, 1999; Stanford and others, 1999, 2000). These profiles, however, were insufficient to predict shear-wave velocities to depths of 100 feet, as required for the determination of soil site classes (FEMA, 1998a, 1998b).

In order to generate a seismic site class map for HAZUS analysis, equations would need to be created from the available borehole and geotechnical data. Such equations, which would predicted V_S with depth, usually have two input variables (depth and SPT blowcounts). Those equations tend to have the most accurate correlations (Sykora, 1987). Equations that rely on depth alone to predict V_S are not very accurate. However, if separate equations are developed for each type of surficial deposit, the equations that predict V_S using depth alone, can have accuracies equal to those with more input variables (Sykora, 1987).

Therefore the objective of this portion of the LDEO Year-Three study was to develop equations to estimate shear-wave velocity as a function of depth for:

- Late Wisconsin-substage glacial deposits of the study area, and
- Holocene alluvium and alluvial fan deposits outside of New York City.

The development of equations to estimate shear-wave velocities as a function of depth for the other surficial materials of the study area is beyond the scope of this investigation.

Procedure

Classification of Borehole Geotechnical Data

The available geotechnical data from the boreholes consisted of soil layer designations assigned using the Unified Soil Classification System (USCS), blowcounts at various depths and for each soil layer, depth to water table, unit weights for selected soil layers, and undrained shear strength (S_u) values for selected cohesive (clays, silts, organic clays, etc.) soil layers.

The available blowcounts were generally not obtained from the recommend procedure for obtaining SPT (Standard Penetration Test) blowcounts. SPT blowcounts are to be obtained from counting the number of blows required to drive a standard soil sampler with liners (outside diameter [Do] = 2.0", and inside diameter [Di] = 1.375"), a distance of 12 inches. The sampler is to be driven by a 140-pound hammer free-falling a distance

of 30 inches. Further, the test is to be done in a borehole of about 4 inches in diameter. Blowcounts, however, are usually obtained using a variety of hammer weights, free-fall heights, and sampler sizes (with or without liners).

Lowe and Zaccheo (1975) published a pair of equations and graphs that can be used to convert blowcounts obtained from non-standard tests, to SPT blowcounts for cohesive and cohesionless soils. The blowcounts available for this study were obtained from nine different combinations of hammer weights, free-fall heights and sampler sizes.

Conversion factors were derived from the equations and graphs in Lowe and Zaccheo (1975) to convert the blowcounts from those non-standard tests into SPT blowcounts.

Listings of the conversion factors as a function of general soil type (cohesive or cohesionless) and test parameters are given in Tables 1 and 2.

Table 1.

Conversion factors for obtaining SPT blowcounts from raw blowcounts determined from non-standard tests – Cohesive soils.

Test Parameters	Conversion Factors As A Function Of Blows-Per-Foot					
	< 2	2-4	4-8	8-15	15-30	>30
Dames and Moore, Easton Site, Borings B1-B19. Hammer weight (HW) = 500 lbs., free-fall height (FH) = 18", sampler outside diameter (Do) = 3.5", and sampler inside diameter (Di) = 2.375"	0.92	0.91	0.89	0.85	0.78	0.72
Dames and Moore, Easton Site, Borings B20-B37. HW = 300 lbs., FH = 24", Do = 3.5", and Di = 2.375"	0.88	0.86	0.83	0.78	0.67	0.59
Dames and Moore, Easton Site, Borings B20-B37. HW = 140 lbs., FH = 30", Do = 2.0", and Di = 1.5"	1.05	1.05	1.06	1.08	1.14	1.18
NYSDOT, Dutchess County. HW = 300 lbs., FH = 18", Do = 1.75", and Di = 1.25"	1.15	1.18	1.24	1.31	1.68	1.68
NYSDOT, Dutchess County. HW = 300 lbs., FH = 18", Do = 2.0", and Di = 1.25"	1.03	1.03	1.04	1.05	1.10	1.10
NYSDOT, Dutchess County. HW = 300 lbs., FH = 18", Do = 2.0", and Di = 1.375"	1.06	1.07	1.10	1.12	1.25	1.25
NYSDOT, Dutchess County. HW = 300 lbs., FH = 18", Do = 2.0", and Di = 1.5"	1.11	1.12	1.16	1.26	1.35	1.48
NYSDOT, Dutchess County. HW = 300 lbs., FH = 18", Do = 3.5", and Di = 3.375"	1.32	1.38	1.53	1.69	2.74	2.74
Stone and Webster, Athens, Cementon, and Quarry sites. HW = 140 lbs., FH = 30", Do = 2.0", and Di = 1.5"	1.05	1.05	1.06	1.08	1.14	1.18

Table 2.

Conversion factors for obtaining SPT blowcounts from raw blowcounts determined from non-standard tests – Cohesionless soils.

Test Parameters	Conversion Factors
Dames and Moore, Easton Site, Borings B1-B19. Hammer weight (HW) = 500 lbs., free-fall height (FH) = 18", sampler outside diameter (Do) = 3.5", and sampler inside diameter (Di) = 2.375"	0.52
Dames and Moore, Easton Site, Borings B20-B37. HW = 300 lbs., FH = 24", Do = 3.5", and Di = 2.375"	0.45
Dames and Moore, Easton Site, Borings B20-B37. HW = 140 lbs., FH = 30", Do = 2.0", and Di = 1.5"	1.11
NYSDOT, Dutchess County. HW = 300 lbs., FH = 18", Do = 1.75", and Di = 1.25"	1.64
NYSDOT, Dutchess County. HW = 300 lbs., FH = 18", Do = 2.0", and Di = 1.25"	1.10
NYSDOT, Dutchess County. HW = 300 lbs., FH = 18", Do = 2.0", and Di = 1.375"	1.19
NYSDOT, Dutchess County. HW = 300 lbs., FH = 18", Do = 2.0", and Di = 1.5"	1.33
NYSDOT, Dutchess County. HW = 300 lbs., FH = 18", Do = 3.5", and Di = 3.375"	1.36
Stone and Webster, Athens, Cementon, and Quarry sites. HW = 140 lbs., FH = 30", Do = 2.0", and Di = 1.5"	1.11

Corrections were also made to the blowcounts for the length of the driving rod attached to the sampler, and the diameter of the borehole. These correction factors were obtained from Skempton (1986).

Once the corrections were made to the blowcounts, the rest of the data classification followed the work of Hwang and others (1990). For each kind of cohesionless soil layer present in the borehole logs, unit weights were assigned based on relative density and ranges of SPT blowcounts (N_{SPT}). Those data are presented in Tables 3 and 4. Also, values of the angle of internal friction (ϕ') for cohesionless soils, classified by soil type and relative density, are presented in Table 5. Those values were taken from Hunt (1984). Similarly, the same was done for cohesive soils using soil consistency descriptions and ranges of N_{SPT} . Tables 6 and 7 contain those data.

An equation was developed relating the undrained shear strength (S_u) of cohesive soils to N_{SPT} . The determined equation is;

$$S_u = 77.421 * N_{SPT} \quad (\text{Eq. 1})$$

where the y-intercept was forced through 0, $n = 49$, and $r = 0.71$. This equation was needed for the later shear-wave velocity calculations.

Table 3

Unit weights for cohesionless soils.

USCS Soil Classification	Relative Density Description	Unit Weight (lbs./ft. ³)
ML-GP	Medium Dense to Very Dense	138
SC*	Loose	120
	Medium Dense	125
	Very Dense	130
SM, SP-SM	Very Loose to Loose	120
	Medium Dense	124
	Dense	130
	Very Dense	135
SM-GC	Medium Dense	147
SM-GM	Medium Dense to Dense	139
SP, SW, and SP-SW	Very Loose to Loose	110
	Medium Dense	123
	Dense	140
	Very Dense	155
GC	Medium Dense	135
GM, SM-GM	Medium Dense	138
	Dense	139
	Very Dense	140
GP, GP-GM**	Medium Dense	125
	Dense	135
	Very Dense	140

* These values represent a best estimate based on comparisons between soil values described by Hwang and others (1990) and those observed for the mid-Hudson Valley soils in this study.

** Estimated values based on information provided in Salchert (1995)

Table 4

Relative density descriptions for cohesionless soils.

Density Description	N_{SPT} Range	Relative Density (D_r)
Very Loose	< 4	< 0.15
Loose	4 – 10	0.15 – 0.35
Medium Dense	10 – 30	0.35 – 0.65
Dense	30 – 50	0.65 – 0.85
Very Dense	> 50	0.85 – 1.0

Table 5

Angles of internal friction $\{\phi'\}$ for cohesionless soils.

Soil Classification	Description	ϕ'
GW	Dense	40°
	Medium Dense	36°
	Loose	32°
GP	Dense	38°
	Medium Dense	35°
	Loose	32°
SW	Dense	37°
	Medium Dense	34°
	Loose	30°
SP	Dense	36°
	Medium Dense	33°
	Loose	29°
SM	Dense	35°
	Medium Dense	32°
	Loose	29°

Table 6

Unit weights for cohesive soils.

USCS Soil Classification	Consistency Description	Unit Weight (lbs./ft. ³)
CH	Soft	115
CL, ML-CL	Very Soft to Soft	119
	Medium Stiff	120
	Stiff	122
	Very Stiff	125
GC-CL (Easton Site)	Stiff to Very Hard	143
ML	Very Soft to Soft	113
	Medium Stiff	116
	Stiff	121
	Very Stiff	130
	Hard	150
OH	Very Soft	90
	Soft	95
	Medium Stiff to Stiff	100
	Very Stiff to Hard	110
	Very Hard	115

Table 7

Consistency descriptions for cohesive soils.

Description	N _{SPT} Range
Very Soft	< 2
Soft	2 – 4
Medium Stiff	4 – 8
Stiff	8 – 15
Very Stiff	15 – 30
Hard	30 – 60
Very Hard	> 60

Equations Used To Compute Shear-Wave Velocities

The equations for estimating shear-wave velocity as a function of depth, which are the essential objective of the study, were generated from estimated shear-wave velocities (V_s) computed for soil layers identified on selected borehole logs. To do that, equations were chosen for the initial shear-wave velocity calculations.

Shear-wave velocity (V_s) for a material can be computed using the equation;

$$V_s = (G_o/p)^{0.5} \quad (\text{Eq. 2})$$

Where G_o is the shear modulus, and p is the soil density determined from unit weight. The shear modulus (G_o) is determined differently for cohesive soils and cohesionless soils in this study. Following Hwang and others (1990), the shear modulus (G_o) for cohesive soils was determined using the equation;

$$G_o = 2,500 * S_u \quad (\text{Eq. 3})$$

where S_u is the undrained shear strength of the cohesive soil.

Shear modulus for cohesionless soils were determined using the equation;

$$G_o = 2,500 * T_{\max} \quad (\text{Eq. 4})$$

where T_{\max} is the maximum shear stress of the soil at very small strains. T_{\max} was calculated for this study using the equation developed by Hardin and Drnevich (1972) which is:

$$T_{\max} = (((1+K_o)/2) * \sigma'_v * \sin(\phi') + c' * \cos(\phi'))^2 - ((1-K_o)/2) * \sigma'_v)^{0.5} \quad (\text{Eq. 5})$$

where σ'_v is the effective vertical stress, ϕ' is the angle of internal friction, c' is the apparent soil cohesion, which is essentially zero for cohesionless soils, and K_o is the coefficient of earth pressure at rest. That value was calculated using the equation;

$$K_o = 1 - \sin(\phi') \quad (\text{Eq. 6})$$

as suggested by Hwang and others (1990).

Sykora (1987) notes that shear modulus values obtained for soils from laboratory testing will most likely be less than those measured in-situ. This is because void ratio decreases with time. The decrease in void ratio results in an increase in shear modulus. Thus a correction factor needs to be applied to G_o obtained in the laboratory, in order to obtain a value of G_o closer to those that may be found in-situ. Mesri and others (1990), as cited in Schmertmann (1992), proposed an equation;

$$G_o(\text{aged}) = (1 + [N_G * \log\{\Delta t\}]) * G_o(\text{unaged}) \quad (\text{Eq. 7})$$

where N_G is the % increase in shear modulus, per log cycle of time, and Δt is the age of the sampled soil deposit in days. N_G may have values of 1%-3% for sands, 3%-6% for silts; and 6%-19% for clays.

The glacial deposits from where most of the boreholes and geotechnical data came from, generally have an age of about 13,000 years (Cadwell and Dineen, 1987; Cadwell, 1989).

For this study N_G values of 2%, 5%, and 9% were chosen for the sands, silts, and clays respectively. Gravels will likely have the same values as sands (Schmertmann, 1992). The 9% value for clays was chosen so that the correction factor for shear modulus would be close to the lower limit factor of 1.5 applied by Anderson and Woods (1976). Testing may show that different N_G values may be more appropriate. As a result, the G_o values for gravels and sands, silts, and clays were multiplied by factors of 1.13, 1.27, and 1.6, respectively. This procedure was not carried-out for soil layers that were part of Holocene-age alluvial deposits. No correction factors were applied to the G_o values obtained for those particular soil layers.

Calculation Of Shear-Wave Velocities For Soil Layers

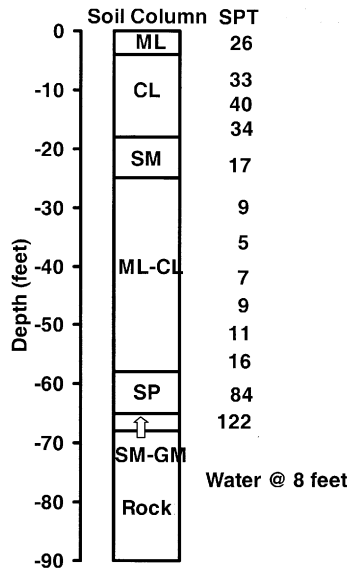
From the available borehole logs for the surficial materials in the study area, at least four representative logs were chosen for each kind of surficial material. Each log was then analyzed, as shown in Fig. 4., with a spreadsheet. Any available geotechnical data on the log was used. This is illustrated in Fig. 4 with values shown in regular type. Any other values were estimated from the equations and tables given in this report, as appropriate. These are shown in Figure 4 as values in italics. The values of effective vertical stress (σ_v') were determined from an Excel spreadsheet presented in Wolff (1995).

Determination Of Equations For Estimating Shear-Wave Velocity As A Function Of Depth

An average shear-wave velocity was determined for each soil layer of a soil column. The mid-point depth of each soil layer was also found. The equations for estimating shear-wave velocities as a function of depth were generated using Excel spreadsheet functions. For each type of surficial deposit, the average shear-wave velocities and mid-point depths of each soil layer from all of the representative logs were used as inputs in the calculation. A power curve was fitted to the data. This process was done for the representative logs of each surficial material.

Results

The shear-wave velocity equations determined in this study are given in Table 8. The data points used to determine each equation and the best-fit power curves and equations are shown in Figs. 5-11. Overall, the power curves have moderate correlations between depth and shear-wave velocity. These results are in keeping with previous ones reported by Sykora (1987). The equation for glacial lake silts and clays was determined with a subset of data and guidance from the shear-wave values reported in Cadwell and Nottis (1999). The data scatter was otherwise too great to obtain an equation for that surficial deposit.



SPT	Unit Weight (lbs/ft ³)	Su (lbs/ft ²)	σ_v' (lbs/ft ²)	ϕ' (degrees)	V _s (ft/sec)
26	120	8,753			3,373
33	119	2,407			1,776
40	124	5,325			2,588
34	131	2,480			1,719
17	117		1,901	32	851
9	120	657			924
5	120	365			689
7	120	2,000			1,614
9	120	657			924
11	120	802			1,021
16	120	1,167			1,232
84	125		4,175	36	1,237
122	135		4,488	40	1,231

Figure 4. Schematic illustration of the velocity computation procedure. Regular type indicates observed data value. Values in italics indicate that they were derived from estimative equations and look-up tables such as those presented above.

Table 8

Predictive equations for shear-wave velocity as a function of depth for surficial materials of the lower Hudson Valley, New York.

Surficial Material	No. of Borings	No. of Data Points	Predictive Equation*	r**	Recommended Depth Range for Equation (feet)
Alluvium and Alluvial Fans	6	22	$V_s = 329.11 * D^{0.2739}$	0.59	0 – 50
Glacial Kames	4	10	$V_s = 133.27 * D^{0.676}$	0.92	0 – 60
Glacial Lake Delta	4	10	$V_s = 642.01 * D^{0.0342}$	0.10	0 – 30
Glacial Lake Sands	5	17	$V_s = 362.48 * D^{0.3134}$	0.51	0 – 50
Glacial Lake Silts and Clays	8	28	$V_s = 619.81 * D^{0.1561}$	----	0 – 100
Glacial Outwash Sand and Gravel	8	37	$V_s = 368.59 * D^{0.2541}$	0.53	0 – 100
Glacial Till	7	28	$V_s = 557.13 * D^{0.3004}$	0.55	0 – 100

* D = Depth in feet, and V_s = Shear-wave velocity in feet/second

** r = correlation coefficient. No value is listed if equation was determined with only a subset of available data points.

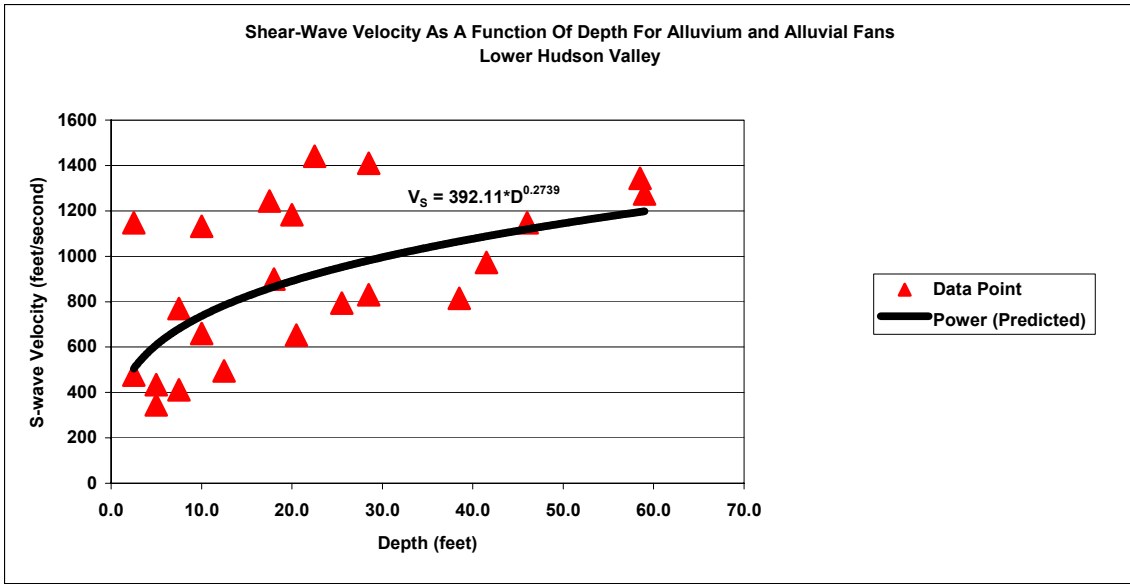


Figure 5. Shear-wave velocity as a function of depth for Holocene-age alluvium and alluvial fans of the lower Hudson Valley.

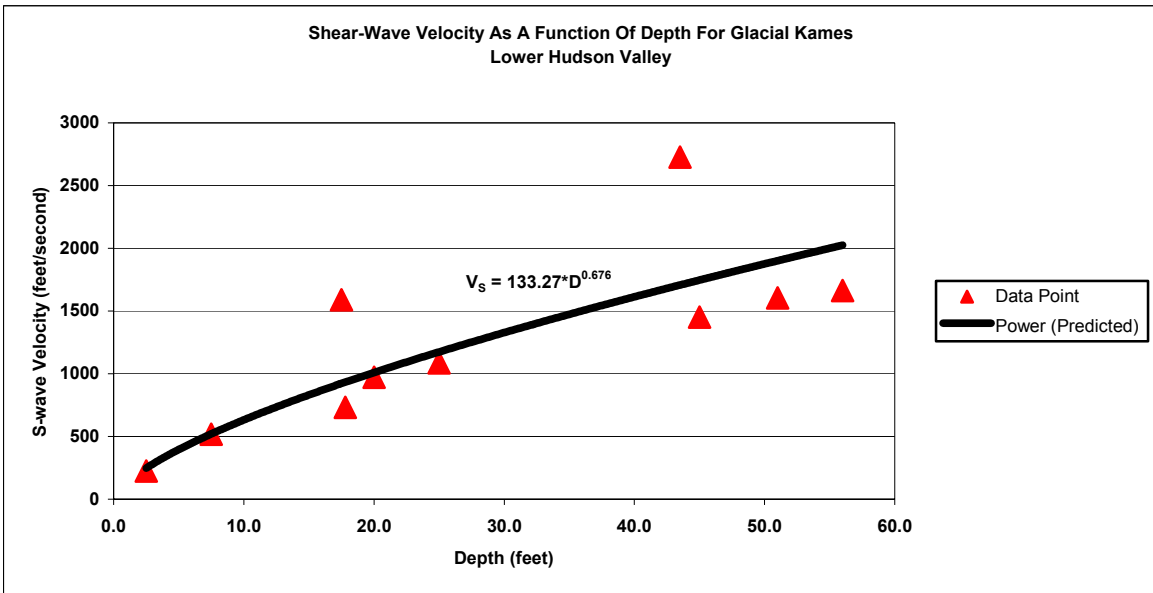


Figure 6. Shear-wave velocity as a function of depth for Late Wisconsin-substage glacial kames in the lower Hudson Valley.

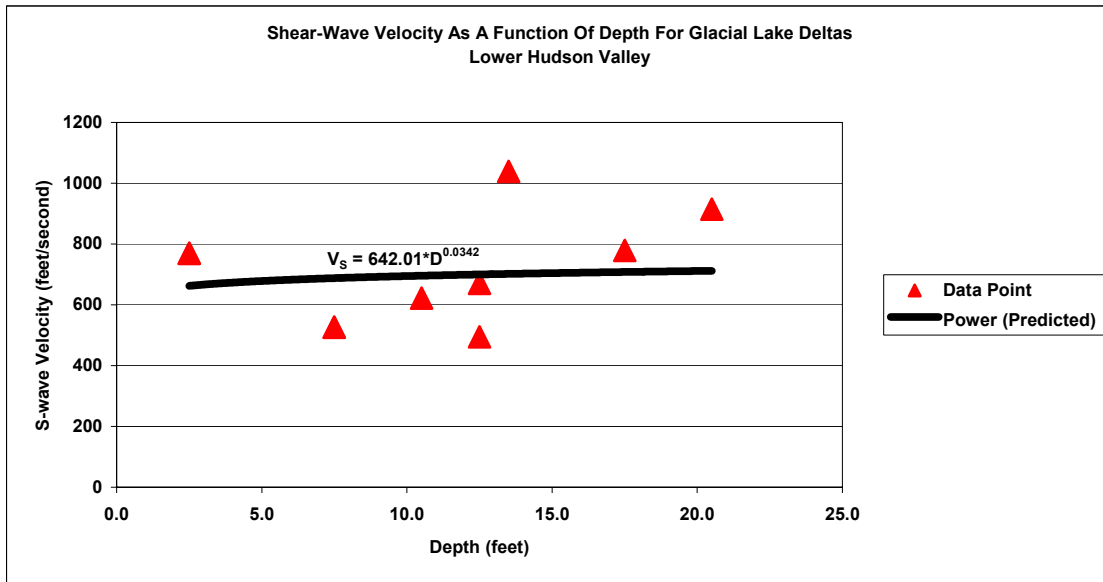


Figure 7. Shear-wave velocity as a function of depth for Late Wisconsin-substage glacial lake deltas in the lower Hudson Valley.

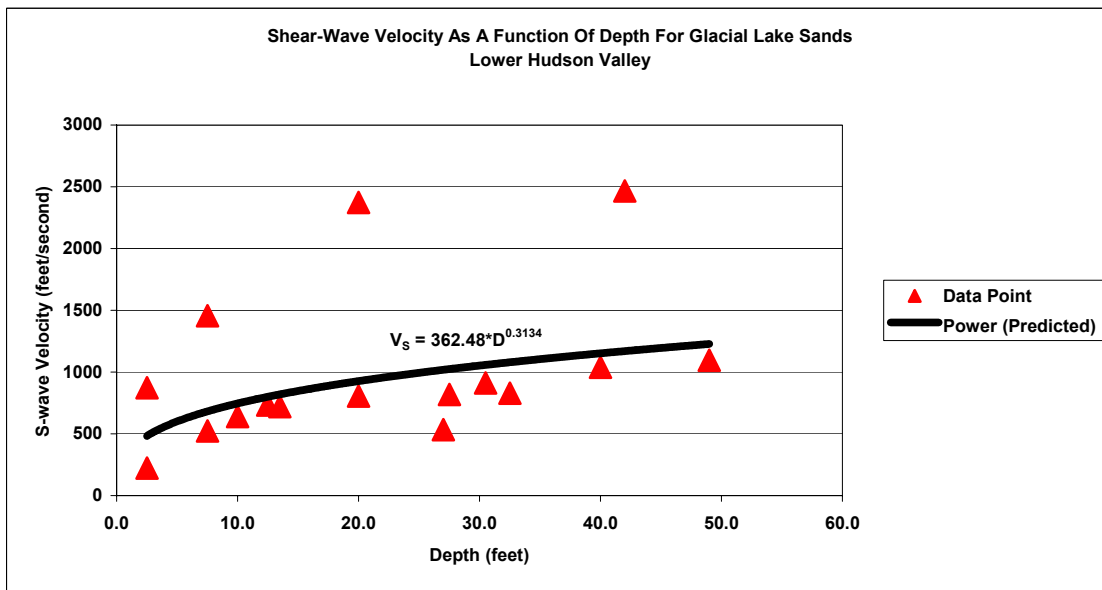


Figure 8. Shear-wave velocity as a function of depth for Late Wisconsin-substage glacial lake sands in the lower Hudson Valley

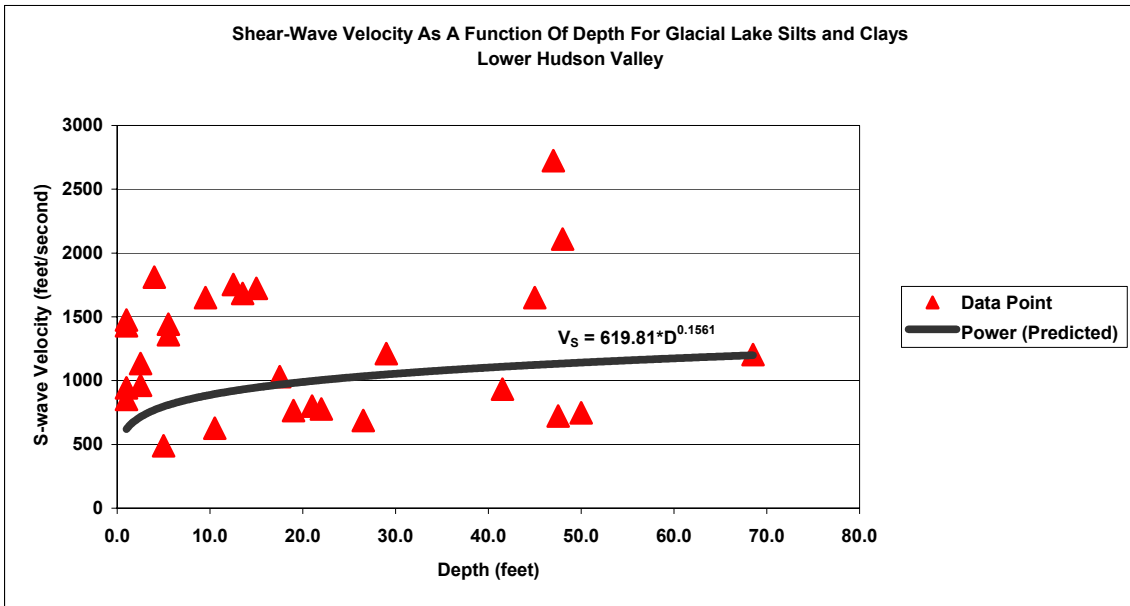


Figure 9. Shear-wave velocity as a function of depth for Late Wisconsin-substage glacial lake silts and clays in the lower Hudson Valley

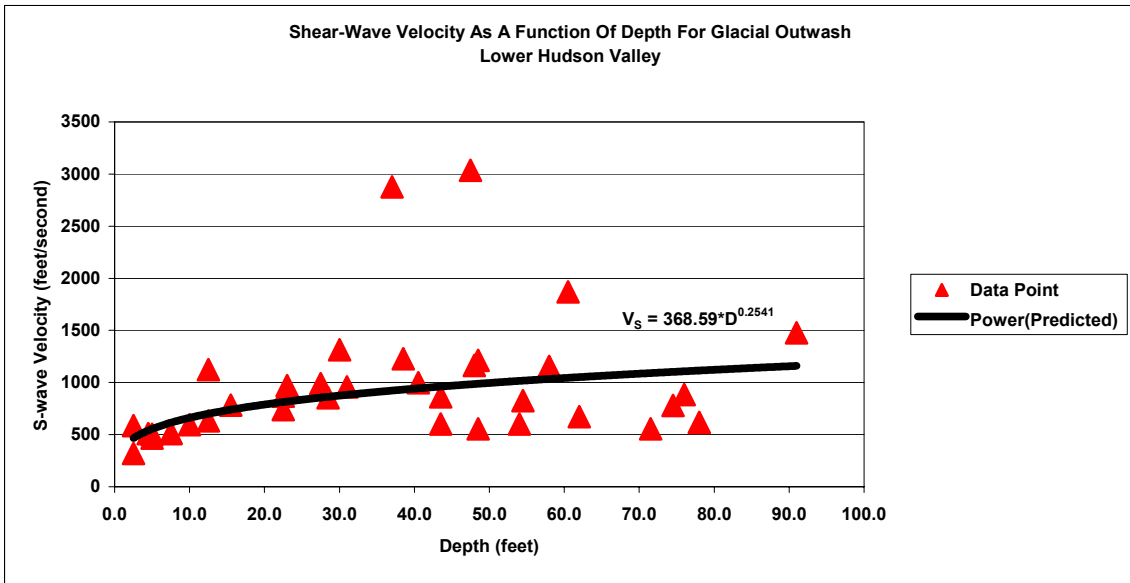


Figure 10. Shear-wave velocity as a function of depth for Late Wisconsin-substage glacial outwash in the lower Hudson Valley

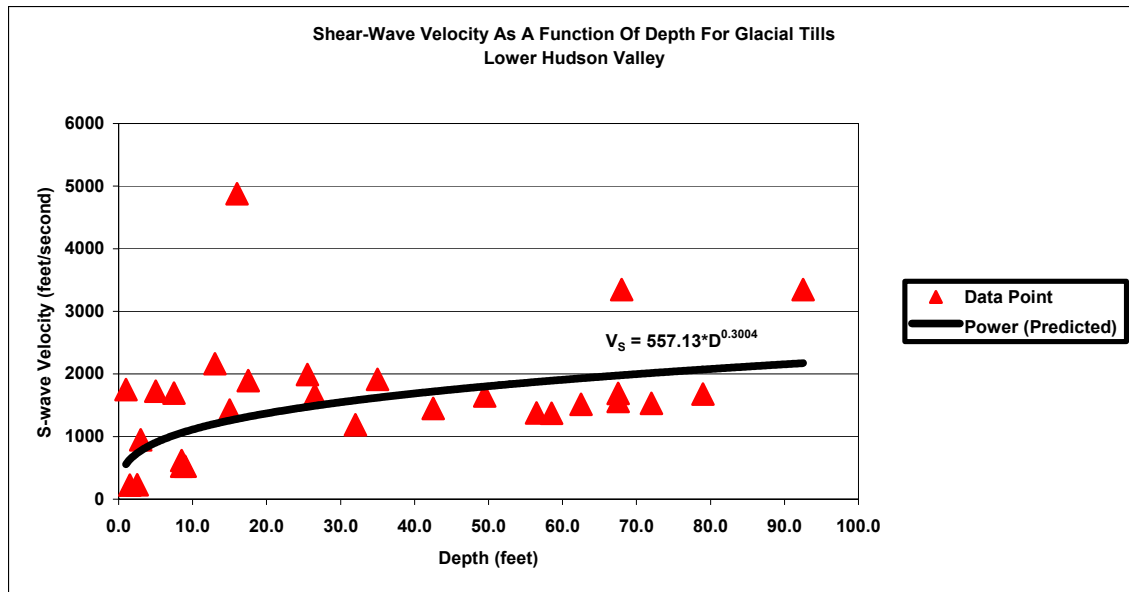


Figure 11. Shear-wave velocity as a function of depth for Late Wisconsin-substage glacial tillis in the lower Hudson Valley

Applicability Of Predictive Equations To The Study Area Deposits

To test the applicability of the determined equations, they were compared against measured shear-wave velocity profiles from Bergen and Hudson counties in New Jersey (Stanford and others, 1999; Stanford and others, 2000), and from Dutchess and Westchester counties in New York (Cadwell and Nottis, 1999). Fig. 12 depicts the locations of those counties.

The measured shear-wave values reported in Cadwell and Nottis (1999) and Stanford and others (1999, 2000) represent average velocities for the upper approximately 35 feet of a surficial deposit. Thus, for comparisons with the equations, average shear-wave velocities were calculated for the upper 35 feet of a surficial deposit. A tabulation of the comparisons is given in Table 9. The comparisons suggest that the predictive equations do a very good job of estimating shear-wave velocities as a function of depth.

It must be emphasized that the developed equations are applicable only to the Holocene-age and Late Wisconsin-substage deposits of the study area. The glacial and non-glacial deposits of the rest of the study area in central New Jersey should have velocities significantly greater than those materials studies here. Void ratios have had a longer time to decrease (800,000 years for Illinoian glacial deposits vs. 13,000 for the Late Wisconsin substage deposits). Thus, shear modulus (G_o) values, soil unit weights, and subsequent shear-wave velocities should be higher. The predictive equations for shear-wave velocities as a function of depth should give under-estimates for those older deposits.

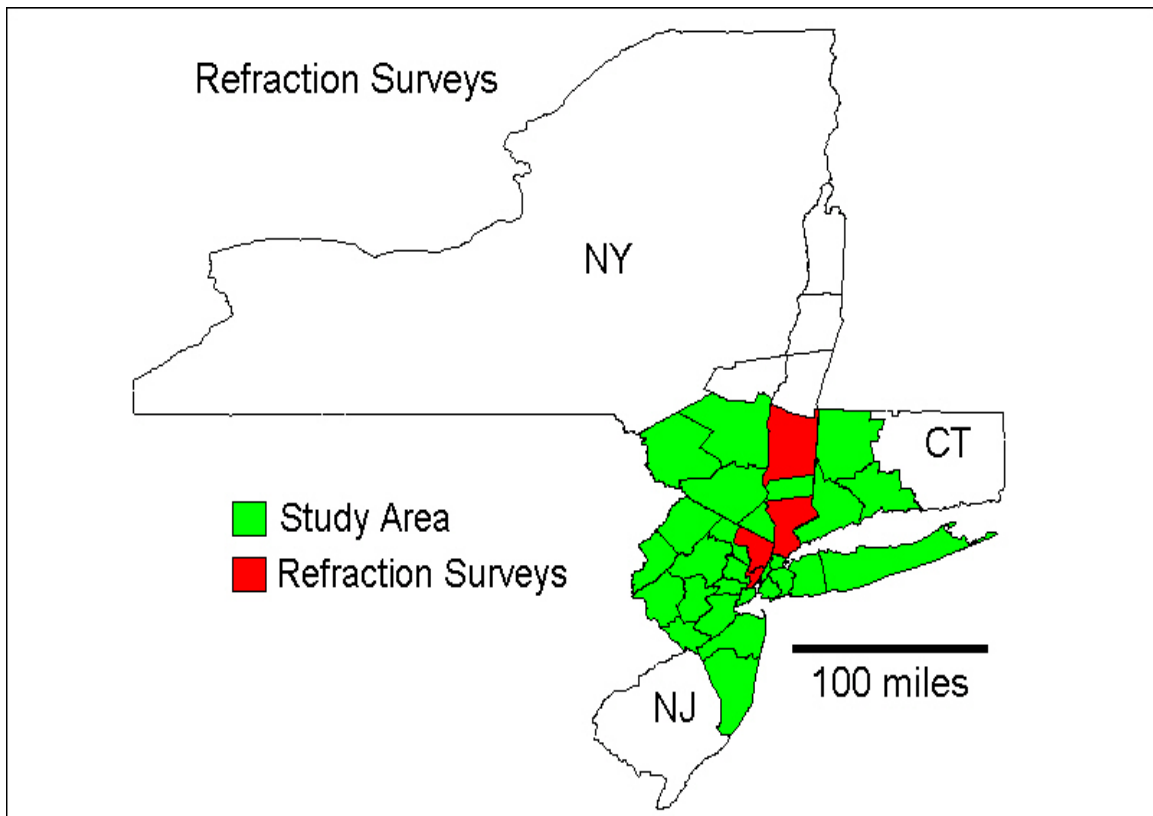


Figure 13. Counties within the study area where seismic refraction surveys were conducted to determine shear-wave velocities in surficial deposits.

Table 9

Comparisons of predicted shear-wave velocities for the upper 35 feet of a surficial material with measured values.

Surficial Material	Predicted Shear-Wave Velocity (ft./sec.)	Measured Shear-Wave Velocities (ft./sec.)	
		New Jersey Counties	New York Counties
Alluvium and Alluvial fans	819	809-1,214	358-1,433
Glacial kames	882		269-1,460
Glacial lake sands	846	916-925	269-833
Glacial lake silts and clays	953	826-925	269-1,532
Glacial outwash	729		489-2,296
Glacial tills	1,253	1,013-2,109	358-2,614

Conclusions

The methodology employed resulted in predictive equations, which, when compared to shallow (<35 feet) measured shear-wave velocity profiles from counties covering a large portion of the Tri-State study area, appear to be applicable to the Late Wisconsin-substage glacial deposits and to the Holocene-age alluvium and alluvial fan deposits. These equations may be used for the current LDEO Year-Three task. Because of known vertical and lateral variability of the surficial deposits examined in this study, use of the equations for more intensive loss estimation projects (Level 3 -- see Whitman and Lagorio, 2001) is not recommended. Further, the determined equations are probably not applicable to the older glacial and non-glacial deposits noted in the southern portion of the study area. Those deposits are likely to have higher velocities due to older age and subsequent void space reduction. Thus, the predictive equations are likely to underestimate shear-wave velocities as a function of depth for those older deposits.

Acknowledgements

I would like to thank my wife and family for their patience and support during the REU internship. Further, I would like to thank Dr. Klaus Jacob of the Lamont-Doherty Earth Observatory and Andrea Dargush of the Multidisciplinary Center for Earthquake Engineering for the opportunity of participating in the internship. Funding for this internship was generously provided by the National Science Foundation Research Experiences for Undergraduates Program, EEC-9701471.

References

- Anderson, D.G.; and Woods, R.D., "Time-dependent increase in shear modulus of clay," *Journal of the Geotechnical Engineering Division, ASCE*, Vol. 102, No. 5, 1976, pp. 525-537.
- Cadwell, D.H., editor, *Surficial Geologic Map of New York: Lower Hudson Sheet, 1:250,000*, New York State Museum - Geological Survey, Map and Chart Series 40_, 1989.
- Cadwell, D.H.; Dineen, R.J., editors, *Surficial Geologic Map of New York: Hudson-Mohawk Sheet, 1:250,000*, New York State Museum - Geological Survey, Map and Chart Series 40_, 1987.
- Cadwell, D.H.; and Nottis, G.N., *Seismic Hazard Assessment, Westchester County, New York*, Submitted to the New York State Emergency Management Office, 1999.
- Connecticut Department of Economic and Community Development, "2000 Census Connecticut County Populations." Available from <http://www.state.ct.us/ecd/research/ceis/population/census2000county.htm>; Internet; accessed 24, November 2001(a).
- Connecticut Department of Economic and Community Development, "CEIS Population, Land Area, and Density by Location." Available from <http://www.state.ct.us/ecd/research/ceis/population/landarea.htm>; Internet; accessed 24, November 2001(b).
- Ebel, J.E., "The seismicity of the northeastern United States," in K.H. Jacob, editor, *Proceedings from the Symposium on Seismic Hazards, Ground Motion, Soil Liquefaction and Engineering Practice in Eastern North America*, National Center for Earthquake Engineering Research, Technical Report NCEER-87-0025, 1987, pp.178-188.
- Empire State Development, "Long Island Region." Available from http://www.empire.state.ny.us/region_longisland.htm; Internet; accessed 10, October 2001(a).

- Empire State Development, "Mid-Hudson Region." Available from http://www.empire.state.ny.us/region_midhudson.htm; Internet; accessed 10, October 2001(b).
- Empire State Development, "New York City Region." Available from http://www.empire.state.ny.us/region_nyc.htm; Internet; accessed 10, October 2001(c).
- FEMA (Federal Emergency Management Agency), *1977 Edition: NEHRP Recommended Provisions for Seismic Regulation for New Buildings, Part 1 – Provisions*, FEMA #302, Washington, DC, 1998(a).
- FEMA (Federal Emergency Management Agency), *1977 Edition: NEHRP Recommended Provisions for Seismic Regulation for New Buildings, Part 2 – Commentary*, FEMA #303, Washington, DC, 1998(b).
- Hardin, B.O.; and Drnevich, V.P., "Shear modulus and damping in soils: Design equations and curves," *Journal of the Soil Mechanics and Foundations Division, ASCE*, Vol. 98, No. SM7, pp. 667-692.
- Hwang, H.; Lee, C.S.; and Ng, K.W., *Soil Effects On Earthquake Ground Motions In The Memphis Area*, National Center for Earthquake Engineering Research, Technical Report NCEER-90-0029, 1990.
- Jacob, K.H., *Site Conditions Effecting Earthquake Loss Estimates for New York City*, First Year (April 1, 1998 to March 31, 1999) Technical Report submitted to MCEER, 1999.
- Lowe, John III; and Zaccheo, P.F., "Subsurface Exploration and Sampling," in H.F Winterkorn and H.-Y. Fang, editors, *Foundation Engineering Handbook*, Van Nostrand Reinhold Company, New York, 1975.
- Mesri, G.; Feng, T.W.; and Benak, J.M., "Postdensification penetration resistance of clean sands," *Journal of Geotechnical Engineering, ASCE*, Vol. 116, No. 7, 1990, pp. 1095-1115.
- NJBRC (New Jersey Business Resource Center), "New Jersey Counties & Land Area." Available from <http://www.njbrc.com/counties.htm>; Internet; accessed 24, November 2001.
- NJDOL (New Jersey Department of Labor), "Total Resident Population, New Jersey Counties: 1980, 1990, and 2000." Available from <http://www.wnjp.in.state.nj.us/OneStopCar...rket Information/lmi25/appres/cntypop.htm>; Internet; accessed 24, November 2001.
- NYSDED (New York State Department of Economic Development). "Table 1: Total Population Change for New York Counties, 1999 to 2000." Available from <http://www.empire.state.ny.us/nysdc/ftp/census2000/pl94/ctytab1.pdf>; Internet; accessed 24, November 2001.
- Nordenson, G.; Deodatis, G.; Tantala, M.; and Kumpf, A., *Earthquake Loss Estimation Study for the New York City Area*, First Year (May 1, 1998 to April 30, 1999) Technical Report submitted to MCEER, 1999.
- Salchert, P., *Region 8 Geotechnical Design Manual, Volume I*, New York State Department of Transportation, Region 8 Office, Poughkeepsie, New York, 1995.
- Schmertmann, J.H., "The mechanical aging of soils," *Journal of Geotechnical Engineering, ASCE*, Vol. 117, No. 9, 1991, pp. 1288-1330.
- Skempton, A.W., "Standard penetration test procedures and the effects in sands of overburden pressure, relative density, particle size, ageing and overconsolidation," *Geotechnique*, Vol. 36, No. 3, 1986, pp. 425-447.
- Stanford, S.D.; Prostas, R.S.; Hall, D.W.; and Walder, J.S., *Earthquake Loss Estimation Study for Hudson County, New Jersey: Geologic Component*, Final Report submitted to the New Jersey State Police, Office of Emergency Management, 1999.
- Stanford, S.D.; Prostas, R.S.; Hall, D.W.; and Walder, J.S., *Earthquake Loss Estimation Study for Bergen County, New Jersey: Geologic Component*, Final Report submitted to the New Jersey State Police, Office of Emergency Management, 2000.

- Sykora, D.W., *Examination Of Existing Shear Wave Velocity And Shear Modulus Correlations In Soils*. Department of the Army, Waterways Experiment Station, Miscellaneous Paper GL-87-22, 1987.
- USGS (United States Geological Survey), "Peak Acceleration (%g) with 10% Probability of Exceedance in 50 Years (site: NEHRP B-C boundary) - June 1996." Available from <http://geohazard.cr.usgs.gov/eq/hazmaps/050pga.pdf>; Internet; accessed 24, November 2001(a).
- USGS (United States Geological Survey), "Peak Acceleration (%g) with 2% Probability of Exceedance in 50 Years (site: NEHRP B-C boundary) - June 1996." Available from <http://geohazard.cr.usgs.gov/eq/hazmaps/250pga.pdf>; Internet; accessed 24, November 2001(b).
- Wheeler, R.L.; Trevor, N.K.; Tarr, A.C; and Crone, A.J., *Earthquakes In and Near the Northeastern United States, 1:1,500,000*, United States Geological Survey, Geologic Investigation Series I-2737, 2001.
- Whitman, R.V.; and Lagorio, H.J., "The FEMA-NIBS Methodology For Earthquake Loss Estimation." Available from <http://www.fema.gov/hazus/hazus4a.htm>; Internet; accessed 5, August 2001.
- Witte, R.W., *Glacial Sediment and the Ice Age in New Jersey*, New Jersey Geological Survey Information Circular IC98-1, 1998.
- Wolff, T.F., *Spreadsheet Applications in Geotechnical Engineering*, PWS Publishing Company, New York, 1995.

Simulating Highway Network Performance in an Earthquake's Aftermath

Michal J. Orlikowski
Princeton University

Hosted at the University of Southern California
Advised by Professor Masanobu Shinozuka

SIMULATING HIGHWAY NETWORK PERFORMANCE IN AN EARTHQUAKE'S AFTERMATH

Michal J. Orlikowski

Princeton University

Hosted at the University of Southern California

Advised by Professor Masanobu Shinozuka

ABSTRACT

The study related here develops a model for the simulation of highway transportation systems' response after an earthquake. Highway systems are examined at component and network levels of analysis to facilitate the study. A synthesis of structural engineering, transportation engineering, seismology, and network analysis is used to produce the model. Importantly, a comprehensive system performance index, "Drivers' Delay," is discussed. Furthermore, repair efforts are simulated so as to produce a complete history of post earthquake system performance. This report closes with a case study testing the model on the Los Angeles Metropolitan Area Highway Transportation System.

INTRODUCTION

The maintenance of an operative transportation system is of paramount importance to the functionality of countless societal institutions. The negative consequences of natural disasters on these systems can disrupt an entire region's way of life. It is critical that some projections be made to assess these systems' post-disaster performance, so as to provide insights on how to mitigate the possible effects.

The October 17, 1989 Loma Prieta Earthquake made the possible negative effects of seismic events on highway transportation systems startlingly apparent. The earthquake's damage to many major commuter and commercial routes caused serious disruptions to the region's immediate post-disaster emergency response, as well as its economy in the long term. This event and others in recent history, (for instance, Northridge, 1994 and Kobe, 1995), have inspired the pursuit of methods for analyzing post-earthquake traffic patterns and highway system response.

This study's purpose is to extend previous research by discussing and developing models for the assessment of highway system performance following a severe earthquake. It relies most

heavily upon the previous research presented by Chang, Shinozuka, and Moore, (2000), as well as Shinozuka, Shiraki, and Kameda (2000). Here, a model is developed to determine immediate post-earthquake system performance, and how that performance improves with time as a result of repair efforts. The end result is a model that can be used to simulate the entire history of system performance from the time of the event until the system is fully repaired. Further, the cumulative data can be used to develop risk curves for an entire highway transportation system. Thus, the groundwork is laid for a simulation tool assessing the indirect losses caused by an earthquake's damage to highway infrastructure.

The method implemented here is a synthesis of structural engineering, transportation engineering, and earthquake engineering. The model is developed by combining component fragility curves, traffic network analyses, repair models, and earthquake scenarios/PGA distributions to develop a comprehensive measure of system performance. Upon discussing the details of the model itself, this report closes with a case study simulating the Los Angeles highway transportation network.

METHODOLOGY

Highway System: Assessing Structural Component Damage

Highway transportation systems are comprised of numerous structural components that are at risk in an earthquake. Roadway pavements, foundations, embankments, tunnels, retaining walls, and bridges are all susceptible to damage caused by ground shaking. For the sake of making this analysis possible, bridges/overpasses are the only structures considered. This decision is made for a variety of reasons; most importantly, the fact that the availability of detailed bridge location data and empirically determined fragility data permits the probabilistic determination of damage based on spatial peak ground acceleration (PGA) distributions. For the

purpose of simulation, every bridge in an examined study region is considered an independent structure. Thus, the determination of the degree of damage to each bridge can be treated as a discrete experiment.

In simulation, the method for assigning the damage suffered by a bridge when subjected to some arbitrary PGA relies on the use of fragility curves. A fragility curve is a cumulative distribution function of the probability of exceeding a certain state of damage versus some measure of ground motion intensity (ordinarily, PGA). Its form is classically assumed to be two-parameter lognormal:

$$F(a) = \Phi \left[\frac{\ln\left(\frac{a}{c}\right)}{\zeta} \right] \quad (1)$$

Here, $F(\mathbf{a})$ is the fragility curve, \mathbf{a} is the PGA, \mathbf{c} is the median, ζ is the log standard deviation, and Φ is the standard normal distribution function. The empirical determination of the curve's form is based on damage records. Using records from past earthquakes, estimators for the parameters \mathbf{c} and ζ can be determined by the maximum likelihood method, as documented in Shinozuka, Feng, et al. (2000).

For the model discussed here, the fragility curves determined by Shinozuka, Feng, et al. (2000) are utilized. They are developed using data from the 1994 Northridge earthquake. The values of the calculated parameter estimators are shown in Table 1. The curves used are those for the case in which all bridges are assumed to have a statistically homogenous vulnerability to earthquake damage. (This is a necessary assumption for this study's sake, but is not necessarily reflective of reality as parameters such as bridge skew and number of spans can make certain bridges more vulnerable than others). The specified four curves separate five damage states, as designated by CalTrans (California Department of Transportation) engineers: no damage, minor

damage, moderate damage, major damage, and collapse. This is illustrated in Figure 1. These damage states are based on qualitative observations made by engineers assessing the post earthquake damage. It is possible that the data collected and the determined curves are specific to this region.

Table 1. Fragility Curve Parameters.

Damage State	Median	Log Standard Deviation
Minor	0.83	0.82
Moderate	1.07	0.82
Major	1.76	0.82
Collapse	3.96	0.82

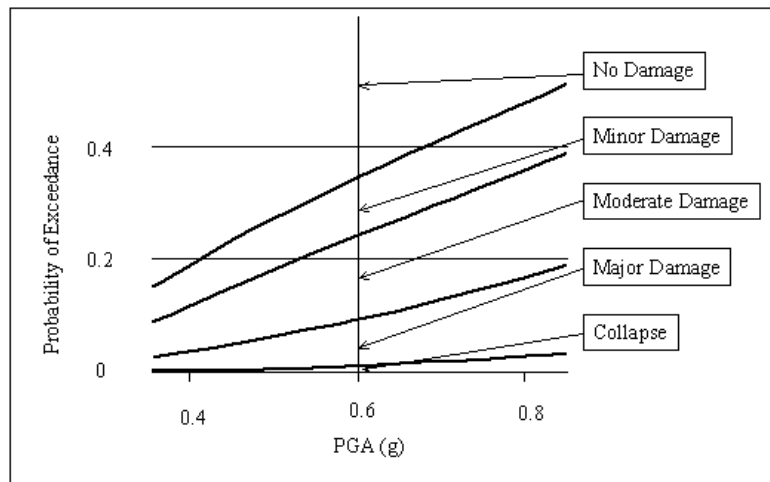


Figure 1. Fragility curve illustration adapted from Shiraki, (2000).

Using these fragility curves, as well as detailed location data of each bridge in a study region, and a spatial PGA distribution, it is possible to perform a Monte Carlo simulation to estimate the damage to each bridge in the event of an earthquake. Coupling the bridge location data with the spatial PGA distribution for a scenario earthquake provides the PGA at each bridge's location. Thus, each bridge's probability of exceeding each of the damage states can also be determined, using the fragility curves. This is where the Monte Carlo method becomes necessary. In the Monte Carlo simulation, a random number generator is used to produce values, (with uniform probability of occurrence), between 0 and 1. For some arbitrary bridge, if the random value is greater than its probability of exceeding minor damage, it is considered to have

no damage. The bridge has minor damage if the random number is between its probability of exceeding minor damage and its probability of exceeding moderate damage, etc. This method is more intuitively grasped by examining Figure 1. For each bridge, the PGA at its location is known. Using the random number generator to provide a value between 0 and 1, the point with x equal to the PGA value, and y equal to the random number is examined. The damage state is assigned based on the region of the chart in which the point rests. This procedure is repeated for all bridges in the study region, with a different random value used for each one. Thus, a probabilistic method is used to simulate each bridge's damage in a scenario earthquake.

Upon determining the damage suffered by all bridges in the region, they are each assigned a Bridge Damage Index value, (BDI), based upon their damage state. This is done to change the qualitative measure of "damage state" to a quantitative value for use in later calculations. The values used here are chosen with respect to those suggested in Chang, Shinozuka, and Moore, (2000). Table 2 lists the conversions. Thus, the damage for each bridge is determined, and quantified for a simulated earthquake.

Table 2. Bridge Damage Indices by Damage State.

Damage State	BDI
No Damage	0
Minor	0.1
Moderate	0.3
Major	0.75
Collapse	1

Highway System: Assessing Network Damage

Having rigorously investigated the simulation of component damage in a scenario earthquake, it is important to note that the impacts on the highway system are not only based on the direct structural damages caused, but also the way in which the functionality of the system is affected as a whole. In order to give proper treatment to this fact, a network analysis must be performed for the system. The highway system of a study region can be examined as a network

consisting of nodes and links. Nodes are defined as points where a highway/freeway either intersects another section of highway/freeway, or a boundary of the study region. Links are defined as the sections of highway/freeway between the nodes. Notably, bridges are located *along* the links- that is, there may be many bridges on the link connecting two nodes. Given these definitions, it is possible to develop a measure for the damage suffered by each *link* in the event of an earthquake. Using the previously determined Bridge Damage Indices for each bridge along a link, a Link Damage Index, (LDI), can be calculated:

$$LDI = \sqrt{\sum_{j=1}^N (BDI_j)^2} \quad (2)$$

This value is calculated separately for each link in a network, using the bridges on that link. (The index *j* in the summation refers only to bridges on the link in question). Given the determined values for each link, changes in capacity and free flow speed for automobiles can be determined based on Shinozuka, Shiraki, and Kameda (2000). This is documented in Table 3.

Table 3. Capacities and Free Flow Speeds by Link Damage Index.

Damage State	LDI	Capacity	Free Flow Speed
No Damage	LDI < 0.5	100%	100%
Minor Damage	0.5 LDI < 1.0	100%	75%
Moderate Damage	1.0 LDI < 1.5	75%	50%
Major Damage	1.5 LDI	50%	50%

The free flow speed for a link is based upon its speed limit, which is estimated as 65 miles per hour on freeways, and 35 miles per hour on highways. This is done for simplicity's sake, and can be adjusted for regional differences. Likewise, the practical capacities for freeway and highway links are simplistically defined as 2500 and 1000 passenger car units per hour, respectively.

Calculating a Comprehensive System Performance Index: Driver's Delay

In order to have some idea of the network's performance as a whole after an earthquake, a comprehensive index of performance must be determined. Following the method documented

by Shinozuka, Shiraki, and Kameda (2000), the index used here is the “Drivers’ Delay.” This is defined as the increase in total daily travel time for all commuters and commercial vehicles caused by earthquake induced delays. Essentially, it is the difference between the total daily travel time for all network travelers on the damaged network, and that on the original undamaged network.

$$TT = \sum_a x_a t_a(x_a) \quad (3)$$

$$Delay = \sum_a x'_a t'_a(x'_a) - \sum_a x_a t_a(x_a) \quad (4)$$

Equation 3 exhibits the calculation of the total daily travel time for all network users, in hours per day; x_a is the flow on link **a** (in Passenger Car Units per day), and t_a is the travel time on link **a** (in hours per Passenger Car Unit). Thus, the product of the two yields the total daily travel time for all network travelers on link **a**. The summation over all the links yields the total daily travel time on the entire network. Equation 4 exhibits the calculation of the Drivers’ Delay. The notation in Equation 4 is the same as that in Equation 3, with the exception that the primed variables denote the case of the damaged network, and the unprimed variables refer to the original undamaged network. Notice that “Drivers’ Delay,” when calculated this way, has units of hours per day. In order to get a total “Driver’s Delay” with units of hours, this expression must be integrated over all the days that a delay persists.

The travel time on a link is calculated by utilizing a link performance function developed by the United States Bureau of Public Roads:

$$t_a = t_a^0 \left[1 + \alpha \left(\frac{x_a}{C_a} \right)^\beta \right] \quad (5)$$

Here, t_a , the travel time per Passenger Car Unit on link **a**, is given as a function of: t_a^0 , the travel time at zero flow on the link (this is simply the link’s length divided by the speed limit); x_a , the

flow on the link (in Passenger Car Units per day); C_a , the practical capacity of the link (in Passenger Car Units per day- a time unit change from the practical capacities defined previously); and α and β , which are variable parameters. Ordinarily, (and in this study), $\alpha=0.15$ and $\beta=4.0$. It is important to note that this empirically derived expression asserts that the travel time on a link carrying 100% of capacity is 15% greater than the free flow time.

Determining the flow on each link depends on the availability of origin-destination data. Given the difficulty of collecting this variety of data, (as it requires a survey), it is fairly rare, and almost certainly does not come in the exact form necessary. An interesting method of converting extensive origin-destination data to a useable form for a defined network is documented in Shinozuka, Shiraki, and Kameda (2000). This method relies upon a conversion by Thiessen function, using GIS software. Upon producing useable origin-destination data, the flow between links must be solved using an equilibrium analysis. That analysis is an important step in developing a model for a region, but is not examined in this study. For the purpose of this simulation, it is assumed that the flow data is available.

Using the methods discussed here, it is possible to develop a rudimentary measure of a system's performance as a network given any state of damage to its components (bridges).

Determining the Effects of Repair Efforts

Earlier, it was noted that the calculated value of Drivers' Delay was actually in units of hours per day, and it would be necessary to integrate the delay over the time that it persists to have a measurement of the total delay. Notably, the Drivers' Delay is not constant over the time it persists. Repair efforts improve the state of damage of the network, thus decreasing Drivers' Delay with time. It is necessary to account for bridge repair efforts to further model a highway system's post earthquake response. Unfortunately, this is fairly difficult, as there exists little data on the processes by which repair is conducted, and little documentation on the priorities

selected by the engineers involved in the operation. Highway repair is conducted at the best judgment of the people involved; despite being effective, this process is not easily modeled. Nonetheless, an attempt is made for this simulation.

Given the lack of information in this situation, the repair efforts are modeled using the cumulative uniform distribution over time, with different functions modeling the probability of repair for each state of damage. Essentially, a family of four linear functions models the probabilities that bridges in any one of the states of damage will be repaired to the no damage state before some arbitrary day. This is illustrated in Figure 2, with the functions used for the case study related later in this report.

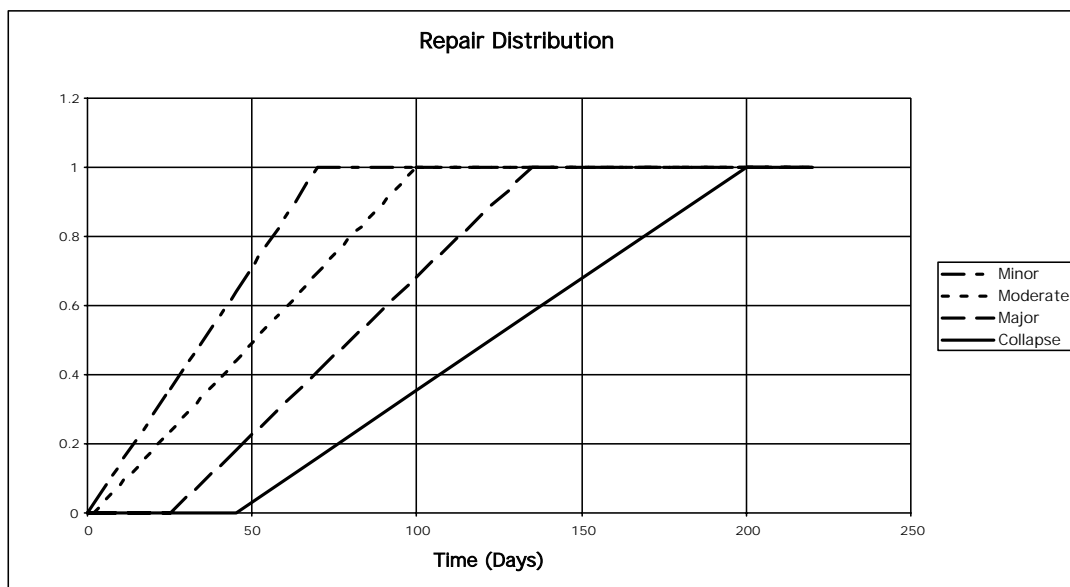


Figure 2. Functions used to model repair processes by Monte Carlo simulation.

Notice that the functions do not necessarily assume that all bridges have the potential to start being repaired on Day 0, nor do they assume that the slopes, (daily probabilities of repair in the non-cumulative distribution), are the same. The choice of the parameters of the optimistic and pessimistic repair scenarios, (essentially, the first and last possible days a bridge of a given damage state can be repaired), are left to the best judgment of those developing the model. It is important to note that there exist numerous different ways that the repair of the system could

have been probabilistically modeled. For instance, link flow data could have been used to estimate the priorities for bridge repair. The method used here is chosen for a pair of reasons: first, because there seems to exist a correlation between the damage state of a bridge and the amount of time for a repair contract to be awarded, and second, for simplicity in simulation.

The repair process is simulated by another use of the Monte Carlo technique. Day 0 represents the day of the earthquake- when the system has the greatest extent of damage. The data available includes the damage state of each bridge, as well as the link damage indices and the Drivers' Delay. The bridge damage data is the relevant information for performing the repair simulation. Considering some arbitrary amount of time after the event, one can perform a Monte Carlo simulation just as before with the repair distributions to determine if each bridge is repaired. This is done by considering each bridge one at a time. Based on the bridge's damage state, the time since the event, and the appropriate repair function for the damage state, one can use a random number generator to decide if the bridge is repaired. (If the random value falls above the function for the given time since the event, it is not repaired; if it falls beneath the function, it is repaired). In this simulation, a repaired bridge shifts from its previous damage state directly to the no damage state, and its record is modified to reflect that change. This process is then repeated for every bridge in the study region. The result is a system with an entirely different state of damage. Link damage Indices and the Drivers' Delay must be recalculated to reflect the change in the system. This method is then iterated, (increasing the time since the event with each step), until every bridge in the network is repaired. (Thus, returning the system to the undamaged state). The final result is a time history of the Drivers' Delays for each step in the iteration from Day 0 until the system is fully repaired. This provides an approximation for the variation of Drivers' Delay with time, and thus completes the simulation of a highway system's post-earthquake response.

Developing a Risk Measure

Given the possibility of performing multiple simulations for a study region, measures of risk for the spatially distributed highway system can be developed using the methods introduced in Chang, Shinozuka, and Moore (2000). By utilizing a number of earthquake scenarios, and calculating their probabilities of exceedance, risk curves can be produced for the system in question. A risk curve is a plot of the probability of exceeding a certain hazard level versus a measure of damage (in this case, Drivers' Delay). A set of these is produced in the case study related later in this report.

CASE STUDY: LOS ANGELES METROPOLITAN AREA HIGHWAY SYSTEM

Study Region: Area, Components, and Network

The study region for the case study simulation is the Los Angeles highway transportation system. The examined area is restricted to Los Angeles and Orange Counties, as illustrated in Figure 3. This region is selected for numerous reasons. First, it is an area with a large risk for earthquake related damage. Second, there exists a wealth of knowledge on past earthquakes as well as the geological properties of the area. Thirdly, detailed highway maps exist, accurately documenting the locations of bridges and overpasses. Lastly, this region is chosen because of the availability of survey origin-destination data collected in 1991. All of these factors combined make this region ideal for a case study simulation.

The region contains 2727 bridges susceptible to damage. The network consists of 118 nodes connected by 185 links. The links are distinguished by their type of road- freeway, or highway. Figure 4 illustrates the network. The flow on the network is based upon the available 1991 origin-destination survey data, as developed by Shinozuka, Shiraki, and Kameda (2000).

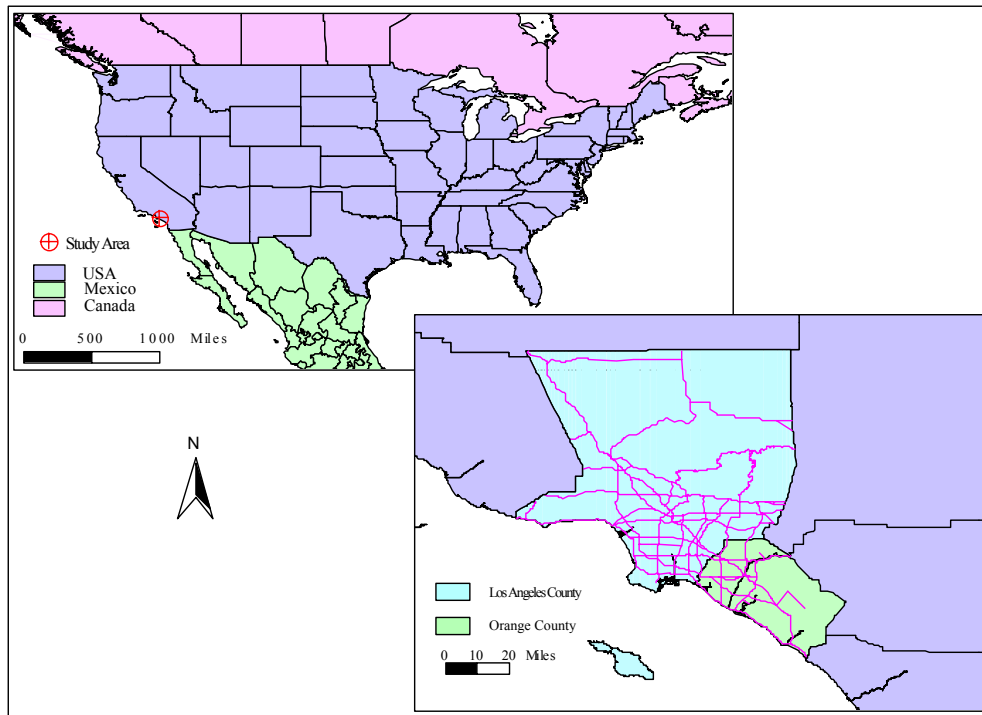


Figure 3. Study Region, adapted from Shiraki, (2000).

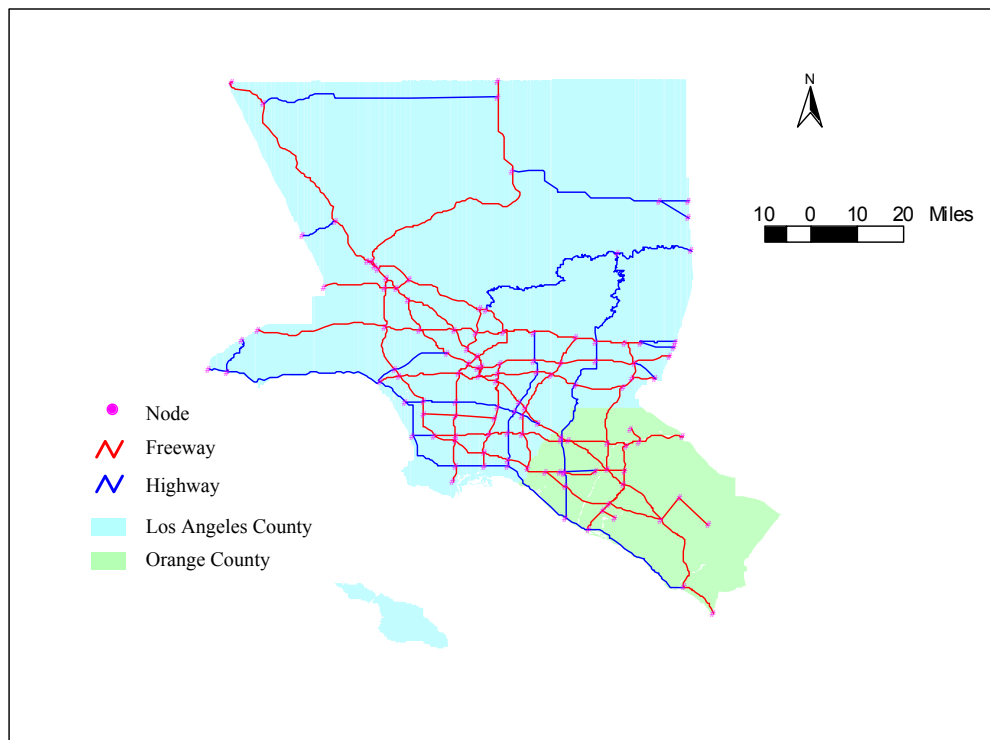


Figure 4. Highway Network, adapted from Shiraki, (2000).

Scenario Earthquakes

For this case study, a set of 47 earthquake scenarios is considered, consistent with Chang, Shinozuka, and Moore (2000). The spatial PGA distributions for the selected event scenarios are modeled using the Early Post Earthquake Damage Assessment Tool, (EPEDAT), software, developed at the University of Southern California and described in Eguchi et al. (1997). A representative PGA distribution is displayed in Figure 5.

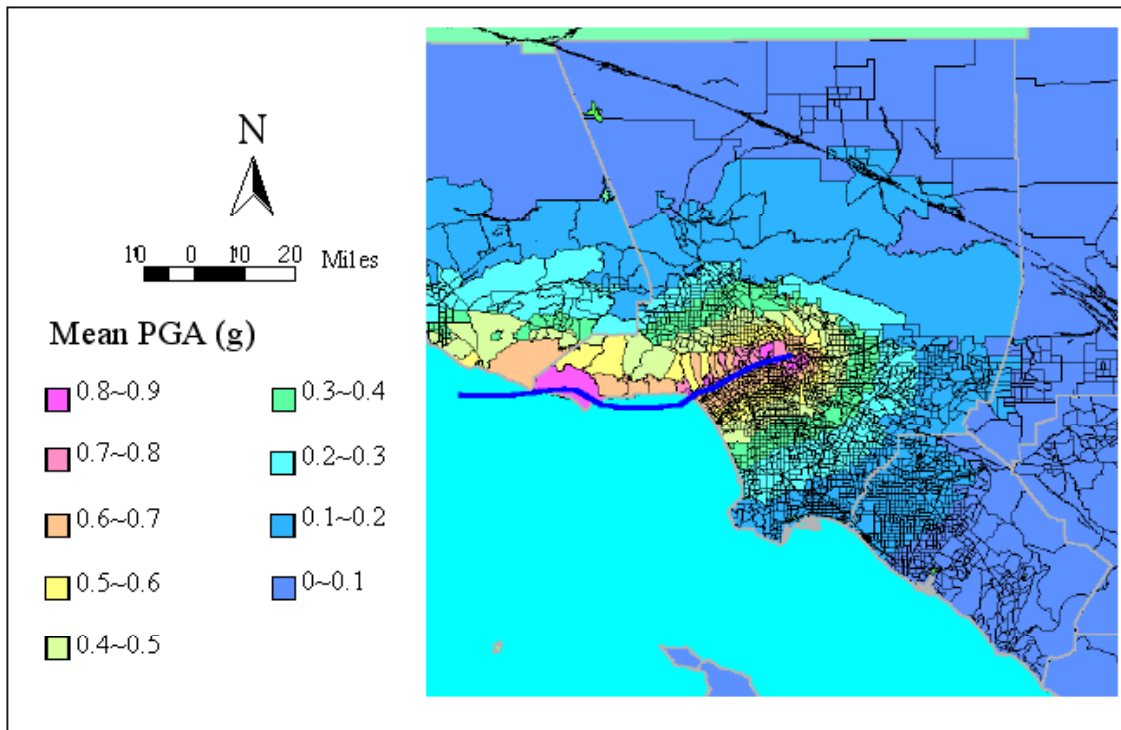


Figure 5. PGA distribution for M 7.3 Malibu Coast Scenario, adapted from Shiraki, (2000).

Logistics of the Simulation

This simulation is conducted by executing ten runs for each of the 47 earthquake scenarios considered. The Drivers' Delay results are then averaged for the purpose of offsetting the variability inherent in the implementations of the Monte Carlo method. The resulting data from each scenario's simulation includes: the damage caused to the network by the earthquake, the resulting Drivers' Delay, and the variation of the Drivers' Delay with time after the event.

Using the Drivers' Delay data, and the calculated probabilities of exceedance for each scenario event, risk curves are then developed for the system.

Results:

The results are summarized in the following figures. Figure 6 illustrates an example variation of Drivers' Delay with time after an earthquake event by exhibiting the values for the second scenario considered (a Magnitude 7.3 earthquake on the Malibu Coast fault, with PGA distribution illustrated in Figure 5). Figure 7 plots the system risk curves for the Drivers' Delay on Days 0, 28, and 84. Though there exists a good deal of noise in the Day 84 curve, it is apparent that the probability for exceeding large Drivers' Delays is virtually eliminated by 12 weeks after an event. Finally, Figure 8 displays a cumulative risk curve. This is the situation in which the daily Drivers' Delays for each scenario are summed to produce a *total* Drivers' Delay for the period of time over which damage persists.

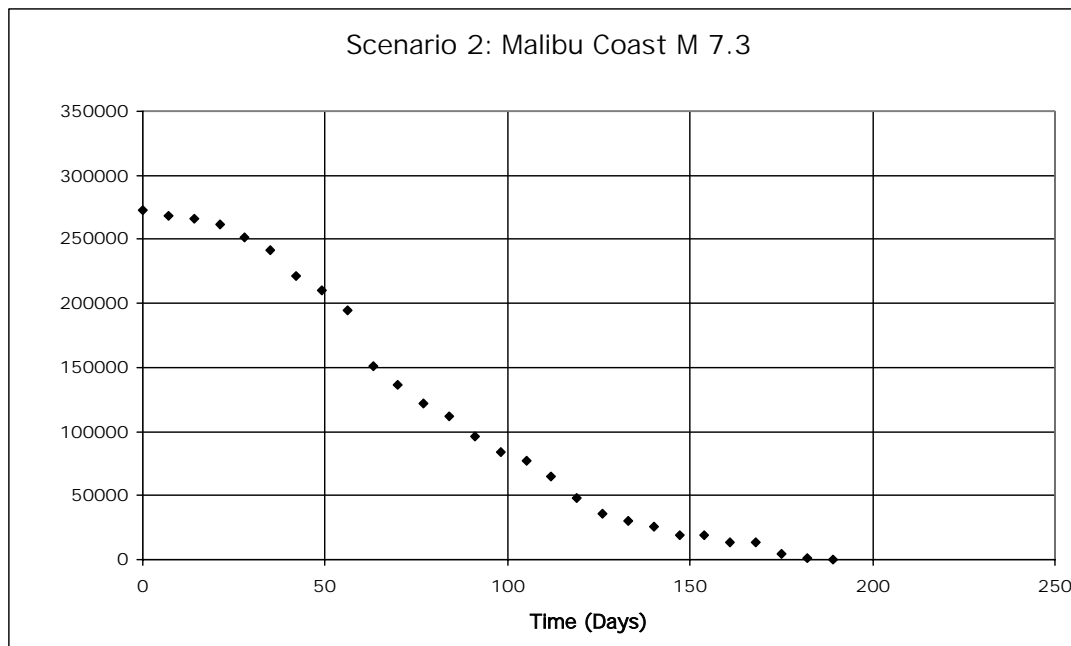


Figure 6. Variation of Drivers' Delay with time after the event.

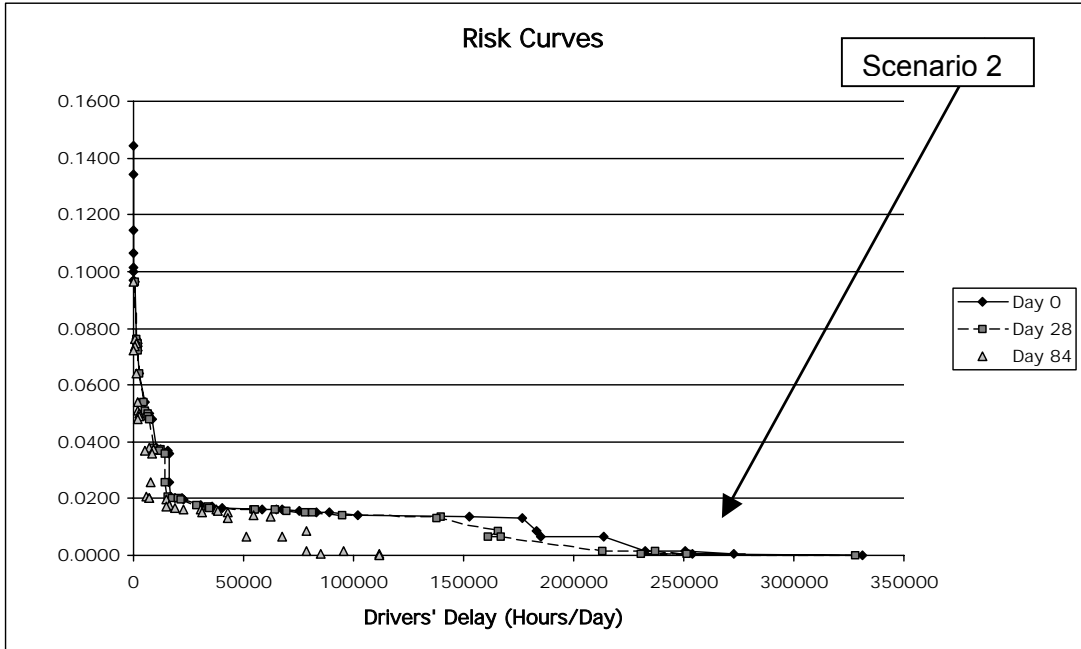


Figure 7. Risk curves, separated by time after event.

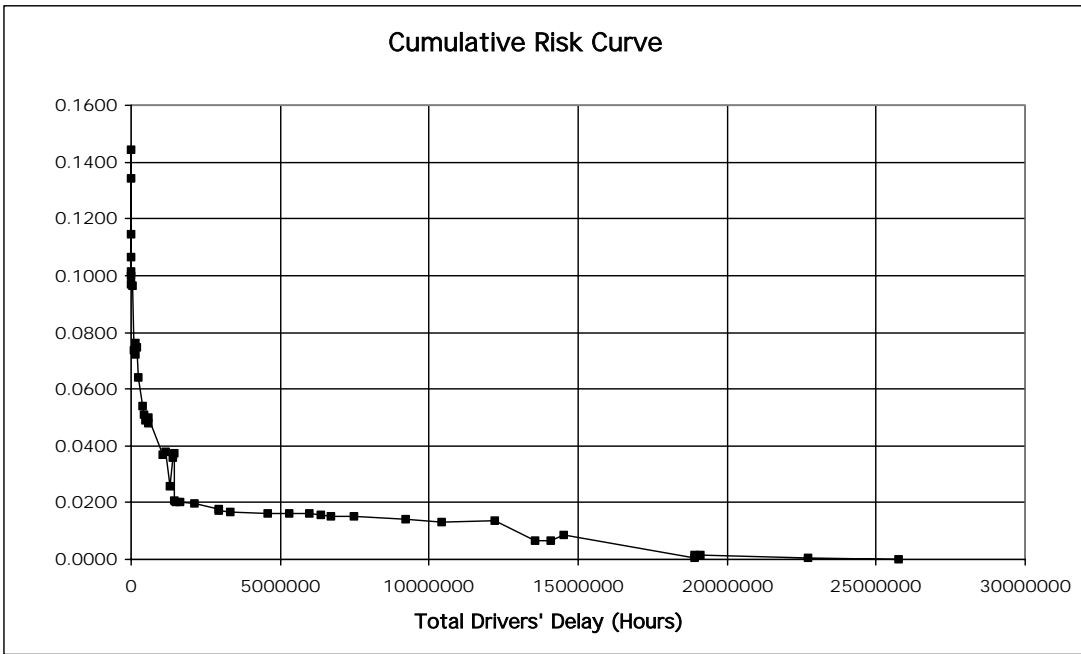


Figure 8. Cumulative risk curve.

CONCLUSIONS

This study illustrates that, through the synthesis of structural engineering, transportation engineering, seismology, and network analysis, a model can be developed to simulate the

response of highway transportation systems after an earthquake. Though simplistic in some areas, this model provides insights into the development of risk measures for spatially distributed networks, as well as, in case studies, insights into the resiliency of the specific systems examined.

In the case study examined, risk curves are developed for the Los Angeles Metropolitan Area Highway Transportation System, and an idea is developed about its performance in response to numerous scenario earthquakes. Notably, given the low probabilities of exceeding even moderate Drivers' Delays, as evidenced by the risk curves, it can be said that the system exhibits remarkable resilience.

This model could benefit from further work focusing on a few areas. First, it would be worthwhile to remove the limitation caused by the assumption that all bridges have a statistically homogenous vulnerability to ground shaking. By incorporating separate fragility curves on the basis of bridges' skews, number of spans, etc. the damage suffered by the network can be more accurately estimated. Second, the model for repair processes is rudimentary, and would benefit heavily from a great deal of review and refinement.

ACKNOWLEDGEMENTS

First, I express my thanks to my advisor for this study, Professor Masanobu Shinozuka, of the University of Southern California, for his guidance in conducting this project.

Special thanks are also in order for Mr. Dong Xuejiang, for his assistance with creating the computer codes used for the model discussed.

In addition, I would like to thank Hungchi Chung, Babak Mansouri, Elsie Ang, and Kerri Tokoro for their support and kindness during my stay at USC.

Finally, I thank the people at the Multidisciplinary Center for Earthquake Engineering Research for providing me with this opportunity, as well as the funding through the National Science Foundation's Research Experiences for Undergraduates Program, EEC-9701471.

REFERENCES

- Chang, E. Stephanie, Shinozuka, M., and Moore, J., "Probabilistic Earthquake Scenarios: Extending Risk Analysis Methodologies to Spatially Distributed Systems," *Earthquake Spectra*, Vol. 16, No. 3, August 2000, pp 557-572
- Eguchi, R.T., Goltz, J. D., Seligson, H.A., Flores, P.J., Blais, N.C., Heaton, T.H., and Bortugno, E., "Real-time Loss Estimation as an Emergency Response Decision Support System: the Early Post-Earthquake Response Tool (EPEDAT)," *Earthquake Spectra*, Vol. 13, 1997, pp. 815-832.
- Shinozuka, M. "Development of Bridge Fragility Curves Based on Damage Data," *Earthquake Engineering and Engineer Seismology: An International Journal*, Vol. 2, No. 2, September 2000, pp. 35-45
- Shinozuka, M., Feng, M. Q., Dong, X., Uzawa, T., and Ueda, T., "Seismic Damage Assessment for Engineering Response Decision Support," *SPIE's Seventh International Symposium on Smart Structures and Materials, Proceedings*, 2000, Paper #3988-29
- Shinozuka, M. Feng, M. Q., Lee, J., and Naganuma, T., "Statistical Analysis of Fragility Curves," *ACSE Journal of Engineering Mechanics*, Vol. 126, No. 12, 2000, pp 1224-1231
- Shinozuka, M., Shiraki, N., and Kameda, H., "Performance of Highway Network Systems Under Earthquake Damage," *Proceedings of the Second International Workshop on Mitigation of Seismic Effects on Transportation Structures*, September 13-15, 2000, Taipei, Taiwan, pp 303-314.
- Shiraki, Nobuhiko. *Performance of Highway Network Systems Under Seismically Induced Traffic Delays*. Kyoto University. 2000 (MS Thesis).

Seismic Response of a Wood Frame Multi-Story Apartment: An Overview



Ryan Petersen

Texas A&M University

The University of California at Berkeley

Faculty Advisor – Jack Moehle

Post Doctorate Researcher – Clay Naito

ABSTRACT

PEER SUMMER INTERNSHIP REPORT: Seismic Evaluation of a Multi-Story Wood Frame Apartment Building

Ryan Petersen

This paper is an overview of Wood Frame Task 1.1.2: Seismic Evaluation of a Multi-Story Wood Frame Apartment Building with Tuck-Under Parking. Testing occurred during the summer of 2001 at the University of California, Berkeley. The setup, implementation, and goals of the building test are the main focus of the paper. Also, along with the primary test, quasi-static component tests of two steel retrofit frames were prepared. Before construction of the apartment can begin, a dummy mass is erected on the table and undergoes the same testing as the apartment. This paper is written to have broad appeal to both engineers and people without rigorous technical background. Therefore, the first part of the paper provides an introduction to earthquake engineering research.

Introduction

On January 17, 1994 a moderate earthquake measuring 6.7 on the Richter scale occurred. Its epicenter was in Northridge, 18 miles northwest of Los Angeles. Sixteen people died when the first floor of the Northridge Meadows Apartment Complex collapsed. Immediately, a three-story structure was converted into two stories. The Canadian Journal of Civil Engineering reported after observation of the complex that the weak first story led to collapse.

Research is being conducted at the University of California, Berkeley to better understand the seismic response of wood frame buildings. The results may lead to a rehabilitation program to prevent future destruction similar to the Northridge collapse.



Figure 1: Collapsed first story of California apartment

California's Building Codes

Californians rely on building codes as their foremost line of defense against the vulnerabilities of buildings. Since the 1906 San Francisco earthquake, seismic design engineers have been developing building codes to achieve the goal of protecting safety by preventing structural collapse. These codes cover all aspects of building design and construction. Design requirements, heating, electrical, and plumbing specifications, and details such as the proper type of nails are covered. Codes are to be adhered to by architects, contractors, engineers and others associated with construction. The Structural Engineers' Association of California states in their Blue Book of seismic provisions: "Structures should be able to resist a moderate level earthquake (such as Northridge) without structural damage, but possibly experience some nonstructural damage."

Following the Northridge earthquake, public attention was on loss of life, high-profile structural failures, and enormous economic losses. The general perception was that building performance was unacceptable, and building codes and the construction process may not be adequate (ref. 3).

After an earthquake engineers study the damage to structures. They determine what went wrong and how it should be corrected. Revisions and advancement of the building code can then be made. However, the damage has already been done. Today earthquakes can be simulated inside a laboratory, and building codes can be updated and revised before an earthquake occurs.

Introduction to earthquake engineering

The following paragraphs provide an introduction to earthquake engineering. An earthquake simulator produces artificial earthquakes. Various instruments are used to measure the effects on the testing structures caused by the simulator.

UC Berkeley Shake Table

The earthquake simulator, or “shake table,” is located at the Richmond Field Station, part of the University of California. It is the first of its kind ever built and is still the largest in the United States. The shake table has six degrees of freedom. This means it can produce motion in the x, y, and z directions, as well as rotation around each of the axes. The table is a heavily reinforced one-foot thick concrete slab measuring 20 x 20 ft. It weighs 100,000 pounds. To allow motion, there is a foot of space between the table and the floor of the building sealed by heavy vinyl compound.

The table is at ground level, but the machines that provide motion are located in a room below. These machines are called hydraulic actuators. Eight provide horizontal motion, while eight more provide vertical motion. The actuators have swivel joints at each end so they can rotate to accommodate components of motion perpendicular to their direction of extension. In operation the pit below the table fills with air. This air pressure balances the weight of the table and what is on it with the ambient air pressure. Therefore no force is placed on the actuators. In essence whatever is on the shake table is floating.

The earthquake simulator can produce any desired ground motion and can be programmed to reproduce past earthquakes. The specific ground motions desired are input through the control room, which is fifteen feet away from the actual shake table (Mosalam, Mahin, Naito, 2000).

Instrumentation

Although the shake table can reproduce any number of ground motions and earthquakes, these are not useful to researchers if the effects cannot be measured. Many instruments for gathering data are located beneath the table. Others must be manually placed on the specimens being tested. These instruments are hooked by cables to a box that sends data to computers in the control room.

Position/Displacement Transducer

Position/displacement transducers are commonly known as string gauges. The electronics for the gauge are housed in a rectangular metal case approximately 5 x 3 x 3 in. Measurements are taken by an electrical signal proportional to the linear extension of a stainless steel cable. Displacement is measured by attaching the cable to the moving part and the body of the gauge to any fixed surface. The cable is retracted by a constant tension spring motor, which maintains uniform tension on the cable. Some transducers can also measure velocity (ref. 1).

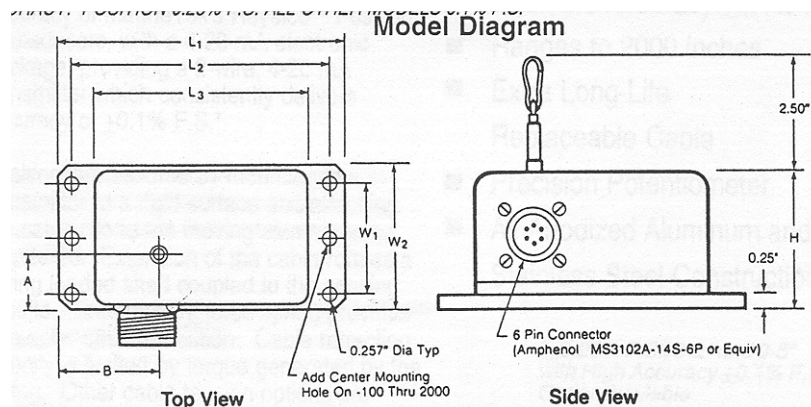


Figure 2: Diagram of a typical string gauge

Accelerometers

Accelerometers are small metal boxes used to measure acceleration. Some measure along only one axis, others along two or three. They consist of two separate, rugged seismic sensors responding to force along the axes. Each sensor consists of a bending beam and mass with bonded foil strain gauges. An advanced solid-state electronic signal conditioning package compliments the mechanical configuration (ref. 4).

Strain Gauges

External force applied to an elastic material generates stress, which subsequently deforms the material. This deformation is called strain. Strain is the ratio of change in length to length.

When a metal (resistor) is expanded or contracted by external force, it experiences a change of electrical resistance. By bonding a metal (resistor) on the surface of a specimen with an electrical insulator between them, the metal changes its dimension according to the expansion or contraction of the specimen, thus resulting in a change of its resistance. A strain gauge is a sensor to detect the strain of a specimen by this resistance change.

A strain gauge is constructed by bonding a fine electric resistance wire to an electrical insulation base, and attaching gauge leads. It is then bonded to the surface of the specimen with adhesive. The magnitude of strain at different parts of a specimen varies. Different parts need different types of strain gauges (ref. 7).

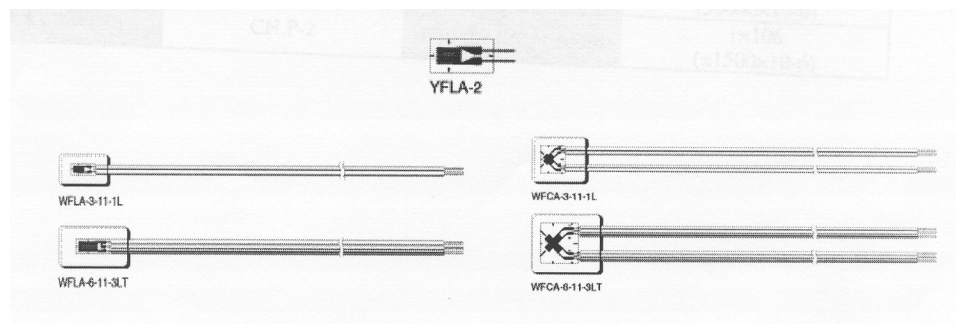


Figure 3: Various types of strain gauges.

Load Cells

Strain gauges can be attached to small sections of pipe to make a load cell. Load cells are used to measure the force applied to a certain area. However, before a strain gauge and piece of pipe can be used as a load cell they need to be prepared.

Load cells are exercised by increasing load from zero to a set amount then decreasing the load back to zero. This is done to accommodate an error called hysteresis. Hysteresis is the difference between the actual load applied and the load output by the gauge. Such things as loose fit, corroded components, misalignment, bolting, or dirt can manifest as hysteresis. Structural hysteresis is the imperfect response of microscopic crystal grains, integrated over the macroscopic dimensions of the strain gauge. Load cells are exercised until they reach repeatability. This is obtained once repeated trials of identical inputs report a consistent output. At this point the load cell is ready for calibration and then used for testing (ref. 2).

Wood Frame Task 1.1.2

The following paragraphs outline the aims, justification, and goals of wood frame task 1.1.2. An overview of the construction and experimental process is provided. Also, two separate tests, both related to the main apartment testing, are described. These are the testing of two moment frames, and the erection and testing of a dummy mass.

Project Aims

The aim of Wood Frame Task 1.1.2 is to build and test a wood frame apartment building on the shake table. The building will be a full-scale re-creation of a multi-family residence typical of California. The building will be three stories tall with the first story used as a garage. This space saving layout is known as tuck under garage parking. The structure will eventually

be tested with a re-creation of the Northridge earthquake. A steel moment frame is to be used for strengthening the first story.

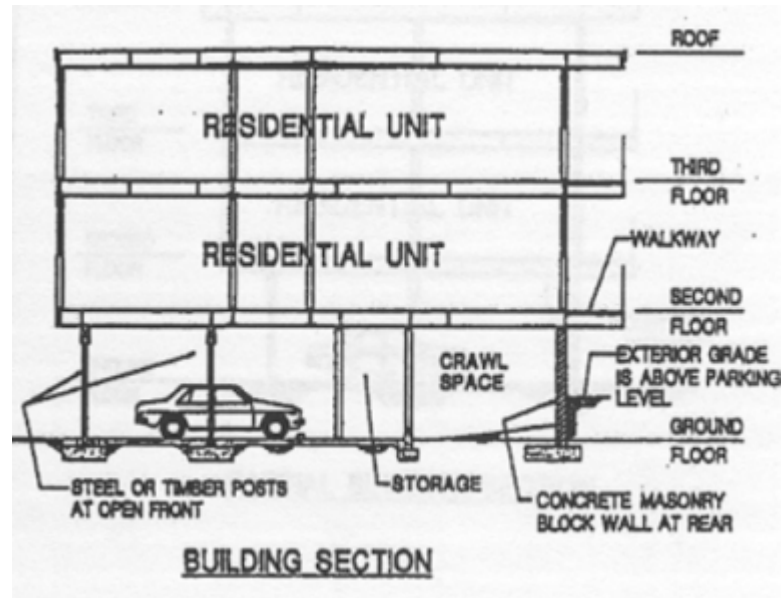


Figure 4: Layout of apartment with tuck-under parking

Justification for Wood Frame Task 1.1.2

The justification for testing stems from the low level of confidence associated with the seismic response of wood-frame construction compared to other construction materials such as steel or concrete. The Northridge earthquake was chosen because it caused significant damage to wood buildings with tuck under parking. The buildings that collapsed had what is known as a "soft" first story. A soft story is any story that has less than 70% of the capacity of the story above. Few seismic tests have been conducted on buildings of this type. Also, their response to ground motion cannot be predicted with existing computational tools.

Goals of Wood Frame Task 1.1.2

Wood Frame Task 1.1.2 will provide more data on the seismic response of multi-story wood frame buildings. This data will apply to current building practices in California. Currently, the design of wood frame tuck-under apartments varies in each part of the state. The goal of this project is to set a universal standard for designing and rehabilitating earthquake resistant wood frame apartments.

Building and Testing of the Structure

The apartment is designed and constructed to represent 1960's engineering practice in Northern California. All measurements are full scale. The footprint of the building is 32 x 16 ft, and each story is nine feet high.

The apartment will be tested as it is constructed. Once the first floor is complete it will be tested. After the second floor is added, the structure will be tested again. The final tests will be on the entire three-story building. The structure will be tested with a full range of ground motion, including a record of the Northridge earthquake. The torsion effect due to the open front garage is of particular interest. The absence of a front wall on the first story creates a twisting, non-linear motion when the structure is subjected to ground motion. One of the goals of the retrofit moment frame is to reduce this twisting motion. Thus, the apartment will be tested both with and without the moment frame in place. The building will also be tested with and without finish materials such as stucco and dry wall board. The final retrofitted, finished, three story apartment will be tested until it collapses (Mosalam, Mahin, Naito, 2000).

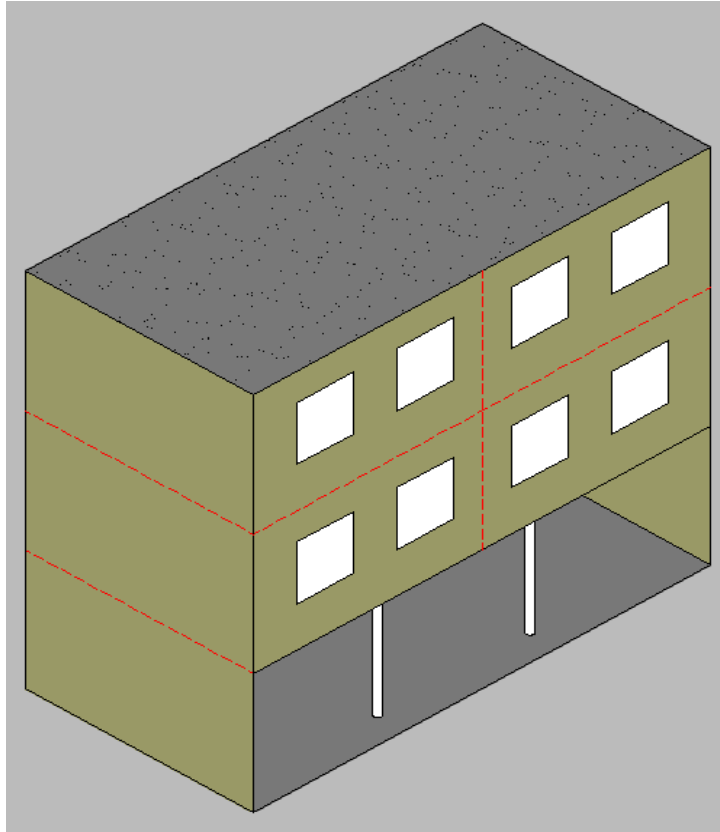


Figure 5: Front view of experimental apartment model

Moment frames

Two moment frames are being tested in a separated lab. One will be placed in the actual apartment. The results of the tests will determine which frame will be used.

The first frame is called a special moment frame (reduced beam section) or "dog bone." This design will direct the forces away from the weld and the heat affected area. When a frame is fabricated, the joints that are welded are also weakened. Thus, if forces are directed away from the weld, overall capacity of the frame is increased.

The second frame is an alternate moment frame. It is stronger than a special moment frame but also larger. In some circumstances the large size makes this type of frame impractical.

However, because it is being used on a wood frame building with a relatively low mass, it can be effective and practical.

During testing the alternate moment frame will stay within its elastic range. It will be deformed but will return to its original shape. The special moment frame will be deformed beyond its elastic range and will not return to its original shape. However, it is not known which frame will fail completely first. For testing the two are bolted to the ground, then horizontally displaced by an actuator until they fail completely.

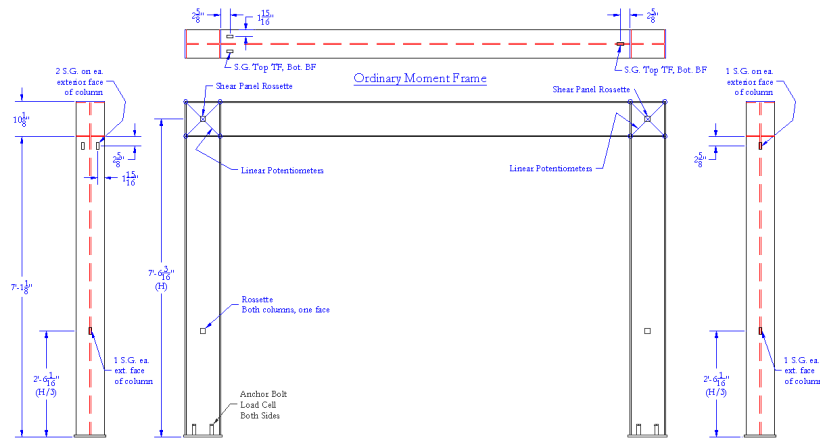


Figure 6: Ordinary moment frame

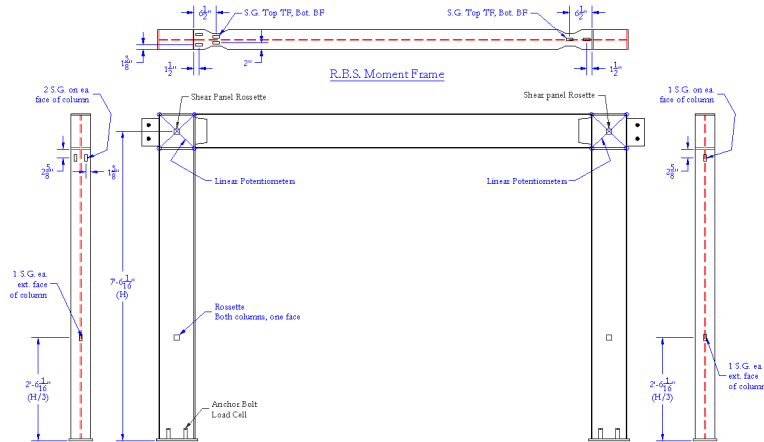


Figure 7: Alternate moment frame

Dummy Mass

Before construction of the apartment can begin, scrap metal and concrete are stacked on top of the shake table to create a dummy mass. This structure is seventeen feet high and weighs 147,000 lb. It is the largest mass ever placed on the table. There are several reasons for erecting the dummy mass.

The dummy mass takes the place of the actual specimen to set the table controls. A record measured during the Northridge earthquake will be used as the input ground motion signal for apartment tests. Researchers want to be able to accurately reproduce this ground motion signal as output on the table. To do this requires tuning specific to the specimen on the table. The table has to be run in order to set the controls. However, if the actual apartment were on the table it would be damaged before testing even begins.

Another use for the dummy mass is to minimize random and uncontrolled motion. Although the shake table has size degrees of freedom, earthquakes are typically measured in only three directions: x, y, and z. Combinations of these directions at different locations can create

pitch, roll, and torsion, which are rotation about the x, y, and z-axes, respectively. Because of the apartment's height and weight, it will naturally create these rotations. The dummy mass is tested allowing programming of the table to minimize these unwanted rotations.

Acknowledgments

The National Science Foundation provided funding for the research experience for undergraduates (REU) summer internship program, under which this paper was written. Thanks are also given to the Pacific Earthquake Engineering Research (PEER) center in Richmond, California and the University of California at Berkeley for hosting the summer interns.

The author would like to thank professor Jack Moehle for acting as REU student mentor. The author worked directly under Clay Naito and Mahmoud Hachem, and their guidance is greatly appreciated. Also appreciated is the help of other graduate students, Ken Elwood, Patxi Uriz and Halil Sezen. Finally, the work of Gerard Pardoen and Gina Ring in coordinating the PEER REU interns is greatly appreciated.

Bibliography

1. Celesco Transducer Products, Inc., www.celesco.com. 28 July 2001.
2. “Error Analysis,” Lebow Load Cell and Torque Sensor Handbook No. 600, pp.14-15.
3. “Findings and Recommendations of the City of Los Angeles/ SEAOSC Task Force on the Northridge Earthquake.’ November 12, 1994.
4. Magnetek, www.magnetek.com 28 July 2001.
5. Mosalam, K.M., Mahin, S.A., Naito, C.J., 2000. “Proposal - Wood Frame Task 1.1.2: Seismic Evaluation of Asymmetric Multi-Story Wood Frame Buildings.”
6. “Seismic weaknesses of some residential wood framed buildings: confirmations from the 1994 Northridge Earthquake,’ Canadian Journal of Civil Engineering, Vol. 22, April 1995, No. 2, pp.403-414.
7. TML Strain Gauges,Ltd., <http://www.tokyosokki.co.jp/e/index.html>. 1 Aug. 2001.

Base Isolation in Steel Structures

Stephen Priddy
University of Tennessee at Martin

REU Host:
Georgia Institute of Technology
Dr. Roberto Leon

ABSTRACT:

This study investigated the use of base isolation in structures. In existing structures, much of the energy generated through ground motion has to be absorbed and dissipated by the structures through yielding and cracking. Thus, these buildings sustain a large amount of damage when subjected to a large earthquake. Previous research has found that if the energy to be absorbed by a structure is reduced, damage can be minimized. The goal of this research is to find out if using base isolation significantly changes the amount of damage the structure experiences. Two buildings were designed and analyzed; one of the structures was pinned at the base and the second structure was base isolated. Findings included a decrease in accelerations of the structure and an increase in the period and displacements. This supports the concept that base isolation reduces the energy that is absorbed by a structure and decreases the damage that is sustained.

Introduction:

When people think of earthquakes, they tend to think of the West Coast area due to the visible evidence of highly active fault lines. However, inhabitants of the Mid-America region are becoming more and more aware of the dangers associated with seismic activity in their own area due to the New Madrid seismic source. One danger that is highly recognized is the structural damage that occurs in existing structures during an earthquake. As seismic activity begins, the ground begins to move and large amounts of energy are released. Where does that energy go? Some of the energy that is liberated by the slip of a fault is absorbed by structures. As the structure absorbs this energy and exceeds its elastic limit, it begins to sustain some form of structural damage. Possible damage includes, but is not limited to, permanent deformation due to yielding in connections and frame members as well as energy dissipated during cracking and fracturing. The amount of structural damage sustained by a building can be directly related to the amount of energy that goes into the structure. Therefore in recent years, researchers began looking for ways to reduce the amount of energy that a structure absorbs. One method that lowers the amount of energy entering a structure is known as base isolation. In a base isolated structure, an extra set of structural elements is placed between the base of the structure and its foundation. These elements are often made of some type of rubber bearings, which will now be referred to as a base isolator. Two requirements that must be met by this extra structural element are that it must have very low horizontal stiffness and very high vertical stiffness. The low horizontal stiffness allows the isolators to displace laterally, which dissipates a portion of the energy, and the high vertical stiffness allows the isolators to carry the dead load of the structure that is resting upon them. Another feature of a base isolated structure is the seismic gap. This is

an area around the base of a structure that is to be kept free of obstructions. Its purpose is to give the base isolated structure room in which to move when excited by ground motion. Also, the plumbing and electrical wiring of such a building must be installed in such a manner that when the building moves it is not damaged.

The main purpose of this research was to allow the author to acquire a basic understanding of base isolation in structures, not to do in-depth analysis or new research in this area. The methods for designing and analyzing the structures the author used during this research will be described in detail. The description of the methods will then be followed by the results and interpretation of the analysis. Finally, conclusions on using base isolation in structures will be given.

Methods and Materials:

To begin the research, the author began by establishing background information on base isolation in structures by reading literature that was written specifically for the design of isolated structures. [Skinner, Robinson, and McVery; 1993, Naeim and Kelley; 1999] These references covered topics ranging from the general overview of base isolation, the process of picking the correct isolator for a given structure, and the actual design of a base isolated structure. Once a background was established, the researcher began working with the structural analysis program SAP2000. [CSI] Using this program, two nearly identical structures were used for the analysis. The only difference between the structures was the way in which they were restrained at the base; in one structure the base was pinned, and in the second structure the base was isolated using rubber bearings. The design included specifying each member and also the types of loading that each member and joint was to be subjected to.

Table 1.

Type of Beam	Size of Beam
Columns	W14x135
Beams	W18x55

This one bay structure was given loadings equal to that of an internal span of a structure. So, the reader should keep in mind that the results could vary somewhat in a larger structure. In addition to the basic loads such as dead, live and wind loads, seismic data from the SAP2000 program was used as the seismic input on the structure. Specifically, the structures were subjected to the loading generated from the 1940 El Centro earthquake acceleration record. Once all members were specified and all loads were applied, SAP2000 was used to run an analysis of both structures. From the analysis, the researcher collected data including the moments applied to members, pseudo-spectral accelerations of all joints due to the loads applied on the structure, and displacements of all joints.

Results and Interpretations:

There are four areas in which the researcher would like to compare data, 1.) the moments applied to frame members; 2.) the pseudo-spectral accelerations of joints; 3.) the period of the structures; and 4.) the displacements of joints.

Moments Applied to Frame Members:

One major consideration in designing a structure is the size of members to use. Whether the member is to serve as a column or a beam, they are each chosen based on several criteria. Part of the criteria used to choose the correctly sized member is the maximum allowable bending moment. As the moment of inertia of the member increases, the maximum allowable moment also increases. However, as the size of the member increases, the cost also grows. Therefore, the building owner and contractor would like to use the smallest feasible member. To decrease the size of the member the maximum bending stress that that member would be subjected to has to be increased. Although the magnitude of the moment was not decreased significantly in these designs, one should keep in mind that this data is only representative of one bay of a large structure. If a large superstructure were being analyzed, the difference might be quite noticeable.

Pseudo Spectral Accelerations

The following figure gives a comparison of the pseudo-spectral accelerations between the two structures based upon records from the 1940 El Centro earthquake. The reader should see an obvious decrease in the acceleration at the first mode in the base isolated structure. This decrease illustrates that base isolation actually achieves the goal of reducing the amount of energy that is going into the building. The isolators actually dissipate some of the energy that would initially go into a structure that is either pinned or fixed at its base.

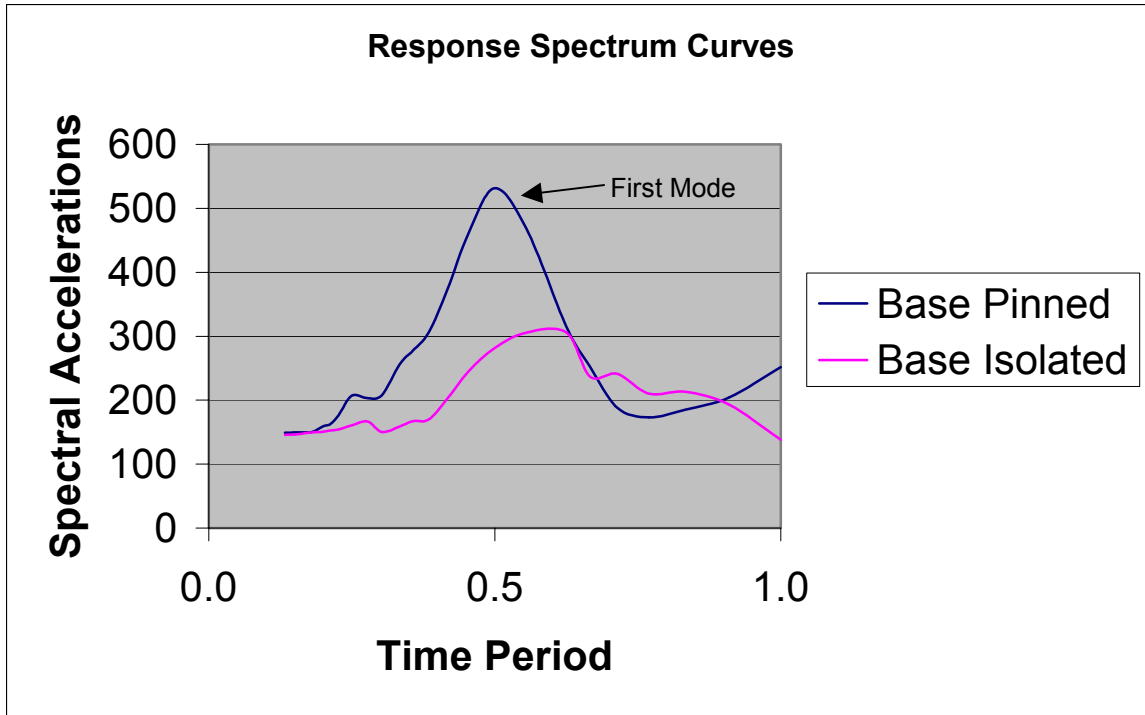


Figure 1.

Period:

The period of a structure is the time it takes for the building to make one full cycle. The change in period is noticeable in Figures 1 and 2. In Figure 1 the reader can see an increase or shift in the period of the base isolated structure. This increase is due to the very low horizontal stiffness of the base isolators. They decrease the overall structural stiffness; therefore, it will take longer for the base isolated structure to complete its period. The increase in the period is more obvious in Figure 2. Another possible advantage of having base isolation in a structure deals with the type of earthquake that might excite the given building. If the designers knew what frequency an earthquake would excite the building, they could use base isolation to lower the frequency of the building enough to where it would not be in a range close to that of the given earthquake. Thus, the amount of structural damage would be reduced greatly.

Displacement of Joints:

Looking again at Figure 2, a dramatic increase in displacements between the two structures can be seen as they were each subjected to the El Centro earthquake. The maximum displacement of the isolated structure is almost three times that of the pinned base structure. This amount of displacement would seem unwanted at first. In this graph, the displacement of the roof is measured relative to the foundation of the structure. Yet, one thing the reader should keep in mind is the fact that most of the displacement that is occurring in the base isolated structure is between the foundation of the structure and its base. From looking at the aforementioned graph, the reader will find that from the base of the pinned structure to its roof level the total displacement is somewhere close to five inches. Previous research has shown that in a base isolated structure from the base to the roof the displacement is negligible; therefore, the moment in the columns are significantly smaller in the base isolated structure than the base pinned structure. Moreover, the occupants on the top floor of the base isolated structure are not feeling the associated larger accelerations. Thus, the comfort of the occupants on the top floor is maintained. However, in the traditional, base pinned structure, all of the displacement is actually felt by the occupants in the top floor of the structure.

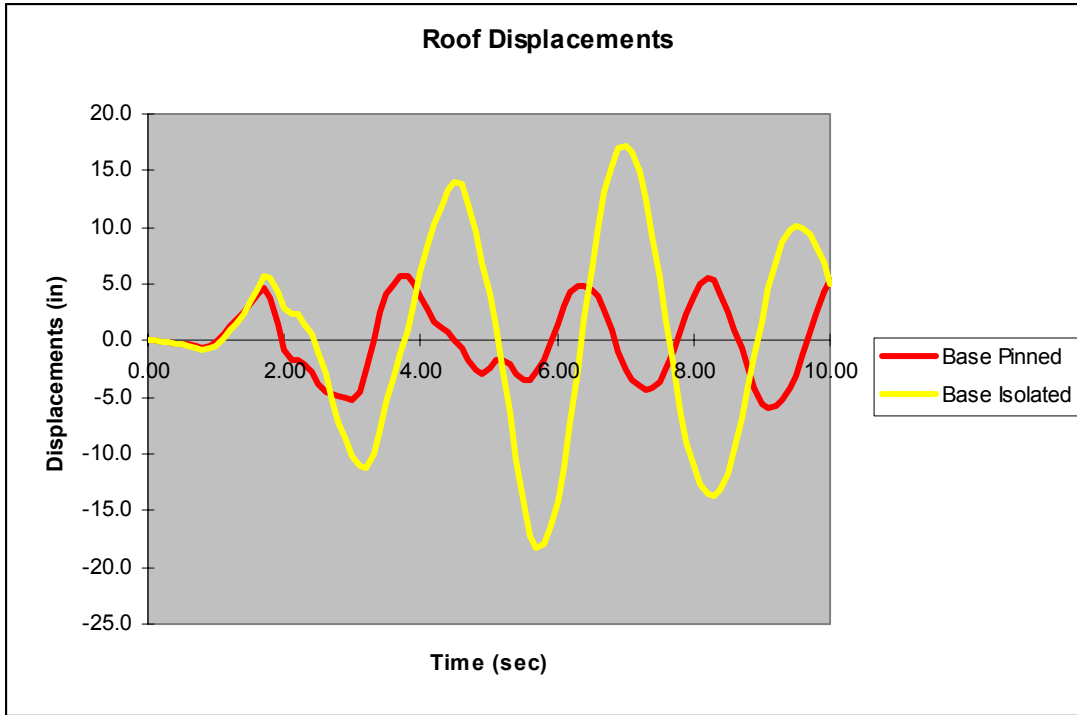


Figure 2.

Conclusions:

Researchers began with the goal of reducing the amount of energy going into a structure. One method in which they achieved their goal was with practice referred to as base isolation. This type of approach in building design has many advantages. One such advantage is its ability to reduce the magnitude of the interstory drift and associated moments on columns in the structure, which allows for the use of smaller members. Furthermore, a decrease in the peak accelerations was achieved with base isolation. This illustrated the fact that base isolators actually decreased the amount of energy entering the structure. The last factor that was considered was the displacements in base isolated structures. People would argue whether or not the displacements would actually be an advantage or a disadvantage to a structure. The biggest factor for one to consider is the fact that base isolation would actually reduce the interstory drift to virtually zero, which would maximize the comfort of the building occupants. Finally, the

upshot of base isolation is the fact that it does reduce the amount of energy that is allowed to enter the structure. Therefore, base isolation achieved the goals that were set at the beginning of the research.

Acknowledgments

The author would like to begin by thanking the National Science Foundation for their financial support. Likewise, the author would like to recognize the Mid America Earthquake Center for choosing him to participate in the Research Experience for Undergraduates program for the summer of 2001. The continued help and patience of Sandra Menke is also noted. For their time, guidance, and direction on his project, the author would like to extend his appreciation to Dr. Roberto Leon and Dr. Reginald DesRoches at Georgia Institute of Technology. Furthermore, the assistance of the author's advisor Dr. Richard Helgeson at the University of Tennessee at Martin is also appreciated.

Works Cited

Naeim, Farzad and James Kelley. Design of Seismic Isolated Structures: From Theory to Practice. New York: John Wiley and Sons, Inc., 1999.

Skinner, Ivan, William H. Robinson, and Graeme H. McVerry. An Introduction to Seismic Isolation. New York: John Wiley and Sons, Inc., 1993.

Damage to Bridges During the 2001 Nisqually Earthquake

Richard Tyler Ranf
Home Institution: Washington University in St. Louis

REU Host Institution: University of Washington
REU Advisor: Dr. Marc O. Eberhard

DAMAGE TO BRIDGES DURING THE 2001 NISQUALLY EARTHQUAKE

Richard Tyler Ranf^α

Home Institution: Washington University in St. Louis

REU Host Institution: University of Washington

REU Advisor: Dr. Marc O. Eberhard

ABSTRACT

Reports of damage sustained by bridges during the February 28, 2001 Nisqually Earthquake were used to correlate likelihood of damage with the following parameters: distance to the epicenter; estimated peak ground acceleration; estimated spectral acceleration at periods of 0.3 s, 1.0 s and 3.0 s; year built; and type of bridge. Reports of bridge damage, collected from state and local agencies, were compared with the population of bridges listed in the Washington State Bridge Inventory. The level of ground shaking was estimated from ShakeMaps, derived from data from the Pacific Northwest Seismic Network.

Of the ground-motion parameters considered, the likelihood of bridge damage was best correlated with spectral acceleration at a period of 0.3 s. For a given level of spectral acceleration, bridges built before 1940 were the most likely to be damaged, while those constructed after 1975 were the least likely to be damaged. Although the number of moveable bridges was small, this type of bridge appeared to be particularly vulnerable. The percentage of bridges with a steel main span was higher than for those constructed of reinforced concrete. However, the number of steel bridges was relatively small, and the most common type of damage to steel bridges was actually damage to the reinforced concrete substructure.

^α Advised by Dr. Marc O. Eberhard, Department of Civil and Environmental Engineering, University of Washington, 233 More Hall, Box 352700, Seattle, Washington 98195-2700. E-mail: rtr1@cec.wustl.edu, Telephone: (314) 935-3650. Effort sponsored by the Pacific Earthquake Engineering Research Institute and the Research Experiences for Undergraduates program, funded by the National Science Foundation.

TABLE OF CONTENTS

1 INTRODUCTION

- 1.1 Background
- 1.2 Research Methodology

2 SUMMARY OF OBSERVED DAMAGE

- 2.1 Damage to Movable Bridges
- 2.2 Damage due to Settlement
- 2.3 Damage to Reinforced or Pre-Stressed Concrete
- 2.4 Damage to Steel
- 2.5 Damage to Restrainers, Joints, or Bearings

3 DAMAGE ANALYSIS

- 3.1 Effect of Spectral Acceleration
 - 3.1.1 *Combined Effect of Spectral Acceleration and Year Constructed*
 - 3.1.2 *Combined Effect of Spectral Acceleration and Bridge Type*

4 CONCLUSION

APPENDIX A: DISTANCE CALCULATION

APPENDIX B: LIST OF CONTRIBUTORS

REFERENCES

ACKNOWLEDGMENTS

LIST OF FIGURES

Figure	Description
2-1	Types of damage for each type of bridge
3-1	Effect of spectral acceleration at a period of 0.3 s
3-2	Combined effect of spectral acceleration and year of construction
3-3	Effect of spectral acceleration on movable bridges
3-4	Combined effect of spectral acceleration and bridge type
3-5	Combined effect of spectral acceleration, year of construction and bridge type

1. INTRODUCTION

The vulnerability of bridges in the Puget Sound area was investigated by analyzing reports of damage to bridges during the 2001 Nisqually Earthquake. By correlating damage with bridge and ground-motion characteristics, it was hoped that characteristics that most contributed to the damage would be identified. The characteristics that were explored included:

- the year that the bridge was constructed
- the distance from the bridge to the earthquake epicenter
- the estimated peak ground acceleration (PGA) at the location of the bridge
- the spectral acceleration at the site of the bridge (SA), and
- the type of bridge that was damaged

If maps of shaking intensity were available shortly after an earthquake, the observed trends could be used to prioritize post-earthquake inspections.

1.1 BACKGROUND

At 10:54:32 AM local time on February 28, 2001, the Nisqually Earthquake of magnitude 6.8 occurred at location 47.1525° N , 122.7197° W. The epicenter was approximately 17.6 km Northeast of Olympia, 23.7 km SW of Tacoma, and 57.5 km SW of Seattle, Washington.¹ The Nisqually earthquake occurred deep below the earth's surface, within the subducting Juan de Fuca plate. Because of the depth of the hypocenter, approximately 52.4 km, the damage throughout the area was moderate. Slight to moderate damage was reported to eighty-two bridges, but no bridges collapsed.

Had the earthquake been more shallow, damage in the Olympia and Seattle regions might have been much more severe.

1.2 RESEARCH METHODOLOGY

Because the state, counties and cities keep separate records, it was necessary to contact each agency independently to obtain detailed damage descriptions and photographs of bridges that were damaged during the Nisqually earthquake. To help with this process, a damage information form was composed to consistently extract all of the pertinent information. Appendix B provides a list of individuals who contributed data or comments to this report.

Concurrently, the Washington State Department of Transportation (WSDOT) provided the Washington State Bridge Inventory (WSBI) in electronic form. This database provides physical and geographical information for nearly all of the bridges in the state, which were used to normalize the damaged data.² The WSBI categories considered in this study were:

- Latitude and longitude of bridge
- Type of bridge (e.g., moveable, truss, etc.)
- Material used for the main span (reinforced concrete, prestressed concrete, or steel)
- Year of construction

The average daily traffic data for each bridge was also determined. Although this information was not used in this analysis, it could be used in future analysis to determine the economic impacts of bridge closures.

To analyze the data, each bridge had to be located, and the corresponding values for the peak ground acceleration and the spectral acceleration had to be estimated. These parameters were extracted from ShakeMaps developed by the Pacific Northwest Seismograph Network (PNSN),³. The PNSN, centered at the University of Washington, operates a network of seismograph stations throughout the Northwest. It is operated through a joint effort by the University of Washington, University of Oregon and Oregon State University, and is funded by the United States Geological Survey (USGS), the United States Department of Energy (USDOE) and the State of Washington. PNSN developed maps of earthquake intensity (ShakeMaps) by interpolating between numerous stations within the network, taking into account geologic conditions.

Access to the ShakeMap data was provided by the Federal Emergency Management Agency (FEMA), which provided GIS support. The maps provided the approximate values for the peak ground acceleration and the spectral acceleration at the location of each damaged and undamaged bridge. The map used to extract the estimated values for each bridge had a range of 48.4125° N - 46.3875° N in latitude, and 124.1125° W – 121.0875° W in longitude.

2. SUMMARY OF OBSERVED DAMAGE

The data for the damaged bridges was collected from the city, county and state governments (Chapter 1). From this data, it was determined that eighty-two bridges had been damaged because of the Nisqually earthquake. The majority of these bridges are owned and maintained by the WSDOT, and are either overpasses or underpasses along the interstate and state highway systems. The city of Seattle reported damage to eighteen bridges.

The damage repair cost for each bridge was classified as slight, mild or moderate, based on damage estimate ranges of \$30,000 or less, \$30,001 to \$100,000, and above \$100,000, respectively. In cases where an estimate was not provided, but where the level was obvious, the researchers categorized the damage levels themselves. For these eighty-two damaged bridges, the number of bridges in each category was:

- Slight (56 bridges)
- Mild (16 bridges)
- Moderate (10 bridges)

No damage was reported to timber or masonry bridges. The four types of bridges that were damaged, were:

- Reinforced concrete bridges (38)
- Pre-stressed concrete bridges (21)
- Steel bridges (17)
- Movable bridges (6)

The damage for the six movable bridges was classified separately from damage to fixed bridges, because moveable bridges have particular vulnerabilities (e.g., lack of alignment). The type of damage observed for three bridges was not specified. For the remaining seventy-three bridges, the types of damage were classified as:

- Damage due to settlement (6)
- Damage to reinforced or pre-stressed concrete (48)
- Damage to steel (6)
- Damage to restrainers, joints, or bearings. (13)

The distribution of damage type, sorted according to bridge type, is shown in Fig. 2-1.

For each type of bridge, Fig. 2-1 displays the type of damage as a percentage of the total amount of damage for that type of bridge.

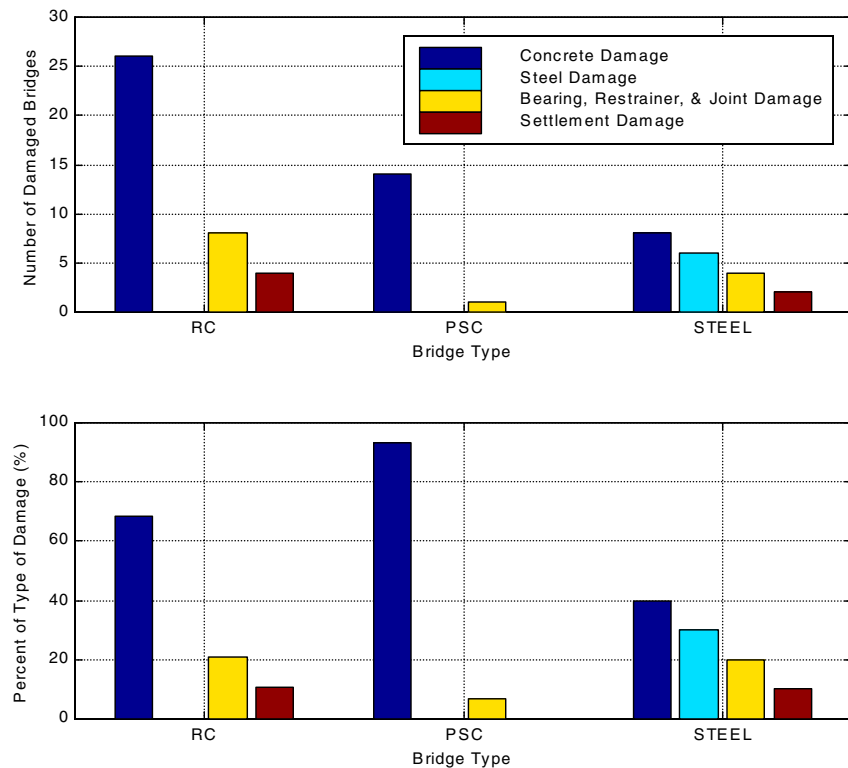


Figure 2-1: Distribution of types of damage for each type of bridge.

According to the figure, concrete damage was the most prevalent type of damage in each of the three types of bridges. It had been expected that concrete damage would predominate in reinforced concrete and pre-stressed concrete bridges. More surprising is that damage to steel components represented only 30% of the damage to steel bridges. By comparison, 40% of damaged steel bridges were reported to have damage primarily to the reinforced concrete substructure. Most of the concrete damage to the steel bridges was due to minor spalling of the concrete columns.

2.1 DAMAGE TO MOVABLE BRIDGES

Of the eighty-two bridges that were damaged by the earthquake, six were classified by the WSBI as movable bridges. Typical types of damage that were reported for these bridges included: damage to the leafs, dislodging of the counterweights, damage to the centerlock, and lateral shifting to the bascule towers.

2.2 DAMAGE DUE TO SETTLEMENT

Significant settlement was reported for six bridges. Five of these settled at the approach or within the bridge embankment. This type of damage ranged from minor differential settlement to a reported movement of 100 yards of the approach. The sixth reported sighting of settlement was attributed to liquefaction around one of the piers.

2.3 DAMAGE TO REINFORCED OR PRE-STRESSED CONCRETE

Out of 76 fixed (not moveable) bridges that were damaged, 48 had damage to a concrete element, which included spalling and cracking of columns, diaphragms and abutments.

2.4 DAMAGE TO STEEL

Only six fixed bridges sustained damage to the steel superstructure. Such damage usually consisted of bent and broken cross frames and bearing stiffeners.

2.5 DAMAGE TO RESTRAINERS, JOINTS OR BEARINGS

Damage to the restrainers, joints or bearings included elongated or broken restrainers, damage of seismic joints, and excessive tipping of rocker bearings. Thirteen of the damaged bridges sustained one of these types of damage.

3. DAMAGE ANALYSIS

This chapter explores the correlation between the percentage of bridges that were damaged and the properties of the bridge and ground motion. Specifically, the analysis considered the effects of: the year of construction of the bridge, the type of bridge, the distance between the bridge and the epicenter, the estimated peak ground acceleration at the location of the bridge, and the spectral acceleration of the bridge. To express the outcome of these analyses in a consistent manner, the data was normalized by dividing the number of damaged bridges by the total number of bridges in the Washington State Bridge Inventory (WSBI) for each category. A total number of 8,445 bridges are listed in the WSBI. However, only the portion of these bridges that fit the sorting categories were considered.

The only analysis that is presented in this paper is that involving the spectral acceleration, since this is the analysis that proved most accurate. For each analysis, a series of three plots are presented. The first plot displays the total number of bridges listed in the WSBI that fit into the categories that are being analyzed. The second plot displays the number of damaged bridges that fit into each category. The third plot displays the percentage of bridges that were damaged within each category, which corresponds to the values in the second plot divided by the values in the first plot, expressed as a percentage. The damage category, “Damage to restrainers, joints or bearings,” could not be expressed in this graphical format, because there was virtually no information in the WSBI on these elements.

3.1 EFFECT OF SPECTRAL ACCELERATION

The correlation between spectral acceleration and damage was also investigated. The PNSN ShakeMap provided data for the spectral acceleration at periods of 0.3, 1.0 and 3.0 seconds. However, damage frequency did not correlate well with the spectral acceleration at periods of 1.0 and 3.0 s. Therefore, further analysis was performed only on the data for the spectral acceleration at a period of 0.3 s.

Analyses were conducted to identify: the effect of spectral acceleration, the combined effect of spectral acceleration and year of construction, and the combined effect of spectral acceleration and bridge type.

The percentage of the bridges that were damaged correlated well with the magnitude of the spectral acceleration at 0.3 s, as shown in Figure 3-1.

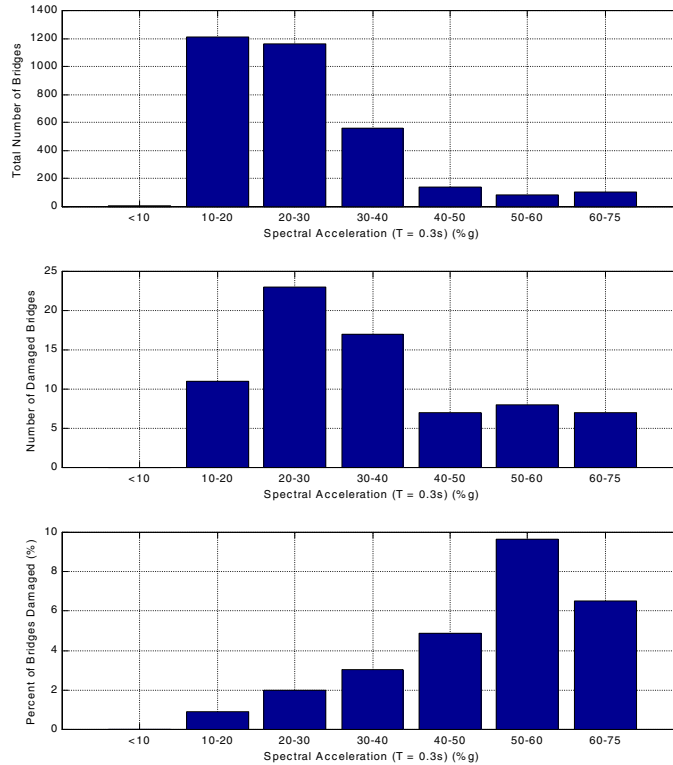


Figure 3-1: Effect of spectral acceleration at a period of 0.3 s.

An exception to the trend displayed in Fig. 3-1 was the slight decrease at the highest range of the spectral acceleration. This anomaly is most likely attributable to the small number of bridges in each category.

3.1.1 Combined Effect of Spectral Acceleration and Year Constructed

The analysis involving the spectral acceleration was further refined by taking into account the year of construction. The years of construction were placed into three categories: before 1940; 1940-1975; and after 1975. The results of this analysis are displayed in Fig. 3-2. At each level of spectral acceleration, the bridges that were built before 1940 had the highest percentage of bridges that were damaged, and in general, those built after 1975 were the least likely to be damaged.

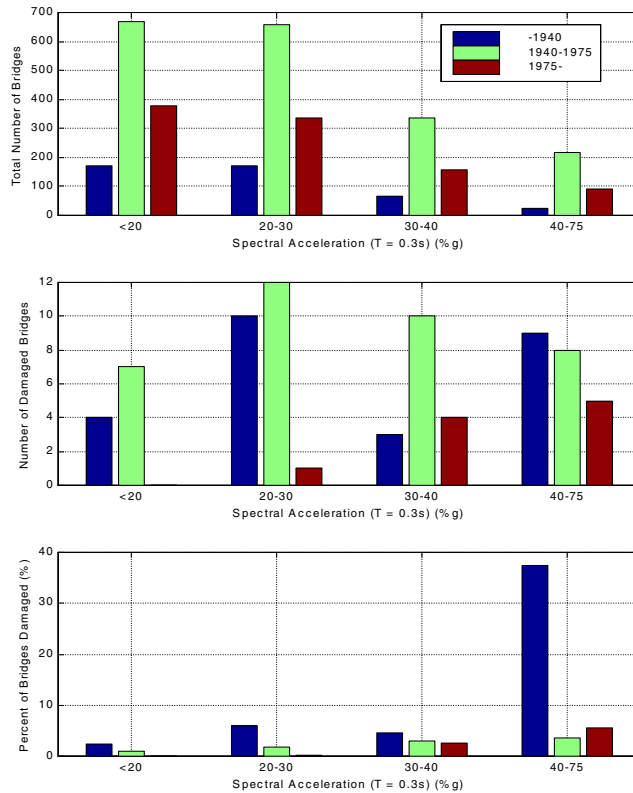


Figure 3-2: Combined effect of spectral acceleration and year of construction

3.1.2 Combined Effect of Spectral Acceleration and Bridge Type

The movable bridges were the most vulnerable type of bridge. Of the forty-two movable bridges within the boundaries of the ShakeMap, six were damaged, resulting in an average damage percentage of 14%. Figure 3-3 shows that the percentage of damaged bridges tended to increase with spectral acceleration. For example, of the nine bridges with estimated spectral accelerations above 0.6g, three (33%) were reported to have suffered damage. There was a notable exception to this trend. None of the eight bridges with estimated spectral accelerations in the range 0.30g to 0.40g were reported to suffer any damage. Such exceptions should be expected for small data sets.

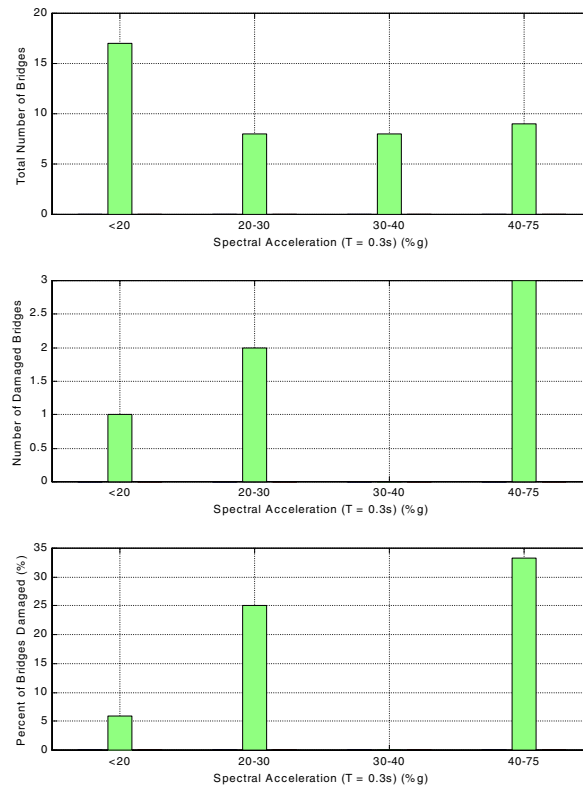


Figure 3-3: Effect of spectral acceleration on movable bridges.

Damage to the three types of immobile bridges; reinforced concrete, pre-stressed concrete and steel, were analyzed as a function of spectral acceleration. In this analysis, movable bridges and bridges with settlement were not considered; settlement damage would not be expected to depend on bridge type. The results of the analysis for the remaining 60 bridges are reported in Figure 3-4.

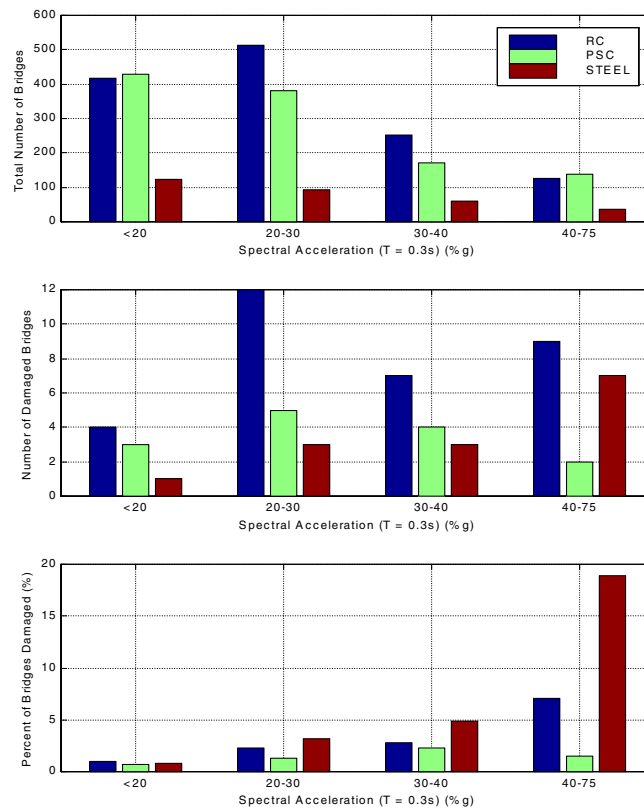


Figure 3-4: Combined effect of spectral acceleration and bridge type

Despite the small number of damaged bridges in each category, Figure 3-4 shows a clear correlation between the percentage of bridges that were damaged and the level of spectral acceleration. Based on this breakdown, it appears that the steel bridges were

more vulnerable than those constructed of reinforced and pre-stressed concrete. However, this observation is not attributable solely to the type of bridge, but to the year that the bridges were constructed, as shown in Fig. 3.5. As shown in this figure, both reinforced concrete and steel bridges that were constructed before 1940 were much vulnerable than bridges constructed later. In addition, 40% of the damage to steel bridges consisted of damage to the reinforced concrete substructure.

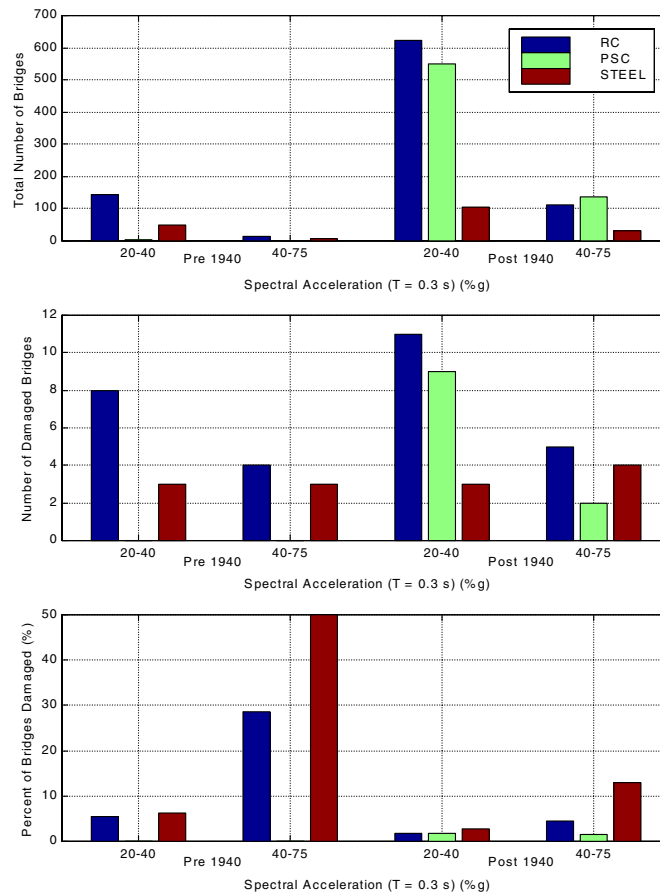


Figure 3-5: Combined effect of spectral acceleration, year of construction, and bridge type.

4. CONCLUSION

Bridge damage data, the Washington State Bridge Inventory and ShakeMaps produced by the Pacific Northwest Seismic Network were used to identify factors that made bridges most vulnerable to the 2001 Nisqually Earthquake. If ShakeMaps are available immediately after an earthquake, the results of this study could be used to prioritize future post-earthquake inspections.

The percentage of bridges that were damaged did not correlate well with the distance from the damaged bridge to the epicenter or the estimated peak ground acceleration at the location of the bridge. The estimated spectral acceleration at 0.3 seconds proved to be a better indicator of the likelihood of bridge damage.

The year in which the bridge was constructed and the type of bridge were also important factors, with the highest percentages of damage were reported for bridges that were built before 1940 and bridges that were movable. For estimated spectral accelerations above 0.4g, damage was reported in 50% of the movable bridges, 29% of the reinforced concrete bridges built before 1940, and 50% of steel bridges built before 1940. Although the percentage of steel bridges damaged was generally higher than for other types of bridges, the number of such bridges was relatively small, and the most common type of damage in steel bridges was not to the steel superstructure, but rather, to the reinforced concrete substructure.

APPENDIX A: DISTANCE CALCULATION

The distance from each bridge to the earthquake epicenter was calculated based on their respective latitudes and longitudes. By knowing the approximate radius of the earth, as well as the latitude and longitude of the point, it is possible to construct the spherical coordinates of this location on the earth's surface. These can then be converted into cartesian coordinates by the following set of equations.

$$\begin{aligned}x &= R \cos \phi \cos \theta \\y &= R \cos \phi \sin \theta \\z &= R \sin \phi\end{aligned}\tag{Eq. A-1}$$

where R is the radius of the earth, ϕ is the latitude and θ is the longitude. ϕ is positive above the equator, and θ is considered positive if east of the International Date Line.

From the rectangular coordinates, the vector formed by connecting the origin to the point on the earth's surface can be determined.

$$P_1 = \begin{bmatrix} x_1 \\ y_1 \\ z_1 \end{bmatrix} \quad P_2 = \begin{bmatrix} x_2 \\ y_2 \\ z_2 \end{bmatrix}\tag{Eq. A-2}$$

P_1 denotes the location of the epicenter, and P_2 denotes the location of the bridge.

The distance between these two points can be calculated as an arc along the earth's surface, or as a straight line (chord) beneath the earth's surface. Because the waves of an earthquake do not follow either of these exactly, and because both calculations would yield approximately the same answer, the arc-based measurement was chosen to estimate epicentral distances.

The angle between the two vectors can be determined by using the equation

$$P_1 \cdot P_2 = \|P_1\| \|P_2\| \cos \beta \quad (\text{Eq. A-3})$$

where β is the angle between the two vectors. Since both the points lay on the Earth's surface, $\|P_1\| = \|P_2\| = R$. Solving for β , the equation becomes

$$\beta = \cos^{-1} \left(\frac{P_1 \cdot P_2}{R^2} \right) \quad (\text{Eq. A-4})$$

Once the angle between the two vectors is known, the arc length between the two points can be determined by the equation

$$D = R\beta \quad (\text{Eq. A-5})$$

where D is the distance between the epicenter and the point of interest. Combining Equations A-1, A-2, A-4 and A-5,

$$D = R \cos^{-1} \frac{\begin{bmatrix} R \cos \phi_1 \cos \theta_1 \\ R \cos \phi_1 \sin \theta_1 \\ R \sin \phi_1 \end{bmatrix} \cdot \begin{bmatrix} R \cos \phi_2 \cos \theta_2 \\ R \cos \phi_2 \sin \theta_2 \\ R \sin \phi_2 \end{bmatrix}}{R^2} \quad (\text{Eq. A-6})$$

Simplifying the above equation, and using the trigonometric identity

$$\cos(A - B) = \cos A \cos B + \sin A \sin B$$

the equation becomes

$$D = R \cos^{-1} [(\cos \phi_1 \cos \phi_2)(\cos(\theta_1 - \theta_2)) + \sin \phi_1 \sin \phi_2] \quad (\text{Eq. A-7})$$

With this equation, the distance from the epicenter to the point of interest can be directly linked to the latitude and longitude of the two points.

APPENDIX B: LIST OF CONTRIBUTORS

Burney, Jay.
Olympia Department of Transportation,
Phone: (360) 753-8740

Buswell, John.
Seattle Department of Transportation,
Phone: (206) 684-5301

Cieri, Dave.
City of Bellevue Department of Transportation,
Phone: (425) 452-2753

Coffman, Harvey.
Washington State Department of Transportation,
Phone: (360) 570-2556

Hale, Mike.
Tacoma Department of Transportation,
Phone: (253) 591-5766

Malone, Steve.
University of Washington,
Phone: (206) 685-3811

Marcus, Jim.
King County Department of Transportation,
Phone: (206) 296-8020

Perry, John.
Federal Emergency Management Agency,
Phone: (360) 596-3015

Pogreba, Don.
Thurston County Department of Transportation,
Phone: (360) 754-4580

Schang, Roger.
Lewis County Engineering Services Division,
Phone: (360) 740-2695

Tahja, Alan.
Mason County Public Works,
Phone: (360) 427-9670 Ext. 461

REFERENCES

1. Earthquake Engineering Research Institute, *The Nisqually Earthquake of 28 February 2001: Preliminary Reconnaissance Report*, March 2001.
2. Washington State Department of Transportation, *Washington State Bridge Inspection Manual*, January 2000
3. Pacific Northwest Earthquake Information - from the PNSN, *Pacific Northwest Seismograph Network*, <http://spike.geophys.washington.edu/SEIS/PNSN/>
4. San Fernando Earthquake Page, <http://www.scecdc.scec.org/sanfer.html>
5. Shake Map, Pacific Northwest Seismograph Network, <http://www.geophys.washington.edu/shake/0102281854/intensity.html>

ACKNOWLEDGMENTS

The author would like to thank the engineers in the bridge agencies who contributed damage reports to this study. A list of the contributors is provided in Appendix D. Harvey Coffman and his staff in the WSDOT Bridge and Structures Preservation Office, and John Buswell (City of Seattle) were particularly helpful.

Dr. Stephen Malone and other members of the PNSN staff provided the ShakeMaps, without which the analyses could not have been conducted. John Perry from Federal Emergency Management Agency provided essential GIS support, which made it possible to link the ShakeMaps and bridge inventory.

Finally, the author would like to recognize the financial support of the National Science Foundation Pacific Earthquake Engineering Research Center, which supported his internship.

Small Scale Rubber Bearing Isolators A Brief Introduction into Low Damping and Lead-Core Bearings

Pamela J Romano
The Catholic University of America
Department of Civil Engineering
Pangborn Hall
Washington, DC 20064-0001

Advisors: Drs A. Reinhorn and A. Whittaker
State University of New York at Buffalo

All research was conducted at the State University of New York at Buffalo and was supported in whole by the National Science Foundation under the Research Experiences for Undergraduates Program, EEC-9701471.

Acknowledgements:

The National Science Foundation provided financial support for this project under the Research Experiences for Undergraduates Program, EEC-9701471. Scougal Rubber Corporation, Seattle, WA manufactured and donated the bearings tested. Special thanks are due to Drs Andrei Reinhorn and Andrew Whittaker for their help in the design of experimentations, contribution in testing and also in the data reduction and formulation of this document and also the presentation that went with it. Also a special thanks to Gordon Warn for his aid in understand the basics of structural dynamics and supervision of testing, and also to Dr Panos Tsopelas of the Catholic University of America for his guidance and suggestion for participating in the REU program.

Outline

- Chapter 1: Introduction
 - 1.1 Seismic Isolation
 - 1.2 Bearing Description
 - Figures 1.1-3
 - Chapter 2: Test Set-Up and Instrumentation
 - 2.1 Description of Small Bearing Testing Machine
 - Figure 2.1
 - 2.2 Description of Load Cell
 - 2.3 Instrumentation
 - Chapter 3: Test Program
 - 3.1 Testing Regimen
 - Figure 3.1
 - 3.2 Description of Input Wave
 - 3.3 Data Collection Procedures
 - Chapter 4: Test Results
 - 4.1 Equations for Determining Characteristics
 - 4.2 Low Damping Bearing Characteristics
 - Figure 4.1
 - 4.3 Lead-Core Bearing Characteristics
 - Figure 4.2
 - 4.4 Response Comparison
 - Figure 4.3
 - 4.5 Scragging
 - Chapter 5: Summary and Conclusions
 - 5.1 Summary
 - 5.2 Conclusion
- References

Figures:

- 1.1: AutoCAD of Bearings
- 1.2: Cross-Section Cutaway of Bearings
- 1.3: Photograph of Bearing
- 2.1: Photograph of Testing Apparatus
- 2.2: Load Cell
- 3.1: Table of Testing Regimen
- 4.1: Force Displacement Graph for Low Damping Bearing
- 4.2: Force Displacement Graph for Lead Core Bearing
- 4.3: Table of Response Comparison

Chapter 1: Introduction

1.1: Base Isolation:

Base isolation is the practice of decoupling a structure from its rigid foundation, by placing an isolation device between the structure and its foundation. Displacement caused by seismic activity is concentrated in the isolator, thus avoiding significant displacement and damage in the structure. Isolation devices are vertically stiff, but horizontally flexible. In elastomeric bearings, this is achieved through a laminated construction of alternating layers of steel (shims) and rubber. The rubber layers provide horizontal flexibility. Steel shims used together with thin layers of rubber provide the high levels of vertical stiffness.

1.2: Bearing Description:

Scougal Rubber Corporation manufactures both the low damping and the lead-core bearings tested. The dimensions of the bearings are as follows; 5.02" tall, with a 7.25" diameter, including the 1/8" casing surrounding the bearing. The total diameter of rubber then is 7". The cylinder is made up of steel shims encased in rubber layers. There are 18 rubber layers 1/8" thick each adding up to a total of 2.25" of rubber. A 1" diameter core is bored through the bearing. This core is filled with lead for the lead core bearings. The bearings are mounted to the endplates by four 3/4" holes in the endplate of 3/4". The following figures are the AutoCAD drawings, made using AutoCAD 2000 (Fig 1.1), a cross-section (Fig 1.2), and a photograph of the bearings under testing, taken with a digital camera (Fig 1.3).

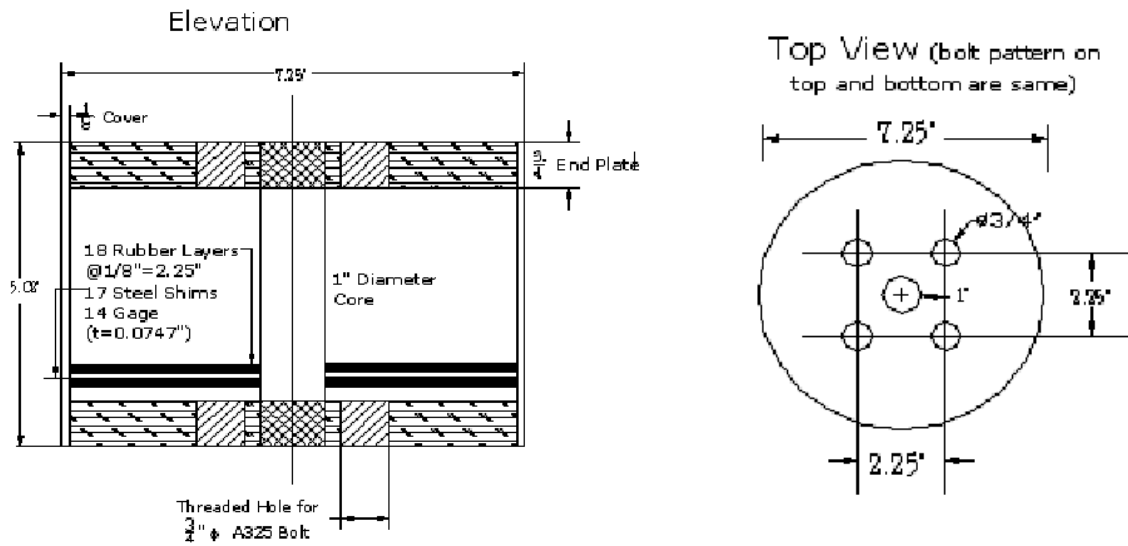


(Fig 1.1)

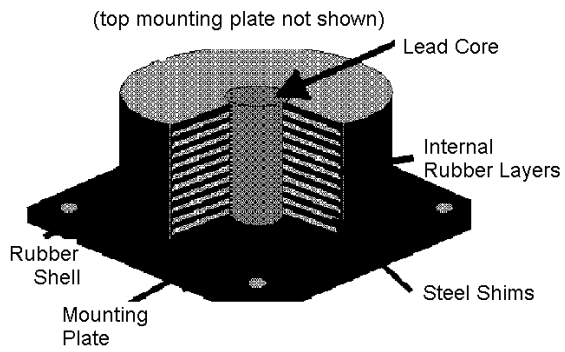


(Fig 1.2)

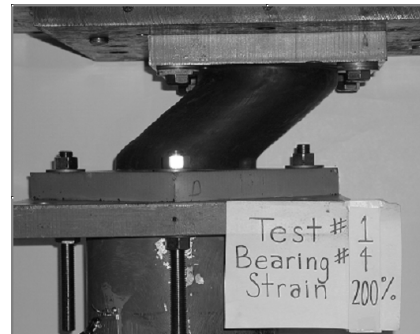


(Fig 1.3)

Chapter 2: Test Set-Up and Instrumentation

2.1: Small Bearing Testing Machine¹:

This machine has been developed for the testing of single bearings under controlled conditions of vertical load, lateral movement and rotational movement. It has a 140 kip (622.8 kN) vertical load capacity, 55 kip (244.7 kN) horizontal load capacity, ± 6 in. (15.24 cm) horizontal movement capacity with up to 15 in./sec (381 mm/sec) velocity, and rotational capability of ± 2 degrees. Reaction forces can be directly measured by a multi-component load cell which currently has a rated capacity of 20 kips (89 kN) shear and 50 kips (222.4 kN) axial load. The machine can be used in the testing of elastomeric and sliding bearings, including tests under variable axial load and tests of bearings pre-stressed by tendons to prevent uplift. Figure 2.1 presents a view of the testing machine during testing of an elastomeric bearing.

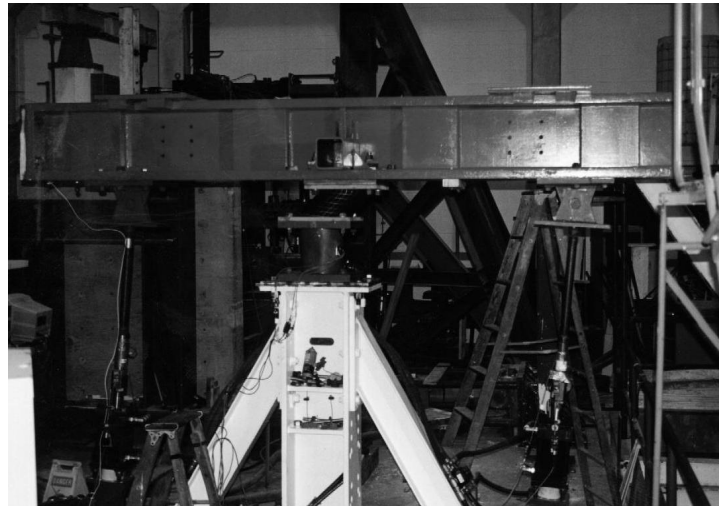


(Fig 2.1)

¹ SEESL Description of Laboratory Equipment
(<http://overlord.eng.buffalo.edu/cie/facilities/seesl/DescriptionOfLaboratoryEquipment.html>)

Chapter 3: Test Program

3.1 Testing Regimen:

Testing followed the load, % shear attained and the frequency at which the bearing was oscillated shown in Figure 3.1. The Recovery test was performed the day after the bearing underwent the previous 5 tests to allow some of the original stiffness to be restored.

Test #	% Shear					Freq (Hz)	Load (kips)
	5	25	50	100	200		
1	5	25	50	100	200	0.01	28
2	5	25	50	100	200	0.50	28
3	200	100	50	25	5	0.01	28
4	5	25	50	100	200	0.01	28
5	5	25	50	100	200	0.01	14
Recovery	5	25	50	100	200	0.01	7

(Fig 4.1)

3.2 Input Wave:

The input wave was a displacement controlled sinusoidal manufactured using Mat LAB 5.0 and inputted into the small bearing testing machine using LabTECH for MS-DOS. Each test was comprised of three cycles at each of the five percent shears (100% shear = 7"). A smoothing function was introduced at each junction between changes in percent shear to lessen the jump in displacements during the transition.

3.3 Data Collection Procedures:

The displacement controlled sinusoidal resulted in a force for each measurement taken. These forces were recorded in the Lab TECH program and then the force-displacement hysteretic data was transferred as an ASCII file to a mainframe computer for data reduction.

Chapter 4: Test Results

4.1 Equations for Determining Characteristics:

Using typical³ equations for the characteristics of low damping and lead core bearings, a comparison could be made. The equation for the stiffness for the low damping and lead core can be found. Stiffness can be found by $K=GA/T_r$; G being the modulus of elasticity, T_r the thickness of the rubber and A the area of the rubber. Damping ($\beta=W_d/2\pi K_{eff}D_{max}^2$) is the same for both low damping and also lead-core bearings where W_d is the area of the hysteretic loop, K_{eff} is the stiffness of the rubber and D_{max} is the maximum displacement the bearing undergoes.

4.2 Low Damping Bearing Characteristics:

Utilizing the above equations and an Excel spreadsheet the typical characteristics of the low damping bearing were found. The characteristic loop of the bearing is the 100% shear loop in the hysteretic graph of force v displacement. Figure 4.1 is the force-displacement graph attained through testing of the low damping bearing. Using this graph and the 100% shear strain loop the K_{eff} , β and G where found.

³ Naiem, F and Kelly, J. *Design of Seismic Isolated Structures*, Wiley and Sons, INC., New York, 1999, pgs 94-98

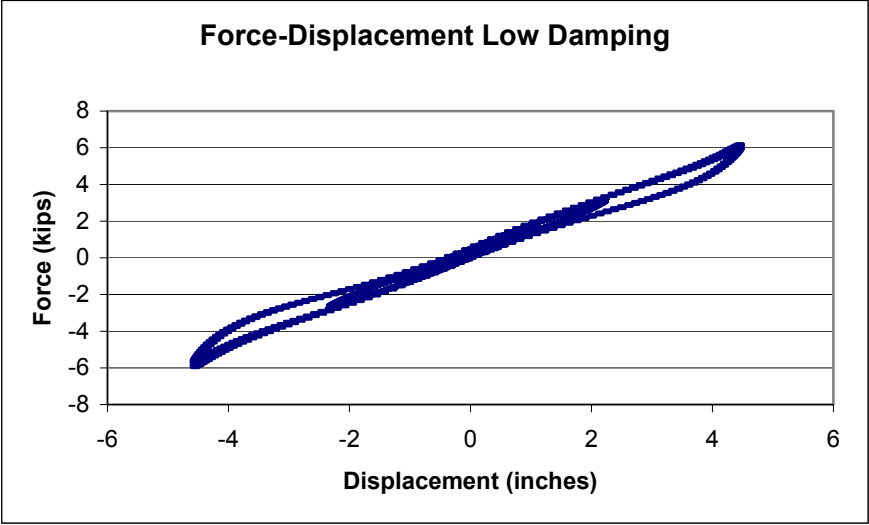


(Fig 4.1)

4.3 Lead-Core Bearing Characteristics:

Similarly the lead-core bearings underwent the data reduction in excel spreadsheets and the K_{eff} , β and G were found. In Figure 4.2 the force-displacement for the lead-core bearing can be found.

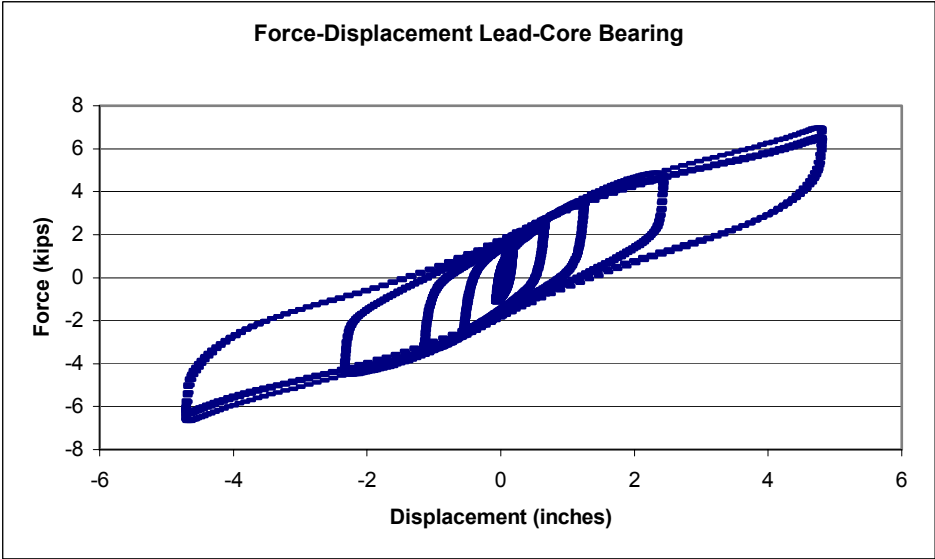


(Fig. 4.2)

4.4 Response Comparison:

Figure 4.3 is a table of the characteristics for both kinds of bearings, the values in the table were found using the equations described above and the 100% shear for each of the tests run. Two of each bearing was tested allowing for a total of four bearings.

Bearing Test	Keff (kips/in)	Disp _{max} (in)	Tr(in)	Ar(in ²)	beta(%)	Geff (psi)
LD1	1.00	1.52	2.30	2.25	38.48	88.80
	2.00	1.43	2.12	2.25	38.48	83.33
	3.00	1.34	2.15	2.25	38.48	78.43
	4.00	1.41	2.12	2.25	38.48	82.68
	5.00	1.43	2.20	2.25	38.48	83.60
	recovery	1.34	2.33	2.25	38.48	78.41
LD3	1.00	1.51	2.25	2.25	38.48	88.40
	2.00	1.44	2.24	2.25	38.48	84.01
	3.00	1.33	2.26	2.25	38.48	77.65
	4.00	1.40	2.20	2.25	38.48	81.67
	5.00	1.41	2.30	2.25	38.48	82.39
	recovery	1.20	2.24	2.25	38.48	70.12
LC4	1.00	1.55	2.12	2.25	38.48	90.36
	2.00	1.48	2.17	2.25	38.48	86.74
	3.00	1.38	2.19	2.25	38.48	80.79
	4.00	1.47	2.12	2.25	38.48	85.92
	5.00	1.49	2.18	2.25	38.48	87.30
	recovery	1.40	2.46	2.25	38.48	81.74
LC3	1.00	1.84	2.55	2.25	38.48	107.57
	2.00	1.88	2.38	2.25	38.48	109.80
	3.00	1.66	2.38	2.25	38.48	97.32
	4.00	1.75	2.41	2.25	38.48	102.15
	5.00	1.72	2.38	2.25	38.48	100.37
	recovery	1.78	2.43	2.25	38.48	104.00

(Fig 4.3)

4.5 Scragging:

Scragging is a very important consideration in every bearing design. Scragging is the response of virgin, or untested bearing versus one that has undergone some seismic activity. Typically an unscragged bearing transmits more of the force to the superstructure than one that has been scragged. For the two types (four bearings) tested the different changes in force

transmitted from the scragged to unscragged bearing can be found. The low damping bearing has about a 7% increase in force, while the lead-core bearing has close to a 16% force increase, which is enough to be more concerned with the forces felt in the superstructure. Scragging is very important because when a bearing has time to recover, that is, it has time to regain some of its natural characteristics, the increase in force transmittance can once again be felt allowing for greater forces in the superstructure.

Chapter 5: Summary and Conclusions

5.1 Summary:

Through testing and data reduction the characteristics of low damping and lead-core rubber bearing isolators could be found. The characteristics for the bearings tested are in line with previous research and also typical for the assumptions in design of bearings. The bearings underwent a displacement controlled sinusoidal so that the force in the bearing could be measured. Using the force-displacement graphs from the resulting tests the characteristics could be determined.

5.2 Conclusions:

By looking at the damping and also the scragging of each type of bearing, it is easy to see that in certain cases one type of bearing would be preferred over the other. In places of high seismic activity, but low initial forces, the lead-core bearings would be beneficial, in that they provide high damping, but also a high transference of force in the unscragged condition.

References:

Naiem, F and Kelly, J. *Design of Seismic Isolated Structures*, Wiley and Sons, INC., New York, 1999.

Kasalanati, A. and Constantinou, M., *Experimental Study of Bridge Elastomeric and Other Isolation and Energy Dissipation Systems with Emphasis on Uplift Prevention and High Velocity Near-Source Seismic Excitation*, MCEER, Buffalo, NY, 1999.

SEESL Description of Laboratory Equipment

(<http://overlord.eng.buffalo.edu/cie/facilities/seesl/DescriptionOfLaboratoryEquipment.html>)

Shear Strength of Rectangular Building Columns Under Seismic Loads

Mike Rookstool
University of Texas at Austin

Pacific Earthquake Engineering Research Center
University of California, Berkeley
Jack Moehle
Halil Sezen

Abstract

Reinforced concrete columns with pre 1970's design do not have adequate shear strength to prevent catastrophic failure during earthquakes. Existing columns in seismic areas must be retrofitted to meet current standards. The current ACI equation is found to be inconsistent in determining shear strength of older columns. An alternative equation is proposed to more accurately predict column shear strength during earthquakes. The proposed equation contains a strength reducing a/d factor and a ductility coefficient.

Column test results were used to compare the measured shear strength to the shear strength predicted by the proposed and ACI equations. Out of 46 columns, the proposed equation had more accuracy and greater consistency than the ACI equation. For reason, the proposed equation is recommended for evaluating the shear strength of existing columns.

“Although we can't predict or prevent earthquakes, we *can* prepare for them.” – **David Schwartz, USGS geologist**



Market Street, San Francisco, after the 1906 earthquake.

INTRODUCTION

Despite all the recent testing, shear strength of reinforced concrete columns is still not well understood. Many of the recent catastrophic failures of columns during earthquakes have been shear failures.

The purpose of this project was to more accurately predict the shear strength of reinforced concrete columns for use in seismic regions. This is part of the wide study of building frame collapse done at the Pacific Earthquake Engineering Research Center (PEER) of the University of California, Berkeley. The study is being conducted by Jack Moehle, Ken Elwood, and Halil Sezen.

Many of the columns failing during earthquakes were designed more than 30 years ago. An alternative equation for measuring shear strength of existing columns is proposed. The proposed equation can be used to determine the shear resistance in existing columns that were designed when possible inadequate shear strength was overlooked.

The main difference between the proposed equation and the current ACI equation is that the ACI code does not account for ductility of the column under lateral loading. The proposed equation considers ductility quantitatively with a ductility factor, which may reduce the shear strength by as much as 30% if there is excessive reinforcement.

BACKGROUND

The columns used in the analytical testing were taken from the University of Washington's PEER website. The columns had to meet the following criteria: $f'_c < 5000$ psi, $.01 < \rho_{long} < .08$, $a/d \text{ ratio} < 4.0$, and failure in shear. Of the 210 columns in the Washington database, 46 met the criteria and were used to evaluate the accuracy of the alternative equation.

The columns used in the database were taken from various tests. Lynn tested eight full-scale double curvature columns under gravity load. Sezen tested four small-scale double curvature columns also under gravity load. Esaki tested six double curvature columns under constant axial and varying lateral load. Li tested nine cantilever columns under varying axial load and cyclic lateral load. Imai tested one full size, double curvature specimen to simulate columns in a damaged school building. Ohue tested eleven double curvature short columns under static and dynamic loading. Ono studied four double curvature columns subjected to fluctuating axial load. Wight & Sozen subjected twelve double-ended columns to large transverse displacement reversals, some under axial load. Zhou tested double curvature small-scale columns under high axial load ratio. Bett tested three double curvature short columns under constant axial compression and reversed cyclic lateral loads. Arakawa tested fourteen double-curvature short columns under different loading directions.

CURRENT ACI EQUATION

The shear strength of a reinforced concrete column is the sum of both the concrete and the transverse steel resistances. The shear strength from the steel is given in Equation 1, and the concrete contribution in Equation 2.

$$V_s = \frac{A_v f_y d}{s} \quad (1)$$

$$V_c = 2 \left(1 + \frac{N}{2000 A_g} \right) \sqrt{f'_c} b_w d \quad (2)$$

Finally, the total shear strength of a column is calculated from Equation 3.

$$V_n = V_c + V_s \quad (3)$$

PROPOSED ALTERNATIVE EQUATION

The shear strength may be reduced if the column is extremely ductile. This is accounted for in the ductility factor k , as seen in Equations 4 and 6. The ductility factor k is calculated using μ , the ductility displacement. Figure 1 is a graph of k vs. μ . Equation 4 is for the steel component of the shear resistance, which is the same as Equation 1 but with the k coefficient.

$$V_s = \frac{A_v f_y d}{s} k \quad (4)$$

The concrete portion of the shear strength is derived using a stress transformation. Given that the tensile strength of concrete is $f_{tc} = 6\sqrt{f'_c}$, the corresponding shear stress at which the maximum tensile stress is reached can be given by Equation 5.

$$\tau_{xy} = 6\sqrt{f'_c} \sqrt{1 + \frac{P}{6A_g\sqrt{f'_c}}} \quad (5)$$

Shear strength is reduced by the tendency of a long, slender column to bend in flexure. This reduction is accounted for by dividing by the shear aspect ratio, a/d . After also applying the ductility factor k , the concrete contribution of the shear strength is shown in Equation 6.

$$V_c = k \left(\frac{6\sqrt{f'_c}}{a/d} \sqrt{1 + \frac{N_u}{6\sqrt{f'_c} A_g}} \right) 0.8 A_g \quad (6)$$

A limit of 2.0 was placed on the strength reducing effects of the a/d ratio, meaning any columns shorter than that were taken as $a/d = 2.0$.

DISPLACEMENT ESTIMATION

To calculate the ductility factor k , the displacement ductility μ was needed. Much of the column testing results did not report yield displacement values and the ones that did we calculated using different methods, so a consistent process for estimating δ_y was necessary.

Yield displacement was determined by drawing a line from the origin to the intersection of the hysteresis curve at 70% maximum shear. This line was extended to the maximum shear level, and then projected onto the horizontal axis, which was the yield displacement. The ultimate displacement, δ_u , was defined as maximum displacement at a force not less than 80% of the maximum applied shear. The accuracy of the δ_y estimation method was compared to the actual δ_y for the columns that reported

it. This comparison is shown in Figure 2. Out of 27 columns that reported δ_y , the average difference between actual and estimated δ_y was 18%. Thus this method of estimating yield displacement was taken to be accurate.

RESULTS

The columns tested failed in one of three ways: flexure, shear, or shear-flexure combination. The column will fail at whichever strength is lower, flexural strength or shear strength, or sometimes in a combination if the strengths are close.

The columns failing in shear should have a V_{flex}/V_{shear} value greater than one, while the flexural failing columns will have a V_{flex}/V_{shear} less than one.

Shear-Flexure combination failures will be slightly above or below one. The column may initially crack in one mode, but ultimately fail in another, resulting in V_{flex}/V_{shear} values of slightly greater than or less than one.

Flexural Failure

Columns failing in flexure are characterized by significant cracking at the top and bottom of the column due to excessive bending. Flexural failure is common in long, slender members because of the large moment value resulting from a lateral load.

The shear strength in columns of this type of failure was far larger than their flexural strength, so the maximum shear strength was never reached. Since the proposed equation deals with predicting shear strength, these columns cannot be used to evaluate the accuracy of the equation. For this reason, flexural failing columns were not used in

the column database. The predicted strength of the flexural failing columns was not accurate for either the proposed equation or ACI equation.

Shear Failure

For columns failing in shear, diagonal cracks appear throughout the column. A diagram of shear cracking in a column subjected to a lateral force is shown in Figure 3.

Shorter columns tend to fail most often in shear because there is not a large enough moment developed for the column to fail in flexure.

The column shear strength from the testing was divided by both the proposed and ACI equations to measure accuracy. Thus, the closer to unity the value is, the more accurate the equation.

The average and standard deviation using each equation are shown in Table 1. Not only did the proposed equation result in a ratio closer to one, the standard deviation is much smaller when using the proposed equation. For its greater consistency and accuracy, the proposed equation is considered a better estimate of column shear strength. Figure 4 compares the actual shear strength to the strength predicted from the proposed and ACI equation.

CONCLUSIONS

Understanding shear behavior in columns is extremely important for two reasons. First, shear failures are often sudden and catastrophic, resulting in severe damage to the structure. Second, columns designed under the pre-1970s code neglected shear failures.

In areas of high seismic activity, shear behavior of columns cannot be overlooked, as it is often the controlling factor.

The following important conclusions should be taken from this report:

- (1) Ductility plays an important role in the shear strength of columns during earthquakes. The shear strength of the column must be understood to make an appropriate retrofit for columns designed under pre-1970s code.
- (2) The current ACI equation greatly overestimates the shear strength of columns using high strength concrete, oftentimes by as much as 300%. While the proposed equation does not provide an accurate estimate either, the current design guidelines for high strength concrete use in seismic regions must be improved.
- (3) The proposed equation is more accurate than the ACI equation in predicting shear strength in shorter and medium length columns with a/d ratios less than four.
- (4) Due to its accuracy and greater consistency, the proposed equation is recommended over the current ACI equation in evaluating existing reinforced concrete columns in seismic regions.

ACKNOWLEDGEMENTS

This research was done at the Pacific Earthquake Engineering Research Center at the University of California, Berkeley, and was funded by the National Science Foundation.

Acknowledgements go to Halil Sezen and Jack Moehle who oversaw the project. Also to Patxi Uriz for computer help and to Chuck James, who helped gather information from various sources.

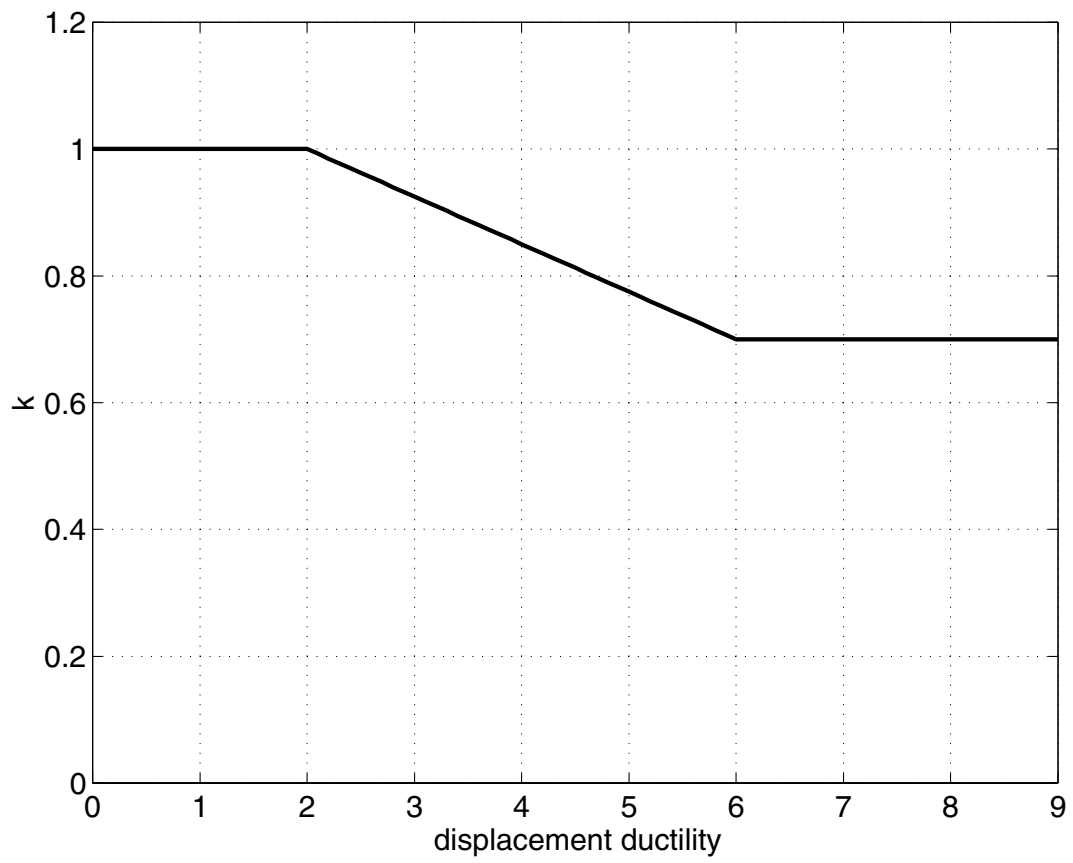


Figure 1. Proposed ductility factor k

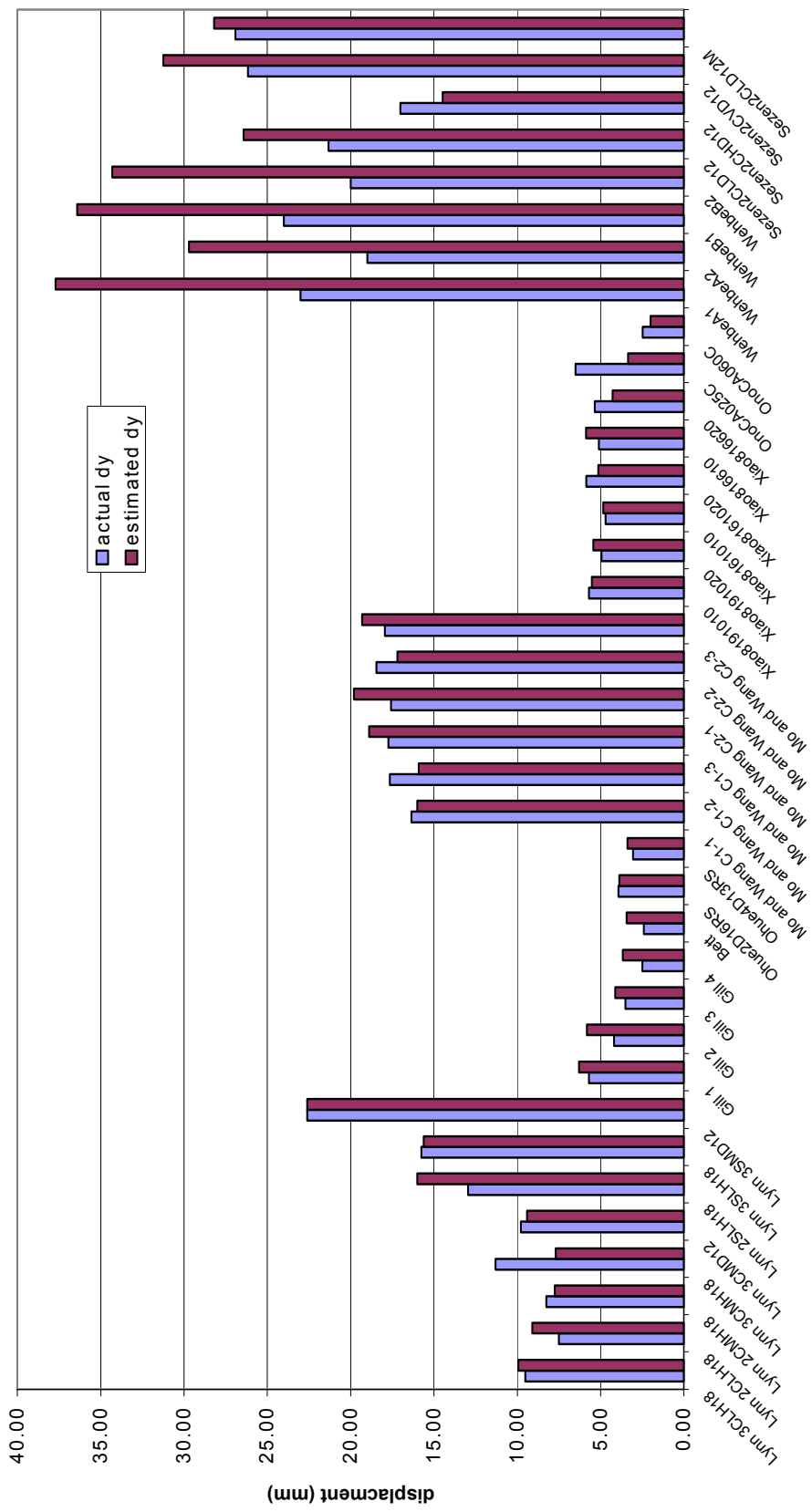


Figure 2. Comparison of estimated yield displacement (dy) to actual yield displacement

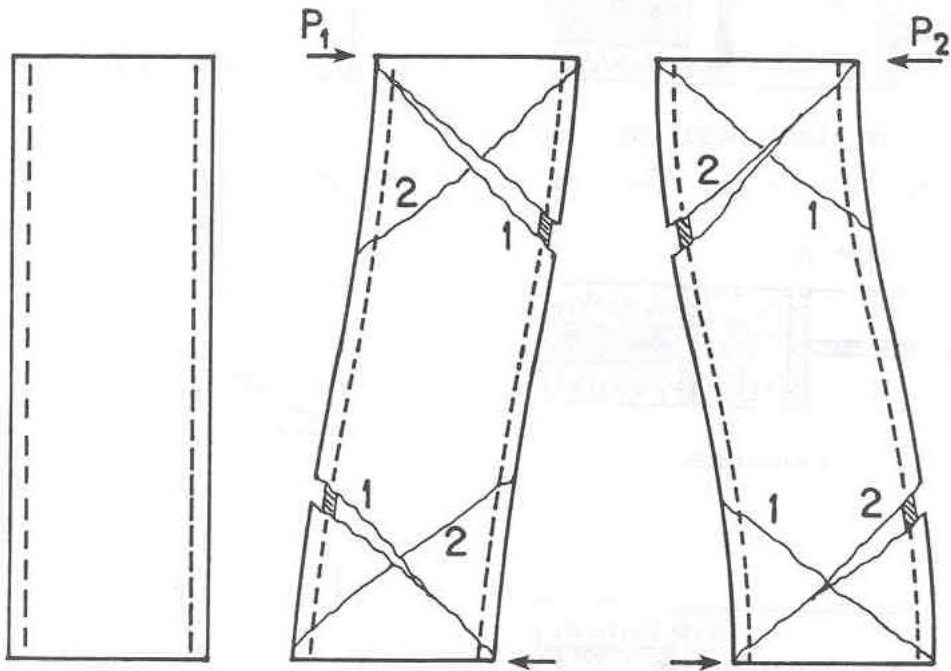


Figure 3. Shear cracking in a column subjected to a lateral load P.

Table 1. Comparison of V_n/V_{test} for Proposed Equation and ACI Equation

	Proposed	ACI
Average*	0.99	1.03
Std. Dev	0.21	0.36
*1 when V_n & V_{test} are the same		

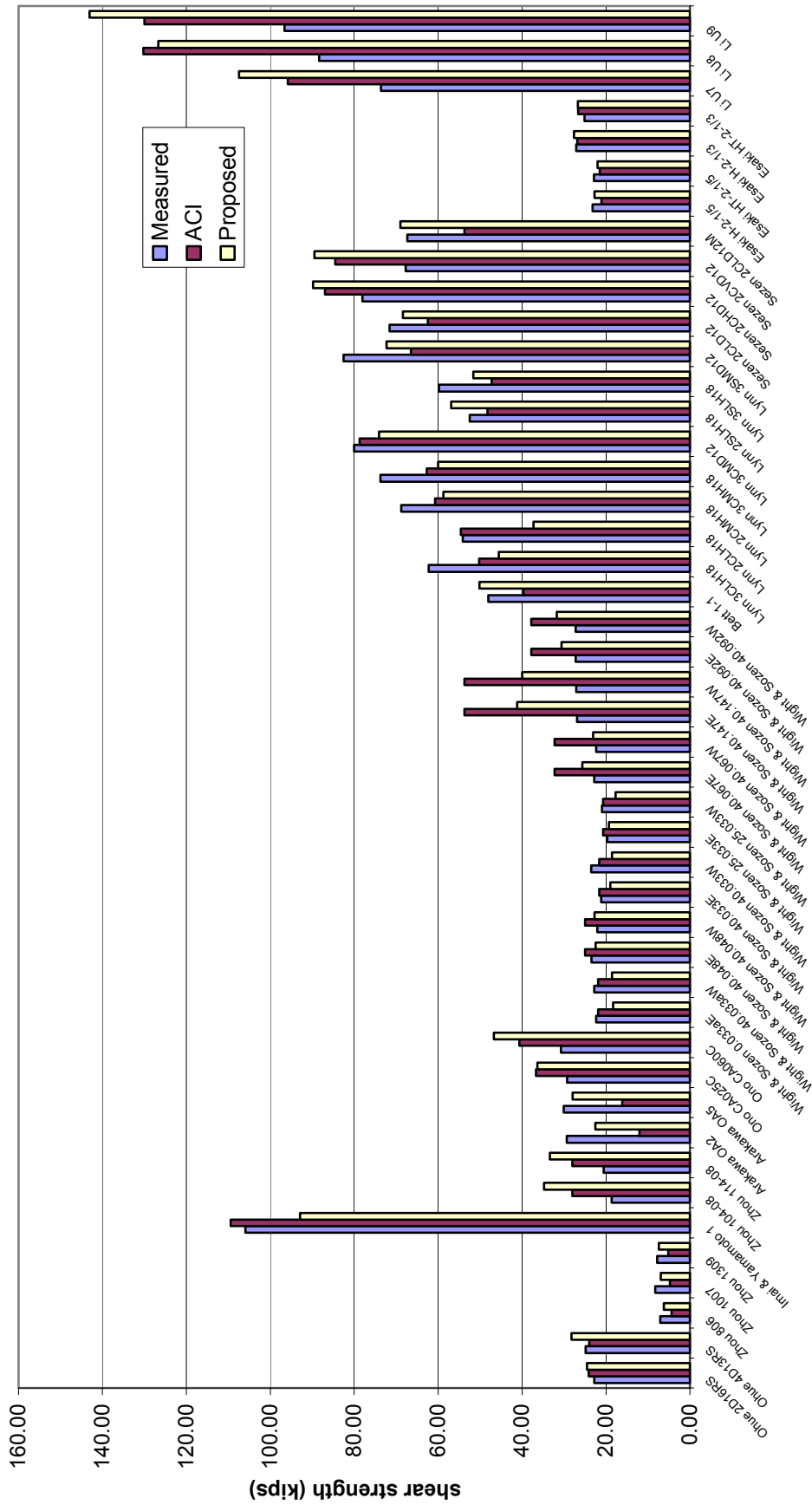


Figure 4. Accuracy of Proposed Equation and ACI Equation

Readability Statistics	
Counts	
Words	1519
Characters	7993
Paragraphs	59
Sentences	86
Averages	
Sentences per Paragraph	2.7
Words per Sentence	16.8
Characters per Word	5.1
Readability	
Passive Sentences	38%
Flesch Reading Ease	46.7
Flesch-Kincaid Grade Level	10.9

OK

References

- 1 Aboutaha, R.S.; and Machado, R.I., "Seismic Resistance of Steel-Tubed High-Strength Reinforced-Concrete Columns", *Journal of Structural Engineering*, May 1999, pp. 485-494.
- 2 Aboutaha, R.S.; Engelhardt, M.D.; Jirsa, J.O.; and Kreger, M.E.; "Rehabilitation of Shear Critical Concrete Columns by Use of Rectangular Steel Jackets", *American Concrete Institute, ACI Structural Journal*, Vol. 96, No.1, January-February 1999, pp.68-78.
- 3 Amitsu, Shigeyuki; Shirai, Nobuaki; Adachi, Hiromi; and Ono, Arata, "Deformation of Reinforced Concrete Column with High or Fluctuating Axial Force," *Transactions of the Japan Concrete Institute*, Vol. 13, 1991, pp. 355-362
- 4 Ang Beng Ghee; Priestley, M.J.N.; and Park, R., "Ductility of Reinforced Bridge Piers Under Seismic Loading," Report 81-3, Department of Civil Engineering, University of Canterbury, Christchurch, New Zealand, February 1981, 109 pages
- 5 Arakawa, Takashi; Arai, Yasuyuki; Egashira, Keiichi; and Fujita, Yutaka, "Effects of the Rate of Cyclic Loading on the Load-Carrying Capacity and Inelastic Behavior of Reinforced Concrete Columns," *Transactions of the Japan Concrete Institute*, Vol. 4, 1982, pp. 485-492
- 6 Arakawa, Takashi; Arai, Yasuyuki; Mizoguchi, Mitsuo; and Yoshida, Minoru, "Shear Resisting Behavior of Short Reinforced Concrete Columns Under Biaxial Bending-Shear," *Transactions of the Japan Concrete Institute*, Vol. 11, 1989, pp. 317-324.
- 7 Atalay, M.B.; and Penzien, J. "The Seismic Behavior of Critical Regions of Reinforced Concrete Components as Influenced by Moment, Shear and Axial Force," Report No. EERC 75-19, University of California, Berkeley, December 1975, 226 pages.
- 8 Azizinamini, Atorod; Johal, Lakhpal S.; Hanson, Norman W.; Musser, Donald W.; and Corley, William G.; "Effects of Transverse Reinforcement on Seismic Performance of Columns – A Partial Parametric Investigation," Project No. CR-9617, Construction Technology Laboratories, Skokie, Illinois, Sept. 1988.
- 9 Bayrak, Oguzhan; Sheikh, Shamim, "Confinement Steel Requirements for High Strength Concrete Columns," Paper No. 463, Eleventh World Conference on Earthquake Engineering, 1996.

- 10 Bett, Bart J.; Klingner, Richard E.; and Jirsa, James O., "Behavior of Strengthened and Repaired Reinforced Concrete Columns Under Cyclic Deformations," PMFSEL Report No. 85-3 Department of Civil Engineering, University of Texas at Austin, Austin, Texas, December 1985, 75 pages.
- 11 Esaki, Fumiya, "Reinforcing Effect of Steel Plate Hoops on Ductility of R/C Square Column," Eleventh World Conference on Earthquake Engineering, Paper No. 199, 1996
- 12 Galeota, D.; Giammatteo, M.M.; Marino, R., "Seismic Resistance of High Strength Concrete Columns." Proceedings of the Eleventh World Conference on Earthquake Engineering, Disc 3, Paper No. 1390, 1996.
- 13 Gill, Wayne Douglas; Park, R.; and Priestley, M.J.N., "Ductility of Rectangular Reinforced Concrete Columns With Axial Load," Report 79-1, Department of Civil Engineering, University of Canterbury, Christchurch, New Zealand, February 1979, 136 pages.
- 14 Imai, Hiroshi; and Yamamoto, Yoshie, "A Study on Causes of Earthquake Damage of Izumi High School Due to Miyagi-Ken-Oki Earthquake in 1978," Transactions of the Japan Concrete Institute, Vol. 8, 1986, pp. 405-418.
- 15 Kanda, Makoto; Shirai, Nobuaki; Adachi, Hiromi; and Sato, Toshio, "Analytical Study on Elasto-Plastic Hysteretic Behaviors of Reinforced Concrete Members," Transactions of the Japan Concrete Institute, Vol.10, 1988, pp. 257-264. (Specimens 85STC-3 and 85PDC-3 only)
- 16 Li, Xinrong; "Reinforced Concrete Columns Under Seismic Lateral Force and Varying Axial Load," Ph.D. Thesis, University of Canterbury, Christchurch, New Zealand, 1995, 342 pages.
- 17 Lynn, A., Moehle, J.P., Mahin, S.A., Holmes, W.T., "Seismic Evaluation of Existing Reinforced Concrete Building Columns," Earthquake Spectra, Nov. 1996, 715-739
- 18 Lynn, Abraham; "Seismic Evaluation of Existing Reinforced Concrete Building Columns," Ph.D. Thesis, University of California at Berkeley, Berkeley, California, 1999, 284 pages.
- 19 Matamoros, A.B.; "Study of Drift Limits for High-Strength Concrete Columns," Department of Civil Engineering, University of Illinois at Urbana-Champaign, Urbana, Illinois, Oct 1999.

- 20 Mo, Y.L.; and Wang, S.J., "Seismic Behavior of RC Columns with Various Tie Configurations", *Journal of Structural Engineering*, ASCE, Vol. 126 No.10, October, 2000, pp. 1122-1130
- 21 Muguruma, Hiroshi; Watanabe, Fumio; and Komuro, Tsutomu, "Applicability of High Strength Concrete to Reinforced Concrete Ductile Column," *Transactions of the Japan Concrete Institute*, Vol. 11, 1989, pp. 309-316.
- 22 Nagasaka, Tomoya, "Effectiveness of Steel Fiber as Web Reinforcement in Reinforced Concrete Columns," *Transactions of the Japan Concrete Institute*, Vol. 4, 1982, pp. 493-500.
- 23 Nosho, Kirk; Stanton, John; and MacRae, Gregory; "Retrofit of Rectangular Reinforced Concrete Columns using Tonen Forca Tow Sheet Carbon Fiber Wrapping," Report No. SGEM 96-2, Department of Civil Engineering, University of Washington, Seattle, Washington, July 1996.
- 24 Ohno, Tomonori; and Nishioka, Takashi, "An Experimental Study on Energy Absorption Capacity of Columns in Reinforced Concrete Structures," *Proceedings of the JSCE, Structural Engineering/Earthquake Engineering*, Vol. 1, No 2., October 1984, pp. 137-147.
- 25 Ohue, Minoru; Morimoto, Hisao, Fujii, Shigeru; and Morita, Shiro, "The Behavior of R.C. Short Columns Failing in Splitting Bond-Shear Under Dynamic Lateral Loading," *Transactions of the Japan Concrete Institute*, Vol. 7, 1985, pp. 293-300.
- 26 Ono, Arata; Shirai, Nobuaki; Adachi, Hiromi; and Sakamaki, Yoshio, "Elasto-Plastic Behavior of Reinforced Concrete Column With Fluctuating Axial Force," *Transactions of the Japan Concrete Institute*, Vol. 11, 1989, pp. 239-246
- 27 Park, R.; and Paulay, T., "Use of Interlocking Spirals for Transverse Reinforcement in Bridge Columns." *Strength and Ductility of Concrete Substructures of Bridges*, RRU (Road Research Unit) Bulletin 84, Vol. 1, 1990, pp. 77-92.
- 28 Saatcioglu, Murat; and Grira, Mongi, "Confinement of Reinforced Concrete Columns with Welded Reinforcement Grids," *American Concrete Institute, ACI Structural Journal*, Vol. 96, No. 1, January-February 1999, pp. 29-39.
- 29 Saatcioglu, Murat; and Ozcebe, Guney, "Response of Reinforced Concrete Columns to Simulated Seismic Loading," *American Concrete Institute, ACI Structural Journal*, January – February, 1989, pp. 3-12.

- 30 Sakai, Yuuki; Hibi, Junichi; Otani, Shunsuke; and Aoyama, Hiroyuki, "Experimental Study on Flexural Behavior of Reinforced Concrete Columns Using High-Strength Concrete," *Transactions of the Japan Concrete Institute*, Vol. 12, 1990, pp. 323-330.
- 31 Sezen, Halil, "Evaluation and Testing of Existing Reinforced Concrete Columns," *CE 299 Report*, Department of Civil and Environmental Engineering, UC Berkeley, 2000
- 32 Soesianawati, M.T.; Park, R; and Priestley, M.J.N., "Limited Ductility Design of Reinforced Concrete Columns," Report 86-10, Department of Civil Engineering, University of Canterbury, Christchurch, New Zealand, March 1986, 208 pages.
- 33 Sugano, Shunsuke, "Seismic Behavior of Reinforced Concrete Columns Which used Ultra High-Strength Concrete," Paper No. 1383, Eleventh World Conference on Earthquake Engineering, 1996.
- 34 Tanaka, H.; and Park, R., "Effect of Lateral Confining Reinforcement on the Ductile Behavior of Reinforced Concrete Columns," Report 90-2, Department of Civil Engineering, University of Canterbury, June 1990, 458 pages.
- 35 Thomsen, John; and Wallace, John, "Lateral Load Behavior of Reinforced Concrete Columns Constructed Using High-Strength Materials," *American Concrete Institute, ACI Structural Journal*, Vol. 91, No. 5, September-October 1994, pp. 605-615.
- 36 Umehara, H.; and Jirsa, J.O., "Shear Strength and Deterioration of Short Reinforced Concrete Columns Under Cyclic Deformations," PMFSEL Report No. 82-3, Department of Civil Engineering, University of Texas at Austin, Austin Texas, July 1982, 256 pages.
- 37 Watson, Soesianawati; and Park, R., "Design of Reinforced Concrete Frames of Limited Ductility," Report 89-4, Department of Civil Engineering, University of Canterbury, Christchurch, New Zealand, January 1989, 232 pages.
- 38 Wehbe, N., Saiidi, M.S., and Sanders, D., "Confinement of Rectangular Bridge Columns for Moderate Seismic Areas," *National Center for Earthquake Engineering Research (NCEER) Bulletin*, Volume 12, Number 1, Spring 1998.
- 39 Wight, J.K.; and Sozen, M.A., "Shear Strength Decay in Reinforced Concrete Columns Subjected to Large Deflection Reversals," *Structural Research Series No. 403*, Civil Engineering Studies, University of Illinois, Urbana-Champaign, Ill., Aug 1973, 290 pages.

- 40 Xiao, Yan; and Martirosyan, Armen, "Seismic Performance of High-Strength Concrete Columns," *Journal of Structural Engineering*, March, 1998, pp. 241-251.
- 41 Zahn, F.A.; Park, R; and Priestley, M.J.N., "Design of Reinforced Bridge Columns for Strength and Ductility," Report 86-7, Department of Civil Engineering, University of Canterbury, Christchurch, New Zealand, March 1986, 330 pages.
- 42 Zhou, Xiaoshen; Satoh, Toshio; Jiang, Weishan; Ono, Arata; and Shimizu, Yasushi, "Behavior of Reinforced Concrete Short Column Under High Axial Load," *Transactions of the Japan Concrete Institute*, Vol. 9, 1987, pp. 541-548.
- 43 Zhou, Xiaozhen; Higashi, Yoichi; Jiang, Weishan; and Shimizu, Yasushi, "Behavior of Reinforced Concrete Column Under High Axial Load," *Transactions of the Japan Concrete Institute*, Vol. 7, 1985, pp. 385-392
- 44 http://www.ce.washington.edu/~peera1/index_columns.html "Reinforced Concrete Column Test Database." August 7, 2001.
- 45 <http://www.johnmartin.com/eqshow/Wweqshow.htm> "Earthquake Images." July 30, 2001.

Seismic Performance of Existing Reinforced Concrete Beam-Column Joints

Susan M. Smilanich
California Polytechnic State University, San Luis Obispo

Host Institution: University of Washington
Professors Dawn E. Lehman and John F. Stanton



It is not enough to study all theories of resistance and all calculation methods. One must absorb all details and experiments until he becomes completely familiar in a natural and intuitive way with all phenomena of stress and deformation.

Eduardo Torroja
Architect and Structural Engineer

Abstract

Reinforced concrete beam and columns are very common in construction today. During an earthquake, concrete structural frames may need to resist the bending moments and shears caused by horizontal inertia forces of that earthquake. The joints during an earthquake have been proven to be particularly vulnerable. This can be of some concern since many older joints were constructed with no or little reinforcement. This study focuses on the seismic performance of joints in older buildings.

The research has been broken down into four phases. The research is currently in the fourth phase. This final phase is based on the information from the previous phases. Previously seven specimens were tested in two test series during the second phase. The first four specimens varied in displacement history, while the target joint shear stress remained constant. The last three specimens had a higher target joint shear stress with one of the first four displacement histories.

Four specimens will be tested in the fourth phase. The focus of this phase is to address varying the concrete strength, increasing the joint shear stress range, and the eliminating of bond stress.

Introduction

Many buildings consist of a structural skeleton of reinforced concrete beams and columns. The primary purpose of these beam-column frames is to support gravity loads. However, during an earthquake, these concrete structural frames may need to resist the bending moments and shears caused by the horizontal inertia forces of that earthquake. The joints are subject to shear loading and have been proven to be particularly vulnerable during an earthquake, as shown in Figs. 1a and 1b. These pictures show how much heavy damage a joint can incur due to shear loading.



Figure 1a: Damage after the 1994 Northridge earthquake (NISEE).



Figure 1b: Damage after the 1999 Turkey earthquake (NISEE).

Many older joints were constructed with no or little joint reinforcement. These unreinforced or minimally reinforced joints are particularly vulnerable in an earthquake. The question then becomes how much retrofitting will be required and what kind of design will be best.

Performance-based engineering has been a focus of many studies in recent years as a method for assessing and designing in engineering. However, the researchers felt that a better qualitative and quantitative understanding of joint performance is needed if performance-based design and assessment is to be used.

This study focuses on the seismic performance of joints in older buildings. The research has been broken down into four phases, each with its own individual thesis.

- Phase I (Moser 2000): This phase included a literature review, an analysis of previous test results and an evaluation of prior codes and construction practices. Mosier evaluated the influence and behavior of a number of parameters and concluded that joint shear stress and displacement history were the most important.
- Phase II (Walker 2001): Walker tested seven specimens without joint reinforcement and subjected them to different shear stresses and displacement histories. Walker used the results of this testing to evaluate the dependence of behavior on the joint shear stress and displacement history.
- Phase III (Yeargin 2002): Yeargin is currently developing a new analytical model that will predict the response of existing beam-column joints. This modeling will be based on testing completed in the second phase.
- Phase IV (2002): Phase IV is about to begin. Four more specimens will be tested. These specimens will be used to explore the effects of variations in concrete strength and a wider range of joint shear stress than was used by Walker in phase II.

Background

Calculation of Joint Shear

The joint shear force, V_j , can be computed using the free body diagrams shown in Figs. 2 and 3.

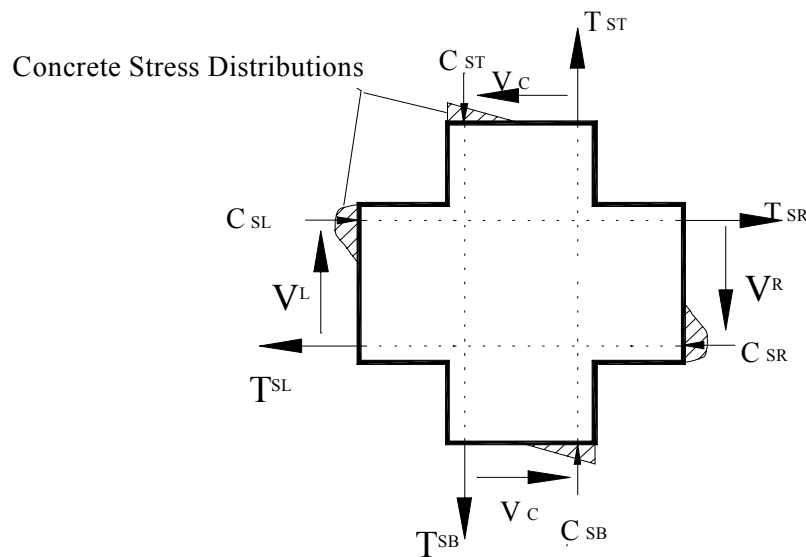


Figure 2: Cut of the beam and column right at the joint.

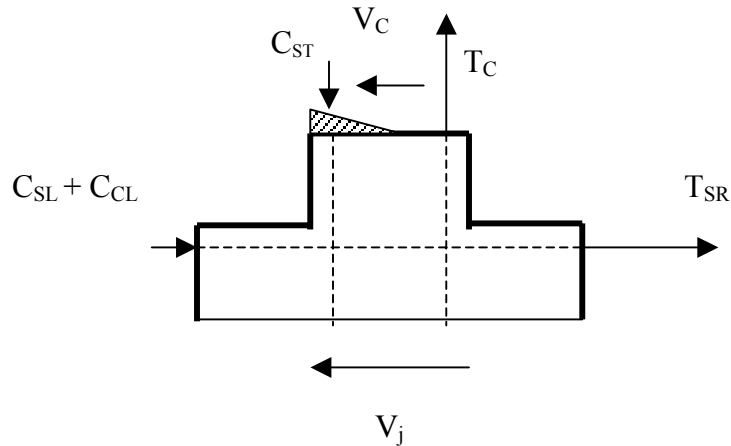


Figure 3: Horizontal cut of the beam and column joint.

The joint shear force, V_j , can be expressed by the following equation:

$$V_j = T_{SR} + C_{SL} + C_{CL} - V_C \quad (1)$$

Where: T_{SR} = force in the tension reinforcement in the right beam.

C_{SL} = force in the compression reinforcement in the left beam.

C_{CL} = concrete compressive force in right-hand beam.

V_C = column shear force.

The compression reinforcement forces in the beam, C_{SL} and C_{CL} , can be redefined as:

$$T_{SL} = C_{SL} + C_{CL} \quad (2)$$

Substituting Eq. 2 into Eq. 1:

$$V_j = T_{SR} + T_{SL} - V_C \quad (3)$$

Walker shows that

$$V_j = V_C [(L_c/jd)(1 - h_c/L_b) - 1] \quad (4)$$

Using dimensions typically found in existing construction, the joint shear is over 3 times the column shear (Walker 2001). The internal joint shear stress, v_j is defined by

$$v_j = V_j/A_j \quad (5)$$

where A_j is the effective area of the joint. In the ACI provisions, A_j is taken as the product of the column dimension in the direction of loading and the smaller of

1. The beam width, plus the column depth

2. Twice the smaller perpendicular distance from the beam centerline to the column edge.

Eq. 4 gives the joint shear stress demand. This joint shear stress must be limited to a value less than or equal to the joint shear stress capacity. ACI 318-99 gives the capacity as $12\sqrt{f'_c}$ and $15\sqrt{f'_c}$ for exterior and interior joints respectively.

American Concrete Institute (ACI) Shear Requirements

Fig. 4 summarizes the ACI shear requirements.

- To avoid bond failure of the bars in the joint, $h_c/d_b \geq 20$ by the ACI 318-99 code.
- The joint shear stress demand, V_u , is obtained from Eqs. 3 and 5, with the forces in the tension reinforcement of the beam, T_{SL} and T_{SR} , computed using $f_s = 1.25f_y$.
- The joint shear stress capacity, V_n , is $15\phi\sqrt{f'_c}$, where f'_c is in pounds per square in (psi), for an interior joint.
- The $15\phi\sqrt{f'_c}$ is contingent on the presence of the specified joint ties.

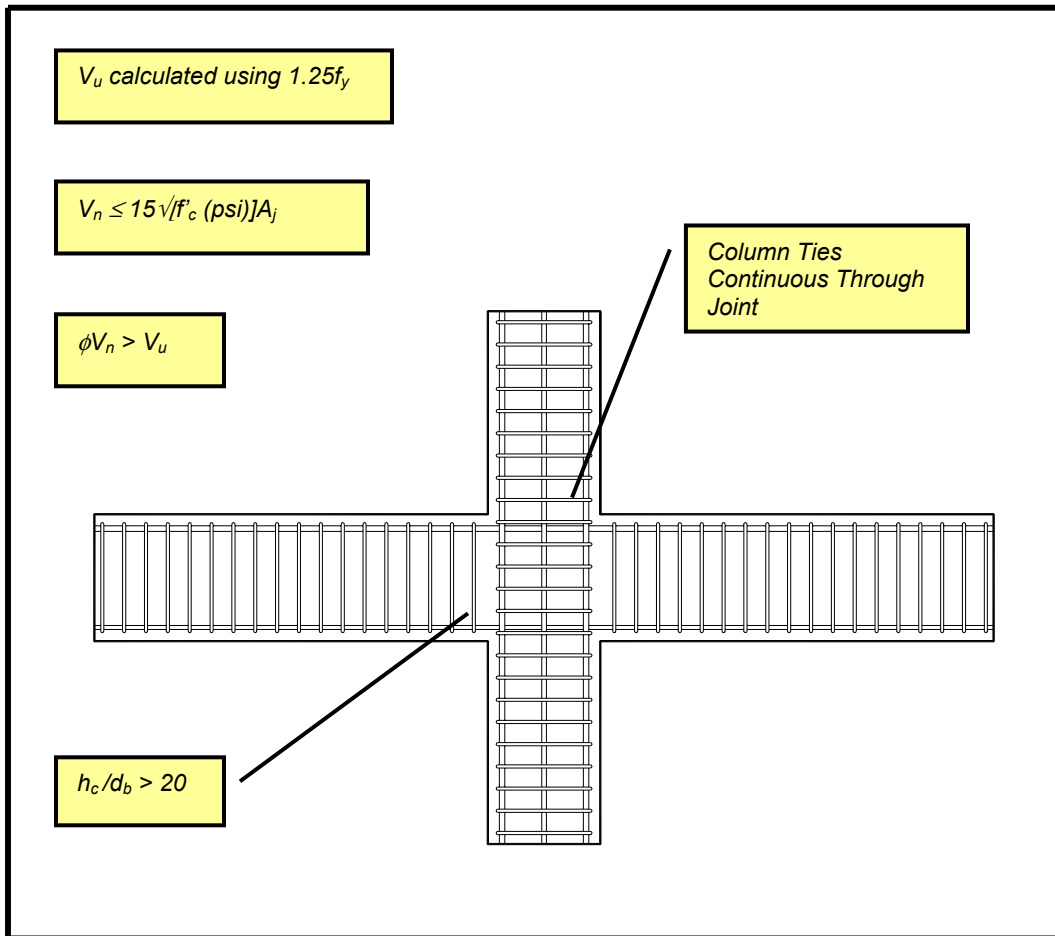


Figure 4: ACI 318-99 joint details.

Walker's Test Series

Seven specimens were tested in two test series. Table 1 lists the seven Walker specimens and the conditions under which they were tested. The first four specimens varied in displacement history, while they all had the same target joint shear stress of $0.14f'_c$ or $9.9\sqrt{f'_c}$ (psi). The last three specimens had a higher target joint shear stress [$0.22f'_c$ or $15.5\sqrt{f'_c}$ (psi)]. The displacement histories of these last three specimens were the same as three of the first four specimens.

Table 1: Walker's test specimens.

Specimen	Drift History	Target Joint Shear Stress		Concrete Strength (nominal)
PEER-14	Standard	$\approx 0.14f'_c$	$9.9\sqrt{f'_c}$	5 ksi
CD15-14	Constant: 1.5%	$\approx 0.14f'_c$	$9.9\sqrt{f'_c}$	5 ksi
CD30-14	Constant: 3%	$\approx 0.14f'_c$	$9.9\sqrt{f'_c}$	5 ksi
PADH-14	Asymmetric	$\approx 0.14f'_c$	$9.9\sqrt{f'_c}$	5 ksi
PEER-22	Standard	$\approx 0.22f'_c$	$15.5\sqrt{f'_c}$	5 ksi
CD30-22	Constant: 3%	$\approx 0.22f'_c$	$15.5\sqrt{f'_c}$	5 ksi
PADH-22	Asymmetric	$\approx 0.22f'_c$	$15.5\sqrt{f'_c}$	5 ksi

Displacement Histories Used

Four displacement histories were used (Fig. 5).

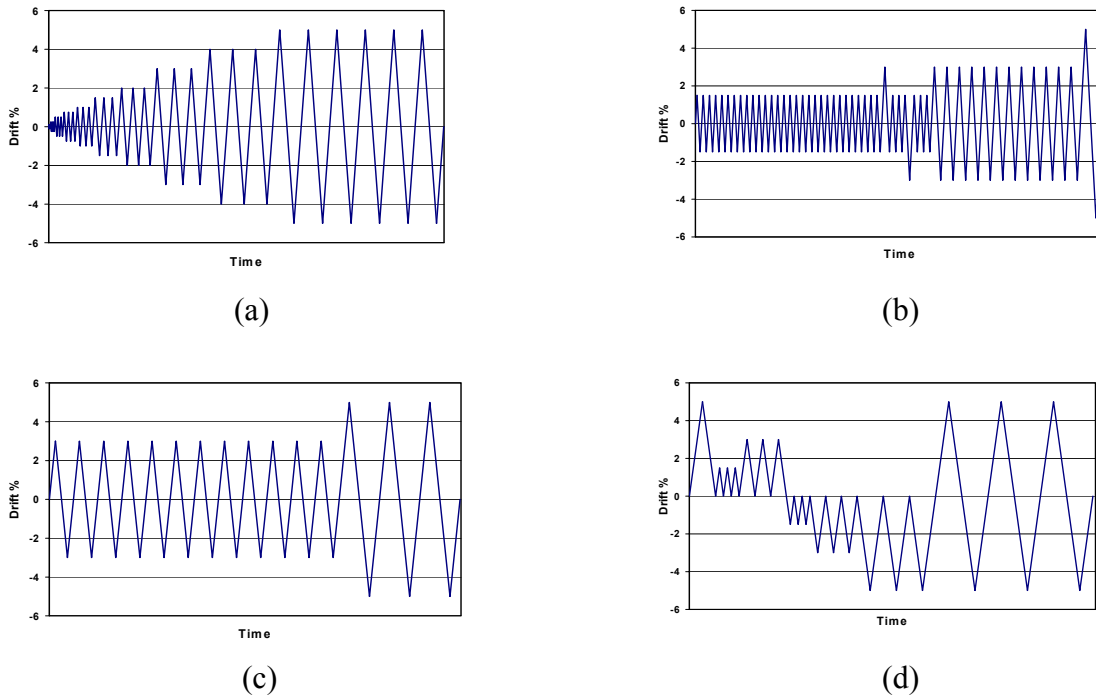


Figure 5: (a) PEER displacement history. (b) CD-15 displacement history. (c) CD-30 displacement history. (d) PADH displacement history.

- The PEER displacement history (Fig. 5a) is the standard displacement history and is often used by PEER researchers. This displacement history was used for comparative purposes.
- The second and third displacement histories, CD-15 and CD-30 (Figs. 5b and 5c, respectively), are for the two Constant Displacement (CD) specimens, CD-15 and CD-30. These displacement histories were designed to look at effects of a long duration earthquake. Long duration earthquakes occur in the Pacific Northwest region.
- The fourth displacement history, PADH (Fig. 5d), represents a pulse earthquake, which is common to California. This displacement history is termed Pulse Asymmetric Displacement History (PADH).

Walker's Findings

The experimental results (Walker 2001) showed that for concentric joints without reinforcement,

- 1) The joint shear stress demand affects the seismic performance. Specifically, an increase in joint shear stress demand yields more joint damage.
- 2) The number and amplitude of displacement cycles can significantly affect joint response. The direction and manner that the cycles are applied are also important.
- 3) The damage observed in the joint is related to the bond conditions of the beam longitudinal reinforcement within the joint.
- 4) The axial load carrying capacity of the column was maintained regardless of the displacement history.
- 5) The contribution of the joint shear deformation to the total drift is significant. Idealizing the joint as a rigid panel will result in significant underestimates of story drift and overestimates of system stiffness.

The results of the displacement histories broke down into three different drift ranges (Walker 2001). The first range was for drifts less than 1.5%. Cycling at these drift levels was not enough to produce any significant damage or loss of strength to the joint region. The next drift range was 1.5% drift to 3% drift. The result was a moderate increase in damage and a minimal loss of capacity. Cycling under a constant drift resulted in small increases in the measured joint shear strain. Cycling at or above 3% drift also showed severe damage and a large reduction in resistance. A constant drift at this higher level resulted in progressive and significant increases in how much the joint shear deformation contributed to the total drift.

The joint shear stress demand plays less of a role after the first cycle than the drift applied. Changes in the stiffness of the beams due to changes in the longitudinal reinforcement ratio are insignificant when the inelastic action is concentrated in the joint. The inelastic action occurs when there is a decrease in joint stiffness compared to the beam stiffness. The residual joint shear strength tends toward $8\sqrt{f'_c}$ (psi) with cycling at large joint shear strains, regardless of the maximum joint shear stress demand.

Phase IV Research Objectives

The joints built in the early 1970's in the United States largely contained little or no confinement reinforcement. The purpose of this phase of the research was to quantify the joint performance in order to determine if it is necessary to retrofit the joints built in the 1970's. This goal will be accomplished through analytical and experimental methods. The analytical component objectives are "to identify the parameters that most influence the performance and to develop analytical models that predict different performance states" (Lehman 2001). In testing the concrete strength will be varied and the joint shear stress range will be increased. Four specimens will be tested, numbered 8 through 11.

In Phase II, all the specimens failed in joint shear. Some of these specimens were stressed to $9.9\sqrt{f'_c}$ and some to $15.5\sqrt{f'_c}$ psi. Those subjected to the lower stress failed after a larger number of load cycles, which suggest that the joint strength can be described in terms similar to fatigue. It is therefore of interest to establish the two extreme stresses: the "endurance strength, which is the stress at which no significant damage would occur regardless of the number of cycles, and the "static strength", which is the shear stress required to cause failure under monotonic loading.

For specimens 10 and 11 the objective is to tell whether the joint strength is related to f'_c or $\sqrt{f'_c}$. In the second phase only one target concrete strength was tested. During this phase the testing will include two specimens with a higher f'_c (9.5 ksi). If the research shows that the joint shear strength is approximately twice as high ($9.5/5.0 \approx 2$), then the joint shear stress is related to f'_c . However, if the joint shear strength is the square root of f'_c [$(9.5/5.0) \approx 1.4$] times as strong, then $\sqrt{f'_c}$ is the better measure. To answer this question, f'_c needs to be much greater than 5.0 ksi, which is the concrete compressive strength used by Walker in Phase II.

Test Matrix

Table 2 summarizes the testing parameters that will be used during the fourth phase of the project. The same displacement history will be used for each specimen. This displacement history will be selected from the four displacement histories already tested.

Table 2: Phase IV testing parameters.

Specimen No.	Drift History	Target Joint Shear Stress		Concrete Strength (nominal)
8	(same for all specimens)	$\approx 0.41f'_c$	$\approx 29\sqrt{f'_c}$	5 ksi
9		$\approx 0.08f'_c$	$\approx 5.7\sqrt{f'_c}$	5 ksi
10		$\approx 0.08f'_c$	$\approx 7.8\sqrt{f'_c}$	9.5 ksi
11		$\approx 0.14f'_c$	$\approx 14\sqrt{f'_c}$	9.5 ksi

Specimen Construction Process

Formwork

Two complete forms were built so that two specimens could be poured and tested at one time. Putting together and taking apart the forms will be required because a total of four specimens will be cast. Appendix A explains the assembly procedure. An explanation of the labeling and a plan view of the formwork are included in Appendix A.

Gauges

Fig. 6 shows a plan view of the bars with the longitudinal strain gauge locations for both the column and beam. The column bar gauges (gauge numbers 4 through 10) were placed on three of the column bars, but are only shown on two bars for readability purposes. The beam gauges are numbered 1 through 7.

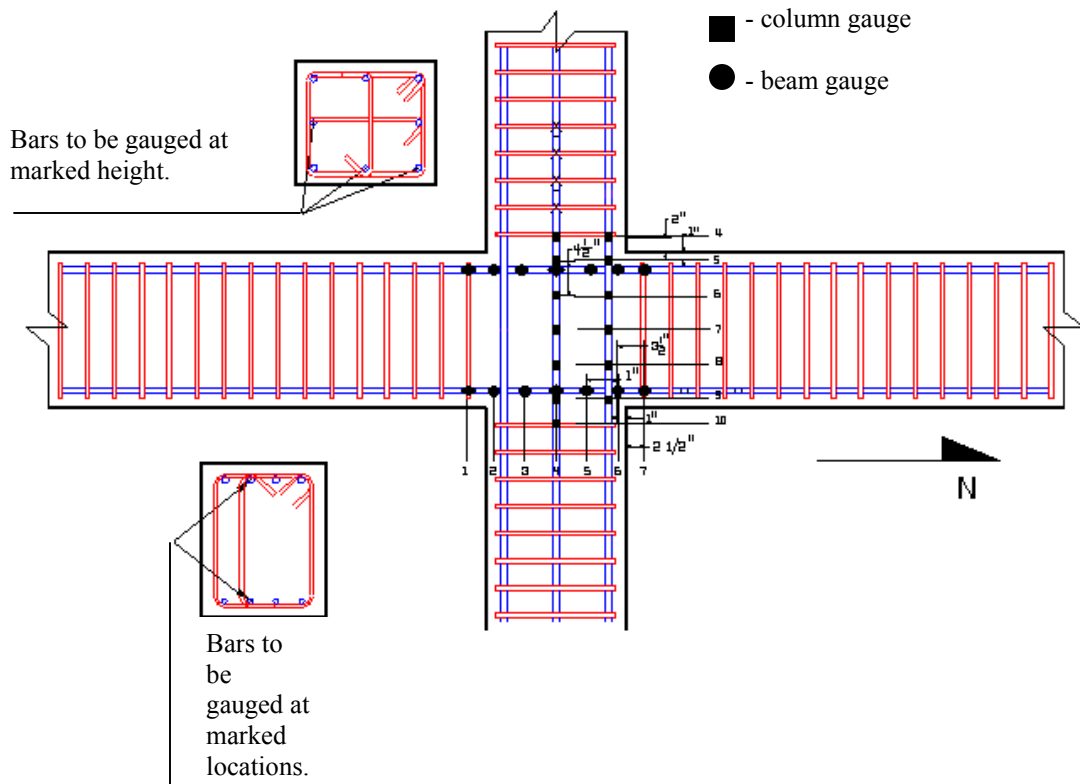


Figure 6: Beam and column longitudinal strain gauge placement.

Each of the gauged bars has a groove along the rib that runs the length of the bar. The groove is where the strain gauges were placed. Figs. 7 and 8 show the groove and strain gauge locations for the beam and column bars, respectively. The purpose of the groove was to minimize the disruption of the bond.

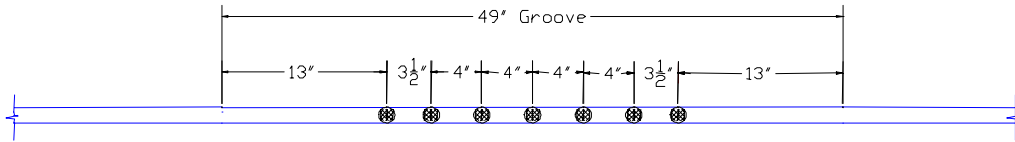


Figure 7: Section of beam bar with groove and gauge locations

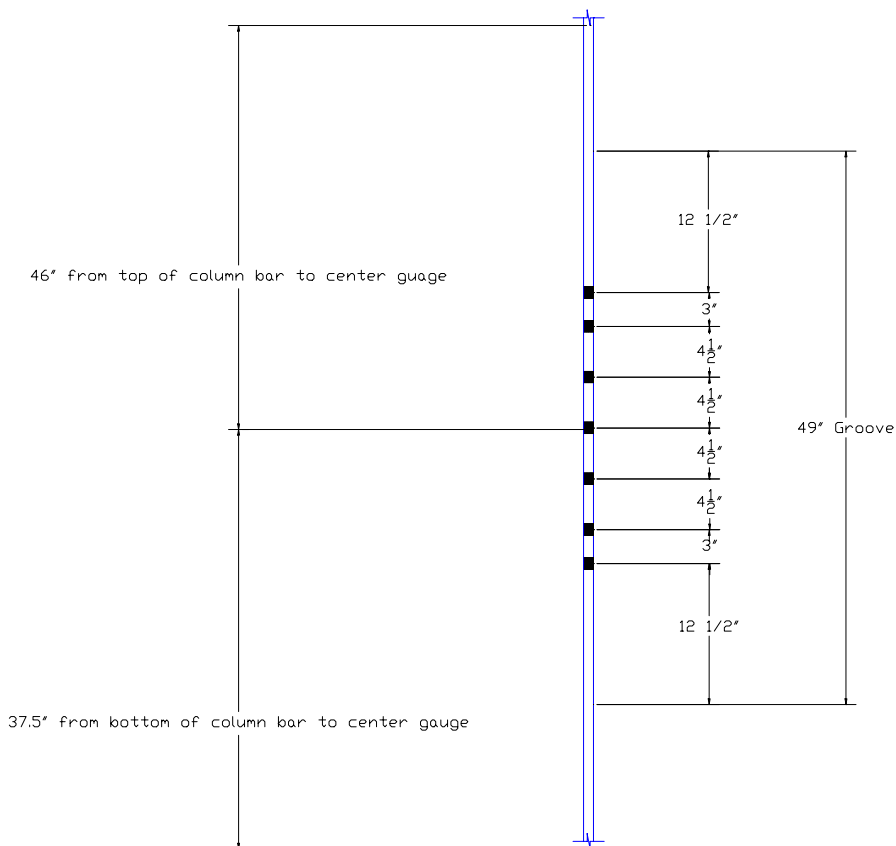


Figure 8: Section of column bar with groove and gauge locations.

There were two types of gauges, YFLA's and FLA's. The beams would endure the larger deformations and strain, therefore the beams were gauged with the YFLA's. The YFLA gauges were able to withstand a greater strain before breaking. The columns were gauged with FLA's. Each strain gauge, the wires, and the leads were all applied in

the same manner within the groove. The strain gauges were initially glued down with a super-glue like substance to hold them in place. The strain gauge wires were then bent into a butterfly-like shape, in order to create some slack within the wire. The strain gauge leads were laid down in an S-shape pattern. M-Coat B, a rubber-like substance was applied to the entire assembly (strain gauge, wires, and leads). Plasti-Dip is waterproof and was brushed on over the M-Coat B. Figs.9a and 9b show the cross-sectional and plan views of the groove and gauge locations.

The combination of the Plasti-Dip over the S-shaped leads came out to be bulky and did sometimes go above the top of the bar. However, if the S-shape in the leads was looser, the bulk would not occur and this slight difficulty could be resolved. The gauges were split into two directions on each bar (4 in one direction, 3 in the other direction) and this also helped alleviate the bulk that the leads created.

Extra slack was placed in each of the wires to help prevent the strain gauges from being over-stressed during the testing and giving false readings. The S-shape added more slack to the wires, thus preventing over-stress to the strain gauge itself. The M-Coat B served as a protective sealant for the assembly, however, it is not waterproof in concrete, thus the need for the Plasti-Dip, which is waterproof. All of this was done to decrease the disruption to the bond during testing.

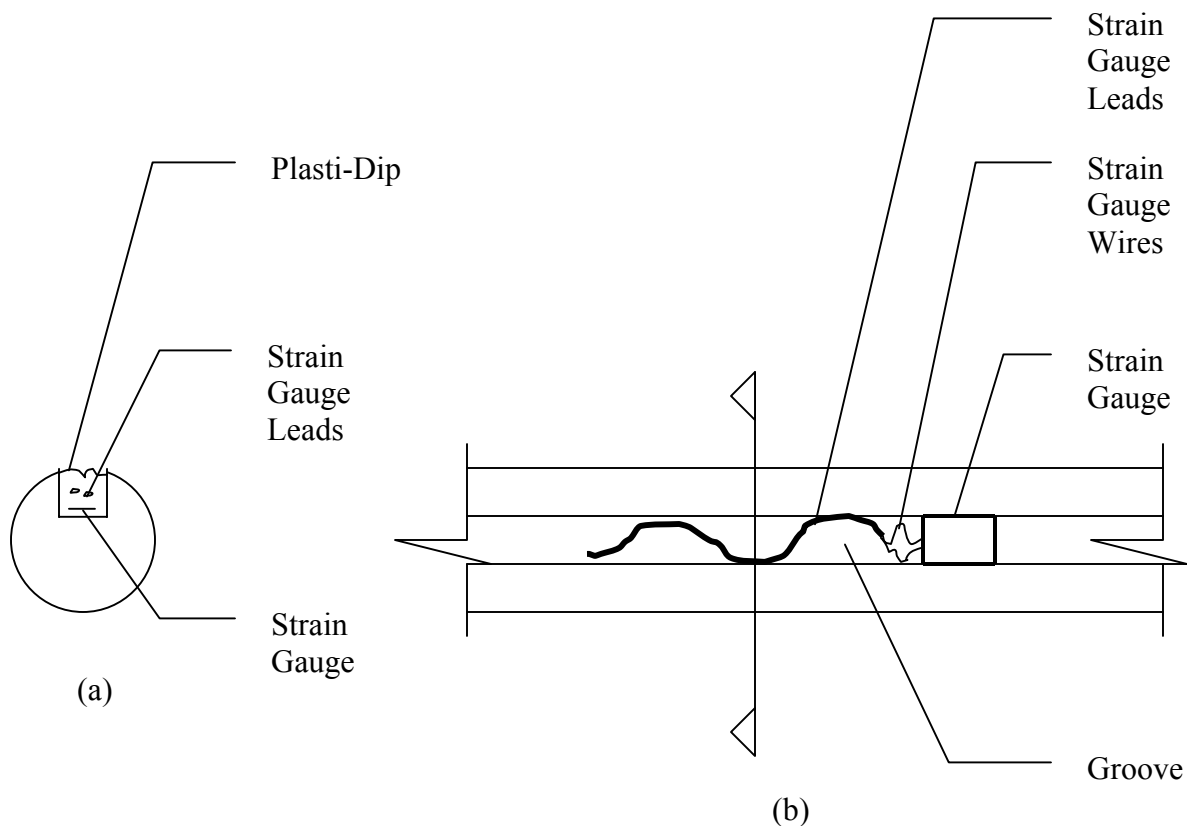


Figure 9: a) Cross-sectional view of gauged bar. b) Plan view of a section of gauged bar.

Conclusion

My participation within this project mainly concerned the construction of the formwork and the strain gauging. I made the following observations during my work.

Overall Observations

- I learned about joint shear stress in reinforced concrete beam-column joints. I have a better understanding of the difficulties of retrofitting. I see that there is a balance between adequate reinforcement and over-reinforcement in a beam-column joint. In other words, more is not better.
- I learned what graduate school looks like and how an experimental project is run. The line to learning is not a straight path and while there were some unexpected occurrences during the internship, I felt the researchers and myself weathered the circumstances well. We worked as a team. I worked independently, however, I was never alone. I know I will be looking for a graduate school that can perform in this team-like fashion.

Formwork Issues

- I would not tighten or loosen the formwork lag bolts located on the outside corners of the forms. The individual pieces are set perfectly or as near perfect to each other as possible. The lag bolts help ensure that fit. Tightening or loosening of the bolts could ruin the delicate balance.
- For drilling the holes, I would find a more accurate method to match up one set of holes to another. Vince, one of the laboratory technicians, suggested possibly using a laser level. This would save time, be more accurate, and get the forms more square.

Strain Gauge Issues

- Plasti-dipping the strain gauges, directly on the gauges was a good idea for flexibility and waterproofing. The area to look at next time is the snaking of the gray plastic-coated part of the gauge. I was not 100% successful in keeping that portion of the gauge completely within the groove. I believe that a less tight snaking pattern could be used.
- Also in regard to the Plasti-Dip, try using a more direct way of funneling the substance into the groove rather than brushing on the application. I believe the application and drying time would be better.

Acknowledgements

I wish to express my deepest appreciation to a few people and organizations that made this internship so worthwhile and a greater academic experience because of their efforts. The first thank you must go to the National Science Foundation, which funded the Pacific Earthquake Engineering Research Center (PEER), who sponsored my internship. I also wish to express my gratitude to PEER. The support from both of these organizations is gratefully acknowledged.

The continued support and guidance provided by Professor Gerald Pardo and Gina Ring was invaluable. Whenever I needed a question answered or a good dose of positive attitude, I knew I could rely on these two people.

To professors Dawn Lehman and John Stanton, thank you for your time and patience. I knew that I was never alone in my work this past summer. Your enthusiasm was contagious. I appreciated the way you shared your knowledge and increased my understanding. I could not have asked for better PEER advisors.

I never could have made it through this summer without the instruction that came from Kenny Knowlan and Vince Chaijaroen, the two men who run the structures lab. Their knowledge is immense, but their willingness to share their experiences was even greater. In addition, they always could add humor to the day.

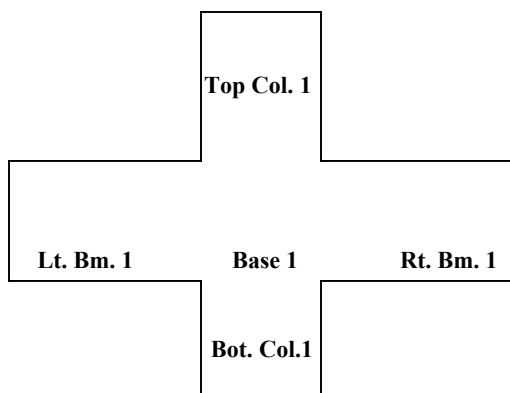
Andrew Ailing and VJ Chaijaroen were two people who helped me on and off throughout the summer. These fellow students always would lend me a hand whenever I needed physical assistance or problem solving an idea. What a great duo these two were. I feel privileged to have had worked with them.

Chris Yeargin is a graduate student on the project, but not the graduate student for my phase of the study. Chris was generous enough to take me under his wing and become my big brother. I have never had a big brother, but I now know how wonderful they can be. Thank you for all your time and perspective.

Appendix

Appendix A: Formwork Assembly Procedure

The following is a set of tips for putting together the formwork for the PEER Joint Project. There are two complete form, which are nominally identical. Form 1 is shown in Fig. A1. They are distinguished as #1 and #2. The parts are labeled as Base 1, Base 2, Top Col. 1, Top Col. 2, etc. Below is a complete list of names I assigned to the formwork. For the most part the naming is pretty common sense, but to help eliminate any confusion, here is the list:



Top Col.: This stands for top of the column; the "1" indicates that this is part of formwork #1.

Lt. Bm.: Left side of the beam as you either stand in front of it or stand over it as it lays on the ground.

Rt. Bm.: Right side of the beam.

Bot. Col.: Bottom of the column.

Base: The bottom of the form.

Figure A1: Plan view of Form 1.

Attached to the sides of the base, are the sides of the form. These sides sit on the floor when being assembled. The sides do not sit on top of the base, but rather they are beside the base. On top of the each side of the side formwork is a label of Top Col., Lt. Bm., Bot. Col, or Rt. Bm. When laying out the forms, lay out the base first, then match the side labeling to the base names. The assembled forms, both of them, are located in the main part of the lab. Ask Kenny or Vince, the two men who supervise the structures laboratory, as to their location. The forms are temporarily covered with plywood, just as a support for the gauged bars. The plywood and the 2x4's separating the two forms are not permanent parts of the project and are to be removed when no longer needed.

In regards to the sides, as a suggestion, I would not tighten or loosen the "L" shapes (side pieces) that are currently in place. On the outside corners (with respect to the base, the base being on the inside) of each "L" there are two lag bolts. I have fit the parts of the "L" with the formwork to the best of the ability of the materials and the base. I have puttied and varnished the inside corners in place. These corners pieces fit pretty well to the base. There are gaps. To get a tighter fit all the way around, bar clamps at the end of each beam and column (after the rods are in place) will close the final gaps, but not completely. Watch the formwork so that it does not start lifting at the corners. These gaps will have to be filled by caulking prior to the pour.

To close the formwork at the end of each column and beam is an end piece. These pieces do rest on the base between the side pieces. On each base, there is a pencil line right where the end pieces should line up so that the formwork will be square.

All the pieces are connected to the base by rods. Most of the rods are around 32" in length, but some are 30" in length. However, all will fit universally anywhere in the formwork. Just remember the rods are universal, the formwork pieces are not. You must have the #1 pieces all together in the correct locations and they cannot be mixed with the #2 pieces. The rods go through the holes outlined in blue (darker color). Some of the holes are outlined in red, ignore these. Some of the pieces have 4, 5, or more holes; in this case, you need to look for the blue-circled holes. There are two rods in each end piece (only one rod is shown in the CAD drawings). The second rod was added during construction to reduce the torque at the bottom of the end piece after the pour.

Lay the formwork on the ground for easy assembly. Next, place all of the pieces (end and side) snugly around the base and insert the rods. Before inserting a rod, take the time to look through the holes and see how they line up. From that vantage point, you will be able to see if there is a partial occlusion and if the forms need to be adjusted. Because the forms were built in a different area than where they will be assembled and the floor was not completely level, the forms will have to be lifted in some spots in order for the rods to go through. A suggestion is to not put on any of the nuts and bolts on until all of the rods are in place. Once you are sure all the rods can go through, start tightening each rod.

The final part of the formwork, which will most likely have to be located by Vince or Kenny, is what I refer to as the Table. The Table sits about table height and sits on top of the formwork right at the joint section. The markings on the Table follow the same naming conventions. The Table's purpose is to add stability to the potentiometers once they are in place in the concrete. Holes for the potentiometers still need to be drilled in the base. These holes should be done after the rebar cage is in place. Discuss when and where the drilling should occur with Professor Stanton.

Bibliography

ACI Committee 318 (1999), *Building Code Requirements for Structural Concrete (ACI 318-99) and Commentary (ACI 318R-99)*, American Concrete Institute, Farmington Hills, MI.

Lehman, D.E., Mosier, W.G., and Stanton, J.F. (2000). "Seismic Assessment of Reinforced Concrete Beam-Column Joints", US-Japan Workshop on Performance-Based Seismic Design of Reinforced Concrete Buildings, September.

MacGregor, James G. (1997), *Reinforced Concrete Mechanics and Design, Third Edition*; Prentice Hall, Upper Saddle River, NJ.

Mosier, William G. (2000), *Seismic Assessment of Reinforced Concrete Beam-Column Joints*, University of Washington, Seattle, WA.

National Information Service for Earthquake Engineering University of California Berkeley (NISEE): http://www2.rcep.dpri.kyoto-u.ac.jp/~sato/taiwan/pict_clas.html (Taiwan) and http://nisee.berkeley.edu/tmp/ejiis_res_4759_2.html (Northridge).

Walker, S., Yeargin, C., Lehman, D., and Stanton, J. (2001). "Influence of Joint Shear Stress Demand and Displacement History on the Seismic Performance-Based Seismic Design of Reinforced Concrete Buildings, Seattle, WA. August.

Walker, Steven (2001), *Seismic Performance of Existing Reinforced Concrete Beam-Column Joints*, University of Washington, Seattle, WA.

Yeargin, Chris (2002), *Analytical Model for Reinforced Concrete Beam-Column Joints*, University of Washington, Seattle, WA.

Analytical Development of Bridge Structural Fragilities Under Near-Fault Loading

Carolyn Stegon
Home Institute: Virginia Tech

Pacific Earthquake Engineering Research Center REU Final Research Report
National Science Foundation
University of California, Irvine
Structural Engineering Test Hall

Graduate Student Researcher: Charles Hamilton
Research Advisor: Dr. Gerard Pardoën

October 22, 2001

ABSTRACT

As research develops in the field of earthquake engineering, the analysis of earthquake affects on structures is modeled using computers. Computers incorporate the use of a probabilistic analysis, which takes into consideration error found in the real world. Most of the research done in earthquake engineering has been conducted on earthquake response located farther from the fault zone. The goal of this project is study the affect of near fault earthquake time histories' behavior of these probability results. The development of this probabilistic study leads to the development of fragility curves. Fragility curves represent the probability of exceeding a certain limit state based on a given earthquake input. Fragility curves have been established in the past by organizations such as FEMA's Hazus but researcher do not how well the effects of near fault earthquakes are incorporated. The study of near fault earthquakes is important because they impose additional demands beyond the current design of the structure. It is intended that this research will help in the future knowledge and understanding of near-field ground motions impact on bridges.

TABLE OF CONTENTS

1.0 INTRODUCTION
2.0 BACKGROUND OF THE PROJECT
3.0 BACKGROUND - NEAR FAULT EARTHQUAKES
• FIGURE 1 - NEAR FAULT EARTHQUAKE TIME HISTORIES
4.0 BACKGROUND – MODELING WITH OPENSEES
5.0 BUILDING BRIDGE MODELS USING FINITE ELEMENT MODELING
• FIGURE 2 – BRIDGE MODEL
5.1 End Connections – Zero Length Elements
5.2 Modeling the Abutments
5.3 Modeling the Deck
5.4 Modeling the Columns
5.5 Material Modeling
5.6 Modeling the Earthquake Excitation
6.0 ANALYSIS GENERATION USING OPENSEES
7.0 RECORDER METHODS USING OPENSEES
8.0 BACKGROUND – MONTE CARLO SIMULATION AND ANALYSIS
9.0 ESTABLISHING FRAGILITY CURVES
9.1 Background - Fragility Curves
9.2 Calculating Fragility Curves
10.0 HOW ACCURATE ARE THE RESULTS
• TABLE 1 – ACCURACY OF DATA
11.0 HOW RESULTS ARE MEASURED USING FRAGILITY CURVES
• FIGURE 3 – CONSTRUCTION OF FRAGILITY CURVE
12.0 WHY IS THIS PROJECT IMPORTANT
13.0 CONCLUSIONS AND FUTURE WORK
14.0 APPENDIX A
Readability Statistics
15.0 REFERENCES

“The Pacific Earthquake Engineering Research Center is an NSF Earthquake Engineering Research Center whose mission is to develop performance-based earthquake engineering technologies to meet the economic and safety needs of owners and society.”

PEER MISSION STATEMENT
<http://peer.berkeley.edu/research/plan.html>

1.0 INTRODUCTION

As the field of earthquake engineering grows, computer analysis is used to simulate and model the effect of earthquakes on given structures. Computer analysis is very desirable because the number of experimental tests that can be conducted in the real world is limited. Computers enable the use of a probabilistic analysis, which takes into consideration error found in the real world. Most of the research done in earthquake engineering has been conducted on earthquake response located farther from the fault zone. Our goal is to examine how near fault earthquake time histories affect the behavior of these probability results. More specifically, fragility curves are developed. Fragility curves represent the probability of exceeding a certain limit state based on a given earthquake input. The study of near fault earthquakes is very important because they impose additional demands beyond the current design of the structure. It is intended that this research will help in the future knowledge and understanding of near-field ground motions impact on bridges.

2.0 BACKGROUND OF THE PROJECT

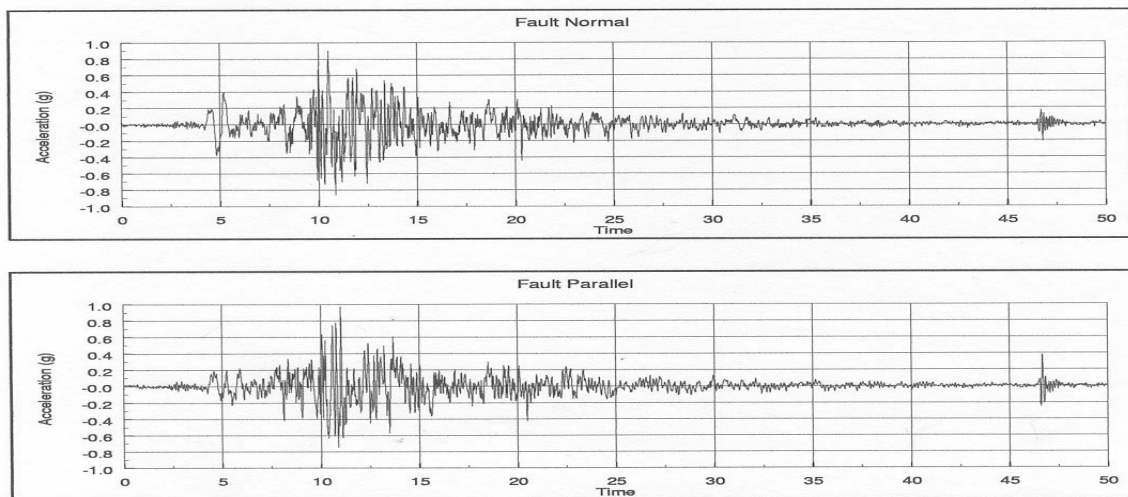
This project began with experimental testing intended to characterize the response of ductile-detail bridge column samples subjected to displacement-controlled monotonic, reversed cyclic, and reversed cyclic with “pulse” motion loading time histories. The testing protocols with and without pulses were examined. Failure modes were examined based on the loading condition.

Next, simple analytical models of bridge systems were developed to model the response of R/C bridge columns under pulse-type loading. The influence of column base plastic hinge length on overall structure response in pulse-containing ground motions was assessed.

The goal of my project was to implement an overall Monte Carlo analysis framework. Because it is impossible to run thousands of experimental tests on columns in real life, computer modeling is used. A disadvantage associated with deterministic computer modeling is that error associated with testing in the real world is not considered; therefore probability analysis is incorporated through a Monte Carlo framework. Monte Carlo results are then used in the construction of fragility curves. These fragility curves represent the probability of failure associated with a given bridge structure, using several different aspect ratios, peak ground accelerations and concrete and steel properties associated with the column. The acceleration records used are based on pulse-containing ground motions typically associated with near fault earthquakes. Fragility curves graphically describe the dependence of the overall bridge structure capacity or survivability, on the pulse-response of the supporting columns. The efforts of this project as a whole are to study the difference in simple bridge bents’ response between “typical” and “near-fault” loading histories.

3.0 BACKGROUND - NEAR FAULT EARTHQUAKES

The near fault region is located 10 to 15 km from the fault. The behavior can substantially differ from regions located further from the fault because ground motions in this region often contain a large “pulse” which is usually best seen in the fault-normal component of the ground motion. This component results from rupture directivity. It is important to study the effects of these large pulse motions because they are typically a source of large damaging motions, which result from significant deformation demands on the structure. Near-fault earthquakes typically cause more damage and response into the nonlinear range. In current design, the efficacy of accounting for near fault loading is unknown because it is more complex and depends highly on the soil conditions, and the structural and earthquake characteristics. Shown below is a near fault time history, which contains the initial large pulse mentioned earlier.



NEAR FAULT EARTHQUAKE TIME HISTORIES

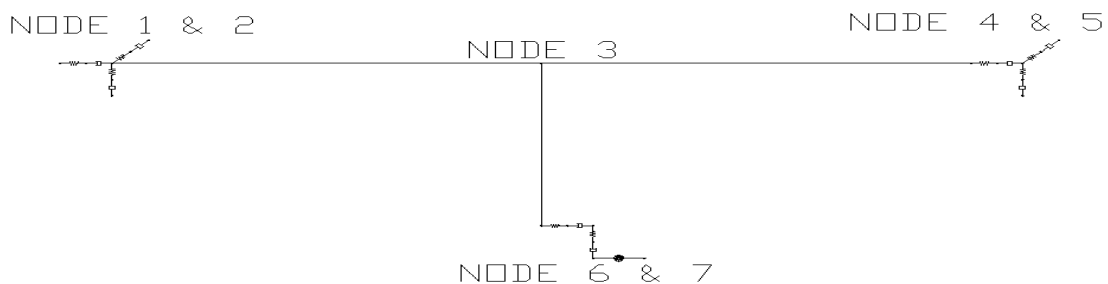
FIGURE 1

4.0 BACKGROUND – MODELING WITH OPENSEES

In order to implement the Monte Carlo analysis, a simulation program called OpenSees was used. OpenSees, Open System for Earthquake Engineering Simulation, is an object-oriented framework, which uses finite element analysis for building models of structural and geotechnical systems. It performs nonlinear analysis of the model and records the response results. In each finite element analysis, the program constructs four main types of objects; the model builder, the domain, the analysis, and the recorder. For further review of the code used in the analytical development of the bridge structure refer to Appendix A.

5.0 BUILDING BRIDGE MODELS USING FINITE ELEMENT MODELING

Our bridge system was designed according to recent California Department of Transportation (Caltrans) standards. By breaking the bridge into its different components - connections, abutments, deck, columns, and materials models - we can more accurately model the bridge. Located below is Figure 2, which is a drawing containing the layout of the bridge model.



BRIDGE MODEL

FIGURE 2

5.1 End Connections – Zero Length Elements

To represent the connection of the abutments with the ground and the column with the foundation, a spring/damper combination is used to model the stiffness and damping the bridge experiences. Zero length elements combine the affects of the springs and dampers.

5.2 Modeling the Abutments

The ends of the bridge deck are connected through a seat abutment to the ground. We modeled our structure with a seat abutment because they are more common in long bridges due to good expansion characteristics.

5.3 Modeling the Deck

The cross section of our bridge is a double box girder. To model this in OpenSees, the section was broken into 5 different pieces. Using a coordinate system, the sections are laid out in OpenSees using the patch quad command and the reinforcing steel using the layer straight command.

5.4 Modeling the Columns

Nonlinear columns are used because inelastic behavior of the structure is expected. Beam columns are used because axial and flexural loads govern. Torsion and shear are neglected at this point. Fiber sections are used to model the layout and reinforcement of the sections.

5.5 Material Modeling

Three different types of material models are used and combined in efforts to more accurately model our bridge. The Elastic model considers stiffness and damping. The Elastic Perfectly Plastic model considers stiffness and plasticity, and finally the Elastic Perfectly Plastic Gap model takes into account stiffness, plasticity, and gapping. By producing combinations of

these models, many different material behaviors can be taken into consideration at the same time. If two models are combined and both account for stiffness, the stiffness in one of the models is set to zero. The combination of these material models is used in the construction of our zero-length members.

Concrete and steel softening models are used in the material modeling of the column and the deck. The concrete material model is broken down into the core and the cover. The steel model combines two Elastic Perfectly Plastic and one Elastic model to parallel a steel model which decreases in strength.

5.6 Modeling the Earthquake Excitation

To model the earthquake excitation, many different pulse-containing ground motion records were used which are usually associated with near fault earthquakes. The records are coded by OpenSees using a pattern Uniform Excitation.

6.0 ANALYSIS GENERATION USING OPENSEES

To begin analysis of the bridge, a convergence test was created called EnergyIncr consisting of tolerance, max iterations, and print flag parameters. The solution algorithm is Newton and the equation storage and solver is Band General. Newmark's linear acceleration method was used to integrate the equations of motion. Finally, the analysis Transient object was used to create the analysis generation.

7.0 RECORDER METHODS USING OPENSEES

The displacements and rotations at the abutments, column cap, and foundation are measured using the recorder node command. Then the displacements of the bent cap are plotted using the recorder plot command. An OpenSees Postprocessor (OSP) is used to record the nodes and the elements.

8.0 BACKGROUND – MONTE CARLO SIMULATION AND ANALYSIS

Due to the extreme rise of digital computer usage, complex problems of the past are now easily solved through the use of computer programming. (Hart, 64) However, the use of computers in structural modeling has created uncertainties in structural response. These consist of first, accuracy contained in round-off and ill-conditioning of the data and second, in the uncertainty due to the properties and loads of the structural model. In order to calculate the uncertainty generated by the structural response, two methods are used. The first method, a Taylor's series expansion, uses "a linear relationship between the response random variables and the random structural parameters." (Hart, 56) The second method, Monte Carlo analysis, uses a computer to simulate an experiment. By generating a series of random numbers substituted into response equations, Monte Carlo analysis can account for the uncertainty generated by the structure's response.

When performing complex problems in which numerous random variables are related in a nonlinear relationship, "Monte Carlo analysis is a powerful engineering tool which enables one to perform a statistical analysis of the uncertainty in structural engineering problems." (Hart, 64) As mentioned above, the analysis begins with the development of a random set of numbers. The numbers generated in our analysis were created using transformation methods. Most

programming languages have their own algorithm for computing uniformly distributed random numbers, which may be used in this analysis. Random numbers are generated from 0 to 1 and there is an equally likely chance that the number will occur anywhere in this range. The number of points selected in the range depends on the desired accuracy associated with your variables. Then the uniformly distributed random variable is mapped onto the desired distribution. The mean and standard distributions are defined as part of defining a desired distribution.

By conducting a Monte Carlo analysis, the structure's performance can be presented in terms of a probability distribution; such as the mean of our steel strength is 66 ksi with a standard variation of 2.5. Ultimately the column will be designed for a steel strength between 63.5 and 68.5 ksi.

The following shows the process conducted at a simulation i:

- (1) two random numbers are generated, one for f'_c and f_y (concrete strength, steel strength)
- (2) the random numbers are mapped out on a certain distribution normal, log-normal, or beta, which best fits the data.
- (3) the model is defined
- (4) the control variables are set
- (5) the analysis is run using OpenSees
- (6) the results are selected, the peak displacement

Located in Appendix A is the code, which implements the Monte Carlo analysis.

It is through Monte Carlo analysis that complex problems of the real world can be solved. It is not practical or possible to build and test thousands of different bridges in the real world. By simulating changes in material properties, structure dimensions, and ground accelerations, these real life situations can be modeled and analyzed easily by the computer.

9.0 ESTABLISHING FRAGILITY CURVES

The field of research is moving from a deterministic to a probabilistic analysis. A probability analysis can help individuals decide and justify where money should be spent. There are three main areas in which money is spent, (1) seismic retrofit and replacement, (2) widening of existing roads and bridges, and (3) research of unsolved and undeveloped problems. It is through probabilistic analysis that we can narrow down the field of uncertainty and justify with reasoning where the money would best be spent.

9.1 Background - Fragility Curves

The area of probability analysis in which this project focuses is the development of fragility curves. Fragility curves represent the probability of exceeding a certain limit state based on the size of the earthquake input. (Hanus99, 203) For example one might analyze the probability that in 50 years the structure's displacement will exceed 1.5 inches given a certain earthquake magnitude. The underlined portion of the following formula represents the fragility curve.

$$P(\Delta_{50} > \Delta_{CAP}) = \underline{P(\Delta_{50} > \Delta_{CAP} | PGA = 0.75)} * (P(PGA = 0.75g)) + \dots\dots\dots$$

(Equation 1)

9.2 Calculating Fragility Curves

When a series of simulations are run there is a certain number that fail. The probability of failure equals the number of failed simulations divided by the number of simulations run. For example if 10,000 simulations are run and 100 fail, the probability of failure is $10,000 / 100 = 0.01$ or 1 percent. The probability of failure is then graphed versus the given peak ground acceleration. This is done for a series of peak ground accelerations, which create different probabilities of failure. Each graph is based on a certain aspect ratio. Ultimately, three different sets of fragility curves are created based on three different aspect ratios.

10.0 HOW ACCURATE ARE THE RESULTS

The scatter of the data reduces as the number of simulations increase. This is calculated by the following formula - $\%Error = 200 - \sqrt{\frac{1 - P(f)}{N * P(f)}}$. (Ang, 292)

(Equation 2)

Contained in the chart below are the calculations for three different cases all consisting of a probability of failure equal to 0.01.

ACCURACY OF DATA

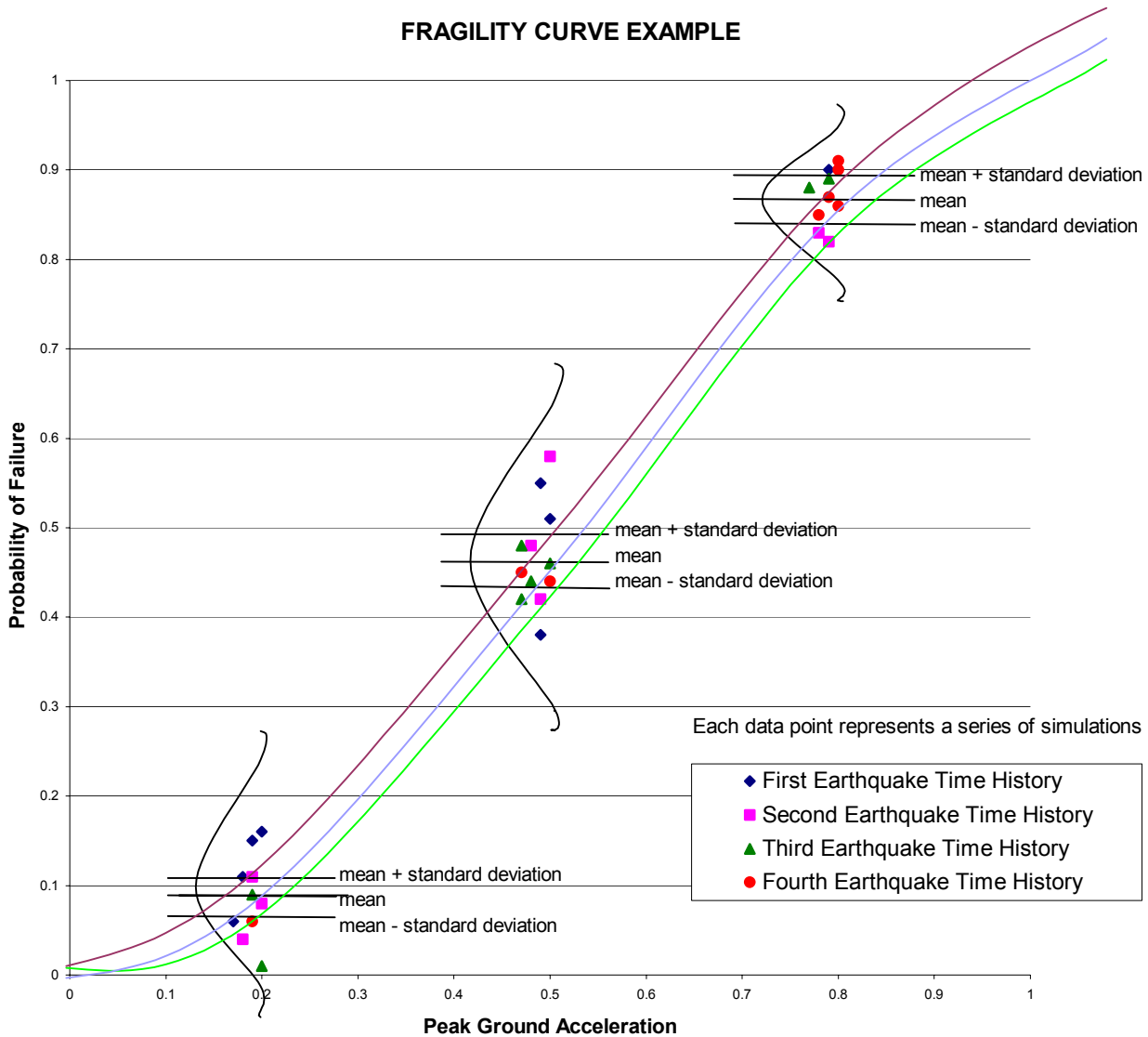
TABLE 1

# of Simulations	# of Failures	% Error	Absolute Error
10,000	100	20	0.0020
1,000	10	63	0.0063
100	1	199	0.0199

As shown here, the absolute error or scatter of the data decreases as the number of simulations increases.

11.0 HOW RESULTS ARE MEASURED USING FRAGILITY CURVES

By using Monte Carlo analysis on the bridge model, data is produced such as forces, displacements, stresses, and strains, which contain statistical properties. One form of data is selected as the performance variable, such as the yield of the column base. The Monte Carlo analysis will output the number of times the column yields given the number of simulations run. As stated earlier, then the probability of failure can be calculated. For each peak ground acceleration the probability of failure is graphed. Then the mean and standard distribution are calculated. After computing the mean and standard distribution for a series of peak ground accelerations, the mean plus one standard deviation, the mean, and the mean minus one standard deviation are established at each peak ground acceleration. These three values are connected at each distribution to form three curves, one at the mean plus one standard deviation, one at the mean, and one at the mean minus one standard deviation. From these three curves, the variability between the data can be examined. Larger variability in the data indicates less accurate results. The following graph is an example of the results that might be obtained by the process described above. The results are for visual purposes of the process only and are not real test results.



CONSTRUCTION OF A FRAGILITY CURVE

FIGURE 3

12.0 WHY IS THIS PROJECT IMPORTANT

Fragility curves have been established in the past by organizations such as FEMA's Hazus but they typically do not incorporate the effects of near fault earthquakes. In the future we would like to study how near fault earthquakes and the use of a probabilistic analysis will affect these fragility curves.

Most bridge systems are designed to withstand seismic activity, however seismic forces of near fault earthquakes impose additional demands beyond the current design of the structure. It is intended that this research will help in the future knowledge and understanding of near-field ground motions on bridges.

13.0 CONCLUSIONS AND FUTURE WORK

Charles Hamilton will use the efforts of this project in his Ph.D. research currently underway. Due to the limited time of the internship, no true results were established. It is intended that fragility curves will be constructed using pulse-containing ground motions for a series of earthquakes. These results will then be compared to previous studies done on typical loading histories.

14.0 APPENDIX A

Readability Statistics

Counts

Words	4904
Characters	27412
Paragraphs	528
Sentences	138

Averages

Sentences per paragraph	3.5
Words per sentence	17.0
Characters per Word	5.3

Readability

Passive Sentences	37%
Flesch Reading Ease	37
Flesch-Kincaid Grade Level	12

15.0 REFERENCES

- Alfredo Ang and Wilson Tang, Probability Concepts in Engineering Planning and Design – Volume II – Decision, Risk, and Reliability (New York: John Wiley & Sons, 1990) 291,292
- Chopra, Anil K, Dynamics of Structures-Theory and Application to Earthquake Engineering (New Jersey: Prentice Hall, 1995) 1-53, 313-459, 567-573
- Federal Emergency Management Agency. Earthquake Loss Estimation Methodology. HAZUS99 User's Manual – ArcView Version. Washington, D.C.: National Institute of Building Sciences, 1999 203-208
- Flynt, Clif, Tcl/Tk for Real Programmers (New York: AP Professional, 1999) 43, 51,59, 67, 121
- Frank McKenna and Gregory L. Fenves, The OpenSees Command Language Manual (University of California, Berkeley, 2001) 1-34
- Frank McKenna and Gregory L. Fenves, The OpenSees Quick Reference Guide (University of California, Berkeley, 2001) 1-5
- Frank McKenna and Michael Scott, The OpenSees Example Primer (University of California, Berkeley, 2001) 1-46
- Hart, Gary C, Uncertainty Analysis, Loads, and Safety in Structural Engineering (New Jersey: Prentice Hall, 1982) 55-74
- Hamilton, Charles, personal interviews, 4 June 2001 to 8 August 2001
- Melchers, Robert, Structural Reliability Analysis and Prediction-Second Edition (New York: John Wiley & Sons, 1999) 64-93
- M. J. N. Priestley, F. Seible, and G. M. Calvi, Seismic Design and Retrofit of Bridges (New York: John Wiley & Sons, 1996) 307-321
- <http://peer.berkeley.edu/research/plan.html>

Finite Element Analysis of Northridge Connections

Josh Tolchinsky

Department of Civil and Environmental Engineering
University of Cincinnati

Department of Civil Engineering,
Washington University, St. Louis

Advised by Dr. Kevin Z. Truman, Department Chairman

September 2001

Finite Element Analysis of Northridge Connections

Josh Tolchinsky¹

September 2001

Abstract

Prior to the 1994 Northridge Earthquake steel moment-resistant frame structures were thought of as the most ductile and earthquake resistant of all modern structural designs. Damage to such structures during the earthquake questioned the basis for structural steel design. Following the earthquake, the SAC Joint Venture was formed to develop methods of repair, retrofit, design, and detect such defects in pre-Northridge steel moment-resistant structures following an earthquake. This paper describes the actions SAC took and the development of a finite element model based on the results of a series of SAC Steel Project tests.

1 Introduction

1.1 Northridge Earthquake

The morning of January 17th, 1994 rattled the world of steel moment-frame building design and construction at its foundations. At 4:30 AM a magnitude 6.7 earthquake shook the ground at Northridge, California, approximately 20 miles northwest of Los Angeles. Despite the moderate magnitude of this earthquake some of the highest ground accelerations ever were recorded during this event. Initially it appeared as though steel moment-frame structures behaved ductility, as expected. There were no steel moment-frame building collapses only reports of superficial damage. Problem were not detected until construction crews returned to buildings under new construction and reported several instances of brittle fracture at bolted web, welded beam flange to column flange moment connections. These connections were inaccessible in existing buildings due to fireproofing and drywall. The bolted web, welded flange connections are referred to as pre-Northridge connections shown in figure 1.1.

¹ Undergraduate Researcher, Department of Civil Engineering, Washington University, St. Louis, MO 63130, Advised by Dr. Kevin Z. Truman, Department Chairman
Senior, University of Cincinnati, Department of Civil and Environmental Engineering, Cincinnati, OH 45221

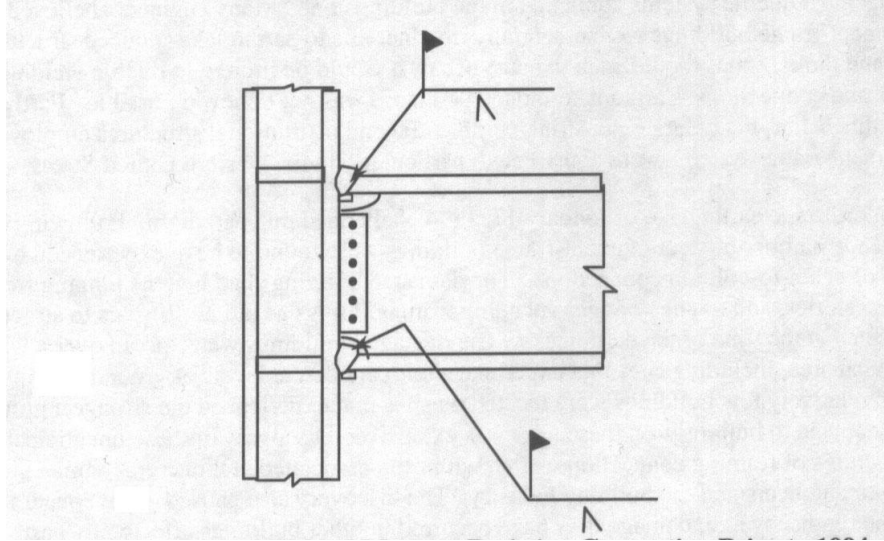


Figure 1.1 Typical Welded Moment-Resisting Connection Prior to 1994

Once this critical discovery was made many buildings in the surrounding areas were found to have exhibited similar responses. Later investigations confirmed such damage in a limited number of buildings affected by the 1989 Loma Prieta, 1992 Landers, and 1992 Big Bear earthquakes. Each of these steel moment-frame buildings damaged met the basic intent of the building codes, however, the structures did not behave as anticipated and significant economic losses occurred as a result even though, in some cases, the buildings experienced ground shaking less severe than the design level (FEMA 350). While these fractures did not pose an immediate threat of collapse, the structures had been significantly weakened and, more importantly, they did not react as once expected. A permanent solution was needed for the damaged buildings; and, because discovery of these brittle fractures was time consuming and expensive, a criteria for determining vulnerability was paramount. In addition, new design and construction procedures, including quality assurance, would need to be developed. The Federal Emergency Management Agency (FEMA) stepped in to set up and fund the SAC joint venture.

1.2 SAC Steel Project

The SAC joint venture is a consortium consisting of the Structural Engineers Association of California (SEAOC), Applied Technology Council (ATC), and California Universities for Research in Earthquake Engineering (CUREE). This consortium was formed specifically to address both immediate and long term needs related to solving performance problems with welded, steel moment-frame connections discovered following the 1994 Northridge earthquake (FEMA 350).

FEMA published 4 documents in June of 2000 with the recommended criteria for the seismic design for new steel moment-frame building (FEMA 350), seismic evaluation and upgrade for existing welded steel moment-frame buildings (FEMA 351), post earthquake evaluation and repair for welded steel moment-frame buildings (FEMA 352), and specifications and quality assurance guidelines for steel moment-frame construction for seismic applications (FEMA 353). These recommended criteria are intended as a resource document for organizations engaging in the development of building codes and consensus

standards for regulations of the design and construction of steel moment-frame structures that may be subject to the effects of earthquake ground shaking (FEMA 350).

1.21 SAC Test Set Up

The test set up used by researchers on the steel project consisted of a beam approximately 12 feet long connected to a column in the bolted web, welded flange manner used in steel moment-frame construction. The column was fixed in both the lateral and vertical directions at the bottom and only the lateral direction at the top. The free end of the beam was connected to a hydraulic actuator that exerted a cyclic load on the beam. This format is used to test an exterior column connection assembly. The load was controlled by a displacement history, simulating the loading of a connection as part of a moment frame subjected to a lateral load history (Warmka 2001). The diagram in figure 1.2 shows this, and figure 1.3 shows the load history applied to the specimen. As phase I of the SAC Steel Project, a pre-Northridge connection design assembly was tested. This specimen exhibited fracture of the top flange to the column flange weld during the first excursion to 3 Delta y, Delta y being equal to 1.40 inches of tip displacement. This fracture occurred in the top flange as opposed to the bottom flange weld fracture observed after the Northridge earthquake because this test set up does not include a composite slab above the beam, which raises the center of gravity and increases the moment arm of the bottom flange.

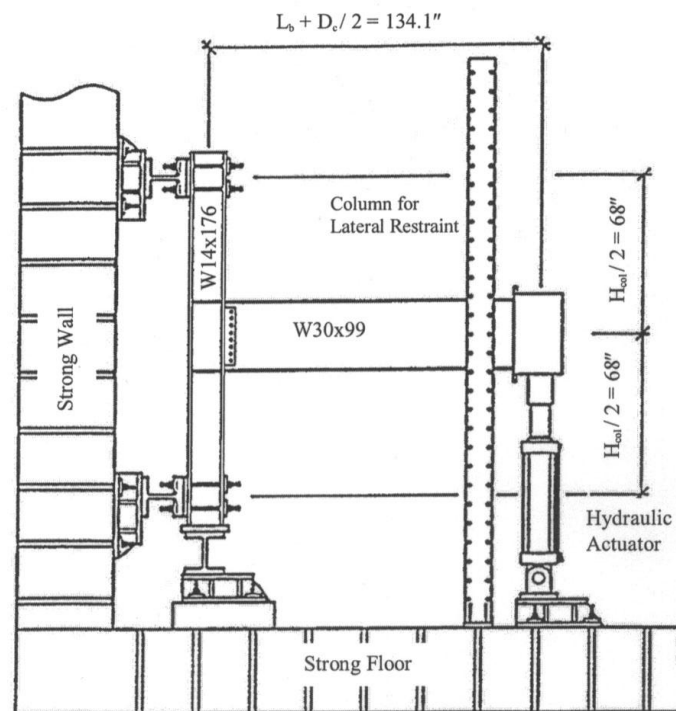


Figure 1.2 SAC test set up

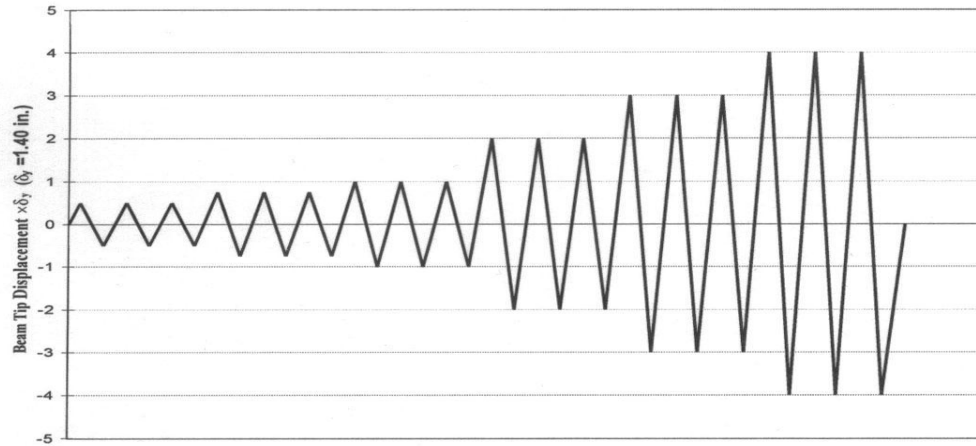


Figure 1.3 Beam tip displacement history (Warmka, 2001)

1.22 Brittle Fractures

Figure 1.4 shows the common zone of fracture initiation in the pre-Northridge connection. It was typical for the fractures to initiate at the complete joint penetration (CJP) weld between the beam bottom flange and column flange. Once the fractures have initiated, they progress along a number of different paths. The path of progression depends on individual joint conditions. Figure 1.5c shows a fracture that progresses completely through the thickness of the weld. Upon removal of the fire protective finish, the fractures were evident as cracks through the exposed faces of the weld. Other patterns developed into the flange of the column directly behind the CJP weld as shown in figures 1.5d – 1.5g. In figure 1.5d the crack has resurfaced above the CJP weld. This portion of the column flange has pulled free of the rest of the column; however, it is still connected to the weld and beam flange. This pattern is often called a “divot” or “nugget” failure. In severe cases the fractures extended completely through the column flange on a near-horizontal plane aligning approximately with the beam lower flange (figure 1.5f). The most severe cases saw these fractures progress all of the way into the web of the column and extended across the panel zone (figure 1.5g) (FEMA 350).

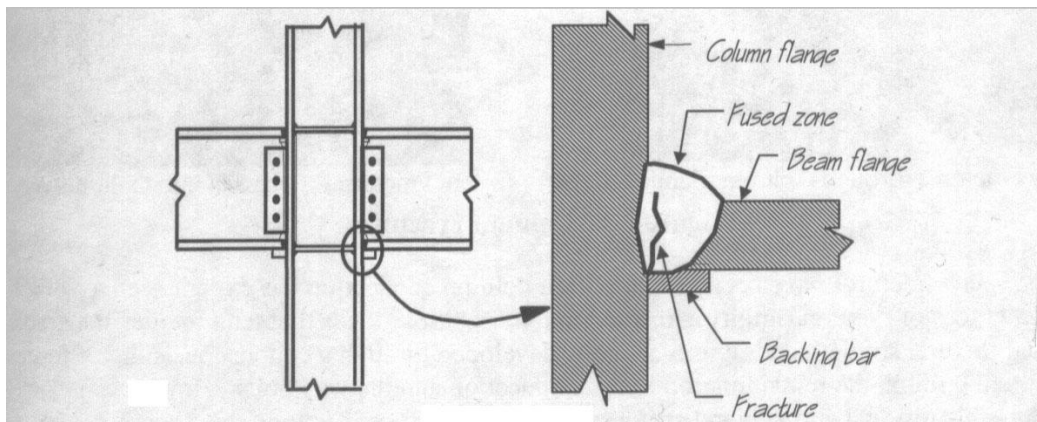


Figure 1.4 Common zone of fracture initiation in beam – column connections (FEMA 350)

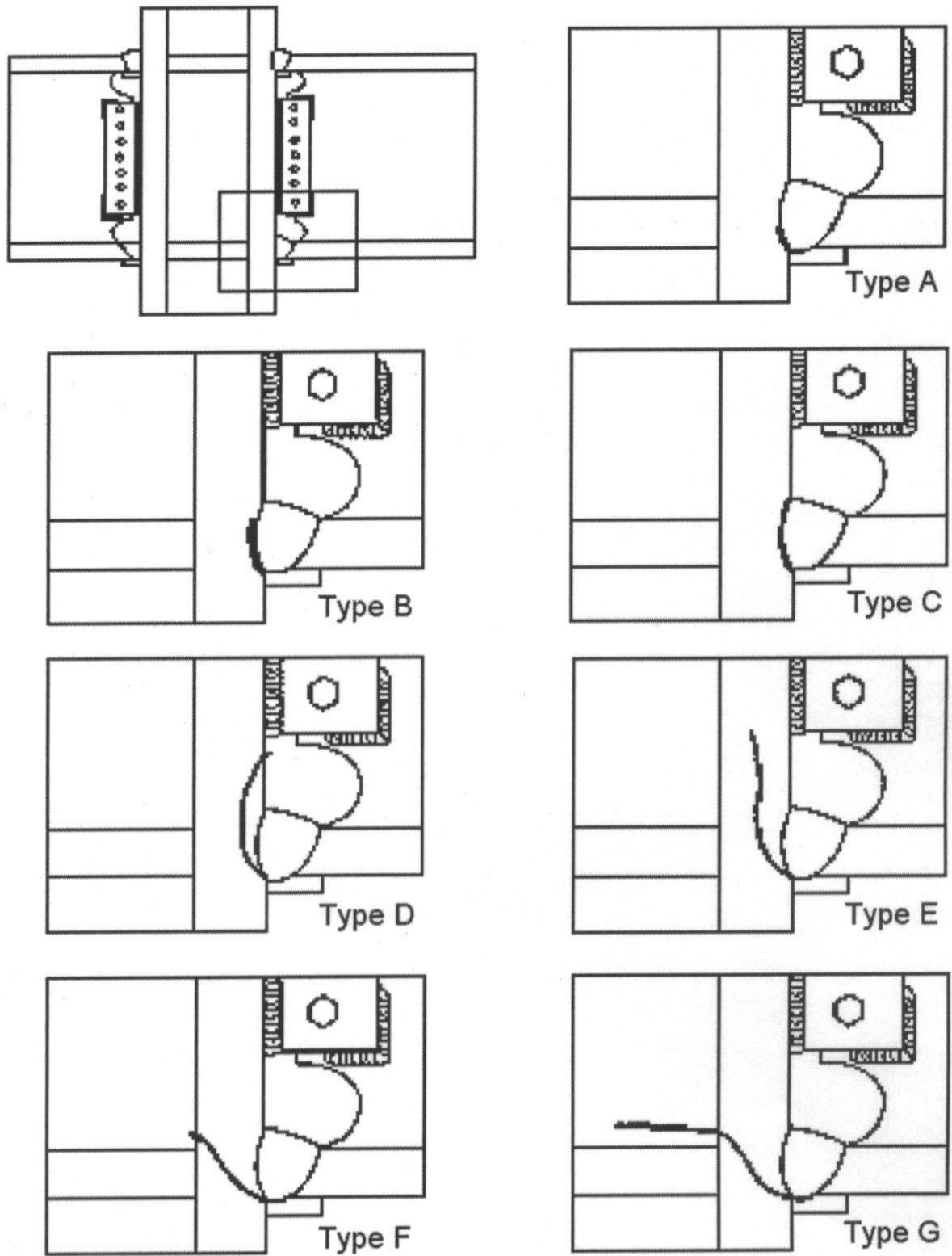


Figure 1.5a-1.5g Examples of the types of fractures seen in steel welded connections following the 1994 Northridge Earthquake (Warmka, 2001)

2 Methodology

2.1 Finite Element Analysis

The data collected from the SAC Steel Project allows for the development of accurate finite element models (FEM) that can be used to test further specimens at a fraction of the cost. In order for these models to work they must first be developed and tested versus the data extrapolated by the SAC researchers. Once the models can be shown to have mimicked the data they can be elaborated on to determine the performance of alternative or more specific designs.

FEM breaks the object into small (finite, having measurable or definable limits) pieces (elements). These elements are defined by nodes. In the case examined here 20 nodes are used to define one element as shown in figure 2.1. Once the model is “drawn” boundary conditions and a load history are applied. The analysis program will then determine the resultant forces on each element and from that the reaction of the entire model.

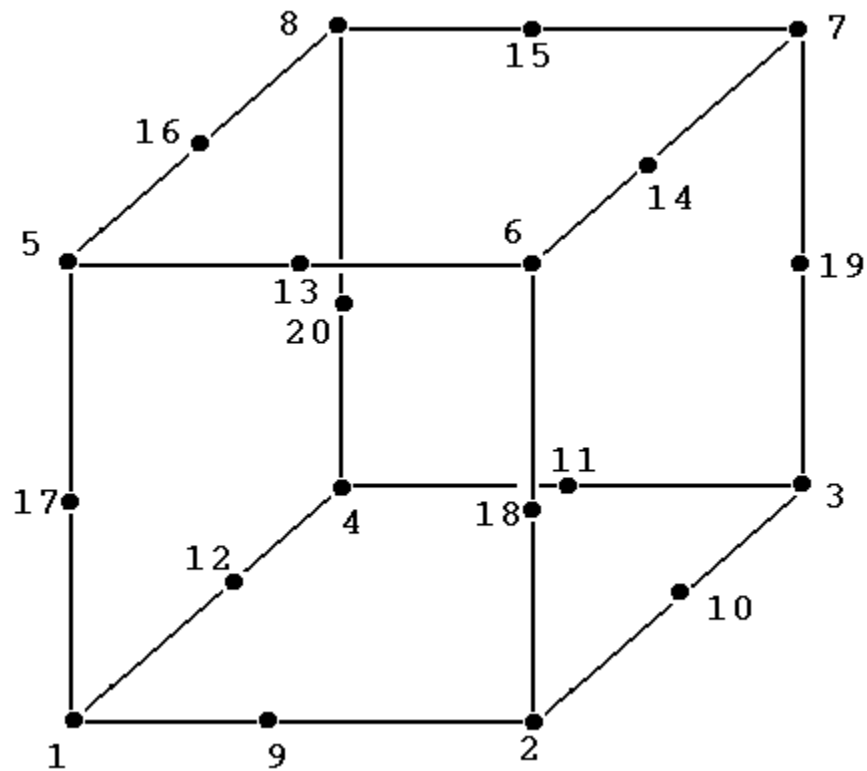


Figure 2.1 ABAQUS C3D20 Element

2.2 ABAQUS

ABAQUS is a medium used for FEM analysis developed by Hibbit, Karlsson, and Sorensen, Inc. Using ABAQUS/Standard a simple 2 dimensional plate was developed and then elaborated on until the model was that of a W30x99 beam. Due to time constraints on

the project the complete connection to a column could not be done. Further research on such models would be quite interesting.

3 Finite Element Model Analysis of a pre-Northridge Connection

3.1 The model shown in figure 3.1 is the model of a pre-Northridge connection used in this research. The beam is a standard W30x99. The density of the model will affect both the validity of the results and the computational time necessary to analyze the model. If a model is too dense it will likely be very accurate, but it will take a very long time to get the results. On the other hand, if a model is not dense enough it will only be accurate to a certain degree, but the computation time will be significantly reduced. Notice that figure 3.1 shows one side of the beam as more dense. That end is the fixed end that would connect into the column flange. This was done to improve the results as well as facilitate the development of the model.

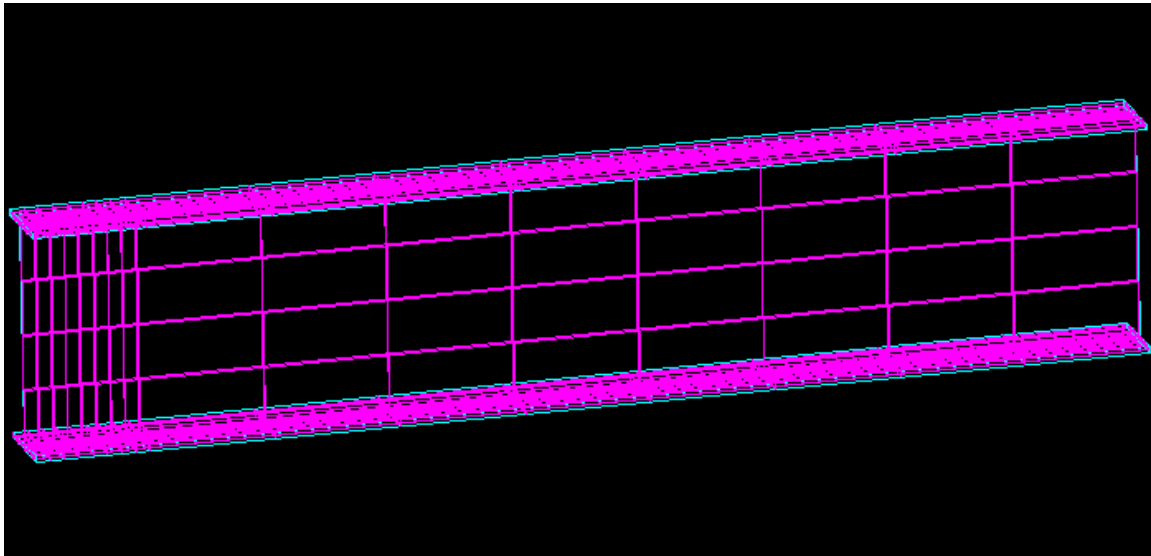


Figure 3.1 pre-Northridge Model

The less dense end of the model was the loaded end. A theoretical point load of 200 kips was applied through the height of the beam and evenly distributed over eight points. This kept the model from showing large stresses at the point of loading. Several assumptions were made in the construction of this model. Some of the assumptions are untrue, but due to time the affect was found to be acceptable. There are three major untrue assumptions. First, it is assumed that the column has no role in the dissipation of the energy introduce by the earthquake. The panel zone in the column web between the stiffeners will be the first portion of the connection to approach first yield (Warmka 2001); therefore, the column plays a rather large role in energy dissipation. However, the purpose of this research was to understand the stress paths in the beam so that the column could be omitted. Second, the material that makes up the beam is of uniform quality and all properties are equal in every direction. This assumption removes the human factor from the connection and assumes the beam was made perfectly isotropic. Also, a rolled steel shape is stronger in the direction of its rolling (Warmka 2001). The third assumption is that this model does not

tie into a composite floor slab. As discussed before a composite slab will raise the center of gravity and increase the stress on the bottom flange connection

3.2 Unfortunately, due to time and problems outside anyone's control, the model was not able to be analyzed. Through reading research done by Gary Warmka, theoretical results can be included. It would be ideal to run through such a process for all of the FEMA pre-qualified connections in order to have a more complete understanding of the steel moment-frame connection. Hopefully time and resources will someday allow for further research on this topic.

Works Sited

Working Papers:

Warmka, Gary. "Northridge Connections" School of Engineering and Applied Science, Washington University, Saint Louis, MO 2001

Government Documents:

Federal Emergency Management Agency. FEMA-350 Recommended Seismic Design Criteria for New Steel Moment-Frame Buildings
FEMA Washington, D.C. 2000

Federal Emergency Management Agency. FEMA-351 Recommended Seismic Evaluation and Upgrade Criteria for Existing Welded Steel Moment-Frame Buildings
FEMA Washington, D.C. 2000

Federal Emergency Management Agency. FEMA-350 Recommended Postearthquake Evaluation and Repair Criteria for Welded Steel Moment-Frame Buildings
FEMA Washington, D.C. 2000

Federal Emergency Management Agency. FEMA-350 Recommended Specifications and Quality Assurance Guidelines for Steel Moment-Frame Construction for Seismic Applications
FEMA Washington, D.C. 2000

Evaluation of Post-Earthquake Functionality of Highway Overpass Bridges

Ryan Vignes

University of Iowa

University of California at Berkeley

Advisors:

Bozidar Stojadinovic, Assistant Professor

Kevin Mackie, Graduate Student

*“London Bridge is falling down,
Falling down, falling down.
London Bridge is falling down...”*



EVALUATION OF POST-EARTHQUAKE FUNCTIONALITY OF HIGHWAY OVERPASS BRIDGES

Ryan Vignes
University of Iowa

University of California at Berkeley

Advisors:

Bozidar Stojadinovic, Assistant Professor

Kevin Mackie, Graduate Student

Abstract

The ability to assess the functionality of a bridge after an earthquake is of vital importance, not only to prevent the loss of lives, but to minimize economic disruptions. Currently, to determine if a bridge is functional after an earthquake, inspectors examine each bridge for structural damage. The inspectors then determine whether the bridge can still support traffic and remain open, or whether the bridge has been damaged to an extent that it must be closed. In the past, when such empirical methods of observation were all that existed, a bridge could only be qualified as open or closed. With the advent of computers and finite element techniques in modern engineering analyses, it has become possible to evaluate bridge functionalities more accurately. One goal of PEER's post-earthquake bridge functionality project is to determine the effect different earthquake intensities have on a bridge's strength and stiffness. These correlations will then be used to help determine when it is necessary to close a bridge to all traffic, when a bridge can remain open to all traffic, and when a bridge can remain open if the amount and speed of traffic are reduced.

INTRODUCTION

When determining whether a bridge is functional after an earthquake, inspectors must travel to each bridge site to examine the columns, abutments, supports and bridge decks for damage. From these observations, the inspectors determine whether the amount of damage requires the bridge to be closed, or whether it can still support traffic and remain open. This decision is based on observations such as the amount of spalling on columns, deck displacement, size, depth, and density of cracks, etc. However, this method for evaluating bridge functionality is extremely subjective in that it is highly dependent upon the inspector and his qualitative judgment. Besides the many qualitative measurements, the amount of experience an inspector has also influences whether a bridge remains open, or whether it is closed and traffic diverted. An overly cautious inspector may needlessly close a still operational bridge, while another inspector could leave a moderately damaged bridge open to traffic. The overly cautious inspection needlessly diverts traffic resulting in an unnecessary disruption of commerce and other economic transactions while the other inspector subjects motorists to poor driving conditions and damaged bridge decks, and if the bridge were to collapse, the possibility of death.

As a supplement to this subjective method of bridge analysis, the Pacific Earthquake Engineering Research Center (PEER) has developed a new probabilistic method that eliminates the dependence on engineering parameters and empirical observations of column and deck damage when determining the bridge's functionality. This model predicts the extent to which the bridge is damaged given that an earthquake

with certain intensities has occurred. Given these earthquake intensities, it can more accurately be determined whether a bridge must be closed or can remain open. With this model, it is also possible for a slightly damaged bridge to remain operable. While the bridge may not have the operational capabilities it had before the earthquake, it can still remain open as long as certain restrictions are applied, such as reduction in number of vehicles on the deck at a given time, or a reduction in speed.

LINEAR-ELASTIC BRIDGE MODEL

Before analyzing how bridges react during an earthquake, a bridge model had to be created. Rather than building a physical scale model of a bridge, computers were used. The first bridge to be modeled consisted of all linear-elastic elements. At the University of California, Berkeley, Professor Filippou has created a finite element package, called FEDEAS, which was used in the modeling and analysis of the linear bridge model. A bridge script file was written so the height, width, span and other properties could be varied. Once these parameters were entered, the program would then create column and beam elements containing relevant material properties such as the modulus of elasticity, inertia, area, etc. for the bridge. Once all the necessary properties were defined, the beams and columns were connected and given boundary conditions. The column boundaries were fixed in all six degrees of freedom: F_x , F_y , F_z , M_x , M_y , and M_z , while the beam elements at the abutments were pinned in the F_z direction. A graphical image of the bridge was then generated from the supplied information (see Fig. 1). The x-axis is oriented along the width of the bridge, while the y-axis runs along the length, and the z-axis is perpendicular to the deck.

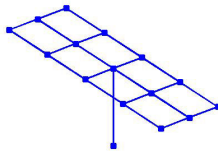


FIGURE 1. Linear bridge model generated by FEDEAS

With the bridge completely defined, the next step was to load the bridge and analyze its performance. Many of the finite element tools from FEDEAS' programs were used to analyze the bridge's performance. After applying point loads at the connectivity nodes, the structural forces and displacements were recorded in output files, and the bridge image from Fig. 1 was recreated, only this time the axial, shear and bending moments each bridge member experienced were imposed on top of the bridge model. Fig.2 depicts the M_x bending moments of the bridge elements' in their local orientations, not the global coordinates. In local coordinates, the x-axis is along the length of each element, while the y and z-axes are in the plane perpendicular to the x-axis.

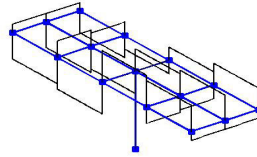


FIGURE 2. M_x bending moment for the linear bridge model

After insuring all the forces and displacements were correctly calculated, the point loadings were changed to a unit loading, which allowed for an influence line to be created. An influence line is a graph that depicts the variation of axial, sheer or bending moments at a given point on a structure due to an applied unit load at any given point on the same structure. It graphically depicts the largest force experienced by a specific point for each load location along the structure. The bridge's influence line was created so that when integrated with a truckload, the bridge's response to traffic could be analyzed.

An extension of the two-dimensional influence line into three-dimensional space created an influence surface. This influence surface represented the bridge deck and the forces it experienced as a truckload moved across the bridge. It depicts the location on the bridge where a truckload will cause the largest moment with respect to the column connection, and hence represents the worst place for a truck to be on the bridge. Fig. 3 depicts the maximum transverse bending experienced by the top of the column as a unit load is moved across the bridge deck. As the figure shows, the unit load created zero

moment when applied at the pinned edges of the bridge, but as the load was moved across the bridge along the outside girders, the induced moment continually increased until it reached a maximum at half the span length. After the maximum moment was reached, the moment decreased until it was once again zero at the far abutment. As Fig. 3 shows, the moments on either side of the column were equal in magnitude, but opposite in sign. Since the moments were calculated with respect to the column joint, the moments had to have opposing signs on opposite sides of the column in order to account for the column's reaction in supporting the bridge deck.

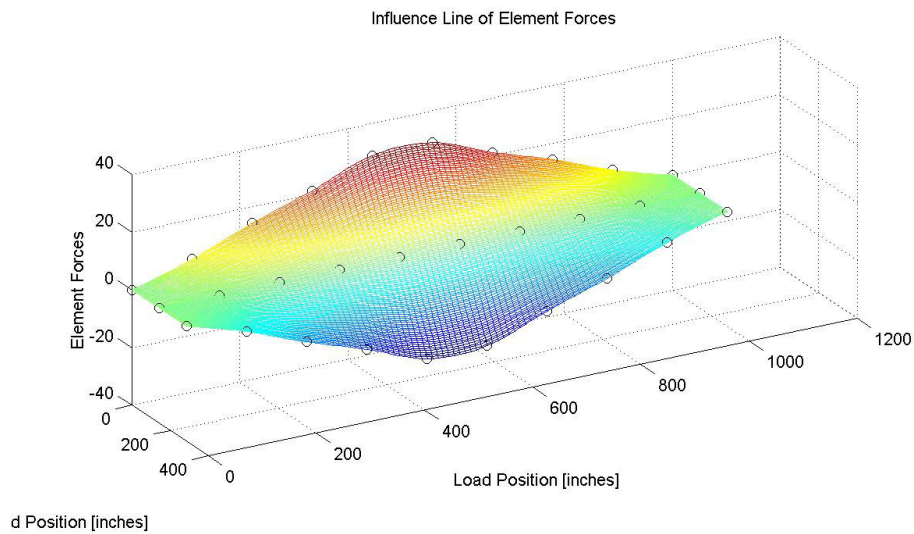


FIGURE 3. M_z influence surface for column connection

NONLINEAR BRIDGE MODEL

Once the linear bridge model was performing correctly, the analysis was extended using a nonlinear bridge model. Nonlinear beam and column elements were required to create the nonlinear bridge model which allowed the bridge model to become damaged. Due to their elastic stress-strain properties, linear elements cannot be damaged, and only served as a rough model as to how a bridge reacted to forces; a nonlinear bridge was needed to portray exactly how an actual bridge responded. FEDEAS can only handle two and three-dimensional linear analysis and two-dimensional nonlinear analysis, so for the nonlinear bridge analysis, it was necessary to switch from FEDEAS to OpenSees. "The Open System for Earthquake Engineering Simulation (OpenSees) is a PEER sponsored project to develop a software framework for simulating the seismic response of structural and geotechnical systems. OpenSees is intended to serve as the computational platform for research in performance-based earthquake engineering" [OpenSees 01].

After converting the linear FEDEAS bridge into an OpenSees model, it was possible to perform a nonlinear analysis on the bridge. Although many bridge properties were already defined from the linear bridge, a few additional ones were still needed for the bridge to be expanded to a nonlinear model. The linear bridge model assumed the beams and columns were created with uniform material properties. The material properties of the linear bridges were unimportant; the materials just needed to be strong enough to supply a resistive force so as not to collapse when the load was applied. Since the linear bridge always remained in the elastic region of the stress-strain diagrams, the internal force within each element could be calculated by statics and interpolation. The

nonlinear bridge, however, did not remain within the elastic region of the stress-strain diagrams. The nonlinear elements initially underwent elastic deformation, but as the force upon the members increased, the bridge elements began to strain harden and inelastically deform.

The extent to which these deformations occurred depends upon the material make-up of the beams and columns. In order to give material properties such as confined concrete, unconfined concrete, and rebar to the beams and columns, it was necessary to break the beams and columns into smaller pieces, which were then further reduced into cross-sectional elements. These cross-sectional elements were reduced even further to fiber elements. The advantage of fiber elements was the ability to specify the material property make-up and location within the beams and columns; the materials no longer had to be uniformly distributed across the cross sectional area. To create these fiber elements, an analysis program called UCFyber was used. "UCFyber can handle the input of any arbitrary cross section (even with holes) made up of any material input from the available nonlinear material models. It then calculates the moment curvature and axial force moment interactions for concrete, steel, prestressed and composite structural cross section" [UCFyber 01]. The bridge deck was modeled in UCFyber as a three-lane wide reinforced concrete box girder, while the supporting column was modeled as a five and a half-foot diameter circle of reinforced concrete. UCFyber then calculated the cross sectional properties of the deck and column, which were then exported into two separate OpenSees files and used in the nonlinear bridge analysis. With these files and the previous information specified from the linear bridge, the beam and column elements

were then connected and the end joints were fixed in the same manner as the linear bridge model.

As with the linear bridge model, once the bridge's properties were defined, the beams and columns connected, and the bridge boundaries fixed, it was time to load the bridge. Initially, the bridge was given a light loading to insure it remained within the elastic region of the stress-strain curve and allowed for the forces and displacement to be compared with an identically load linear bridge. Once these calculated forces and displacements were in agreement, the nonlinear bridge was given a uniformly distributed gravity load, and OpenSees' finite element tools were then used to load the bridge incrementally until failure.

OpenSees contained two different methods in which structures could be loaded. One method allowed for load increment control, which increased the loading applied to the bridge by a constant amount until the bridge reached failure and collapsed. For each load, the resulting structural displacements, forces, and moments were calculated. In a similar manner, the second loading method used displacement control, which increased the structural displacement by a constant amount with the magnitude of the load depending upon the degree of displacement. At each displacement level, the resulting load, forces and moments were calculated. These displacements, forces, and moments, from either of the two methods, were then used in a pushover analysis to examine how the bridge reacted when loaded.

Following this, the nonlinear bridge was employed to analyze the bridge when the strength and stiffness of the column and beams were reduced. The bridge was then reloaded, with either a displacement control or load control setting, for the various reduced strength and stiffness states until the bridge again reached failure. These reduced strength and stiffness bridges were used to establish a reference state to which an earthquake damaged bridge could be compared.

To create an earthquake-damaged bridge, an earthquake that behaved in the manner of the 1980 Livermore earthquake, as recorded from the San Ramon Fire Station, was selected to damage the bridge. All of the San Ramon Fire Station's intensity measures were scaled by a factor of two, and the undamaged, nonlinear bridge was simulated being hit by this scaled earthquake. This gave the bridge an unknown reduction in strength and stiffness, which was then loaded by OpenSees in the same manner as previously discussed. The amount of force required to displace the earthquake-damaged bridge was compared to the known reduced-state bridges, which enabled the extent of damage the earthquake had inflicted upon the bridge to be established. This analyze necessitated the creation of the force-displacement diagram shown in Fig. 4.

Fig. 4 shows that as the bridge elements were reduced in strength and stiffness, less force was required for a larger displacement. By matching the slope of the earthquake-damaged bridge to a bridge with the known damage state, the extent of damage done by the earthquake was determined.

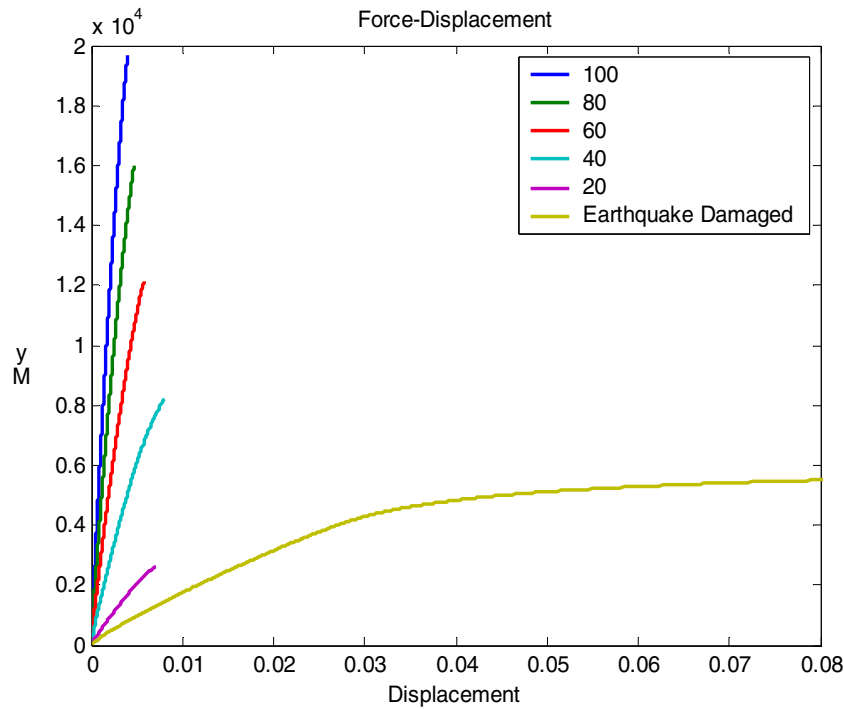


FIGURE 4: Force-displacement plot of different damage levels in the nonlinear bridge model, along with an earthquake-damaged bridge

CONCLUSION AND FUTURE WORK

Now that the nonlinear bridge is calculating and operating correctly, it would be useful to create an influence surfaces of the nonlinear bridge. The nonlinear bridge deck's influence surface would allow for an analysis of how a dynamic deck will alter the linear bridge's influence surfaces.

Also of interest would be how the bridge reacts to earthquakes of different magnitudes and durations. To make this comparison, the bridge will have to be damaged by many different earthquakes of differing intensities. Damaging the bridge may be accomplished by choosing an earthquake from a suite of recorded ground motions typical

for the region from PEER's Strong Motion Database. In a manner similar to PSHA (Probabilistic Seismic Hazard Analysis), the suite of recorded ground motions would be divided into bins based on characteristics such as magnitude and epicentral distance data. A benefit of using this bin approach is the ability to abstract individual earthquakes and consider the effect of generalized earthquake characteristics, such as frequency domain content, dominant period, or duration, on structural demand [Mackie 01]. Damaging the bridge with the previously discussed San Ramon Fire Station earthquake acted as a stepping stone toward the PSDA bin approach by relating the amount of structural damage (maximum traffic load that can be supported) sustained by the bridge to a specific earthquake. The method used for the San Ramon earthquake will be made more general to allow for different earthquakes from the different bins to damage the bridge. The bin approach allows specific earthquake intensities measures to be chosen and their affects on structural damage to be analyzed. By repeatedly damaging the bridge in this manner, trends in how an intensity measure correlates to the structural damage can be determined.

The goal of the OpenSees' bridge model was not to be an exact replica of an existing bridge, but rather to match a class of bridges. All the bridges in a seismic area would be classified as a certain type based on parameters such as the number of columns. After an earthquake, the functionality of all the different bridge classes can be evaluated instead of having to perform an inspection and evaluation on each individual bridge. The bridge's functionality is determined by examining the extent to which the earthquake reduced the bridge's strength and stiffness. To correlate the bridge's functionality to an

earthquake intensity measure, the maximum force the bridge can withstand can be determined from the force-displacement graphs. A demand model plot of maximum force versus earthquake measure can be created by repeatedly damaging a specific bridge class with different earthquakes, and then graphing the accumulated set of the maximum withstandable forces versus an earthquake intensity measure. By combining this demand model with a capacity model, the bridge's functionality can be determined. Once the bridge's functionality has been determined, the bridge's operating capabilities, such as a reduction in speed or traffic load carrying capacity, can be determined as a ratio of the undamaged capabilities to the damage capabilities. With the bridge's operating capabilities known, it can then be determined whether the bridge must be closed, can remain open with specified restrictions, or remain fully functional.

Fig. 5 depicts a sample fragility curve. The fragility plot displays the probability that the bridge sustains more damage than actually calculated (for a given damage state). This allows for the more general bridge class functionality to be determined. While the bridges in a specific class will perform similarly, the fragility curve allows for defects in the materials and other variations to be taken into account. The fragility curve depicts the probability that a given damage state is exceeded, while also representing the associated deviation by which the damage state was exceeded.

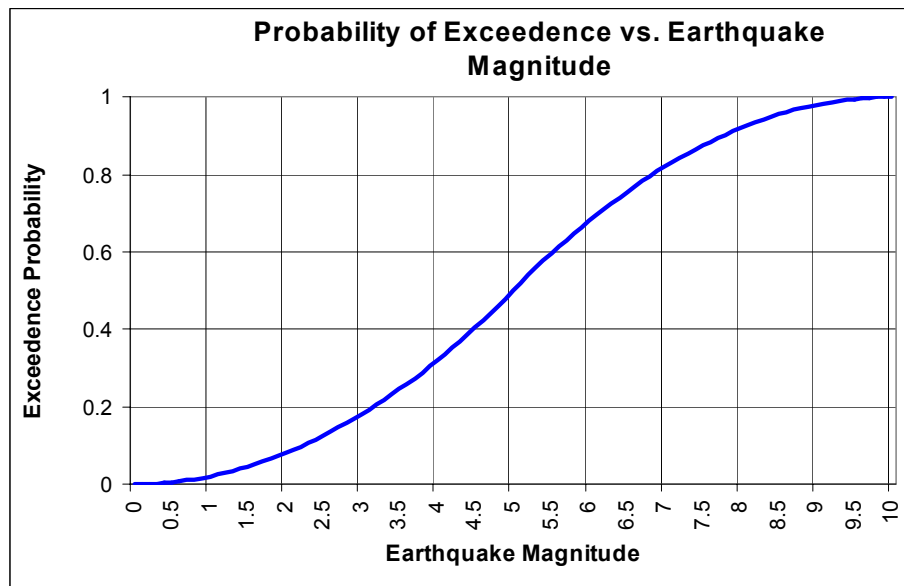


FIGURE 5: Sample plot of earthquake magnitude versus probability of damage state being exceeded.

So now, given that an earthquake of certain magnitude has occurred, the extent of structural damage to a bridge class can be determined. By knowing the extent of structural damage the bridge's functionality can then be ascertained, which allows for the bridge's operating capabilities to be determined. By knowing the extent of damage and the reduction in operating capabilities an earthquake of given intensities will cause to a class of bridges, it will be possible to develop and plan alternative emergency vehicle, traffic flow and network routes prior to an earthquake occurring.

ACKNOWLEDEMENTS

The research described in this paper has been made possible by the National Science Foundation, PEER Research Experience for Undergraduates Summer Internship Program 2001, and PEER Project 312 grant. I wish to thank Mr. Kevin Mackie and Professor Bozidar Stojadinovic for their help and advice during my internship and work on this paper.

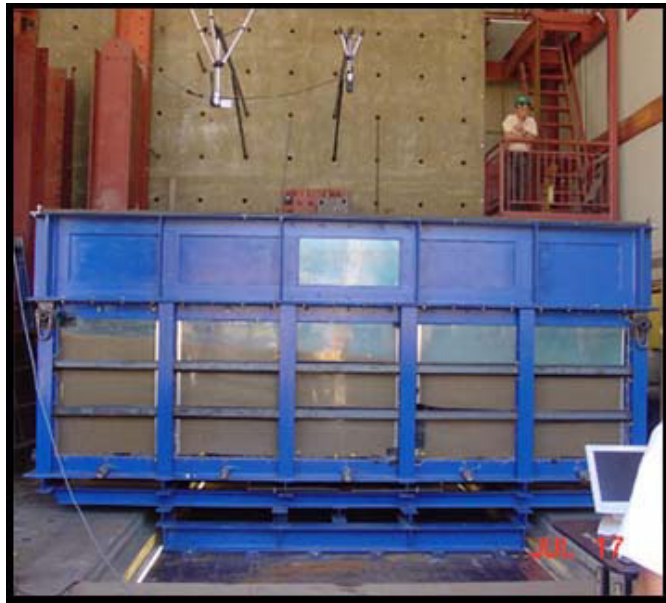
References

- [Mackie 01] K.Mackie and B.Stojadinovic, "Probabilistic Seismic Demand Model for California Highway Bridges", {ASCE Journal of Bridge Engineering}, to appear in November/December 2001.
- [OpenSees 01] Pacific Earthquake Engineering Research Center. (2001). Open System for Earthquake Engineering Simulation. Retrieved August 4, 2001, from the World Wide Web: <http://millen.ce.berkeley.edu/OpenSees/OpenSees.html>.
- [UCFyber 01] ZEvent Structural Engineering Computer Software. (2001). UCFyber. Retrieved August 4, 2001, from the World Wide Web: <http://www.zevent.com/>.

1g Shake Table Tests on Lateral Spread and Liquefied Sand-Pile Seismic Interaction

Claire Vukajlovich
California Polytechnic State University, San Luis Obispo

University of California, San Diego
Professor Ahmed Elgamal



Abstract

These experiments study lateral spreading occurring in liquefied soil during an earthquake. The final three tests evaluate the interaction of liquefied soil with model piles, two aluminum and one concrete. Tests occur in a large rigid-wall soil box mounted on a shake table. The box is filled with saturated sand whose ground surface is inclined six percent. Shaking lasts 12 seconds, with an amplitude of 0.35g and a frequency of 3 Hertz.

The ground-surface displacement, measured during the tests with a digital camcorder, shows lateral spreading. Strain gages in the model piles measure soil-pile interaction. Acceleration and pore water pressure are also recorded during shaking. The data from these experiments will be used to evaluate the modeling capabilities of OpenSees, a computer analysis program. Data from these experiments are posted on a Web site so people can learn about this new method of studying soil liquefaction.

Problem Studied

In 1985 when an earthquake hit Mexico City, some buildings remained standing but tilted at a significant angle. San Francisco has experienced large damages and fires during every recorded earthquake. A phenomenon called soil liquefaction causes these types of damage. Liquefaction occurs in saturated sand during earthquakes. The shaking settles the sand particles into a denser arrangement, forcing out the water that occupied the space between the sand particles. Since this occurs throughout the sand simultaneously the water cannot move. The pressure in the water increases, separating the individual sand particles. While the sand particles are separated, the soil loses its stiffness and acts like a liquid. In Mexico City the liquefied soil could not support the buildings. Liquefied soil flowed downhill and broke the gas and water lines in San Francisco.

Lateral spreading occurs when liquefied soil is inclined. During liquefaction the soil flows downhill, causing large displacements of the ground surface. These displacements break underground pipes and move buildings. Lateral spreading damages large areas that might not have been otherwise damaged during the earthquake.

Unfortunately, several major cities are built on liquefiable soil, including San Francisco, Mexico City, and many cities on the coast of Japan. The liquefiable soil is often a result of filling in an area of water with soil. For example, Mexico City was once a lake, and many coastal cities have filled in areas of their bays to expand the cities. The mechanics of soil liquefaction are not understood well enough to effectively design buildings to withstand its forces.

Objectives

The series of experiments studied the phenomenon of lateral spreading, where liquefied soil “flows” downhill, focusing on surface ground displacements. The last three experiments evaluated the interaction between liquefied sand and model piles. The data from these experiments will be compared to behavior predicted the computer modeling program Open System for Earthquake Engineering Simulation (OpenSees).

Research Approach

Previously in the United States, liquefaction studies relied on field tests. In these tests, full-scale piles are built at a site with liquefiable soil. Explosive charges liquefy the soil. During liquefaction, an actuator pushes against the piles, causing them to move in opposite directions. These tests are very expensive and time consuming.

The method used in this series of experiments uses a large, rigid-walled soil box on a shake table. The benefits of this method are: it is less expensive, it is easier to perform multiple experiments in a limited time, and the ground surface displacements can be accurately measured. Since the focus of the experiments was on ground surface displacements, the new method was appropriate for the project.

Preparation of Model Ground

All tests used sand #60, whose properties are shown in Fig. 1. The soil box was filled with water. Dry sand was poured into the water, where it passed through a vibrating screen to remove any air trapped between sand particles, shown in Fig. 2. The sand was deposited uniformly in the soil box. A sloping ground surface was made by altering the sand deposition. The soil height at the center of the soil box was 1.0 meter for the first two experiments, 1.4 meters for the third and fourth experiments, and 1.8 meters for the final three experiments. The ground surface was smoothed to the exact slope of six percent before the excess water was pumped out.

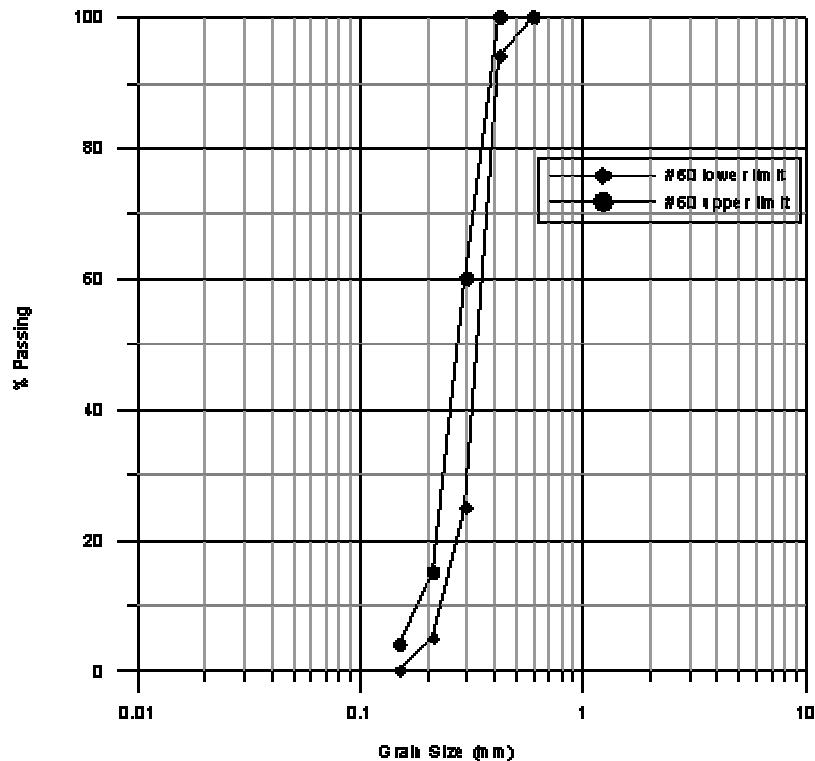


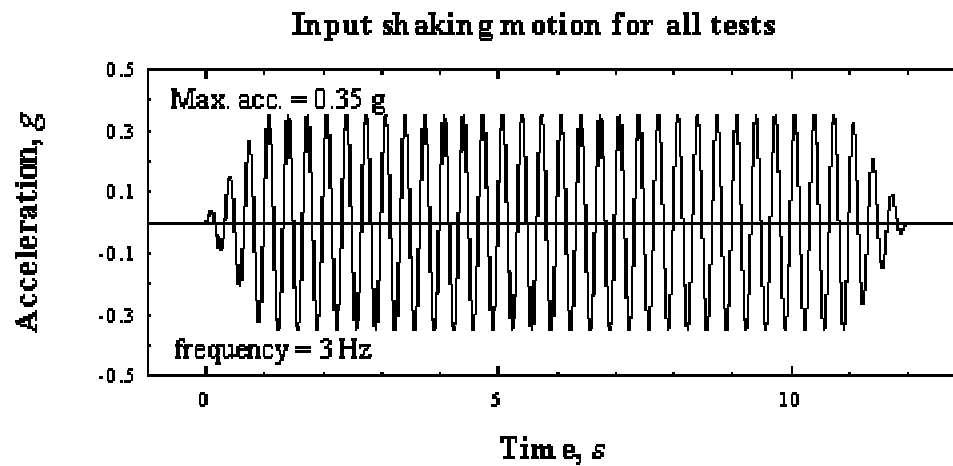
Figure 1: Grain size of #60 sand



Figure 2: Preparing model ground

Data Acquisition

All experiments used the input motion for the shake table shown in Fig. 3. The amplitude was 0.35g, the frequency was 3 Hertz, and the duration of shaking was 12 seconds. The first and last seconds were a linear increase from and decrease to zero respectively.



Acceleration and pore water pressure

During shaking, accelerometers measured surface accelerations and accelerations along a vertical array within the soil. Pore water pressure transducers measured the pore water pressure at several depths in the soil. The locations of all accelerometers and pore water pressure transducers for the final experiment are shown in Fig. 4.

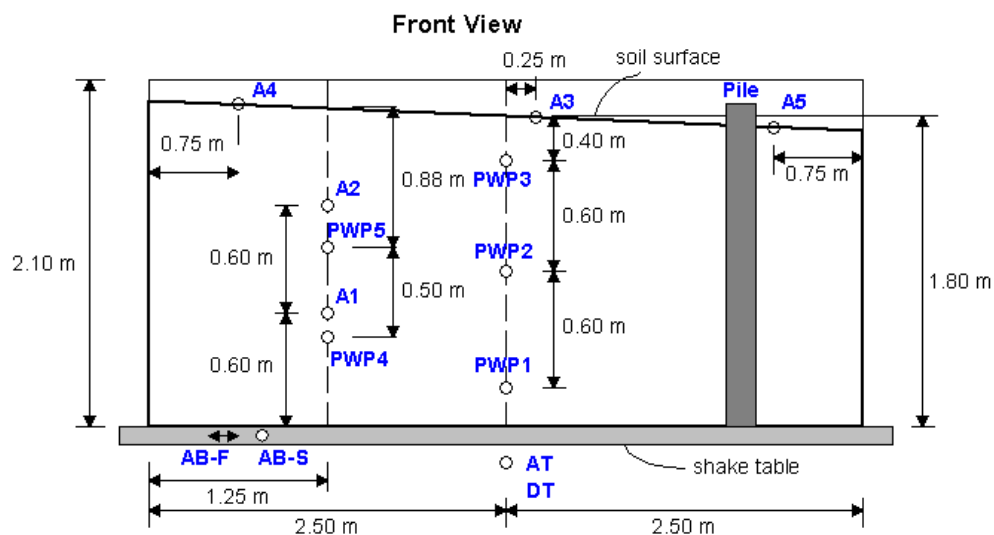


Figure 4: Instrument locations

Displacement

There were two methods of recording the ground surface displacements. One-inch diameter targets were placed on a 0.3-meter by 0.5-meter grid, and their positions were measured before and after the shaking. These displacements showed the overall displacement of the ground surface. There were also two sets of four targets placed on 0.1-meter by 0.1-meter squares. These targets were videotaped with a high-speed camcorder connected to a computer that generated a time history of the displacement of each target. Fig. 5 shows the ground surface before shaking.

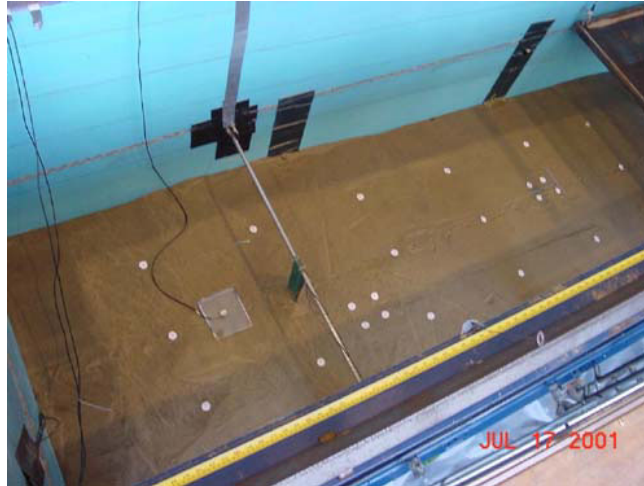


Figure 5: Targets placed on the ground surface

Strain in Piles

The fifth and sixth tests had two aluminum model piles fixed to the bottom of the soil box. These piles had strain gages attached at the uphill and downhill inside faces at locations shown in Fig. 6. The data from these strain gages showed how the pile and the soil interacted. A concrete model pile with similar instrumentation replaced the aluminum piles in the final test.

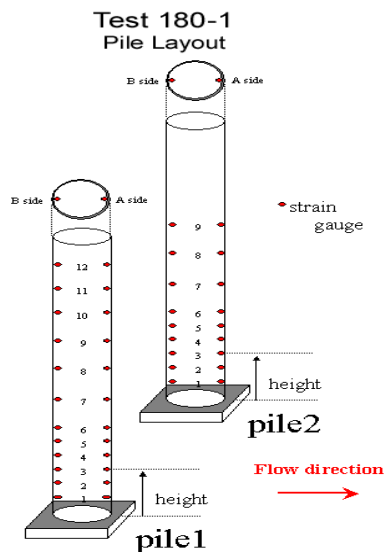


Figure 6: Strain gage locations on aluminum piles

Data Processing

The acceleration time histories were not very accurate because the accelerometers rotated when the sand liquefied. This caused the recorded acceleration to be smaller than the actual acceleration. Several attempts were made to prevent rotation of the, but none of the solutions allowed the accelerometer to move with the soil.

The pore water pressure data identified when the soil liquefied. As seen in Fig. 7, the first point the pore water pressure reaches the effective stress is when the soil liquefies. The horizontal line at approximately three kPa is the effective stress, which is based on the depth of the location and the density of the soil above the location. At approximately one second, the pore water pressure crosses this line, so the soil liquefied approximately one second after the shaking began. When combined with the displacement time histories, this data shows how the soil behaves before and after liquefaction.

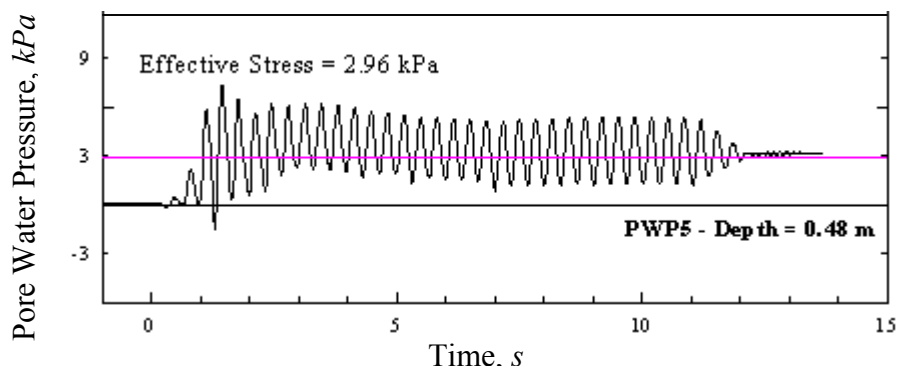


Figure 7: Pore Water Pressure

The displacement data was plotted to show the initial and final target locations, as seen in Fig. 8. The displacement time histories of the videotaped targets were used to find the velocity of the soil. The maximum displacement of the soil, approximately 0.1 meter, occurred at the center of the soil box.

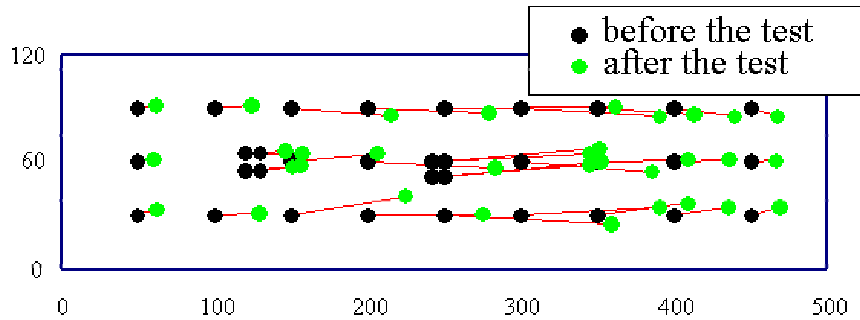


Figure 8: Target locations before and after the test

Computer Model

Another group will build and analyze a computer model of the soil with OpenSees. The data from the experiments will be compared to the results of the computer analysis to check the accuracy of the program.

Website

Since this was the first test of its kind performed in the United States, it was important to document the experiment so other researchers could learn about this new method. A Web site, earthquake.ucsd.edu/lqexperiment, shows the procedure used to prepare the model ground, conduct the experiment, and remove the sand afterwards. Data and videos from all experiments are also available on the site.

Outcomes

Testing ended at the end of the internship, so analysis of the data is not yet available. Some general observations can be made, though. The strain gage data from the experiments with piles show that the liquefied soil applies a lateral load to the pile. The data from one of the strain gages in the uphill side of a pile is shown in Fig. 9. The strain is positive, indicating that face of the pile is in tension. The increase in strain, and thus lateral load, coincides with the liquefaction and lasts approximately three seconds. During the last eight seconds of shaking, there is no strain in the pile. The liquefied soil flows downhill and pushes on the pile as it flows. Further analysis of the strain will give the loading applied to the pile during liquefaction.

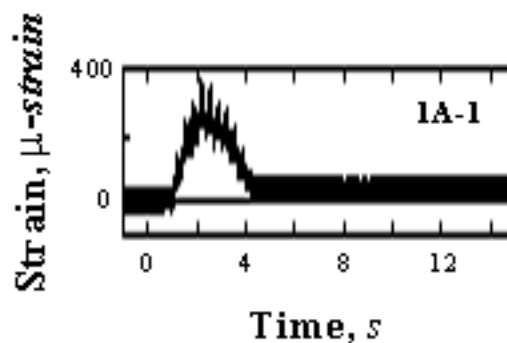


Figure 9: Strain in aluminum pile

Possible Future Work

As mentioned previously, the data from these experiments will be used to verify the accuracy of the program OpenSees. Conducting further experiments with different soil properties would help further evaluate the capabilities of OpenSees. The soil box used in the experiments

has rigid walls that interact with the soil. Since the distance between the walls was relatively small, 1.2 meters, the rigid walls affected the soil behavior. Further experiments could be conducted with a larger distance between the walls or with little lateral stiffness.

Acknowledgements

I would like to thank the Pacific Earthquake Engineering Research Center and the National Science Foundation for the opportunity to participate in this internship program. I have learned many things this summer, both about my research topic and about graduate research in general. I thank Professor Pardoen and Gina Ring from PEER for their help and friendship, and for making the program run so smoothly.

I am grateful for the opportunity to work at the Structural Engineering department at the University of California, San Diego. I appreciate the help of Professor Ahmed Elgamal and Dr. Jorge Meneses, who made my internship enjoyable and educational. Thanks to Ryan Suarez, Yuji Fujiwara, Atsushi Hirao, and Makoto Kurita for answering my questions and making my time in San Diego fun.

References

- Gibson, A. D. and Scott, R. F. "Comparison of a 1g and centrifuge model dynamic liquefaction test: preliminary results", Earthquake Geotechnical Engineering, First International Conference on, A.A. Balkema, Rotterdam, Vol. 2, 1995, pages 773-778.
- Gohl, W. B.; Finn, W. D. Liam. "Seismic response of single piles in shake table studies", Earthquake engineering: Fifth Canadian Conference, proceedings; Ottawa, July 6-8, 1987. A A Balkema, Rotterdam, 1987, pages 435-444.
- Gupta, M. K. and Prakash, S. "Sand liquefaction during shake table vibration", Proceedings, Sixth World Conference on Earthquake Engineering, Sarita Prakashan, Meerut, India, 1977, Vol. III, pages 2169-2174.
- Hamada, M.; Sato, H.; Nakamura, T. "An experimental and numerical study on liquefaction-induced ground displacement", Fifth U.S. National Conference on Earthquake Engineering, Proceedings, Earthquake Engineering Research Inst., Oakland, California, Vol. IV, 1994, pages 169-178.
- Isihara, K.; Kagawa, T.; Ogawa, N.; Minowa, C.; Sakai, K. and Abe, A. "Design of large-scale liquefaction experiment system", Wind and Seismic Effects: Proceedings of the 28th Joint Meeting of the US-Japan Cooperative Program in Natural Resources Panel on Wind and Seismic Effects; Gaithersburg, Maryland, May 14-17, 1996.
- Kanatani, M.; Nishi, K. and Touma, J. "Large shake table tests of saturated sand layer and numerical simulations by nonlinear analysis method", Earthquake Geotechnical Engineering, First International Conference on, A.A. Balkema, Rotterdam, Vol. 2, 1995, pages 705-710.
- Raufaste, Noel J, ed. National Institute of Standards and Technology, Gaithersburg, MD, August 1996, pages 327-329.

Seismic Instrumentation of the I-40 Mississippi River Bridge in Memphis, Tennessee

Vickie L Watson

URA Final Research Report

National Science Foundation

The University of Memphis, Memphis, TN

Research Advisor: Dr. Shahram Pezeshk

October 12, 2001

ABSTRACT

The New Madrid seismic zone (NMSZ) is regarded by seismologists, engineers, and public officials as the most hazardous seismic zone in the Eastern United States. The city of Memphis in Shelby County, Tennessee, is geographically close to the southwestern segment of this zone. The purpose of this proposal is to develop and install a seismic instrumentation system to be deployed on and in the vicinity of the I-40 Hernando DeSoto Mississippi River Bridge in Memphis, Tennessee. This bridge is currently undergoing a retrofit in order to withstand a magnitude (m_b) 7 event at 65 km distance from the site with a depth of 20 km. The proposed I-40 bridge strong-motion instrumentation system, with 114 data channels at 25 different locations and at free-fields in the vicinity of the bridge, will provide a sufficient number of sensors to reconstruct of the behavior of the structure verify the response predicted by mathematical models. An accurate bridge model will be a cost-effective approach to evaluate the retrofit scheme, to investigate ways to improve bridge performance, and to reduce the possibility of catastrophic failure during a large seismic event. The data will be used to assess the performance of the bridge following the retrofit with emphasis in assessment of the performance of the base-isolation system used in the retrofit project. In addition, the sensors can also be used to develop a rapid warning system.

Introduction

The New Madrid seismic zone (NMSZ) is regarded by seismologists, engineers, and public officials as the most hazardous seismic zone in the Eastern United States. The city of Memphis in Shelby County, Tennessee, is geographically close to the southwestern segment of this zone. Memphis is potentially exposed to significant seismic hazards. Any large seismic event occurring anywhere within the NMSZ could cause widespread loss of life with damage to buildings, bridges, and lifelines due to ground shaking and ground failure induced by the seismic event it is vitally important to

develop and install a seismic instrumentation system in the vicinity of the I-40 Hernando DeSoto Mississippi River Bridge in Memphis, Tennessee. This bridge is currently undergoing a retrofit in order to withstand a magnitude (m_b) 7 event at 65 km distance from the site with a depth of 20 km. The goal of the retrofit is to have the bridge fully operational following the maximum probable earthquake (2500 year return period). As part of the I-40 bridge retrofit, Friction Pendulum™ Isolation Bearings are being used to insure the integrity of the main spans of the bridge.

The retrofit will be completed in several phases. The first phase began in the summer of 1999. During the retrofit process, it is proposed to install strong motion instrumentation with 114 data channels at 25 different locations on the bridge and at the free field in the vicinity of the bridge.

Very little data is available on the response of long-span bridges during seismic events in the United States and elsewhere in the world. Due to the limited data, the ability to understand the behavior of such structures and to verify dynamic analyses performed on such structures during design, analyses, and retrofit phases is limited. Currently there are no long-span bridges instrumented in the NMSZ. Instrumentation of the I-40 Bridge in Memphis will provide valuable data in evaluating the structure. The data will be used to assess the performance of the bridge following the retrofit and in particular for the assessment of the performance of the base-isolation system that will be used in the retrofit project.

The proposed I-40 bridge strong-motion instrumentation system with 114 data channels at 38 different locations will provide a sufficient number of sensors to reconstruct of the behavior of the structure in sufficient detail to verify the response predicted by mathematical models. Using data collected from smaller earthquakes, an improved mathematical model of the bridge can be developed. Furthermore, a well-instrumented structure for which a complete set of recordings has been obtained, should provide useful information to:

- (1) check the appropriateness of the dynamic model in the elastic range,

- (2) determine the importance of nonlinear behavior on the overall and local response of the structure,
- (3) follow the spreading nonlinear behavior throughout the structure as the response increases and determine the effect of this nonlinear behavior on the frequency and damping,
- (4) correlate the damage with inelastic behavior models,
- (5) determine the ground-motion parameters that correlate well with bridge response and/or damage,
- (6) quantify the interaction of soil and structure (this is particularly important for the I-40 bridge which is located on 3000 feet of soil), and
- (7) make recommendations to improve seismic codes and/or future bridge designs.

An improved model of the I-40 bridge can be used to predict potential damage/failure that the structure may experience during larger seismic events. An accurate bridge model will be a cost-effective approach in evaluating the retrofit scheme, investigating ways to improve bridge performance, and reducing the possibility of catastrophic failure during a large seismic event. A good example is the data recorded from the Vincent-Thomas Bridge in Los Angeles Harbor. Figure 1 shows the vertical acceleration record obtained from center of side span of the bridge during the Northridge earthquake. This location recorded the largest peak acceleration. The amplitude spectra for two 40-second bands (20-60 second and 80-120 second) exhibit two distinctive frequencies suggesting that some form of deformation occurred in the mid-span to alter its frequency (Celebi, paper in preparation). As a result of studies of the bridge, including those that utilized this record, deficiencies in the bridge were

realized and a retrofit program was developed that will eliminate possible failure during a larger event.

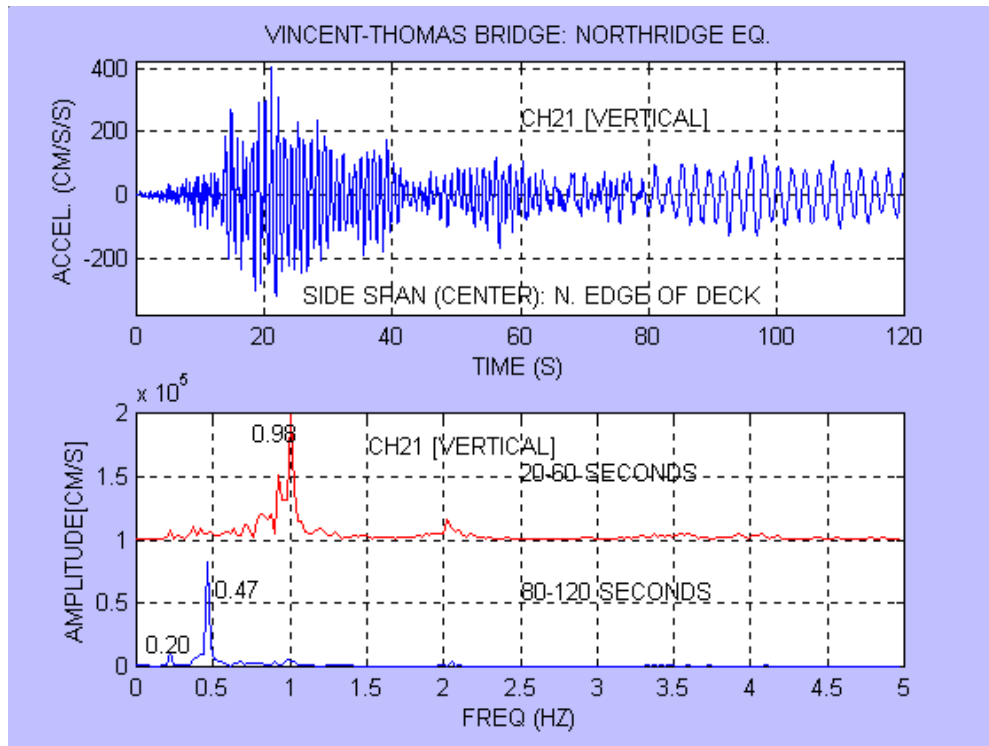


Figure 1. The recorded acceleration time-history of vertical motions at center of side-span exhibited the largest peak acceleration during the 1994 Northridge earthquake. This record also shows that the frequency of the bridge changed drastically (to 0.47 Hz [~ 2 sec]) during the last 40 seconds of the record as compared to the 20-60 second band (0.98 Hz [~ 1 sec]).

The I-40 bridge instrumentation, when complete, will be used to develop a rapid warning system. The system will be triggered when certain acceleration thresholds at designated locations on the bridge are exceeded. Key officials at the Tennessee Department of Transportation will be automatically notified of the exceedance of a

threshold earthquake within minutes over standard communication devices. This information will help determine the forces that the bridge sustained in a large earthquake and should aid engineers in determining if the bridge should be closed or/and what precautions rescuers and engineers should take. This type of monitoring and the associated rapid response may save lives.

Project Plan

In this project, we plan to install 114 sensors on the I-40 Hernando Desoto Mississippi River Bridge in Memphis, Tennessee to fully characterize the response of the bridge to strong ground motion. The location of the I-40 bridge is shown in Figure 2. Figures 3 and 4 shows the main two-span tied arch bridge. The general location and sensing directions for sensors on the main span are marked in Figures 3 and 4. The final locations of the sensors may be adjusted based on field investigations. Figure 6 shows Arkansas-side approach spans, while Figure 5 shows the east main approach structure and connecting ramps on the Memphis side. Figure 6 also shows the general location and sensing direction for sensors on the approach spans. The information to be measured from the sensors includes: (1) free-field ground motion near the instrumented bridge; (2) motion of the bridge foundation; (3) motion of the bridge below the isolation bearings; (4) motion of the bridge above the isolation bearings; (5) the spatial variation of ground motion along the total span; and (6) lateral and torsional motion of the bridge.

Measurement of Free-Field Motion

The free-field ground motion is the basic required information for a seismic response analysis of the bridge. It can be measured by two triaxial accelerometer located in Mud Island near the main span of the bridge (see Figure 4). These sensors

record the ground motion in two horizontal directions and in the vertical direction. Placing the free-field sensors on Mud Island will help avoid the effect of structural response (soil-structure interaction) on the recorded ground motion; thus, the free-field sensors should not be placed too close to the instrumented bridge. The free field sensors will be installed and operated through funds from the Advanced National Seismic System (ANSS).

Measurement of Bridge Foundation Motion

The motion at the bridge foundation can be measured by a tri-axial accelerometer placed on the pile cap at Pier C and Pier 28. These sensors will record the foundation motion, including the effect of soil-structure interaction, in two horizontal directions and a vertical direction. An estimate of the soil-structure interaction effect may be obtained by comparing the motion recorded at the bridge foundation and in the free field.

Measurement of Bridge Motion

Sensors in transverse, longitudinal, and vertical directions can measure the bridge motion as shown in Figure 3. These sensors will record the motion at bridge piers above and below their isolation bearings and at the mid-spans of the main span. These sensors will measure transverse, longitudinal, and vertical motions of approach spans. Using data recorded by these sensors, we can establish the dynamic characteristics of the bridge, such as vibrational mode shapes, structural periods, and main span deflections in the longitudinal, the transverse, and the vertical direction. The torsional response will be estimated from the motion recorded by pairs of sensors

placed on opposite sides of the bridge deck. The effect of base-isolation will be estimated by comparing the motion recorded above and below the isolation bearings.

Instrumentation

The bridge monitoring system will consist of a network of 32 tri-axial accelerometers. Two sensors will be located in boreholes in the footings at either end of the monitored section of the bridge. Two additional down-hole sensors are planned for Piers A and B, as the retrofit of the bridge piers continues. All other sensors will be located at the roadway level above and below the isolation bearings, and on either side of expansion joints.

Low noise FBA type sensors will be utilized for the locations on the pier caps, in the footings and at some locations on the bridge deck. The significantly noisier locations on the bridge deck will be monitored using lower cost silicon microelectronic accelerometers. All of the low noise site accelerometers will be connected to 19 bit digital, 12 channel recorders located at five locations on the bridge. Data from these recorders will be digitally telemetered at 2.4 GHz (utilizing free wave ISM band modems) to an existing recording site located at the Autozone Headquarters building on the riverfront in Memphis, Tennessee. The remaining bridge deck sensors will be telemetered at 218 MHz using high quality FDM systems to the same location where they will be digitally recorded at a resolution of 16 bits.

The sensor system will be configured with individual power systems for each digital recorder and FDM telemetry site. Furthermore, each of the seven recording and telemetry sites will have sufficient battery-supplied back up power to provide for one to three days of operation after an AC line failure. An additional battery backup system will allow for operation up to an additional 4 days after a power failure.

Data that can be collected from a felt earthquake will be valuable in a realistic, quantitative assessment of earthquake hazards of this region. Valuable lessons have been learned from the study of data obtained from well-instrumented structures. For example, the Imperial County Buildings, during the moderate-sized Imperial Valley earthquake (*M_s* 6.5) of October 15, 1979 (Cassaro et al. 1987 and Rojahn and Mork, 1982) and many buildings in San Francisco, during the Loma Prieta of October 18, 1989 (Krawinker et al. 1991) provided invaluable data about seismicity and structural performance. The collected data can be used in future code modifications and improvement of existing seismic codes.

Acknowledgments

This work was supported by the Mid-America Earthquake Center under National Science Foundation Grant EEC-9701785

Reference

- Cassaro, M., Celebi, M. (Coordinator), W. Durbin, P. Gould, W. Grahm, A. Johnston, H. Karabinis, A. Lin, R. Maley, O. Nuttli, G. Schwable, J. Theiss, M. Walsh, T. Winstead. (1987). "Report on Recommended List of Structures for Seismic Instrumentation in San Bernardino County, California; USGS Open-File, Report 85-583.
- Krawinkler, H., A. Nassar, and M. Rahnema. (1991). "Damage Potential of Loma Prieta Ground Motions." *Bulletin of the Seismological Society of America*, Vol. 81, No. 5, pp. 2048-2069.
- Rojahn, C. and P.N. Mork. (1982). "An Analysis of strong-motion Data from a Severely Damaged Structure - The Imperial County Services, El Centro,

California, in The Imperial Valley, California, Earthquake October 15, 1979." USGS Professional Paper. 1254.

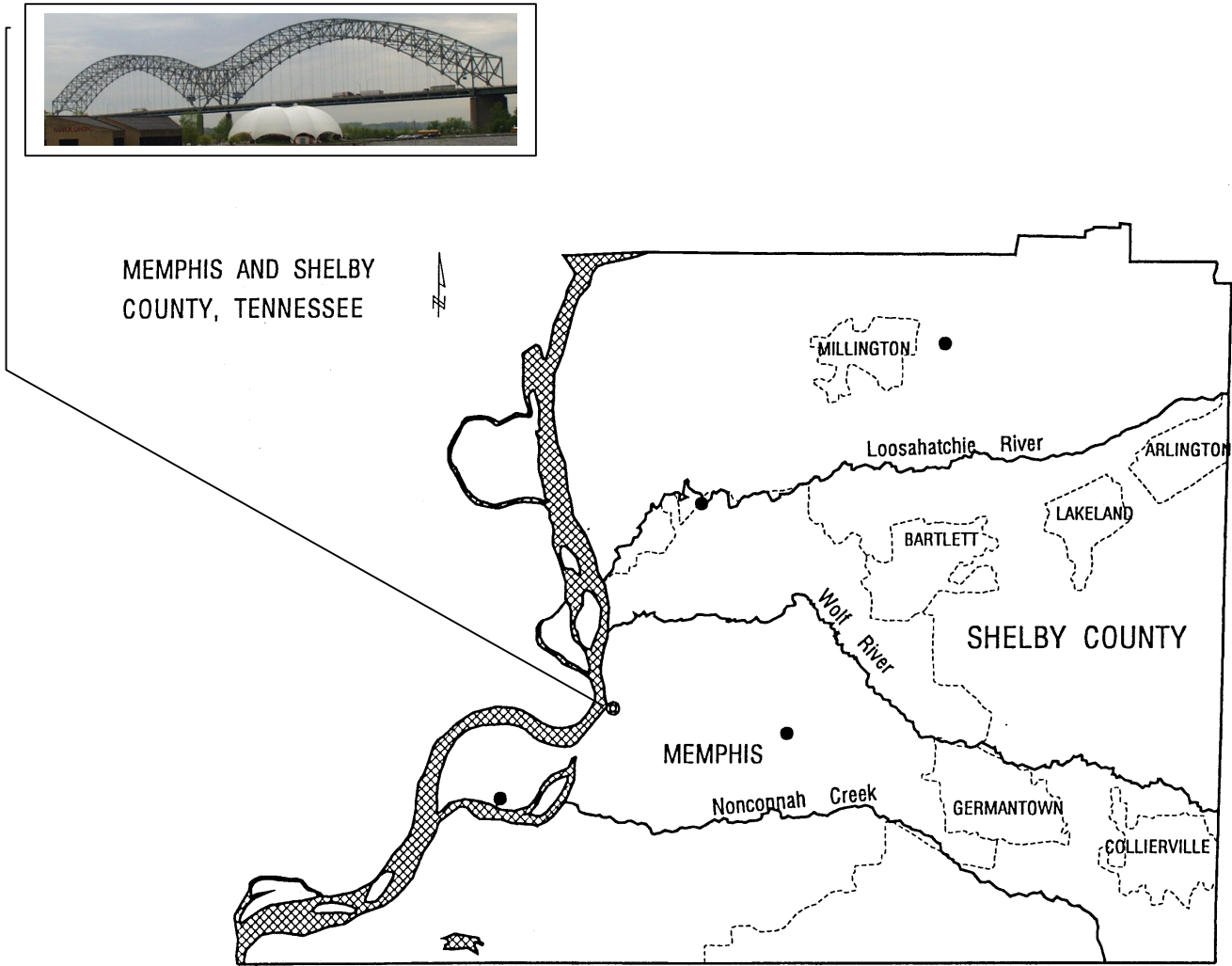


Figure 2. Location of the I-40 Hernando Desoto Mississippi River Bridge.

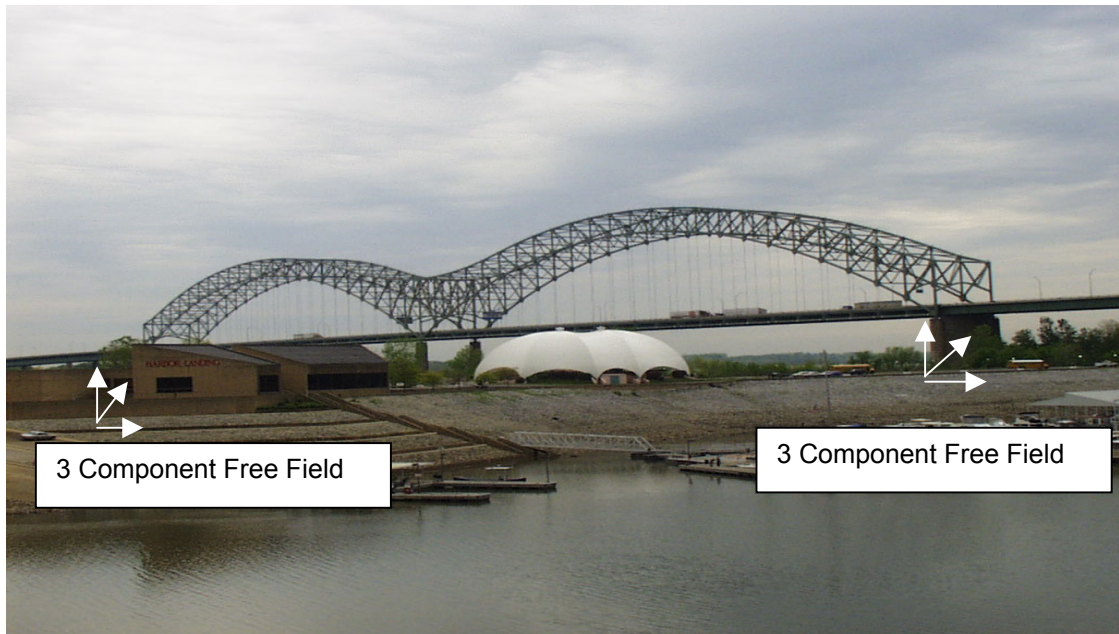


Figure 3. Mud Island and the location of the free field sensors.

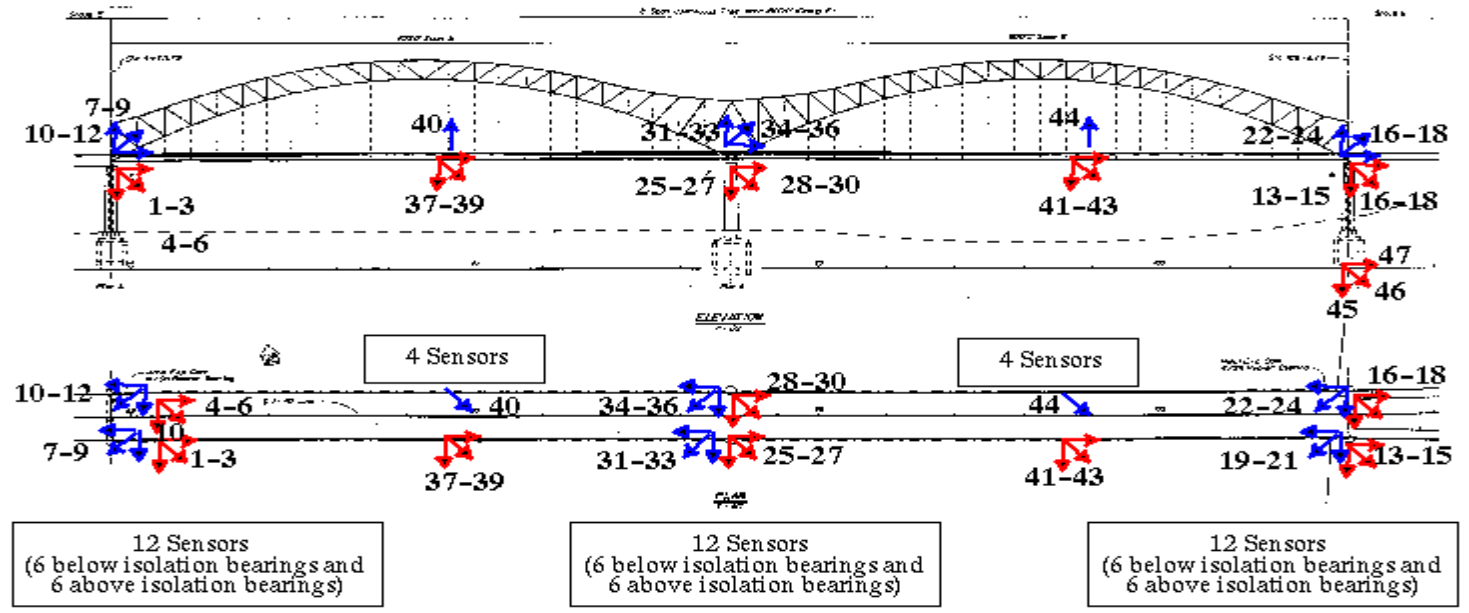


Figure 4. Main Two-Span Tied Arch of the I-40 Bridge and Sensor Locations

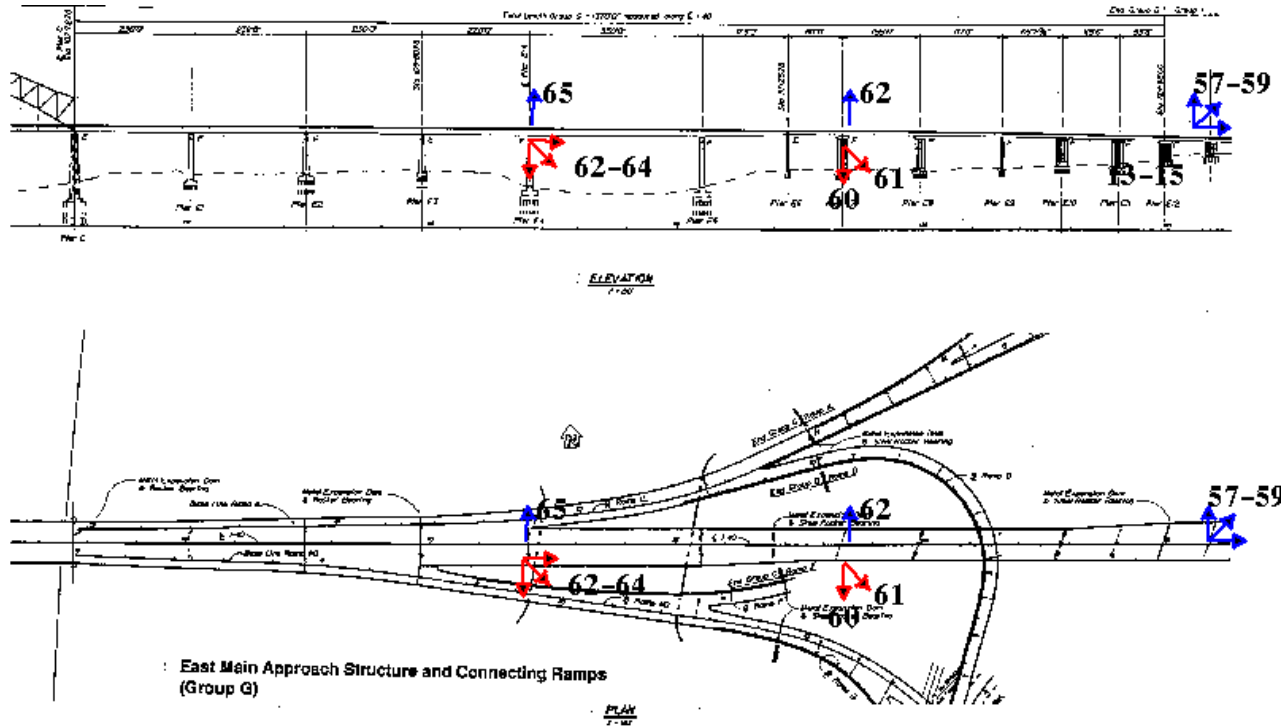


Figure 5. East Approach to the I-40 Bridge and Sensor Locations.

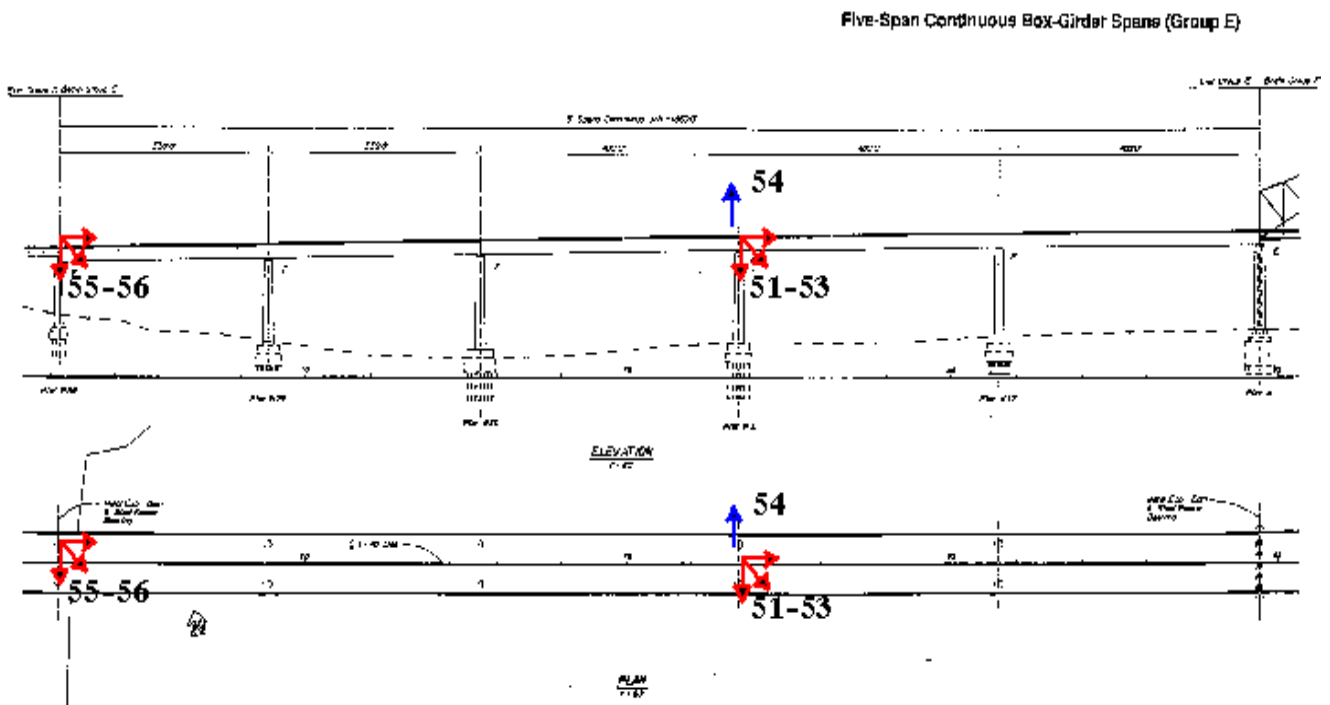


Figure 6 West Approach to the I-40 Bridge and Sensor Locations

**REU 2001 - EERC SYMPOSIUM FOR STUDENT RESEARCHERS
AUGUST 10 - 11, 2001**

**SPONSORED BY THE NATIONAL SCIENCE FOUNDATION
WYNDHAM HOTEL
SALT LAKE CITY, UTAH**

Thursday, August 9, 2001: *Participants arrive in Salt Lake City*

Friday, August 10, 2001: *Wasatch Room 3*

7:30 am *Continental Breakfast and Conference Registration*

8:15 am Plenary Session

- Welcome: EERC Representatives
Andrea Dargush, Multidisciplinary Center for Earthquake
Engineering Research (MCEER)
Professor Phillip Gould, Mid-America Earthquake Center (MAE)
Professor Gerard Pardoen, Pacific Earthquake Engineering
Research Center (PEER)
- Introductions: All
- Conference Overview: Andrea Dargush

8:30 am Student presentations: REU research project results
[Each presentation is allotted 10 minutes; 8 minutes for presentation,
2 minutes for questions.]

1. Malita Anders
2. Laura Barton
3. Rachel Dooley
4. Matthew Dryden
5. Malcom Foss
6. Peggy Ho

9:30 am *Break*

10:00 am Student presentations: REU research project results continued

7. Cathleen Kennedy
8. Ryan McDaniel
9. Michael Mio
10. Carlos Nazario
11. Gary Nottis
12. Michal Orlikowski

11:00 am *Break*

11:10 am Student presentations: REU research project results continued

13. Ryan Petersen
14. Stephen Priddy
15. Tyler Ranf

REU 2001 - EERC SYMPOSIUM FOR STUDENT RESEARCHERS
AUGUST 10 - 11, 2001

Friday, August 10, 2001 (continued)

- 11:40 am Discussion
- 12:00 pm *Lunch - Wasatch Room 4*
- 1:00pm Presentation: "Ethics in Engineering," Professor Ed Harris, Texas A & M University
- 2:00 pm Concurrent Breakout Sessions: Discussions of Engineering Ethics Case Studies assigned by Professor Harris (*Wasatch 3, Cedar, Juniper*)
- 3:00 pm *Refreshment break*
- 3:15 pm General Session: Group presentations of assigned ethical dilemma and approaches to resolution
- 4:15 pm Adjournment of Friday Program
- 6:00 pm *Reception - Hors D'oeuvres and No-host Bar - Parleys Room 1*
- 7:00 pm *Banquet - Red Butte*
- 7:45 pm After Dinner Presentation: "Designing for Earthquakes in Salt Lake City," Dr. Lawrence Reaveley, University of Utah
- 9:00 pm Wrap-up

Saturday, August 11, 2001

- 7:30 am *Continental Breakfast - Cottonwood Rooms 1 and 2*
- 8:30 am Student presentations: REU research project results continued
16. Pamela Romano
17. Mike Rookstool
18. John Sanders
19. Susan Smilanich
20. Carolyn Stegon
21. Josh Tolchinsky
- 10:30 am *Break*

REU 2001 - EERC SYMPOSIUM FOR STUDENT RESEARCHERS
AUGUST 10 - 11, 2001

Saturday, August 11, 2001 (continued)

- 10:45 am Student presentations: REU research project results continued
 22. Ryan Vignes
 23. Claire Vukajlovich
 24. Vickie Watson
- 11:15 am Discussion
 Wrap-up
- 11:45 am Adjournment
- 12:15 pm *Lunch - **Blue Spruce***
- 1:00 pm Pre-field Trip Presentation: Professor T. Leslie Youd, Brigham Young University
- 2:15 pm Meet in Lobby of Hotel for Downtown Salt Lake City Tour. Sites are accessible on foot or by TRAXX, free above-ground transit system.
- 2:30 pm Tour of Salt Lake City and County Building
- 4:00 pm TRAXX to Temple Square
- 4:30 pm Engineering Tour of LDS Church Conference Center
- 5:15 pm Walking Tour of Temple Square and Salt Palace Convention Center to view seismic design strategies
- 6:00 pm Arrive back at Wyndham Hotel. Symposium concludes.
- 6:30 pm Bus transportation to Snowbird.
 Informal picnic supper at Snowbird Resort.
- 10:00 pm Bus transportation to hotel.

Sunday, August 12, 2001.

Return home or sightsee and relax on your own.

REU Symposium, Salt Lake City, August 9-12, 2001

Participants List

Multidisciplinary Center for Earthquake Engineering Research Center (MCEER)

Malita Anders
Host Institution/EERC: University at
Buffalo/MCEER
REU Faculty Advisor : Professor Andrei Reinhorn,
Professor Andrew Whittaker
Home Institution: Central Florida University
1510 Emerald Lake Cove #109
Casselberry, FL 32707
Email: sparkle_be_dazzle@yahoo.com

Laura Barton
Host Institution/EERC: Cornell University/MCEER
REU Faculty Advisor: Tom O'Rourke
Home Institution: Rensselaer Polytechnic Institute
414 Nugent, RPI Residence
1999 Burdett Ave.
Troy, NY 12180
Email: bartol@rpi.edu

Michael Mio
Host Institution/EERC: ImageCat, Inc./
University of Southern California/MCEER
REU Faculty Advisor: Ron Eguchi
Home Institution: Univ. of California Santa Barbara
796 Embarcadero Del Norte #215
Goleta, CA 93117
Email : mmio00@umail.ucsb.edu

Gary N. Nottis
Host Institution/EERC: Lamont Doherty Earth
Observatory of Columbia University
REU Faculty Advisor : Klaus Jacob
Home Institution: Bucknell University
1605 W. Market Street
Lewisburg, PA 17837
Email: gnottis@yahoo.com

Michal Orlikowski
Host Institution/EERC: Univ. of Southern
California/MCEER
REU Faculty Advisor: Masanobu Shinozuka
Home Institution: Princeton University
412 Scully Hall
Princeton, NJ 08544
Email: morlikow@princeton.edu

Pamela J. Romano
Host Institution/EERC: Univ. at Buffalo/MCEER
REU Faculty Advisors: Drs. Andrei Reinhorn,
Andrew Whittaker
Home Institution: The Catholic University of
America
307C Millennium North
Cardinal Station
Washington, DC 20064-0001
Email: pjromano_cua@yahoo.com

John Sanders
Host Institution/EERC: Univ. of Delaware/MCEER
REU Faculty Advisor : Kathleen Tierney
Home Institution: Univ. of Illinois, Urbana
Champaign
2517 Clayton Boulevard
Champaign, IL 61822
Phone: 217-351-9858
Cell phone : 217-778-6119
Email: jrsander@uiuc.edu

MCEER Staff:

Andrea Dargush
Assistant Director for Education and Research
Administration
Multidisciplinary Center for Earthquake Engineering
Research
State University of New York at Buffalo
107 Red Jacket Quadrangle
Buffalo, NY 14261-0025
Phone: 716-645-3391 x 106
Fax: 716-645-3399
email: dargush@acsu.buffalo.edu

Karen Buchheit
Staff Assistant
Multidisciplinary Center for Earthquake Engineering
Research
State University of New York at Buffalo
Red Jacket Quadrangle
Buffalo, NY 14261-0025
Phone: 716-645-3391 x 126
Fax: 716-645-3399
email: saraf@acsu.buffalo.edu

REU Symposium, Salt Lake City, August 9-12, 2001

Participants List

Pacific Earthquake Engineering Research Center (PEER)

Rachel Dooley
Host Institution/EERC: Univ. of California,
Berkeley/PEER
REU Faculty Advisor: Mary Comerio
Home Institution: University of Michigan
2250 Woodlawn S.E.
Grand Rapids, MI 49546
Email: rdooley@engin.umich.edu

Carlos Nazario
Host Institution/EERC: Stanford University/PEER
REU Faculty Advisor: Eduardo Miranda
Home Institution: Univ. of Puerto Rico, Mayaguez
P.O. Box 6503
Mayaguez, PR 00681-6503
Email: carlosnazario@hotmail.com

Ryan Petersen
Host Institution/EERC: Univ. of California,
Berkeley/PEER
REU Faculty Advisor: Jack Moehle
Home Institution: Texas A & M University
6293 Wrangler Lane
San Angelo, TX 76904
Email: Boba7077@hotmail.com

R. Tyler Ranf
Host Institution/EERC: Univ. of Washington/PEER
REU Faculty Advisor: Dr. Marc O. Eberhard
Home Institution: Washington Univ. in St. Louis
6111 Pershing Ave. Apt. B
St. Louis, MO 63112
Email: rtr1@cec.wustl.edu

Mike Rookstool
Host Institution/EERC: Univ. of California,
Berkeley/PEER
REU Faculty Advisor: Jack Moehle
Home Institution: Univ. of Texas at Austin
4539 Guadalupe St. #A301
Austin, TX 78751
Email: mrook@mail.utexas.edu

Susan Smilanich
Host Institution/EERC: Univ. of Washington
REU Faculty Advisor: Professor John Stanton,
Professor Dawn Lehman
Home Institution: Cal Poly
San Luis Obispo
Email: bapsms@pacbell.net

Carolyn Stegon
Host Institution/EERC: Univ. of California,
Irvine/PEER
REU Faculty Advisor: Dr. Pardoen
Home Institution: Virginia Tech
434 Marlinton St.
Blacksburg, VA 24060
Email: cstegon@vt.edu

Ryan Vignes
Host Institution/EERC : Univ. California at
Berkeley/PEER
REU Faculty Advisor: Bozidar Stojadinovic
Home Institution: University of Iowa
Email: rvignes@engineering.uiowa.edu

Claire Vukajlovich

PEER Staff:

Professor Gerard Pardoen
PEER Assistant Director for Education
University of California, Irvine
Civil and Environmental Engineering Dept.
Engineering Gateway E4167
Irvine, CA 92697-2175
Phone: 949-824-7094
Fax: 949-824-2117
Email: gpardoen@uci.edu

Gina Ring
PEER Education Program Assistant
University of California, Irvine
Civil and Environmental Engineering Dept.
Engineering Gateway E4136
Irvine, CA 92697-2175
Phone: 949-824-3961
Fax: 949-824-2117
Email: gring@uci.edu

REU Symposium, Salt Lake City, August 9-12, 2001

Participants List

Mid-America Earthquake Center (MAE)

Matthew Dryden
Host Institution/EERC: Univ. of Memphis, Center
for Earthquake Research and Information/MAE
REU Faculty Advisors: Dr. Michael Ellis,
Dr. Roy Van Arsdale
Home Institution: Univ. of Illinois at Urbana-
Champaign
1001 S. Wright St.
Champaign, IL 61820
Email: dryden@uiuc.edu

Malcom Foss

Peggy Ho
Host Institution/EERC: MAE
REU Faculty advisors: Daniele Veneziano,
Joseph Sussman
Home Institution: Univ. Illinois Urbana-Champaign
904 West Green Street, Rm. 201
Urbana, IL 61801
Email: peggyho@uiuc.edu

Cathleen Kennedy
Host Institution/EERC: MAE
REU Faculty Advisor: Dr. Brad Cross
Home Institution: So. Illinois Univ. Edwardsville
109 Club Center Ct.
Apt. 2
Edwardsville, IL 62025
Phone : 618-692-1473
Email : cakenne@siue.edu

Ryan McDaniel
Host Institution/EERC: MAE
REU Faculty Advisor: Steve Horton
Home Institution: Univ. of Tennessee at Martin
117 Eunice St.
Martin, TN 38237
Email: pika@aeneas.net
ryadmcda@mars.utm.edu

Stephen Priddy
Host Institution/EERC: Georgia Inst. Of
Technology/MAE
REU Faculty Advisor: Dr. Roberto Leon
Home Institution: Univ. of Tennessee at Martin
1215 New Friendship Rd.
Beech Bluff, TN 38313

Josh Tolchinsky
Host Institution/EERC: Washington Univ. in St.
Louis
REU Faculty Advisor: Dr. Kevin Truman
Home Institution: University of Cincinnati
2824 Digby Avenue
Cincinnati, OH 45220
Email: tolchijb@email.uc.edu

Vickie Watson
Host Institution/EERC: MAE
REU Faculty Advisor: Dr. Shraham Pezeshk
Home Institution: University of Memphis
3996 Canterbury Drive
Memphis, TN 38122
Email: watsonvickie@hotmail.com

MAE Staff:

Professor Philip Gould
MAE Education Program Director
Washington University, St. Louis
Civil Engineering
Box 1130
1 Brookings Drive
St. Louis, MO 63130-4899
Phone: 314-935-6303
Fax: 314-935-4338
Email: pgoul@seas.wustl.edu

Sandra Menke
MAE Education Program Assistant
University of Illinois, Urbana-Champaign
Department of Civil and Environmental Engineering
1241 Newmark Laboratory
205 N. Mathews Ave.
Urbana, IL 61801
Phone: 217-244-8297
Email : smenke@uiuc.edu

REU Symposium, Salt Lake City, August 9-12, 2001

Participants List
Speakers and Tour Leaders

Ed Harris
Professor
Department of Philosophy and Humanities
Texas A & M University
Mail Stop 4237
College Station, TX 77801
Phone: 979-845-5697
Fax: 409-845-0455
Email: e-harris@philosophy.tamu.edu

T. Leslie Youd
Brigham Young University
Dept. of Civil & Environmental Engineering
368 Clyde Building
Provo, UT 84602-4081
Phone: 801-378-6327
Fax: 801-378-4449
Email: tyoud@buy.edu

Lawrence Reaveley
Department of Civil & Environmental Engineering
University of Utah
160 South Central Campus Drive, Room 104
Salt Lake City, UT 84112-0561
Phone: 801-581-6931
Fax: 801-585-5477
Email: reaveley@civil.utah.edu

Cover Images

Cover Images (from left, top row with inset): Dr. T. Leslie Youd is shown with a group of students during the field trip; (top row, middle): student research interns at the Symposium; (top right, with inset): Dr. T. Leslie Youd led a field trip to several seismically designed or retrofitted buildings in the Salt Lake City area. Shown is the historic city and county building, which was retrofitted with base isolators; (bottom left): Susan M. Smilanich, California Polytechnic State University; (bottom middle): view of Salt Lake City; (bottom right): Ryan Petersen's experience at PEER included testing of a woodframe multi-story apartment building.

Acknowledgements

This report was prepared by the Multidisciplinary Center for Earthquake Engineering Research through a grant from the National Science Foundation Earthquake Engineering Research Centers Program, New York State and other sponsors.

The material herein is based upon work supported in whole or in part by the National Science Foundation, New York State and other sponsors. Opinions, findings, conclusions or recommendations expressed in this publication do not necessarily reflect the views of these sponsors or the Research Foundation of the State University of New York.



MULTIDISCIPLINARY CENTER FOR EARTHQUAKE ENGINEERING RESEARCH

A National Center of Excellence in Advanced Technology Applications

University at Buffalo, State University of New York
Red Jacket Quadrangle ■ Buffalo, New York 14261-0025
Phone: 716/645-3391 ■ Fax: 716/645-3399
E-mail: mceer@acsu.buffalo.edu ■ WWW Site: <http://mceer.buffalo.edu>



Headquartered at the University at Buffalo